Unmanned Aerial Vehicle (UAV) Navigation and Image Processing Techniques for Underground Tunnel Infrastructure Assessment

A Dissertation Presented

by

Ran Zhang

for the degree of

Doctor of Philosophy

in

Civil and Environmental Engineering

University College Cork

Head of School: Prof. Jorge Oliveira

Supervisors:

Dr. Zili Li

2024

Thesis Declaration

This is to certify that the work I am submitting is my own and has not been submitted for another degree, either at University College Cork or elsewhere. All external references and sources are clearly acknowledged and identified within the contents. I have read and understood the regulations of University College Cork concerning plagiarism.

Signed:

Ran Zhang

Date:

17/12/2024

Acknowledgements

To begin with, I would like to extend my heartfelt thanks for Dr. Zili Li's constant help, unwavering support, and invaluable encouragement during this long voyage of mine. He began this journey with the foundation and ongoing guidance I received from their well-expanded field of knowledge as well as insightful evaluation. Their assurance in my abilities has been very influential in shaping this study into its present form.

I would like to express my special appreciation to Dr. Paul Leahy, Dr. Ciaran Hanley and Dr. Camillo J. Taylor who served on my dissertation committee; their penetrating critiques, guided questions about the methodology employed throughout my research, and insightful suggestions made at crucial junctures all combined to raise the intrinsic quality of this work considerably.

My deepest thanks go to all the faculty members and staff in the Civil Engineering department at University College Cork for providing me with a fertile academic atmosphere and the necessary means and ability to carry out research. The invaluable help and advice on data collection and analysis were generously offered by Dr. Jimmy Murphy, Dr. Brian Sheil, Dr. Chao Wang, Dr. Kai Zhao, Mr. Wei Lin, and Ms. Wanru Yang. I cannot express enough gratitude for the success of this research.

I must say that nothing more to my studies has meant so much as the constant loving encouragement given to me by my parents. Their trust in my abilities has encouraged me and put a great deal of wind under the wings of sensibility.

I must also pay tribute to my friends and fellow students: Dr. Zhipeng Xiao, Dr. Di Wang, Dr. Chongming Tian, Mr. Jian Liu, Dr. Ye Li, Dr. Kun Zhang, Dr. Shuoshuo Xu, Dr. Qinglai Zhang and more from various institutions in Europe, for all of the times we spent together in and after work, and for leading me in the direction that I wanted to go. Finally, I would like to extend my thanks to participants who offered the use of their time and revealed their own experiences. I could not have undertaken this study without you!

Dissemination of Research

Published

Zhang, R., Hao, G., Zhang, K., Li, Z.* (2023). Unmanned aerial vehicle navigation in underground structure inspection: A review. Geological Journal, 58(6), pp. 2454-2472. DOI: https://doi.org/10.1002/gj.4763

Zhang, R., Hao, G., Zhang, K., Li, Z.* (2024). Reactive UAV-based automatic tunnel surface defect inspection with a field test. Automation in Construction, 163, p. 105424, https://doi.org/10.1016/j.autcon.2024.105424

Papers under review

Zhang, R., Galvin, R., Li, Z.* (2023). Drone-Based Geological Heritage Conservation and Exploration: Insights from Copper UNESCO Geopark - [EMID:27f045a7d7d59950]

Zhang, R., Wang, C., Li, Z.* (2024). Automatic inspection of underground twin tunnel cross passage using a reactive UAV-based method

Selection of Oral Presentations

Zhang, R., Ouyang, A., Li, Z.* (2023). Automatic UAV Inspection of Tunnel Infrastructure in GPS-Denied Underground Environment. In: Rizzo, P., Milazzo, A. (eds) European Workshop on Structural Health Monitoring. EWSHM 2022. Lecture Notes in Civil Engineering, vol 254. Springer, Cham.

Zhang, R., Li, Z., (2023) UAV data acquisition method for transportation tunnel inspection, 4th International Symposium on Machine Learning and Big Data in Geoscience symposium series, Cork, Ireland, pp. 212-214

Zhang, R., Li, Z., (2023) Automatic UAV surface inspection method for underground infrastructure – a case study of Dublin Port Tunnel, International Conference on Sustainable Development in Building and Environment - SuDBE 2023, Aalto, Finland.

Zhang, R., Li, Z.* (2024) Data extraction of tunnel point clouds from images captured by robotic camera, Proceedings of 85th EAGE Annual Conference & Exhibition, Oslo, Norway.

Awards received for this work

John Murphy Fellowship in Civil Engineering Department, UCC

Excellent presentation on UAV inspection research at the Ireland-China PhD Forum.

Abstract

In many countries across the world, hundreds of kilometres of tunnel infrastructure networks require regular inspection and maintenance to ensure the safety and serviceability of lifeline transportation systems. Large-scale underground infrastructure comprises twin tunnel cross passages, shafts, caverns, and other complex geometries, which poses great challenges for efficient onsite inspection and even health and safety issues for workers in underground environments. Compared to conventional inspections by workers and ground vehicles or robotics, Unmanned Aerial Vehicles (UAVs) emerge as a cost-effective and adaptive monitoring tool, particularly suited for the access to shafts and caverns. However, there are challenges in implementing UAV-based inspection for tunnels, including GPS-denied environments, complex geometries, and limited flight time. To address these issues, this study proposes a UAV inspection method to provide an efficient and reliable UAV-based solution for tunnel infrastructure assessment.

The Proximity Move-Pause-Photo for Surface Defect Inspection (PMPP-SDI) methodology is a technique for UAV tunnel inspection. The method uses flexible flight routines to follow the tunnel lining, enabling comprehensive coverage of the tunnel surface. This real-time reactive control generates coloured imagery data, as well as a densified point cloud for precise local spatial information. The method demonstrates a balance between cost and performance of automatic tunnel inspection. And it has the potential to reveal defects and irregularities at a smaller scale compared to previous research using tunnel segments as the unit of analysis. It also allows for image processing-based surface defect identification.

An innovative image processing workflow is presented for UAV tunnel image

processing. This workflow allows the generation of 3D tunnel models, an area that hasn't been accomplished in previous research. This workflow facilitates tunnel geometry and defect analysis for comprehensive tunnel health inspection in both spatial information and surface defects. Spatial information extraction is enabled using a Digital Surface Model (DSM), which supports UAV control examination and geometry examination. Additionally, surface defect identification and quantification are carried out through segmentation of the orthomosaics of the model. Furthermore, the workflow integrates machine learning (ML)-driven point cloud trimming and defect identification to ensure precise model reconstruction and defect analysis, thereby improving overall accuracy in tunnel inspections.

A field test of the proposed UAV navigation and image processing method is carried out in a railway tunnel, targeting defect detection and tunnel health assessment. The uneven illumination and lack of GNSS signals in the tunnel make manual inspection challenging. The findings reveal the tunnel lining's deformation pattern, with distinct deformation zones identified based on the colour of the stone and brick tunnel lining. The study also explains the structural health of the railway tunnel under moisture impact. These results demonstrate the potential of UAV-based tunnel inspection for infrastructure assessment, offering advantages in terms of safety, efficiency, cost savings, and data accuracy.

In the second field study, a road tunnel's surface defect distribution was examined using the PMPP-SDI method. The tunnel inspection faced challenges due to its intricate geometry, including twin tunnels, vehicle cross passages (VCPs), and laybys. Specific attention was given to compressive defect distribution during the analysis. The results identified three separate zones depending on their distance from VCPs, each displaying varying surface defect densities and distributions. High-density cracks and spalling in vulnerable zones suggest further specific monitoring and maintenance. The test showcases the PMPP-SDI method's value in evaluating and prioritizing maintenance for complex transportation infrastructure.

In conclusion, this thesis presents a systematic UAV-based tunnel inspection method, consisting of PMPP-SDI for real-time underground navigation and innovative image processing workflow. The effectiveness of the proposed inspection method was evaluated in two field tests on a road tunnel and a railway tunnel, respectively. Field test results identified distribution patterns of surface defects and deformation, highlighting the potential of UAV-based tunnel inspection for infrastructure assessment. Moreover, the study demonstrated the potential of ML-driven technologies to enhance model quality, suggesting further research directions for the advancement of UAV-based tunnel inspection systems.

Table of contents

Nomenclature

Roman symbols

$\boldsymbol{a}_i^{'}$	Deviation of coordinates between the origins of $\boldsymbol{S_i}$ and $\boldsymbol{S}^{'}$
$\boldsymbol{b}_i^{'}$	Projection of $\boldsymbol{a}_i'$ on tunnel cross-sections
Currentheight	Real-time distance reading from UAV's bottom infrared sensors
D_f, D_b	Real-time distance reading of UAV front/back obstacle sensor
D_p	Real-time distance reading to the front surface
D_h	UAV input parameter of panning length along the longitudinal axis
D_{li}, D_{ri}	Real-time distance readings from left to right of the UAV's front
ΔD_f, ΔD_b	Change in front/back obstacle distance between longitudinal moves
getpitch	Real-time gimbal angle reading
gimbalpitch	UAV input parameter of angle-based camera heading
Height	UAV input parameter of expected flight height
$\boldsymbol{n}_i^{'}$	$\boldsymbol{i}$ ($\boldsymbol{x}$, $\boldsymbol{y}$ or z) vector of $\boldsymbol{S}^{'}$ coordinate system
roll	UAV input parameter of velocity-based longitudinal position
roll2	Adjustment of roll between steps
R_0	Radius of tunnel lining fitting circle
$\boldsymbol{R_c}$	orientation of camera rotation
$\boldsymbol{R_i}$	rotation matrix from Si to S'.
$\boldsymbol{S_i}$	Coordinate systems of DSMs in DPT data resources.
$\boldsymbol{S}^{'}$	Unified spatial coordinate system is created for organizing data.
$\boldsymbol{t_c}$	UAV camera lenses' position
throttle	Control variable of distance-based height control

$\boldsymbol{tp_w}$, $\boldsymbol{tp_e}$	West and east lining coordinates
$\boldsymbol{tp}'$	Coordinates in S' after coordinate conversion
W	Scene width in a single frame
x, y, z	3D coordinates in coordinate systems $\boldsymbol{S}$
yaw	UAV's heading in inspection task

Greek symbols

ω, φ, κ	Camera rotation around the X, Y, and Z axis.
$\Delta\rho^*$	Radial deviation in circular tunnel deformation analysis
θ	Angle in circular tunnel deformation analysis
θx, θy, θz	Pitch, roll, yaw

Abbreviations

3D	Three-Dimensional
AI	Artificial Intelligence
AIS	Intelligent Unmanned Systems
APF	Artificial Potential Fields
ASL	Autonomous System Lab
ATP	Automatic Tie Point
BA	Bundle Adjustment
bp	before present
BGS	British Geological Survey
CERN	European Organization for Nuclear Research
CNN	Convolutional Neural Network
CV	Computer Vision
DDPG	Deep Deterministic Policy Gradient
DDQN-PER	Dual-Depth Q Network with Preferential Experience Replay
DL	Deep Learning

DOF	Degree of Freedom
DPT	Dublin Port Tunnel
DQN	Deep Q-Network
DSM	Digital Surface Model
DJI	Da-Jiang Innovations
DRL	Deep Reinforcement Learning
EKF	Extended Kalman Filter
FoV	Field of view
GAN	Generative Adversarial Network
GIS	Geographic Information System
GNSS	Global Navigation Satellite System
GPU	Graphics Processing Unit
GPS	Global Positioning System
HER	Hindsight Experience Replay
IAA	Irish Aviation Authority
IDT	Inspection Digital Twin
IMU	Inertial Measurement Unit
IP	Image Processing
KF	Kalman Filter
L	Likelihood
LDM	Local Dynamic Map
LED	Light Emitting Diode
LiDAR	Light Detection and Ranging
LR	Laser Rangefinder
LSTM	Long Short-Term Memory
M2ED	Mavic 2 Enterprise Dual
MCL	Monte Carlo Localization
ML	Machine Learning

MSDK	Mobile Software Development Kit
MTPs	Manual Tie Points
MVS	Multi View Stereo
mya	million years ago
NB	Northbound Bore
NBV	Next Best View
ORB	Oriented FAST and Rotated BRIEF
PCI	Pavement Condition Index
PCL	Point Cloud Library
PEM	Probabilistic Exploration and Mapping
PF	Particle Filter
PMPP-SDI	Proximity Move-Pause-Photo for Surface Defect Inspection
POMDP	Partially-Observable Markov Decision Process
PPK	Post-Processed Kinematic
PRM	Probabilistic Roadmap
PnP	Perspective-n-Point
PTAM	Parallel Tracking and Mapping
RANSAC	Random Sample Consensus
RGB	Red, Green, Blue
RPG	Robotics and Perception Group
RR	Risk Rating
RRT	Rapid Exploration Random Tree
S	Severity
SAC	Soft Actor-Critic
SACHER	Soft Actor-Critic with Hindsight Experience Replay
SAM	Segment Anything Model
SB	Southbound Bore
SFM	Structure from Motion

SIFT	Scale-Invariant Feature Transform
SLAM	Simultaneous Localization and Mapping
SOR	Statistical Outlier Removal
SQP	Sequential Quadratic Programming
ST	Shi-Tomasi (detector)
SURF	Speeded Up Robust Features
SWaP	Size, Weight, and Power
TOF	Time of Flight
TLS	Terrestrial Laser Scanning
UAS	Unmanned Aircraft Systems
UAV	Unmanned Aerial Vehicle
UNESCO	United Nations Educational, Scientific and Cultural Organization
UZH	University of Zürich
VCP	Vehicle Cross Passage
VFH	Vector Field Histogram
VINS	Visual-Inertial System
VO	Visual Odometer
VR	Virtual Reality
WI-FI	Wireless Fidelity
UWB	Ultra-Wideband
UKF	Unscented Kalman Filter

List of Figures

Figure 4-16 Data extraction in four linings (tunnel mileage starts from VCP and is in the unit m)

Figure 4-17 Coordinate system conversion schematic (with projection space for DSM and orthomosaic extraction)

List of Tables

1. Introduction

1.1 Background and motivation

Modern tunnels are among the critical conduits in contemporary infrastructure networks, playing an instrumental role in ensuring the uninterrupted flow of people, goods, and related services. However, tunnels are also vulnerable to structural deterioration due to exposure to the environment and the abrasive effect of vehicular overuse. When even a single section of the underground structure develops weaknesses, its reliability and functionality are put into question as evidenced by various case scenarios. It is, therefore, necessary to carry out interior inspections at regular intervals to avert such incidences.

Conventional methods for inspecting tunnel interiors have relied on manual processes involving human inspectors or ground vehicles. These approaches are characterized by labour intensity, time consumption, and high costs. While ground vehicles may be suitable for certain tunnel geometries, their applicability is limited, and they often require partial lane closures, causing traffic disruptions. Additionally, they frequently fail to provide comprehensive coverage due to constraints in accessing cramped spaces, areas with low visibility, or restricted entry points in narrow tunnels.

Drone technology offers promising solutions for tunnel lining inspection, overcoming the limitations of traditional methods. Drones provide enhanced access to confined spaces, automate and standardize inspections, and capture high-quality data with advanced sensors. Despite these advantages, challenges such as navigation in GPS-denied areas and ensuring data accuracy persist. Moreover, while UAV inspections can be conducted during tunnel closures, they still require coordination and planning to minimize operational disruptions, like traditional methods.

The main drive behind this research is to harness the capabilities of UAVs for tunnel lining inspection, particularly focusing on addressing navigation and data quality challenges. Through a comprehensive assessment of the operational feasibility, effectiveness, and data quality of UAV-based assessments, this study seeks to affirm the potential of UAV technology in tunnel inspection practices. The overarching objective is to establish a viable workflow for tunnel inspection utilizing commercial drones, thereby enhancing safety, reliability, and cost-effectiveness in tunnel infrastructure management by capitalizing on the benefits of UAV inspections while mitigating their current limitations.

1.2 Research objectives and contributions

While UAVs offer promising capabilities for tunnel lining inspection, their implementation in this domain is still an emerging area of research and development. Key challenges remain, such as automatic navigation in GPS-denied tunnel environments and ensuring reliable and accurate data collection.

Motivated by the need to address these current limitations and establish a standardized approach, this research aims to propose a comprehensive workflow and methodology for enabling and enhancing the use of UAVs for tunnel lining inspections. Consequently, the following specific research objectives have been formulated:

1. Develop effective navigation and positioning strategies for UAV operations in GPS-denied tunnels: This objective focuses on exploring and evaluating various technologies in UAV navigation. It aims at identifying necessary payloads and comprehensive UAV path planning for accurate and reliable navigation of UAVs in tunnels without GPS signals.

2. Optimize data acquisition methods for comprehensive tunnel lining inspection using UAV-mounted sensors: This objective involves developing methodologies for effective data collection. The aim is to capture detailed and comprehensive information about the condition of tunnel linings, enabling the identification of cracks, spalling, and other defects.

3. Propose a standardized workflow for UAV-based tunnel lining inspections: This objective focuses on developing a standardized and systematic workflow that ensures consistent and reliable results across different tunnel environments. Consequently, the stages are included from mission planning and data acquisition to post-processing and analysis.

4. Conduct comprehensive interpretation of UAV data: Through extensive field trials and data analysis, this objective seeks to quantitatively and qualitatively analyse tunnel deterioration findings. Key aspects are got from surface colour coverage, lining defect distribution, and tunnel deformation.

By addressing these objectives, this research aims to make contributions to the field of UAV-based infrastructure inspection, specifically in the context of tunnel lining inspections, advocating the widespread adoption of UAV technology in tunnel infrastructure management practices.

1.3 Thesis outline

This thesis is structured as follows:

Chapter 2: Literature review on UAV navigation for tunnel inspection, covering UAV characteristics in tunnel inspection, underground navigation methods (visual techniques), and path planning strategies.

Chapter 3: Literature review on processing UAV image data from tunnels, including 3D reconstruction, point cloud denoising, tunnel image processing methods, expected outputs, and applications for tunnel health assessment.

Chapter 4: Overview of the UAV tunnel inspection system developed, detailing the robotic platform, inspection tasks, navigation and data acquisition processes, control systems, and image processing workflow.

Chapter 5: Field test in a railway tunnel, describing the site, challenges, 3D reconstruction, defect identification, spatial deformation analysis, navigation verification, and deterioration mechanisms.

Chapter 6: Field test in a road tunnel, covering surface defect identification, quantification, modelling accuracy, spatial deformation extraction, and deterioration analysis.

Chapter 7: Summary of key findings, limitations, future research directions, and concluding remarks on the implications of UAV-based tunnel inspection.

Additionally, relevant appendices are included to provide supplementary information, such as detailed procedures for UAV data acquisition in coastal heritage protection, documents for obtaining approvals for tunnel inspections using UAVs, and additional results and data from the field tests.

2. Literature review on UAV navigation

2.1 Introduction

In this chapter, we focus on the technology and methodologies used for acquiring tunnel surface data using Unmanned Aerial Vehicles (UAVs) within challenging GPS-denied environments. Firstly, the literature review clarifies the current positioning of UAV infrastructure inspection. Specifically, the literature review delves into the capability of UAVs mounting LiDAR, photogrammetry, and other sensors-based technologies for data acquisition, along with a comparison of their adaptability in tunnel environments. The chapter then explores various path planning strategies for UAV data acquisition, illustrating the significance of balancing between robust algorithms and computation cost with field tests in infrastructure assessment and management.

2.2 UAV tunnel inspection

2.2.1 UAVs characteristics for tunnel inspection

Small size and multiple positioning sensors are essential requirements for UAVs operating for underground structural health inspection. And the UAV inspection's capability is greatly influenced by the quality of controlling and data collection sensors. A common multi-sensor combination is a combination of laser imaging, detection, and ranging (LiDAR), inertial navigation, and ultrasonic positioning detection methods. The use of a single-sensor inspection is limited in its accuracy and robustness in complex environments. For example, in long linear corridors or tunnel scenes, laser point clouds can drift. And gyroscopes and accelerometers have constant errors that can lead to low accuracy results for inertial navigation. However, multi-sensor fusion techniques increase the complexity of the algorithm. Data fusion uses Kalman filtering and graphical optimization techniques for data with different coordinate systems, data formats, acquisition frequencies, and confidence levels. In addition to the extra sensors, one type of solution is encased UAV for anti-collision protection [1].

The flight quality of the UAV inspection is assessed in terms of overlap ratio and image quality. The UAV inspection results include 3D models and terrain contours, surface textures, or other types of data support. Inspection and acceptance based on digital mapping results on the ground have to meet a minimum of 53% overlap in heading and 8% overlap in side direction for adjacent images [2]. The evaluation of data quality in UAV infrastructure inspections involves scrutinizing image resolution, sharpness, clarity, as well as the accuracy and completeness of collected data compared to other methods [3]. Moreover, researchers may employ machine learning algorithms and computer vision techniques to autonomously identify anomalies in the data, thereby enhancing the reliability of inspections [4].

Drones used for underground structure inspection can be divided into commercial/consumer drones and DIY drones. DJI is currently the world's largest commercial drone manufacturer, with proven modules and secondary development environments for users to adapt to their inspection needs. Other research and development organizations have their own drone inspection solutions containing hardware, operational systems, and control programs. Chinese inspection UAV manufacturers include Chengdu JOUAV [5], Shenzhen Feima Robotics [6], and Yuneec [7]. International models of the complete solution include Flyability's Elios series [8], Kespry, skycatch's explore series, microdrone's md4 series, precision-Hawk [9], and Trimble's quadrotor and hexrotor UAVs. Innovations from other research institutions are largely based on existing technologies with minor improvements. Some governmental research initiatives were conducted within the United States aiming at facilitating the deployment of UAVs in GPS-denied settings, including natural caves, engineered tunnels, and urban underground environments.

Unmanned aircraft are capable of three levels of automation, programming-based unmanned systems, automated unmanned systems, and intelligent unmanned systems (AIS). The three levels of intelligence for automatic control are, respectively, not environmentally adaptive, with basic perceptual decision control capabilities, and capable of autonomous, intelligent, beyond human task understanding and realization. Current UAV inspection in general underground structures is only capable of human-in-the-loop automatic UAV control. It’s a combination of digital design and robotics for control that relies on a human to oversee the inspection process and avoid risk.

Recent developments in UAVs have driven the use of UAVs in automated structural inspection. The development of UAV navigation is summarized in Figure 2-1. UAV aerial inspection is an interdisciplinary subject [10], involving new technologies including drone’s structural design, use of new materials, wireless communication, flight control, and artificial intelligence. Developments in the UAV industry have focused on GPS-independent information sensing and fusion in a complex environment, optimization of communication networks, development of cooperative systems for multi-UAV tasks, navigation with artificial intelligence to predict UAV attitude and obstacle movement for fast travel in unknown environments, and automatic trajectory planning control algorithms.

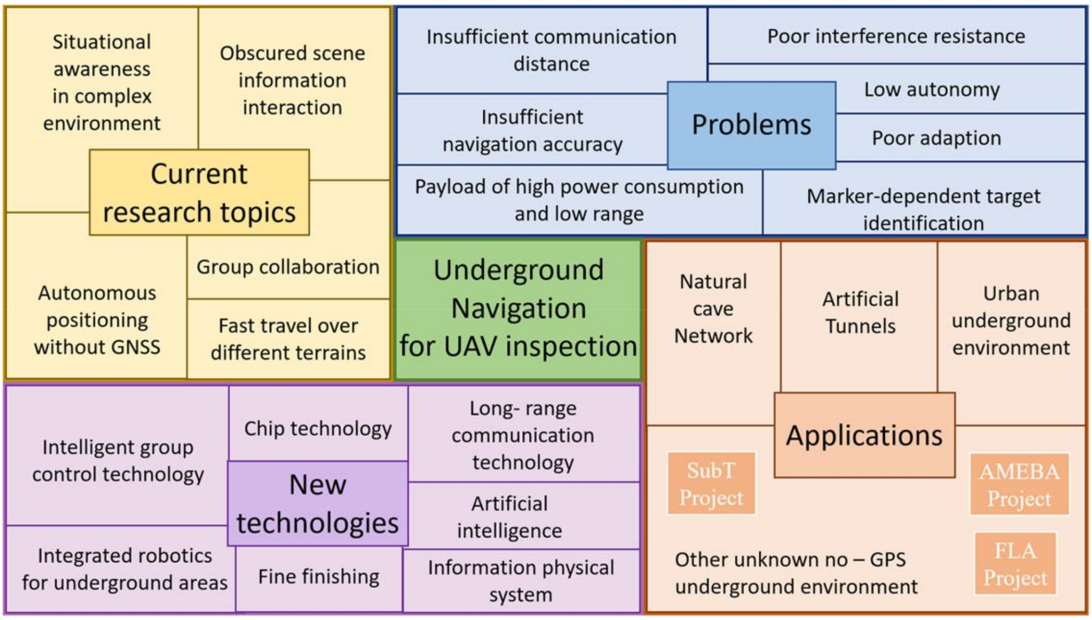

Figure 2-1 Overview of UAV navigation for underground infrastructure inspection

The inspection of underground structures by UAVs is still subject to several limitations that constrain its efficacy. Firstly, current hardware limitations, including both high cost and low endurance, as well as constraints on energy supply, result in reduced capacity for conducting comprehensive inspections in a single flight. While modular UAV DIY improves platform and payload integration, the development of the payloads remains inadequate for conducting specialized inspections. Real-time inspection is also impeded by limited onboard computing power, with current practice entailing pre-processing on UAVs and online computing. Moreover, autonomous UAV control and information processing are still in the early stages, which is a major obstacle to intelligent infrastructure inspection.

2.2.2 Advantages of using UAVs for tunnel inspection

Regular health monitoring is crucial for ageing infrastructure asset assessment and maintenance, whereas conventional manual inspection is usually subjective, time-consuming, and expensive, particularly for large-scale infrastructure. Over recent years, the rapid development of robotic technologies has enabled UAVs for large-scale infrastructure inspection on a more frequent basis at significantly lower cost [11], [12]. Table 2-1 compares the cost of common tunnel remote sensing methods. For large-scale infrastructure monitoring, automatic UAV inspection can save significant equipment costs and ensure consistency of data information. The substantial volume of high-quality data obtained from these inspections can be archived [13] and processed using computer vision (CV), enabling automatic inspection. Moreover, compared to other inspection platforms (e.g., ground vehicles), UAVs' manoeuvrability in three-dimensional space allows them to inspect confined infrastructure from multiple views at different angles. This can largely reduce perspective error, surpassing manual inspections [14], camera-equipped railcars[15], and ground robots [16]. In addition, UAVs offer an adaptable control solution for data acquisition in 3D-complex underground infrastructure networks, including inclined tunnels, cross passages, and shafts[17]. In comparison to different detection sensors, UAV photogrammetry enables the creation of continuous and realistic close-range models [7]. In contrast, Light Detection and Ranging (LiDAR) inspection generates extensive point cloud data but lacks rich textures. In summary, the efficiency, adaptability, and data quality of UAVs enable long-term automatic digital inspection for ageing infrastructure maintenance.

Table 2-1 Financial comparison among common remote sensing methods for tunnel infrastructure

Methods	Indicative monitoring layout and procedure	Indicative Cost
Manual inspection [18]	The inspector captures defects holding the camera; Subjective, unable to access the shaft, giving discontinuous data	Equipment cost: camera in close-range photogrammetry (~€0.5k); High labour cost
Specialised vehicle surveying [19]	Operate a specialised vehicle (e.g., van) equipped with 5+ cameras and laser sensors along the tunnel; difficult to survey tunnel shaft or other sections with/without rail track;	Equipment cost: ~€60k: a van (~€40k), high-quality camera and sensors (~€20k); High maintenance cost and long idle time when equipment is not in use
Manual UAV	Manually fly UAV along a designated route in the tunnel network section and	Equipment cost: ~€6k: UAV and accessories; High labour cost, and

inspection [20]	record videos; subjective routine planning, and possible omitted inspection contents.	inexpensive equipment maintenance cost within ~€500 per annum
Automatic UAV inspection	Automatically fly UAV along a designated route in the tunnel network section and take photos; adaptive for different underground sites (e.g., shaft, tunnel, cavern)	Equipment cost: ~€6k: UAV and accessories; Low labour cost and inexpensive equipment maintenance cost within ~€500 per annum

Many underground structures built in the past few decades are facing the problem of automatic and rapid inspection. It is particularly evident in underground structures for transportation, industry, and scientific research. Regular inspections help ensure the integrity of these underground structures and the continued stable service they provide. However, due to the unfavourable underground conditions, there is no fully automatic structure inspection system at present.

Commonly used methods are surface inspection of images from manual inspection, UAV inspection, and ground vehicle surveys. Structural health inspection could provide global knowledge of tunnel surface defects, including water leakage, cracks, salt accumulation, frost damage, and rust. This information could further reveal the structural deformation and other health issues in a tunnel. Manual inspection has disadvantages in terms of cost, mobility, and security concerns compared to the other two methods based on image processing (IP). But at the same time, IP methods also require the high quality of regularly collected image data to make accurate judgments. Ground vehicles can be used to scan tunnel walls, like rail cars, multi-wheeled cars, or even large ultrasonic or thermodynamic radar scanning machines.

However, these methods either require the construction of tracks in advance, which is costly and requires regular maintenance, or they can only work in a limited space, such as flat ground. Especially in confined underground spaces, the customized ground vehicles image acquisition platform brings high costs and poor adaptability. In contrast, more flexible and autonomous drone navigation is increasingly promising in terms of software and hardware development. Compared with numerous manual inspections [21] and ground vehicles [22] inspections, UAVs have great advantages of security, economy, efficiency in deployment and movement, versatility in task switching, and flexibility in photography. UAV image acquisition could provide consistent photography and has the flexibility to work at different heights and angles in irregular and inaccessible environments for humans.

Research on controlling UAVs for image acquisition has a rich development history [23]. Researchers operate drones for regular inspection of industrial equipment. They also adopt high-speed navigation and obstacle avoidance algorithms to quickly traverse natural environments such as forests [26]. UAVs could already carry out fast and autonomous navigation under limited localization conditions. The realization of localization and navigation is based on the algorithm on the onboard computer, remote calculation and control, installed sensors, and prior map.

However, data acquisition in a tunnel is not as convenient as within outdoor conditions. The main challenges include a lack of global positioning system (GPS) signal, weak texture, strong dynamics, and unfavourable structure shape. The geometry of long tunnels has extra longitudinal freedom compared to 2D navigation. It results in error accumulation on the estimation of the motion along the tunnel axis. The same can happen if the vehicle moves around a cylindrical object. Also, the shape, size, and material of the tunnel structure change along the inspection mileage. Existing outdoor control schemes are ineffective in providing high-quality image data sources for tunnel inspection. Therefore, the tunnel environment poses challenges for localization and navigation in tunnel inspection.

In the next section, the problem of UAV flight control in underground structures is reviewed, which is equivalent to UAV control in low illumination and low texture environments and GPS rejection conditions, including its own position and attitude perception and path planning. The goal of UAV automatic control is to achieve the shortest journey, the shortest time, prolong the vehicle life cycle, minimize energy, reduce calculation time, reduce risk, etc.

2.3 UAV underground navigation technologies

2.3.1 UAVs for underground navigation and mapping

The drone's navigation and data collection in confined spaces allow it to effectively assess problems such as cracks, corrosion, and other visual features of defects. Based on the SLAM algorithm it is also possible to obtain structure maps and better organize the data. Simultaneous localization and mapping (SLAM) is a method of UAV navigation that simultaneously determines its position and attitude and incrementally builds maps in an unknown environment. SLAM consists of four parts: sensory information acquisition, odometer pose estimation, map matching pose estimation, and map construction.

The sensor data allows depth estimation and thus the determination of the UAV's pose. Depth estimation methods include mainly structured light and TOF-based methods commonly used indoors, multi-vision camera methods at close range, and LiDAR-based methods for use in structurally distinct environments. And tunnels can be thought of as GPS-denied indoor inspection environments.

In underground environments, relying on only one sensor can easily cause measurement errors and low robustness to environmental disturbances. In early scientific research, the combination of various localization methods improves localization efficiency. In a tunnel, multiple sensors can be added to assist in positioning. In addition to inertial, vision [27] [28] [29] and LiDAR, WI-FI, ultra-wideband (UWB)

[30], radar [31], and ultrasonic are also common positioning methods. Details of the application, advantages, and disadvantages of these methods are described in the following section. Later, with the development of image processing technology and computer vision, research on visual localization progressed.

At present, visual localization and its combination with other localization technologies are the mainstream of localization methods, accounting for 94% of the total. Visual location technology relies on visual odometers (VO). The optical flow-based algorithm compares continuous images to obtain the depth of the image and can detect the spatial position of obstacles without relying on sensors other than the visual odometer. Common visual odometers include monocular cameras [32], multi-ocular cameras [33], and camera combinations with different angles [34], [35].

2.3.2 Challenges associated with underground navigation

Previous studies have extensively investigated UAV open-air structural health inspections, such as road pavements [36] and building exteriors[37]. In general, these environments are well-lit and have global navigation satellite system (GNSS) availability. However, conducting UAV structure surface inspections without priori maps [38] in complex flight conditions presents challenges, particularly in positioning and control [17]. To overcome these challenges, the focus is on improving sensing capabilities, especially in confined environments where real-time absolute GNSS positioning data is unavailable for UAV attitude adjustment. On the other hand, in weak GNSS conditions like bridges, common UAV navigation methods[39] rely on visual positioning. The dark and confined environments of tunnels pose a significant challenge, requiring UAVs positioning to rely on additional sensors [40], including passive payloads like spectrum cameras[41], [42] or active payloads like LiDAR[43], Wi-Fi[44], Ultra-wideband (UWB) [45], etc. There are also some mechanical modifications, for example, UAV cages [46], [47] for collision-permitted automatic search. However, such disorganized UAV movement is not suitable for effectively traversing and inspecting underground structure surfaces. Among common methods, combining cameras and lighting is a widely adopted approach in UAV sensing due to its convenience, energy-saving features, and cost-effectiveness.

2.3.2.1 Environmental interference to sensors

The environment in underground structures is complex, and many factors affect localization, path planning, and control. For example, the change in air density and altitude could lead to a deviation in the route. The lift of an aircraft is proportional to the density of the air. In an environment with uniform air density, higher air density corresponds to stronger UAV speed control performance [48]. To cope with the change of air density when the UAV is flying at different altitudes or due to other reasons, ranging methods are also required to assist in correcting errors.

In addition, there may be dust, smoke, water droplets, and other aerogels in the underground space that interfere with the sensor for localization based on the principle of time of flight (TOF). Using only this type of sensor will result in inaccurate localization. Therefore, auxiliary means should be adopted.

2.3.2.2 Structural restriction

Compared with the open space, the underground structure has more obstacles and flight limitations, such as the equipment, narrow passages, and doors in Conseil Européen pour la Recherche Nucléaire (CERN), as well as the fire hydrants, street signs, and power distribution areas in road tunnels.

The structural shape makes stronger airflow than in open air. The shaft collar tends to have more air circulation than the bottom of the shaft. When the resistance of the airflow is too large, it is difficult for the drone to reach the designated position.

The drone also has a ground effect when flying close to structural surfaces. When the suction and thrust of the airflow are too large, the twisted wind turbulence will make it harder for a drone to hover close to the structure. The first way to reduce the control difficulty of UAVs in an underground environment is to lower the weight of the drone. In this way, the force for flight path correction can work easier. Another way is through a reasonable path planning to make the UAV fly along the centreline or axis of the passage so that the UAV could minimize the thrust from a single direction.

2.3.2.3 Light condition

Insufficient visible light in underground structures has detrimental effects. On the one hand, the localization of the UAV gets inaccurate, which reduces the sight distance of the pilot, and brings difficulties to both manual control and automatic flight; on the other hand, it's unfavourable for the subsequent data processing. During inspection tasks, low light introduces more noise into the images and video, making information extraction more difficult.

In pilot operation, the first solution to avoid short-sight distance is to provide enough LED lighting sources [49]. Other available methods include advanced switching commands between static and moving states for pilots [50], and built-in low-level commands that enable automatic control of the drone with a certain velocity and pitch. Also, Galtarossa [51], Quenzel [52], Kominiak [53], and Jiun [54] combined multiple sensors to ensure navigation in an environment with either loss of GPS or light.

2.3.2.4 Communication problem

There are many types of communication problems in underground structures. Apart from the GPS-denied condition, there're also unfavourable factors to setting communication base stations due to the following issues:

1. The horizontal and vertical bending of the underground structure can cause communication problems due to signal blocks. While radio signals can be transmitted as far as 1.5km in open space, the distance is reduced to 100m in an indoor environment [50].

2. In underground structures in mountains, the structure might be affected by the magnetic field. This will interfere with the work of the UAV compass and affect its localization accuracy.

3. Moisture and water leakage can damage the parts of the drone and interfere with the communication between the drone and the remote control, so avoid flying in wet environments.

To reduce the interference of the UAV communication problem in the underground structure, UAV control, and image transmission adopt radio transmission signals of different frequencies. The data can be pre-processed on the UAV's onboard computer [55], or through data prediction to reduce the amount of data transmission [56] and ensure stable communication.

2.3.3 Typical UAV underground localization methods

UAV-assisted data acquisition faces the main challenge of autonomous flight. Therefore, in various inspection scenarios, two or more combination localization methods are often used together [57]. The most common combination in surface structure inspection is to use GPS and an optical camera, which allows for obtaining the absolute position of the UAV. However, in GPS-denied underground environments, visual localization is commonly used together with other suitable sensors as shown in Table 1. The accuracy of these combination methods can be verified by simulated flights and tests. Further developments in the use of vision-related navigation by UAVs are described in section

2.3.4.

Table 2-2 Comparison of localization technologies in underground structures.

Sensor	Pros	Cons
Inertia	• Low SWaP (Size, weight, and power) • Low cost • High update rate • Short start-up time	• Drifts over time • Low precision at low acceleration and angular velocity • Accuracy affected by knowledge of the initial state
Vision	• Lightweight • Semantic information	• Low precision at extreme illumination • Susceptibility to light interference • Indirect state observation • High computational load • Loss of depth information in imaging
LiDAR	• Precise • Direct measurements • High update rate	• Dependent on reflecting properties • Energy consuming
UWB radar	• High resolution and range in aerosol • Low power consumption • Robust outcome	• Limited range • Susceptibility to interference • Being expensive
Ultrasound	• Simple operation • Low cost • Stable to EMI	• Limited range • Low noise resistance

2.3.3.1 Visual inertial localization

Visual SLAM relies on a visual-inertial system (VINS) to include inertial measurement unit (IMU) data for real-time mapping and path planning of UAVs in static or dynamic environments. An IMU sensor is shown in Figure 2-2. Table 2-2 presents the benefits and drawbacks of vision sensors, with a recommended light intensity range of 15 to 100 lx for optimal camera sensor navigation. Visual sensors are cheap and provide photography information, but have limited performance on black, transparent, reflective objects. Inertial positioning relies on coordinate conversion and digital integration of the output data from inertial sensors, with errors arising from random walks in device readings [58] and truncation errors of numerical calculation [59].

Inertial positioning system errors include external forces such as heavy overhangs and wind [60]. Therefore, other sensors provide necessary complementary data such as visual, UWB, and LiDAR sensors [61]. There are also studies on the reduction of systematic error through machine learning [62], [63].

The Robotics and Perception Group (RPG) and Autonomous System Lab (ASL) teams at the University of Zürich (UZH) both focus on the improvement of navigation methods for visual perception [64]. They make Agilicious an open-source framework for quadrotor drones [65]. Feng proposes a panoramic vision network drone for collecting stereo information [66]. Yang [63] and Yamashita [67] used the visual-inertial localization method and CV to provide a collision-free path for the UAV. Yang also published a data set obtained in the tunnel.

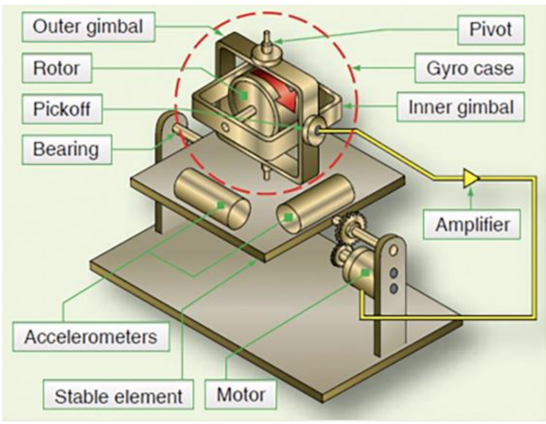

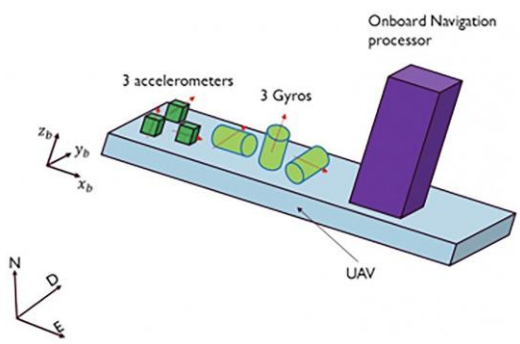

(1) Inertial system components (2) Installation [68]

Figure 2-2 Schematic diagram of UAV inertial system platform

Navigation data processing of multiple sensors adopts data fusion algorithms, including tight coupling and loose coupling. In loosely coupled vision and inertial motion estimation systems are independent of each other. Tight coupling is to share the raw data of two sensors [69]. The latter one has sensor noises interacting with each other, uses variables in common, and has complex algorithms. Famous algorithms include Vins-Mono [70], Vins-Fusion, Kimera, ALVIO, StereoMSCKF, ORB-Slam2 Stereo, LINS, and ROVIO.

Dominant data fusion and pose estimation methods include Kalman Filter (KF) (represented by monoslam), bundle adjustment (BA) applying the structure of motion (SFM) principle (represented by Parallel Tracking and Mapping (PTAM)), large-scale direct monoslam, and deep learning-based methods. Further details are introduced in section 3.2. An extended Kalman filter (EKF) can be used to fuse optical flow and IMU data to estimate the velocity [71]. They use the inter-frame differencing method to match points of interest in adjacent frames. Using the inter-frame difference method in the moving pictures, a centimetre-level precision 3D reconstruction model can be obtained.

Improvements in the efficiency of UAV data acquisition can be achieved by expanding the area of a single shot, either through multi-camera stitching techniques or by increasing the size of the sensor frame.

2.3.3.2 LiDAR-assisted localization

LiDAR is widely used in UAV navigation due to its high accuracy and interference resistance. Compared with the 1% mileage error of visual positioning, LiDAR could achieve a 0.5% mileage error and reduce the error by 50%. LiDAR uses the reflection of light waves for ranging and could assist with position and attitude estimation.

LiDAR can be used for mapping, but one of the main disadvantages is the sparse point clouds in SLAM at its lower frequency, so they are used to correct the aero-triangulation results from visual positioning. Another limitation of laser localization is that it can only be used for ranging, but not for recording colours and textures. This means that laser localization needs to be used with other sensors when applied to 3D surveying [72]. A practical LiDAR data fusion requires a well-defined geographical coordinate system in the application scenario, a post-processed kinematic (PPK) base station, an overlap of more than 50% of the data, and elevation data as control points.

An industrial LiDAR tracker can be used to verify the actual position, but it's expensive too. A LiDAR like Leica AT901 and FARO costs from €10K to €30K. The Toyota Institute of Technology at the University of Chicago, Baidu Apollo, and Google Waymo are using LiDAR in drone navigation. The Elios3 LiDAR UAV from Flyability uses the FlyAware system and the Inspector 4.0 control program. The LiDAR datasets EuRoC MAV, TUM RGB-D, and KITTI are used for training in LiDAR automated navigation. Major manufacturers of LiDAR include Riegl, Beike Tianhui, RoboSense, Hesai, and others. One example of a LiDAR module installed for vertical distance measurement is shown in Figure 2-3.

LiDAR SLAM research has a long history and has become a mature field of study. Several researchers have contributed to the development of LiDAR-SLAM technology, including Tokida [73], Li [74], Tripicchio [75], Bi [76], Mansouri [77], Vong [78], and others. These researchers have demonstrated the possibility of using LiDAR and laser sensors for autonomous path planning, collision avoidance, and navigation in indoor and underground environments. For example, Bi [52]'s study used a sensor fusion-based positioning system that achieved a precision of 0.095m on a fast mobility platform. As pioneers of drone automation in underground space, Mansouri and Vong's studies involved LiDAR-based algorithms for autonomous navigation and path planning in tunnels. Furthermore, a LiDAR-based DJI drone hovermap system [79] was developed for SLAM in underground mining, providing three levels of automation with 10-mm precision. Not only for automated drone inspection, LiDAR scans are also useful for mapping underground structures for geotechnical analysis[80], providing high-resolution reconstruction and information on structural discontinuities. For example, a recent study [20] equipped drones with laser-ranging arrays to navigate autonomously in tunnels and collect distortion-free images of the structural surface through rotating cameras.

Figure 2-3 A LiDAR module for vertical distance measurement [81]

2.3.3.3 UWB radar-assisted localization

Like the Laser range finder, UWB uses reflection time ranging to detect obstacles. UWB uses large-bandwidth radio waves as shown in Figure 2-4, so it is robust to detect various targets. In addition, UWB has low interference with the radio control link. It has tens of centimetres' precision and could cover a larger area of 60 m compared to other methods. UWB radar-assisted drone localization can adapt to underground structures with dusty, high humidity [82]. And UWB is especially commonly used in multi-UAV systems[83].

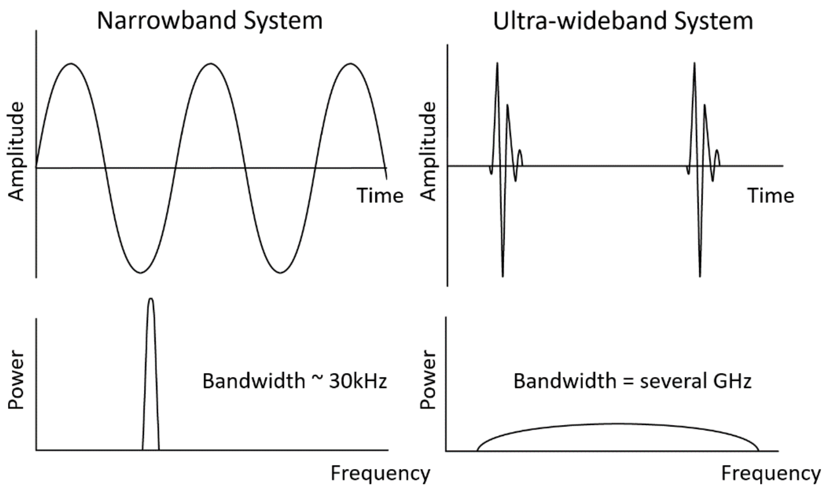

Figure 2-4 Spectrum of narrowband and UWB system

2.3.3.3 Ultrasonic-assisted localization

Ultrasonic sensors detect obstacles by radiating high-frequency sound waves and collecting reflected waves. Its principle is based on the time of arrival (TOA). But unlike most of the sensors described above, ultrasonic sensors are not affected by electromagnetic wave interference and can work normally in the environment of light radiation and aerosols. Ultrasonic signals are easy to process and low cost. Ultrasonic localization has an accuracy of a few meters. The disadvantage is that there will be crosstalk between multiple ultrasonic sensors, the performance is poor when measuring non-vertical surfaces, and it cannot be used to obtain the exact position of the measured object due to weak directivity. In UAV monitoring, ultrasonic sensors can be used for height measurement and control [84] and obstacle identification, but are not suitable for scanning structural details due to their limited range and sensitivity to noises.

An example is the installation of six ultrasonic sensors on the DJI M100 drone to detect and avoid obstacles in the underground space as shown in (Figure 2-5) [85]. The strategy is to balance the distances measured from two opposite ultrasonic sensors. Then LiDAR is used to map the underground space.

(1) 

(2) 

Figure 2-5 (1) DJI Guidance for Ultrasonic guidance node and (2) DJI M100 for MSDK control

2.3.4 Research progress of visual localization

UAV navigation in underground space relies on distance sensing from nearby obstacles.

Therefore, the accuracy of obstacle identification and distance sensing is important in visual localization. This section gives some experiences on the application of traditional methods, as well as computer vision-based research progress for GPS-denied visual localization.

Some researchers have also worked on enhancing UAV visual perception to improve navigation reliability. In practice, weak light conditions can lead to drift and potential collisions with surrounding structures during automatic flight. One approach to improve light conditions is the use of searchlights in conjunction with operators. However, even with enhanced navigation, the autonomous control error can still be as high as 0.12 m in a 15m-long flight [86].

Furthermore, vision-based algorithms using artificial intelligence have shown promise in improving navigation stability and reducing flight time [74], [87], [88], [89]. There are also image depth estimation methods based on convolutional neural networks (CNN) [90], and navigation algorithms using deep learning (DL) [77], [91]. However, these methods require high computing power from onboard computers [92], excessive data communication between UAV and ground station computers [78], and pre-training of navigation models.

Hence, these methods usually face the challenge of limited flight time[93] or still lack robustness to new environments. In the context of underground structure inspections, small UAVs are often preferred to strike a balance between energy consumption and navigation intelligence and accuracy, making complex and time-consuming methods (e.g., image-based machine learning methods) less suitable. Finally, well-designed flight paths are necessary for the inspection of curved tunnel surfaces at close range. The flight should normally be carried out at multiple heights over gimbal rotation to obtain various views for the purpose of alleviating perspective error [20], [94], [95].

2.3.4.1 Feature-based methods

Visual localization technology determines the spatial position of objects through feature-based algorithms [96], [97], such as straight lines, curves, texture, and colour [98]. Common feature extraction algorithms include SIFT, SURF, ORB, and Harris corner point [99], as shown in Table 2-3. ORB and Harris angle are common UAV navigation methods as their rotational invariance properties prevent miscalculations. Eventually, the spatial position can be obtained either by texture-based SFM calculation or by using a priori information. In recent years, the traditional visual localization algorithm has improved through better information extraction and sensor fusion error reduction.

Table 2-3 Visual features and applications.

Features	Pros	Cons
Harris corner point	• Rotation invariant • Intensity shift invariant	• Sensitive to image scaling • Pixel-level precision
SIFT	• Scale and rotation invariant	• Computationally slow • Not applicable on a smooth surface
SURF	• Scale and rotation invariant	• Computationally slow
ORB	• Computationally fast • Accurate • Rotation, scale, noise, and illumination invariant	• High repeatability

One challenge in UAV image acquisition in tunnels is the darkness and uneven artificial light. This is because of image noises, which are unfavourable to feature-based optical flow algorithms. To this end, some researchers improved the optical flow algorithm by brightness compensation of adjacent frames [100]. It adopts a Shi-Tomasi (ST) detector to make up for the poor resistance of the optical flow algorithm to illumination changes.

With prior information on navigation problems, an autonomous correction algorithm can be used to compare visual maps with topographic maps. Tanchenko [101] integrated prior information by computing the least squares of homography between two maps, one of which is from machine vision and the other from prior vector maps. Its effectiveness is verified by mathematics calculation and flight experiments.

Also, early visual algorithms had difficulty in pose estimation compared to ground vehicles, due to the additional degree of freedom (DOF) on UAVs [102]. One most typical visual method aligns its results with the direction of gravity to accommodate the DOF. Zhao [103] used homography in the normalized image plane to mitigate noise impact and the iterative calculation along camera trajectory for stable pose estimation.

Zhou [104] further improved the collinear line calculation performance from visual odometer data. This algorithm reveals the relationship between the inverse depth of the line and the 3D spatial coordinates of points on it. It has the advantages of variable number reduction, performance augmentation than the most advanced direct VO algorithm, and a speed improvement of at most 44%.

2.3.4.2 Computer vision-based methods

The CV-based approach offers advantages in terms of depth information acquisition and computational speed. By contrast, traditional IP-based algorithms have limited performance in structure size configuration. The monocular visual SLAM algorithm without CV can restore the shape of the object, but cannot restore the real size of the object due to the lack of depth information [105], while CV enables depth estimation. The CV-based approach allows for reduced reliance on multiple sensors but requires huge computational power and is less robust to environment variance.

Also, learning-based computer vision methods improve processing speed and reduce image stitching errors through the understanding of the image. Deep reinforcement learning (DRL) methods develop rapidly and have increasing applications in UAV navigation.

Knyaz [106] used a generative neural network (GAN) before semantic segmentation and depth map estimations. The principle is to choose the best result from several voxel GAN models. And it brings the advantage of adaptability in scenes with incomplete scenery.

Deraz [107] used long short-term memory (LSTM) to give an estimation of the vehicle velocity. Based on the initial flight information, long-term information on positioning error, velocity, time, and yaw is calculated and will be the basis for short-term estimation when sensor disconnection happens.

The neural network can also be used to predict the depth map and scene segmentation, as shown in Figure 2-6. It could segment and estimate the depth map of the scene in the environment with an incomplete view of objects [106]. The specific method is to generate an adversarial model, transform the input colour image into the output voxel model, and estimate the degree of approximation to the real data. The above visual depth prediction might allow monocular visual navigation on special occasions in underground structures. Possible benefits could be a better understanding of the indoor structure and drone gesture, and therefore the application of a depth map allows for a more reasonable flight strategy and navigation safety in autonomous flight.

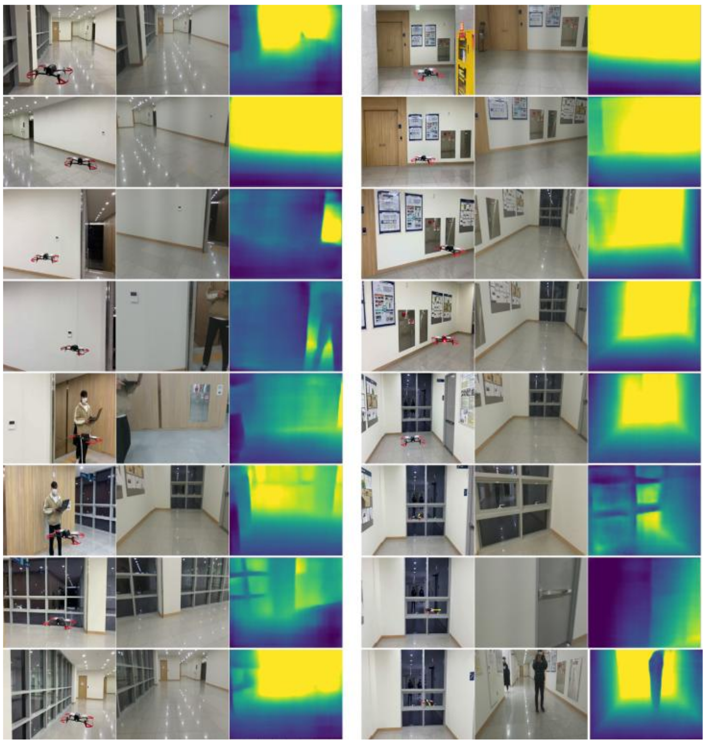
Figure 2-6 Sample of depth estimation based on images from a monocular camera in an indoor environment [106], [108], [109].

2.4 UAV path planning in underground inspection

This section discusses two categories of environments in UAV path planning, based on the availability of prior knowledge. The first category focuses on structured and predictable geometries, such as pipelines, where path planning can be designed with prior knowledge, enabling efficient navigation but with limited adaptability. The second category covers complex and dynamic environments, like underground settings with multiple branches and changing conditions. In such environments, advanced UAV navigation algorithms are essential, often necessitating a combination of simulation and real-world flight tests for reliable real-time navigation. Despite the differences, effective path planning and inspection tasks can be accomplished through various strategies in both categories.

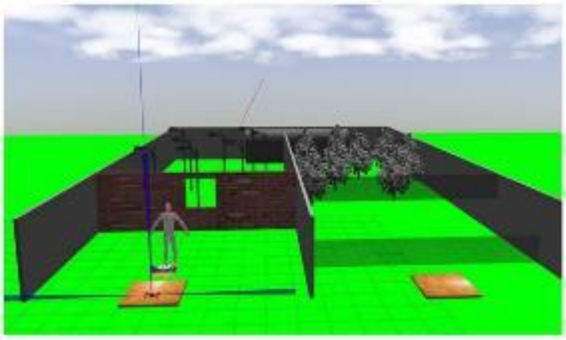

(1)

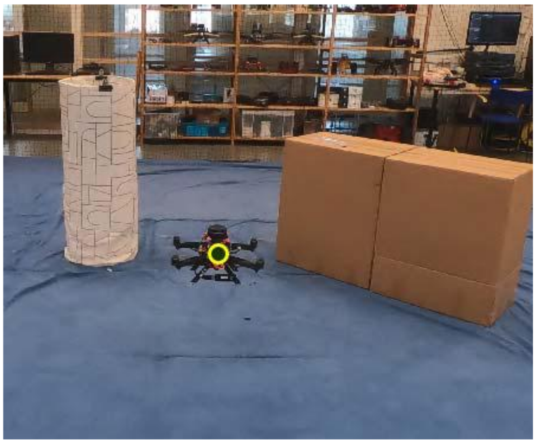

(2)

Figure 2-7 (1) Gazebo environment for drone controlling simulation (2) real-world flight tests

2.4.1 Path planning with prior knowledge

In path planning with prior knowledge, the UAV's control is affected by structural constraints, obstacles, and airflow disturbances. Consequently, static path planning may have limited relevance in real-world navigation scenarios. Nevertheless, it remains beneficial for simple and predictable environments like tunnels, where the UAV can follow a fixed path with minimal deviations. The control of the UAV in static path planning is usually addressed using high-precision pose control methods. However, the main challenge arises from the increased complexity of a three-dimensional environment, which introduces difficulties in computing time and accuracy.

2.4.1.1 Grid/ graph search

Grid/ graph search algorithms, such as Dijkstra, A*, and D*, are widely used in static path planning problems. These algorithms calculate the optimal path by defining cost functions and traversing all possible nodes. They are particularly useful for path planning in global and connected areas.

Grid-based graph search algorithms divide the real world into finite grids and calculate the optimal path. This approach can be visualized as a grid (Figure 2-8 (1)), where each node represents a possible location in the environment, and the edges between nodes represent the possible paths. The graph-based search uses the environment shape (Figure 2-8 (2)) and includes methods such as 3D Voronoi and visibility graphs. The differences between grid-based and graph-based approaches are presented in Table 2-4.

Table 2-4 Comparison between grid-based and graph-based approaches

	Grid-Based	Graph-Based
Environment type	Environments with known and uniform structures, where discretization is reasonable.	Environments with complex and irregular structures, where key points and connections are essential.
Computational efficiency	Can be computationally expensive for fine-grained grids.	Often more computationally efficient, particularly in scenarios with sparse connectivity.
Flexibility	Limited flexibility in representing complex connectivity patterns.	More flexible in capturing complex relationships between points in the environment
Memory requirements	Memory requirements can be high, especially for detailed grids.	Typically has lower memory requirements, especially in sparse graphs.

Grid and graph search algorithms can handle complex environments with many obstacles. However, they can be computationally expensive, especially in large environments with many nodes. Additionally, their poor adaptability to dynamic complex occlusion environments is a disadvantage, as they require a dense mesh to complete tasks in such scenarios.

Research has been conducted to improve the adaptability of graph search algorithms in dynamic environments. For example, Akmandor [110] achieved passive navigation of mobile robots in unknown environments using a heuristic feature grid-based algorithm. This algorithm navigates through a weighted cost function of heuristic features in a robot-centric 3D grid structure, using features such as proximity to the target, previously selected trajectories, and nearby obstacles. The research has been verified through physical simulation, demonstrating a drone's ability to fly autonomously in an environment with the same type of obstacle.

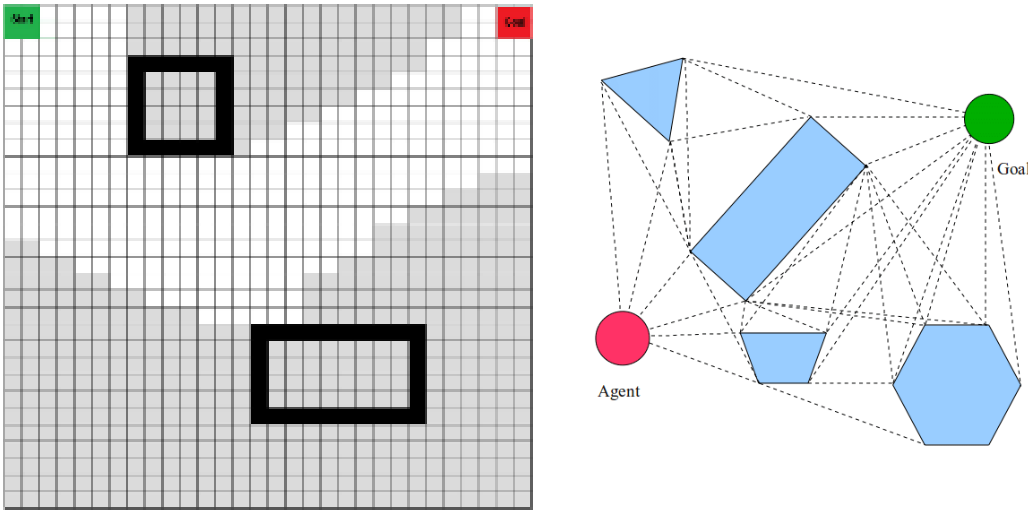

(1) (2)

Figure 2-8 (1) Grid search path planning method [111]. (2) Visibility Graphs path planning method [110], [112].

2.4.1.2 Sampling-based methods

Sampling-based algorithms create a graph from sampled points (nodes). The principle is to find the optimal path among adjacent nodes randomly generated in the connection space. The main methods include Rapid Exploration Random Tree (RRT) and Probabilistic Roadmap (PRM) (Figure 2-9). However, the randomness of sampling might affect the path's stability, leading to the possibility of not finding a result or obtaining an unstable one.

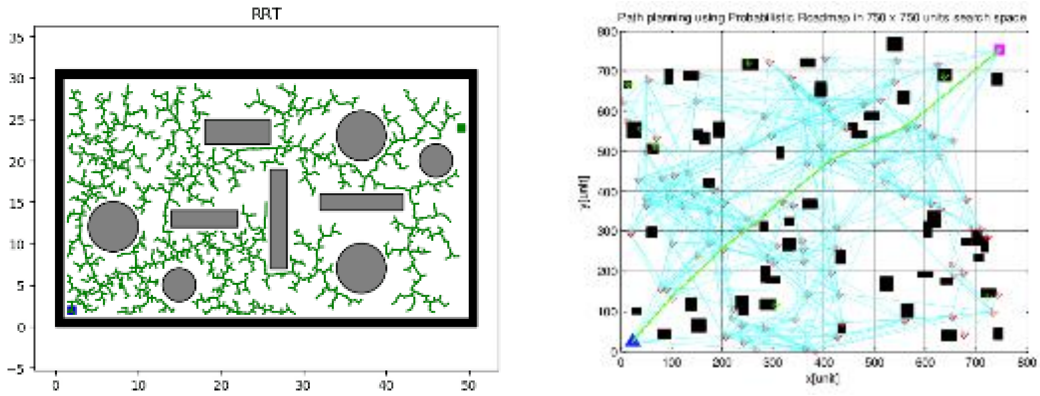

(1) (2)

Figure 2-9 Sampling-based (1) RRT and (2) PRM [113] path planning method.

Some applications and improvements of sampling-based methods include:

Brunel [55] used frontier reasoning of obstacle shapes to filter paths planned by RRT, reducing parameters and increasing computational efficiency through one-step spatial information aggregation. This method has proven real-time performance on an onboard computer.

Campos-Macías [114] used depth sensors and RT-Connect random methods for online path planning in unknown chaotic environments. Dynamic constraints, such as yaw and acceleration, are considered to avoid collisions, and streamlined data transmission allows for dynamic navigation independent from the GPU.

Lee [115] adopted a Local Dynamic Map (LDM) for UAV dynamic and static obstacle perception in 3D path planning. A probability-based occupancy map is used for obstacle location and velocity estimation, consisting of a particle filter to reduce the computational size and a circular buffer to minimize occupancy. Simulation and field experiments prove the feasibility of the algorithm for real-time grid navigation forecasting.

2.4.1.3 Other automatic planning algorithms

There are additional methods tailored for specific path planning scenarios. Potential Field Methods including Artificial Potential Fields (APF) in Figure 2-10, are a classical approach using attractive and repulsive forces. And Vector Field Histogram (VFH) incorporates sensor data to create a potential field. APF is primarily used for real-time local path planning.

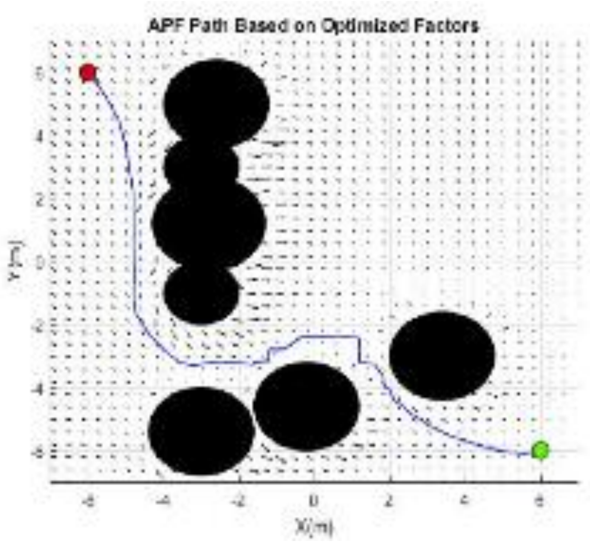

Figure 2-10 APF [116] path planning method.

Optimization-based methods search through the solution space to find a path that satisfies certain defined constraints. Examples include Sequential Quadratic Programming (SQP) and Interior Point Methods.

Machine learning in static environments has significance for sensor fusion and data integration. Information from various sensors, such as cameras and lidar, contributes to a more comprehensive understanding of the environment and enhanced situational awareness in unseen scenarios. Machine learning also enables reduced manual tuning of UAV flying parameters for accurate control. In computational-heavy scenarios, intelligent deep reinforcement learning algorithms enable fast convergence of other path planning algorithms.

Table 2-5 compares the above-mentioned methods, listing their pros and cons.

Table 2-5 Sampling-based algorithms compared to experience-based algorithms.

	Pros	Cons
3D Voronoi (Graph search)	• Constructed expediently	• Not smoothed trajectory
RRT (Sampling-based)	• Convergence guaranteed • Low computational requirements	• Slow convergence rate • Large memory requirements • Rejection of not connected nodes • Path randomness and bias • Depend on parameter settings
PRM (Sampling-based)	• Low computational requirements	• Dependent on knowledge of obstacle geometry
APF	• Simple model	• Local minima problem • Narrow passages not applicable
Grid search	• Search directly for open areas • Narrow passages and polygonal obstacles applicable • Computationally fast	• Slow in complex environments

2.4.2 Path planning without prior knowledge

Path planning in environments without prior knowledge allows UAVs to navigate in complex and changeable settings where information about obstacles and the environment is limited or unknown. An illustration is given in Figure 2-11. In such scenarios, the UAV's pose is calculated using the trajectory tracking method, and the control problem is solved by high-precision pose control methods.

UAV path planning algorithms for environments without prior knowledge have evolved from ground vehicle algorithms designed for two-dimensional environments [117]. However, the added complexity of three-dimensional environments and the need for real-time adaptation present challenges in computing time and accuracy. Key performance indicators include computational speed, robustness, and adaptability to various unknown obstacles and environments.

With the development of visual localization and real-time sensing technologies, UAVs can perform path planning in increasingly complex and changeable environments without prior knowledge. Implementing real-time path planning using learning-based approaches in environments without prior knowledge requires powerful computing power to collect data from multiple sensors, synchronize input data, and handle the computational burden of 3D path planning. As a result, data processing efficiency should be considered in practice.

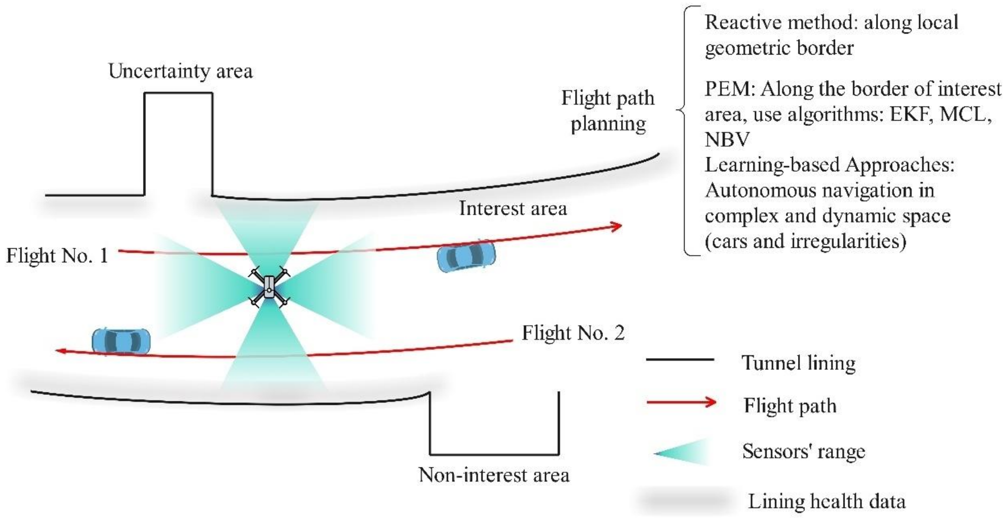

Figure 2-11 Illustration of path planning in tunnels without prior knowledge

2.4.2.1 Reactive obstacle avoidance

In environments without prior knowledge, reactive algorithms play a crucial role in UAV navigation. These algorithms rely on sensor information [110], such as lidar, sonar, or cameras, to make instantaneous decisions in response to the environment. Different control methods and response modes are set for various types of obstacles, depending on the specific scenario. For instance, in a simple tunnel environment, drones can navigate by flying along the tunnel axis [118], while for open obstacles like windows and doors, drones need to pass through the middle perpendicular to the obstacle. Some novel reactive navigation methods and applications are given in Table 2-6.

Table 2-6 Some novel reactive navigation methods and applications

Authors	Scenarios	Improvements	limitations
Elmokadem [119]	Unknown tunnel-like environments	A 3D collision-free control strategy using recent sensor observations	The need for a realistic sensing model and possible ineffectiveness in low visibility or complex obstacle scenarios
Shang [120]	3D tunnel wall-following navigation, in GPS-Denied environments	With an ultrasonic sensor for reactive control, measuring the distance between the UAV and walls to	Its potential inaccuracy in tunnels with poor ultrasonic reflectivity or when other objects interfere with sensor readings
Elmokadem [92]	unknown 3D tunnel-like environments, other UAV types, and autonomous underwater vehicles	With sensor observations, it guides the UAV along the tunnel axis.	It may face challenges in more complex scenarios with multiple intersecting tunnels or tunnels with significant changes in shape, as
Lindqvist [121]	Various laboratory settings for fast solutions using limited onboard computational power	Using nonlinear model predictive control (NMPC) and an onboard 2-D LiDAR, enabling real-time UAV obstacle avoidance in constrained environments.	Challenges with sensor performance in dusty conditions or the need for additional sensing modalities for better perception in specific scenarios
Mansouri [77]	UAV rapid exploration of unknown areas in mine and tunnel-like environments	Considering the flying platform as a floating object and composing a velocity controller on the x, y axes, and altitude control to navigate along the tunnel	The reliance on low-cost sensors, which might not provide the same level of accuracy and performance as more expensive sensors, especially in complex tunnel environments with challenging conditions.
Kanellakis [122]	Autonomous tunnel navigation of low-cost aerial robots	NMPC and visual processing align the vehicle's heading to the tunnels' open space in the image frame of the most distant area.	The need for some visual processing, which may not be feasible in extremely dark tunnels
Tan [20]	Deep tunnel sewage systems (DTSS) that	Use of a rotating camera system that minimizes	The reliance on a purpose-built UAV platform, as

	have limited access and are potentially hazardous for manual inspection	image distortion and captures high-resolution images of the tunnel's inner surface	commercial off-the-shelf UAVs may not be suitable for tunnel inspection due to their optics and GPS dependence
Padhy [123]	Indoor corridor environments where GPS technology is unavailable or imprecise	Forward-facing camera on a UAV to process video data and generate the next set of control commands for safe autonomous navigation in real-time	may not be as effective in tunnel navigation scenarios, as tunnels often have curved or irregular shapes, which could pose challenges for the vanishing point-based approach used in this method

Researchers proposed meta-learning training to enable UAVs to switch appropriate models in the adaptive environment, to overcome the limitations of fixed models on the adaptability of different inspection environments [124]. While the UAV is in operation, the monitoring verification technology determines when the system needs to adjust its model by considering the data-pruning process of effective learning. Meta-learning training can accurately predict the future state of the system.

However, most reactive control local path planning algorithms still face the limitations of the sensor field of view. Applying sensor methods [125] for obstacle avoidance is direct, but for tunnel navigation scenarios, the sensor field of view in the shape of a spherical wedge will require additional customization if the tunnel's geometry is complex.

2.4.2.2 Probabilistic exploration and mapping

The probabilistic exploration and mapping (PEM) techniques for underground UAV flight often integrate Simultaneous Localization and Mapping (SLAM) methods with probabilistic approaches. Commonly used algorithms in underground UAV navigation include the Extended Kalman Filter (EKF), Monte Carlo Localization (MCL), and

Information Gain-Based Methods.

EKF, used for state estimation and sensor fusion, is a representative algorithm in UAV navigation, as seen in [21] and [22]. MCL with exploration is a probabilistic algorithm for UAV tunnel navigation, using particles to represent possible UAV locations and updating them based on sensor data alignment, as in [126]. Both methods incorporate exploration strategies to guide the UAV towards unexplored regions, efficiently updating their position estimate in complex tunnels with limited prior knowledge. Information gain-based methods prioritize paths that maximize sensor information in tunnel navigation, focusing on less certain tunnel structures or features. Next-Best-View (NBV) planning algorithms assess potential information gain for different flight paths, ensuring thorough exploration and accurate maps. This strategy is valuable in underground environments with irregularities and unknown sections.

Li [74], [127] used PEM to explore the environment and build a 3D map of the underground tunnel. Bendris [128] described a method using NBV through the FastSLAM algorithm for autonomous tunnel inspection and 3D voxel map reconstruction in GPS-denied environments with poor lighting and obstacles. However, limitations include challenges in long, safe autonomous inspection in poorly illuminated, uneven, and symmetrical tunnel environments and height and weight limitations for better sensors.

Vanegas [129] adopted a probabilistic control method using Partially-Observable Markov Decision Process (POMDP) for UAV navigation in cluttered and GPS-denied environments. Mansouri [130] proposed a probabilistic control method using potential fields to avoid collisions with walls in underground mine tunnels. This method relies on low computational complexity image processing to correct the UAV heading towards the tunnel axis. However, limitations include the dependence on surrounding environments with good distinctive features and high computation power, which might be limited in real-life underground mining applications.

2.4.2.3 Learning-based approaches

Deep learning-based methodologies have shown great potential in UAV path planning for unknown tunnels, offering several advantages that enhance autonomous navigation capabilities in complex and dynamic underground environments. By automatically learning complex spatial patterns and relationships from sensor data, deep learning models can adapt to various tunnel structures, including irregular shapes, changing elevations, and dynamic obstacles. End-to-end learning streamlines the development process, while real-time decision-making and dynamic obstacle avoidance enable UAVs to navigate safely and efficiently. Furthermore, reinforcement learning-based approaches allow UAVs to learn from experience, leading to improved decision-making over time. Deep learning models also reduce the dependency on explicit maps, optimize exploration strategies, and adapt quickly to environmental changes, making them robust in scenarios with limited prior knowledge or evolving surroundings. However, the success of these methodologies relies on the quality and diversity of training data, model architecture, and safety constraints consideration.

A neural network combined with a reinforcement learning algorithm requires a large number of UAV paths for supervised training to regulate UAV route planning behaviour. The advantage of deep reinforcement learning algorithms is that they do not depend on the information of the environment and UAV model. Deep learning algorithms excel at understanding visual perception problems, while reinforcement learning algorithms are good at learning route formulation strategies. However, dealing with sparse rewards in binary learning is one of the biggest challenges in reinforcement learning. Training convergence can be accelerated by setting reward functions and penalty functions and using artificially set reward and punishment standards.

Deep reinforcement learning can be divided into two types: on-policy and off-policy. The former can learn what behaviour patterns drones adopt in various situations, using target strategies as behavioural strategies. However, on-policy methods have low data use efficiency, and modification of formulas or models can lead to extensive labour for training and fine-tuning processes. The latter learns the input data of UAVs in various situations and collects data as a separate task in training, such as Deep Q-Network (DQN), deep deterministic policy gradient (DDPG), and other excellent methods. Off-policy approaches are more effective because all historical input is used for effective learning.

Some relative research includes:

Bouhamed [131] used DDPG in continuous action space, which is a kind of off-policy training method. DDPG deep reinforcement learning algorithm, compared with DQN, has the ability to deal with larger dimensions or infinite action space. Users could define customized reward and collision penalty functions before training. The penalty function is defined as a function of the collision depth σ of the collision, not as a state function of a collision or not. A such non-discrete function has the advantage of fast convergence.

Guo [132] used a layered RQN based on long short-term memory (LSTM), and a manually set DRL loss function to avoid drifting obstacles. The method used has better convergence and efficiency than state-of-the-art DRL methods, with denser positive rewards in the grid.

Lee [133] used the soft actor-critic algorithm with hindsight experience replay (SACHER) to improve DRL efficiency. HER can improve the sample efficiency and obtain the experience of achieving goals from both successful and failed tasks. Compared with the most advanced DRL algorithm, SAC algorithm, and DDPG algorithm, the SACHER algorithm tracks the effectiveness of error and cumulative reward and has universal applicability.

Yang [134] used a dual-depth Q network (DDQN-PER) with a preferential empirical replay to avoid multiple static and dynamic obstacles. It solves the navigation problem of the traditional Q-learning algorithm of overestimating the action value in a dynamic environment, and it adapts to each environment without adjusting the architecture or learning algorithm.

Mandel [135] used semantic information to reduce UAV navigation commands. The UAV acts independently to achieve the target mission once it has the semantic content of the environment. Semantic segmentation facilitates UAV tasks and is robust to environmental changes.

2.4.2.4 Other methods and trends

In the realm of UAV inspection, there are methods that don't rely heavily on high computation power. One such method is the use of UAVs in a cage (Figure 2-12), where 3D-printed cages [48], [136] are designed for specific inspection purposes or environments. These cages [137] [138] [1], fitted around the rotors of the UAV, act as a physical barrier to prevent collisions with obstacles, making them ideal for confined spaces or areas with potential hazards.

Figure 2-12 Elios 2 UAV positioned within a protective cage for entry into confined spaces with high collision risks during routine inspections [139]

Another approach is contact-based UAV inspection in Figure 3-13, where UAVs physically contact surfaces like tunnel walls, ceilings, pipelines, and bridges. This method allows for a more detailed inspection and can be particularly useful in situations where other methods may fall short. This method has been successfully applied in tunnel-like environments[140], mines, and even ceilings [141], pipelines [142], and bridges[143], [144].

Figure 2-13 Prototype of multirotor system operating in contact with the ceiling. [144]

In scenarios that require real-time performance, optimization of visual algorithms can be achieved through simplified input information and omitting data processing steps. This enhances the speed and efficiency of the UAV's path planning capabilities. Techniques such as local replanner [145] [146] and 3D circular buffer zone, and semantic segmentation for the alleviation of huge data transmission [147] are all examples of this approach.

Additionally, direct processing [148] of unfused sensor data and the local multi-resolution method [149] can further improve real-time performance. These methods maintain raw historical information in an in-memory data structure, and adopt a high-dimensional state lattice including velocity and acceleration for the area close to the UAV. This significantly reduces the computation of remote scene correlation and improves computational efficiency.

In cases of abnormal flight conditions, an immune paradigm can be used for UAV position and speed estimation. Artificial immune system (AIS) [150] uses flight data under nominal conditions to produce navigation commands based on the UAV's pose. This reduces the computational cost and allows the UAV to adapt to abnormal flight status.

Visual target identification [151], such as target detection and obstacle avoidance based on vision, can further enhance the efficiency of flight path generation. By using target detection to eliminate the influence of wrong predictions in a deep network, collision-free travel can be achieved using monocular sensor data alone. This reduces flight time and unnecessary turns, making the UAV inspection process even more efficient.

In summary, there are various UAV inspection methods and trends that don't require high computation power. These methods, including UAVs in a Cage, contact-based UAV inspection, and optimization of visual algorithms, can greatly enhance the efficiency and effectiveness of UAV inspections.

2.5 Summary

This chapter reviews different types of methods for automatic control of UAVs in underground structures, from traditional multi-sensor fusion methods to computer vision-based path planning. In this literature review, of particular interest are automatic flight methods based on visual localization, including pose estimation, obstacle avoidance, path planning, and scene recognition. The main findings of this chapter include the unfavourable characteristics of UAV inspections in the underground environment and some strategic solutions for the applications as follows:

1. For automatic drone inspection in underground structures, the main difficulties in drone localization are attributed to the limited or rather absent availability of GNSS signals, poor lighting conditions, weak features, and the complexity of the underground geometry. Likewise, difficulties in path planning algorithms also lie in the difficulty of adapting to complex geometric underground environments (e.g., complex tunnel/mine networks).

2. To address the lack of GNSS signals, sensors such as optical and LiDAR are the best alternatives for reliable positioning data sensors. They are suitable for small low-dynamics lighted environments and geometrically regular textured environments, respectively. Unlike traditional binocular vision or RGB-D cameras with limited scale information, LiDAR provides sparse depth information and can work in low-luminance conditions. Similarly, multi-cameras also produce long-range scale information in large underground structures. In practice, accurate and robust localization can therefore be achieved by the fusion of multi-sensors (e.g., LiDAR and multi-cameras) as opposed to individual ones.

3. To address the effect of weak textures on localization, learning-based algorithms further enhance the depth perception of the monocular sensors. In theory, deep reinforced learning (DRL) can offer a depth map, while its wide application is limited by its adaptability and training cost in dynamic and complex unknown environments. In future studies, advances in both CV-based algorithms and computational hardware will contribute to the improvement of localization accuracy.

4. Another major challenge for drone underground inspection is obstacle avoidance in complex underground geometric conditions, which requires path planning using

advanced strategies. Conventionally, Sampling-based and grid-based methods work in simple environments with map information, whereas in complex environments, their accuracy and computational cost have to be balanced by manual parameter settings. As an alternative, a distance-based penalty function could navigate the drone away from obstacles in complex and dynamic environments. To address this challenge, promising development lies in DRL for the understanding of obstacle patterns, predictions, and decision-making for real-time navigation. Another prospective research direction is to use multiple drones for simultaneous data acquisition and management.

Overall, current GNSS-independent sensing and autonomous navigation are only applicable in small, static, environments with good lighting conditions and require human supervision in the loop. Challenges and opportunities in this research field include the development of sensors and unmanned systems for large-range operational requirements, and the adaptation to dynamic scenarios, such as luminance variations, and structural change in environments. The current limitations for UAVs in underground space inspection include their inability to effectively operate in large-scale geometric inspection environments, perform obstacle avoidance, and do feature recognition and semantic recognition, while these topics represent potential avenues for future development.

3. Literature review on image data processing

3.1 Introduction

This chapter specifically reviews image processing techniques for identifying defects and measuring dimensions in the context of UAV image-based tunnel surface inspection. The literature review highlights the latest advancement in this field, emphasizing the critical role of image processing in extracting valuable information from the acquired data. We reviewed various data processing techniques used in point cloud and image processing, including the identification of cracks and other defects on tunnel surfaces. This chapter elucidates the benefits and potential applications of these technologies in infrastructure assessment and management, shedding light on how they can contribute to more efficient and accurate inspection of tunnel surfaces.

3.2 Methods of tunnel surface data processing

The data processing needs to go from the collected image dataset to a 3D reconstruction model or organized digital twin [152], and then to extract useful information. To organize the UAV image dataset in tunnel inspection, image registration is an essential step. It aligns images taken from different locations and angles to create an accurate 3D model of the tunnel surface. It then facilitates accurate dimension measurements and the detection of any surface defects or irregularities.

The next step in processing is to detect the location of building edges. Most relevant methods are based on laser point cloud data. Images processing for facility deterioration monitoring and management still don't have mature applications yet. Point clouds from image data generally have larger errors than LiDAR, and these errors might be mitigated in the future over the development of image processing technologies. Therefore, the following literature review of tunnel surface data processing includes the most advanced research related to laser point clouds.

The unique challenges in tunnel image data processing include perspective distortion, noise, and motion blur. Due to these challenges and the lack of advanced data processing methods, the current image-based deformation monitoring of tunnels still has deficiencies in its effectiveness. Geometric distortion in tunnel model reconstruction occurs due to the camera's wide-angle lenses, instability from UAV motion, and the tunnel's cylindrical geometry. It requires image rectification and calibration to correct dimensions in images. Noise arises from poor lighting conditions, sensor interference, and data transmission errors. It is mitigated by filtering techniques and denoising algorithms supported by computer vision. Motion blur can be avoided by employing fast camera shutter speeds and deblurring techniques.

3.2.1 Geometric reconstruction

Geometric reconstruction is to get digital representation from an unstructured image dataset. The geometry reconstruction methods can be broadly classified into two categories: feature-based and dense methods.

3.2.1.1 Feature-based method

Feature-based methods in UAV tunnel image processing start from detecting and matching distinctive features across multiple images to create a sparse point cloud of the tunnel surface. Then with a sparse point cloud, the camera pose is estimated, typically with an off-the-shelf solver for the Perspective-n-Point (PnP) problem[153], or through Random Sample Consensus (RANSAC) [154]. Based on matches between images, structure from motion (SfM) and multi-view stereo (MVS) techniques are used to create a dense point cloud of the tunnel surface.

The feature-based method gives a rough feature point distribution. It's computationally efficient and robust to variations in viewpoint and illumination. However, it is not capable of processing the scenes with as many details as other methods do. Without highly intelligent computer vision, feature-based methods will produce large errors in spatial due to various reasons (Figure 3-1). Without specific segments in tunnel environments, the feature matching is still subject to interference of tunnel-excepted obstructions, like facilities, humans, cables, deficiencies, the misalignments due to incapability of calculation, and the simple presentation with B-spline approximation will face overfitting in dense points and underfitting in spare points. The errors could reach 0.1m in a tunnel inspection occasion [155].

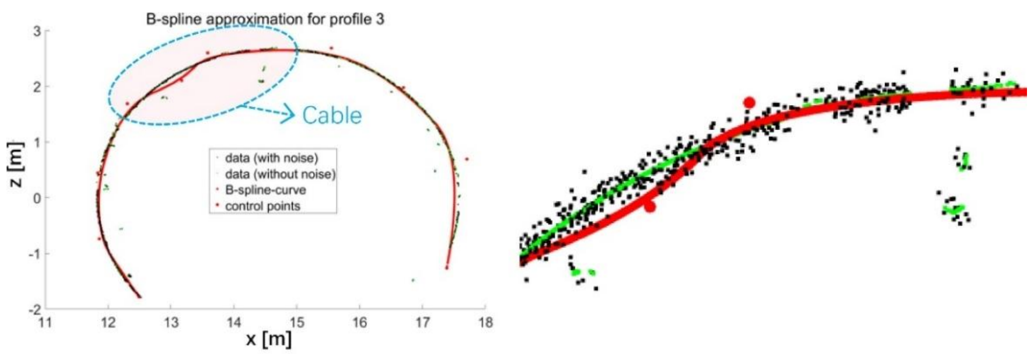

(1) Errors from obstructions of cables

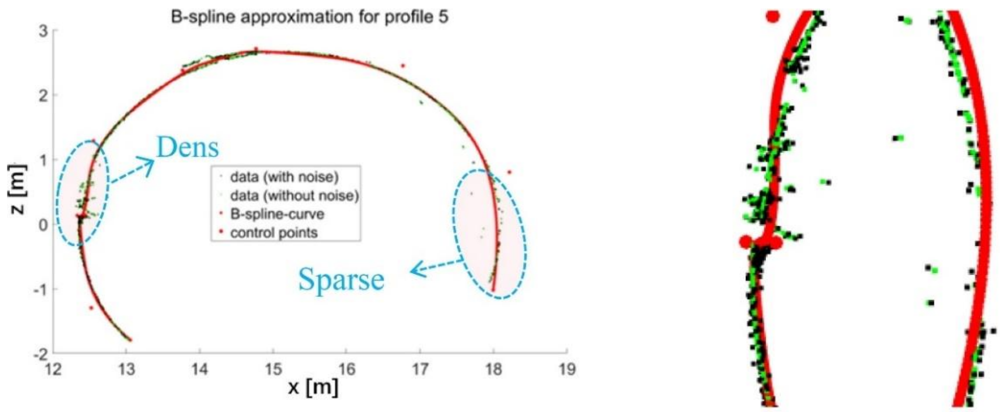

(2) Errors from overfitting and underfitting

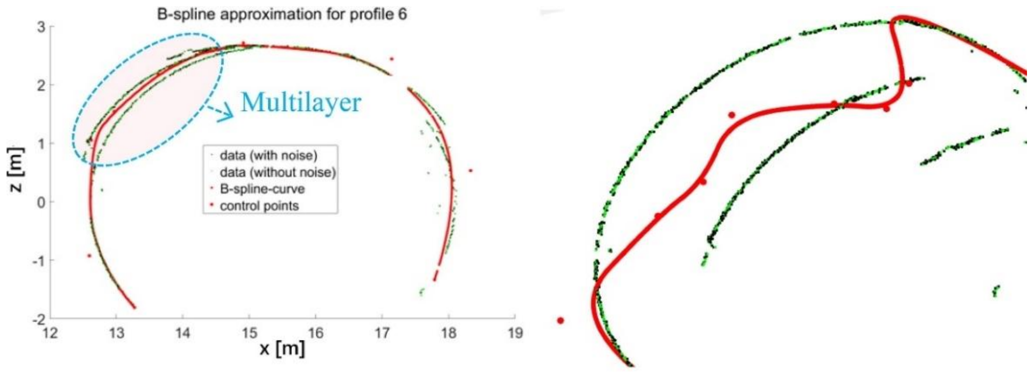

(3) Errors of incorrect multilayers due to misalignments

Figure 3-1 Error types in feature-based visual geometry reconstruction (Profile on the left and local feature on the right) [155]

3.2.1.2 Dense methods

Dense methods in UAV tunnel image processing involve creating a dense point cloud of the tunnel surface using dense methods [118]. This is done by estimating depth maps for each pixel in images. Depth estimation takes a major role in constructing a 3D point cloud. Depth could be estimated under a monocular vision, or a binocular vision.

Monocular vision attempts to estimate the depth information from a single image. This may rely on a variety of cues, for example, shading, texture, and perspective. On the other hand, Binocular vision attempts to calculate the 3D information from two or more images. This may be achieved through stereo matching or parallax mapping.

These depth maps for each image are then combined to create a complete 3D model of the tunnel surface [156]. This process involves aligning and merging the depth maps to create a unified 3D point cloud, structured as a triangle mesh representing the surface of the tunnel. This is often completed using the techniques of shape from shading (SfS) and SfM. SfS attempts to infer shape or surface orientation form based on image intensity variations, whereas SfM does so from images from multiple viewpoints.

The limitation of dense methods limitation is an intensive computational cost in high-definition scene reconstruction, where each image is processed for depth estimation. Both these methods are limited to the application in tunnel scene reconstruction. Therefore, further processing to optimize the data to conform tunnel situation is a must.

3.2.2 Point cloud processing

3.2.2.1 Point cloud denoise and optimization

UAV images can generate point clouds to inspect transport infrastructures. However, the UAV images may be influenced by low/uneven illuminance and sensor defects [157]. Therefore, noise and outliers may appear in the point cloud. The noises might cause interference in crack width identification [158]. Therefore, noise reduction and optimization of point clouds are vital in UAV image processing.

Advanced research on point cloud denoise is mainly based on terrestrial laser scanning (TLS) point clouds field test (Figure 3-2). This is because TLS inspection appears earlier than UAV infrastructure inspection. The experiences on LiDAR point cloud noise removal are referenced for based UAV data processing in the tunnel inspection practice.

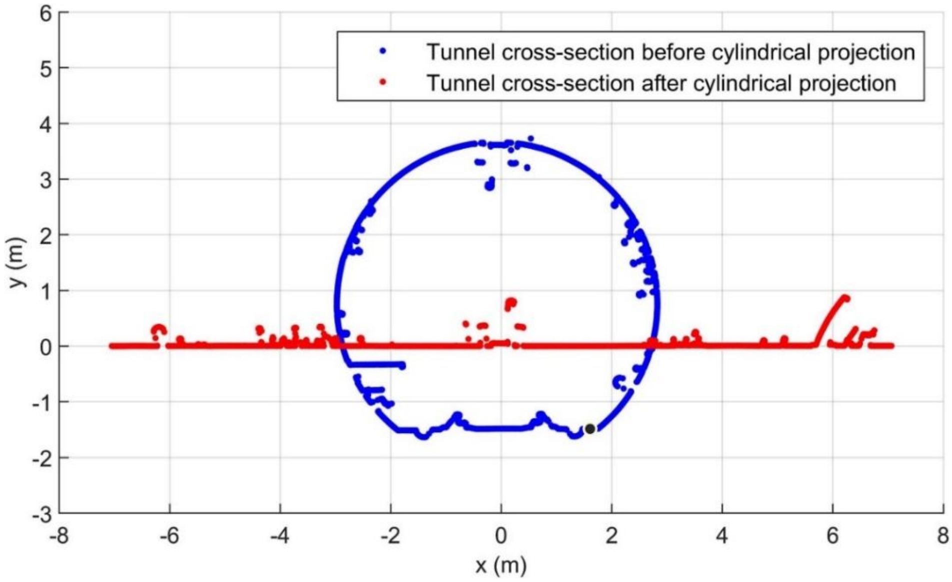

(1)

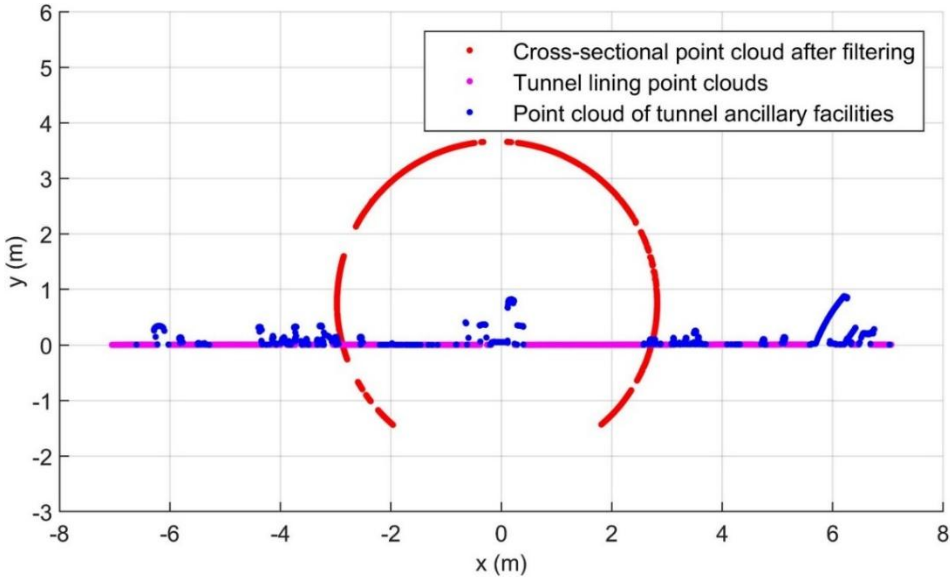

(2)

Figure 3-2 Noise removal in a tunnel cross section (1) before removal and (2) after removal

3.2.2.1.1 Manual denoise

Firstly, manual noise removal is necessary for obvious measurement error-related outliers [159]. This is because automated methods may not always effectively identify or address such extreme anomalies. A widely applied software Cloudcompare is used for the basic operation in primary processing. Then noise reduction techniques seek to get rid of unwanted data from the point cloud such as noise and outliers while preserving the object's or surface's geometric properties. These techniques can be broadly divided into two kinds of methods: filtering-based and model-based.

3.2.2.1.2 Filtering-based denoise

Filtering-based methods utilize statistical or morphological filters to clean the point cloud data. These filters can be applied in the spatial domain, frequency domain, or a hybrid of the two. For instance, a standard filtering technique is the statistical outlier removal (SOR) filter (Figure 3-3) that eliminates the points which are situated far away from their neighbour distance or density [160]. A popular filtering method is also the radius-based filter that removes the points which have fewer neighbours in a given radius.

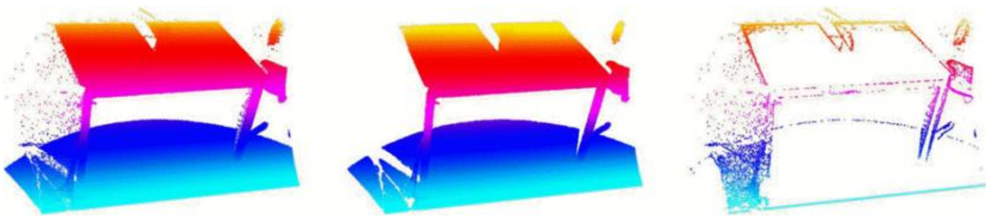

Figure 3-3 Point Cloud Library (PCL)'s SOR illustration. Left: a raw point cloud acquired, middle: the resultant SOR filtered point cloud, right: the rejected points

3.2.2.1.3 Model-based denoise

Model-based methods utilize mathematical models, which can be linear or nonlinear, to fit and clear point cloud data of noise (Figure 3-4). These methods aim to represent geometric features of objects or surfaces [161]. Tunnel surface fitting projects the 3D point cloud, potentially containing uncertainties (or noises), onto a presumed surface to facilitate geometry construction. This approach often assumes cross sections in tunnels to be either circular or elliptical based on nearly known tunnel geometry from design blueprints. While this method directly eliminates noise point clusters located away from presumed surfaces through projection, it's tailored for laser point cloud processing. It assumes both measuring error and tunnel deformation to be at the millimetre level.

The advantage is easier outlier point removal and the convenience in later image information processing. Information extraction and segmentation on curved surfaces could then be transformed into a 2D shape from the undevelopable surface of a curved tunnel to a developable surface [162].

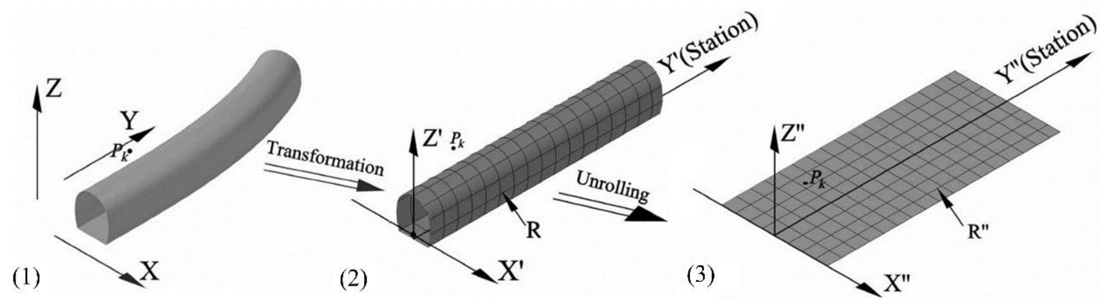

Figure 3-4 The method for generating the tunnel unwrapped map: (1) Cartesian coordinate system; (2) tunnel stationing coordinate system; (3) unwrapped map [163]

The convenience of tunnel health inspection is demonstrated in a deformation study. It utilizes coordinate conversion to get the distance to the curved surface as an additional depth scalar for each pixel. They then presume that the deviation from the extraction points to the ideal fitting surface, either circular or elliptical, represents the cumulative deformation from the construction phase. This deformation accumulates from the construction phase to the current state during inspection.

The authors also suggest that the tunnel cross sections experience convergence deformation after years of operation and compare the inspection result to the tunnel convergence deformation simulation result. Figure 3-5 (2) shows that the maximum radial error from TLS data could be as minimal as 0.5 mm.

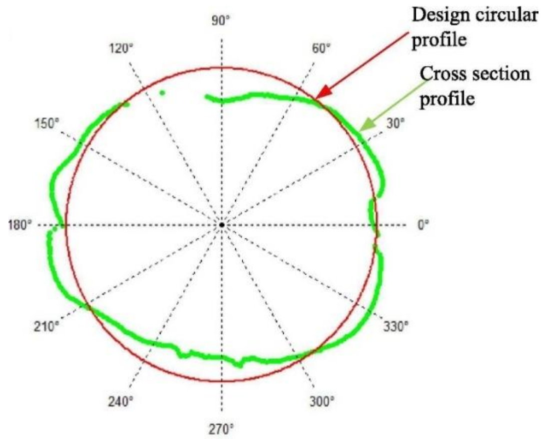

(1) Deformed (R_0+50 $\Delta\rho^*$, θ) cross section shown on designed shape (R_0, θ) (radial deviation ($\Delta\rho^*$) magnifies by 50 times)

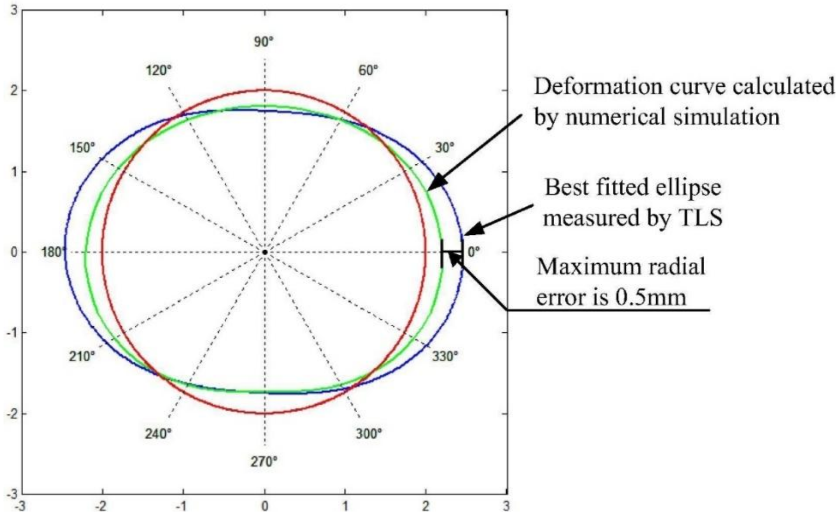

(2) Comparison between fitting TLS measurement and simulated deformation

Figure 3-5 Comparison between measured and theoretical convergence deformation [161]

A model-based method for example is the RANSAC algorithm [164] which fits a plane model to the point cloud data and in the process, it also eliminates the points that do not match the model. A commonly used model-based method is also the moving least squares (MLS) surface fitting, which fits a surface to the point cloud data and interpolates the missing data points.

Some researchers employ machine learning-based segmentation techniques to eliminate noise (Figure 3-6) [165]. This type of research increases the compatibility of tunnel geometries from circular and ellipse to other smooth surface shapes. To validate the accuracy of machine learning methods, they compare the point cloud fitting results to the computed results of the deformed convergence surface. The agreement between ML results and manual segmentation results provides enough precision for a tunnel deterioration mechanism study [166].

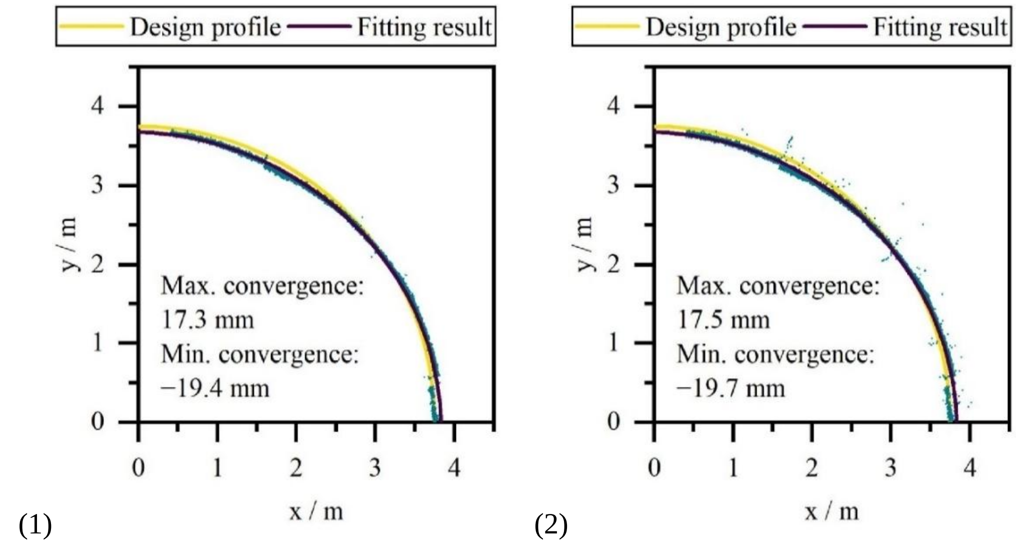

Figure 3-6 Comparison between elliptical fitting results compared to (1) manually annotated dataset and (2) trained segmented data [165]

In previous studies, most model-based methods typically move the point clouds to the assumed surface, rather than deleting the noises. This makes the subtle local deformation less detectable. For example, some research realized the segment seams detection based on the dislocations of the fitting surfaces [167]. Recently Zhang [168] claimed to progress on tunnel deformation analysis, which is achieved by 3D unrolling on an ellipse surface and calculation of the deviation of the point cloud from the designed section. A LiDAR point cloud processing example is shown in Figure 3-7 to illustrate the quality of noise removal methods.

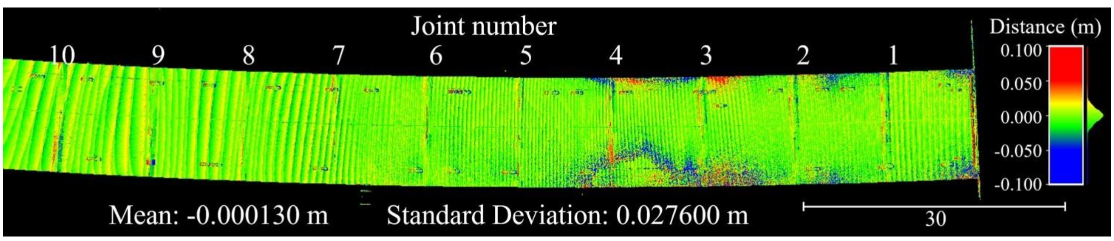

(1) Corrected point cloud comparison (g-h Filter).

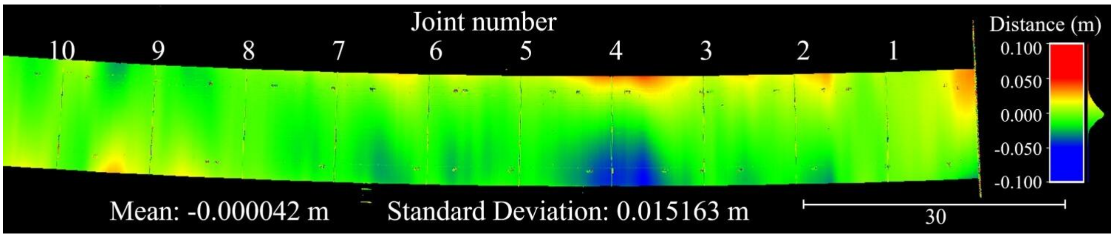

(2) Corrected point cloud comparison (Particle Filter).

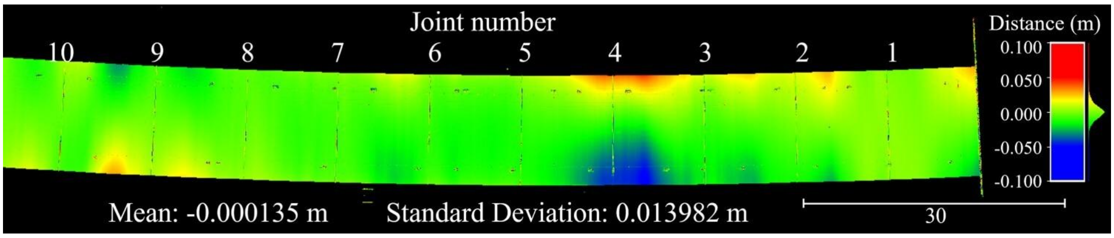

(3) Corrected point cloud comparison (Extended Kalman Filter).

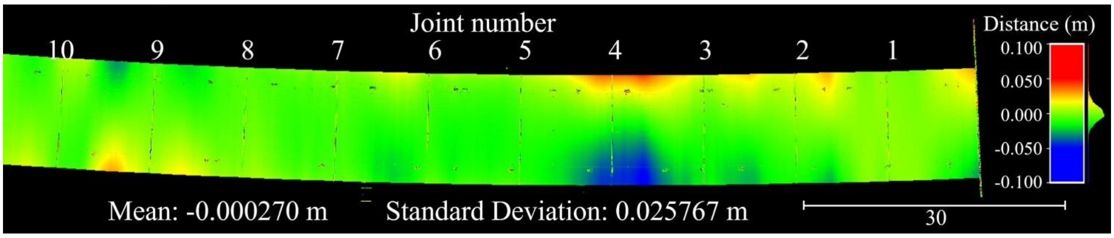

(4) Corrected point cloud comparison (Unscented Kalman Filter).

Figure 3-7 Quality of noise removal methods for a LiDAR point cloud example [169]

3.2.2.1.4 Challenges in the noise reduction

Despite recent advancements in noise reduction and the optimization of point clouds derived from UAV imagery, there remain noteworthy shortcomings and challenges. Chief among these is the computational complexity and time expenditure inherent in noise reduction and optimization algorithms. Notably, the computational demands escalate with the augmentation of point cloud data size and resolution. Consequently, this computational burden can impede real-time or large-scale applications.

Furthermore, a significant challenge lies in striking the balance between noise reduction and feature preservation. Certain noise reduction methodologies, like subsamples and filters to reduce computation burden, may inadvertently eliminate valuable data points alongside noise [170], potentially resulting in the loss of crucial geometric features. Therefore, achieving an optimal equilibrium between noise reduction and feature preservation is paramount for yielding accurate outcomes.

In summary, it is evident that noise reduction and optimization processes for point clouds sourced from UAV imagery are pivotal for ensuring the precision and dependability of 3D data. Despite notable progress in this domain, persistent challenges necessitate further research and development efforts in refining noise reduction and optimization algorithms. Such endeavours are essential for enhancing the efficiency and efficacy of utilizing point cloud data across diverse applications.

3.2.2.2 Point cloud quality assessment

As the assessment reference of image processing result, LiDAR data processing of point cloud models is summarized in Table 3-1 and compared. The research in the table is organized by the inspected subject, technical approach, data format (fused model from multimodal data or not), reported accuracy, and point cloud density.

Specifically, the image-based model should have accuracy and point cloud density no smaller than most LiDAR results in similar cases. The point cloud density of LiDAR is generally lower compared to that from RGB photographs in close-range tunnel surface defect inspections. From Table 3-1, a fused model could make up for the noises of both models but sacrifice the point cloud density. Lower density in the fused model is observed than single data type model.

Table 3-1 Comparison of LiDAR and fused point clouds in tunnel and pipeline inspections

Reference	Inspection subject	Data processing methods	Data format	Accuracy (m)	Density (pts/m^2)
[171]	Railway Tunnel Clearance	Pre-treatment of point cloud by segments along the line	MLS[1] data	0.03	100
[172]	One track of	Tunnel cross-section extraction on	TLS[2] data	0.0008	2.8×10^4

	railway tunnel	an estimated boundary line			
[173]	Railway tunnels with power lines	Clearance gauge and the deflection of the aerial contact line in	MMS[3] data	0.0252	1.7×10^4
[174]	Subway tunnel deformation measurement	Region segmentation and projection of original point cloud to elliptic cylinder model	Laser scanning data	0.002	1.7×10^4
[162]	Shield tunnels	Projection along the axis and projection on cylindrical model	TLS data	0.0000004	6.4×10^4
[175]	Highway tunnel	A partially movable robotic arm measures the defect information	RGB and laser data	0.0001	-
[176]	Metro tunnels in Shanghai and Nanjing	Segments aligned to the local fitted quadric surface	TLS data	0.0046	6.6×10^4
[177]	Metro tunnel	Hierarchical segmentation for data fusion between LiDAR and RGB data	RGB and TLS data	0.012	7.1×10^3
[178]	Construction stage tunnel	Data fusion using the angle calibration method	RGB and TLS data	0.010	5.5×10^3

[1] Mobile 3D laser scanning system.

[2] Terrestrial laser scanning.

[3] Mobile Mapper System

In this occasion, the accuracy and density of image point clouds are used for image point cloud quality assessment to some degree. Inevitably the image point cloud quality is lower in accuracy compared to LiDAR point cloud. However, the efficiency of image processing continues to improve with the development of computation power. It has been shown that among 17 image processing algorithms for surface defects commonly used in recent years, the training time with GPU prediction and the percentage of accuracy shows a roughly positive correlation [179].

Other frequently used metrics for the UAV image quality assessment include spatial resolution, noise, and defect reflection level index, such as highway surfaces using the pavement condition index (PCI) [179]. Specifically, the defect size in images can be quantified compared with the actual or evaluated with the image quality indices as well as data extraction confidence. However, the indices-based measurement might lack a huge amount of data for training, and even the index threshold might be variable in multiple similar but different inspection environments [180].

3.2.3 Image processing

Image processing serves several goals, including object detection and recognition, feature extraction, and change detection in organized data. Object detection and recognition involves segmenting the image into regions representing the objects of interest, such as cracks, spalls, water leakage etc. This will enhance the accuracy in detecting and recognizing these features. Similarly, feature extraction involves dividing the image into regions that possess some salient properties, such as shape, colour, or texture, which can be extracted as the composite image of regions that have these distinct attributes. Change detection involves identifying differences between images in time series, such as changes in tunnel surface or the appearance of new objects; this can be achieved by segmenting the image into regions that suggest the change.

3.2.3.1 Image segmentation

UAV tunnel images can be segmented with, for example, thresholding, edge-based segmentation, region-based segmentation, and machine-learning segmentation. Thresholding works by setting an attribute value (like lightness or colour) for some pixels at much lower levels than is usual, and segments the image based on all pixels greater than this level (Figure 3-8) [158]. Edge-based segmentation works by finding edges in the image and based on using them as an underlying criterion to segment into distinct areas which alone have meaning. Region-based segmentation consists of the process of segmenting the image into areas or clusters which are composed of similar or identical pixels. Machine learning-based segmentation works by employing the learned results or patterns to algorithmically segment the image, using such learning techniques as random forests or neural networks.

Numerous research using computer vision presents accurate outcomes in cracks [181], rebar exposure [182], and leakage [183] identification. The detection of crack direction and structural crack identification is straightforward. Advanced research aims at detecting defects without too much noise, enabling the quantification of crack width [158].

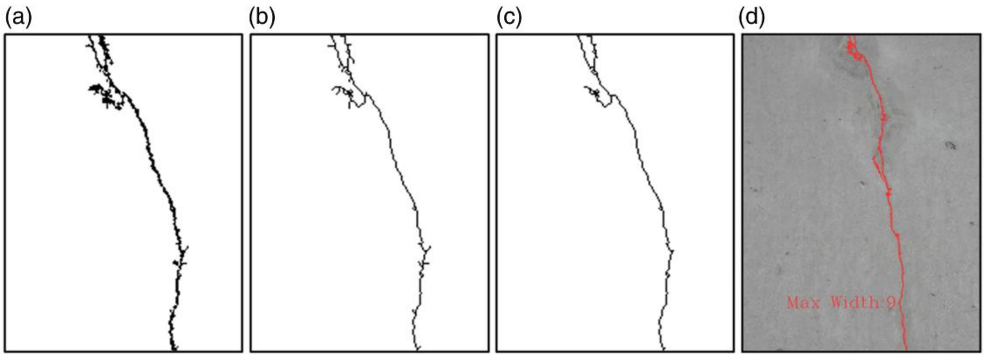

Figure 3-8 Crack recognition that allows for crack width identification [158] (a) crack, (b) image thinning, (c) burr removal, and (d) width calculation

3.2.3.2 Tunnel image processing

Each tunnel has different environmental factors such as complex lighting conditions (colour and shadows) and the smoothness of the surface. It is challenging to achieve accurate recognition of features in the tunnel structure. Besides, the data resource for tunnel inspection is often owned by the asset owner, while rare standard image dataset is shared or available for public use. In the limited size of the tunnel image dataset, the content is often repetitive, which may not be large enough for computer vision training.

To achieve the generalization in variant tunnel conditions, an idea of image expansion is applied by synthetic image creation for training (Figure 3-9) [184]. This study managed to increase the amount of data available for defect identification under various tunnel conditions by changing the image background among other inspections.

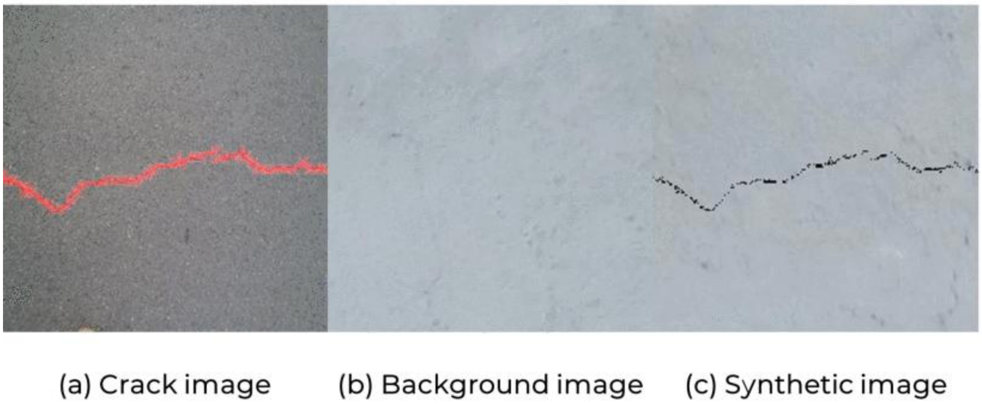

Figure 3-9 The generation of a synthetic tunnel lining surface image for crack identification [184]

The correctness identification of cracks' length is important in the subsequent analysis of tunnel degradation level, as a long crack is more severe than discontinuous short cracks. To address this issue, a perspective (Figure 3-10) [185] is through understanding the crack shape and informing the AI algorithms of the crack continuity. Instead of judging independently whether each pixel belongs to a crack or not, this tunnel crack inspection considers the homogeneous patterns in cracks and discovers the association of neighbour pixels instead.

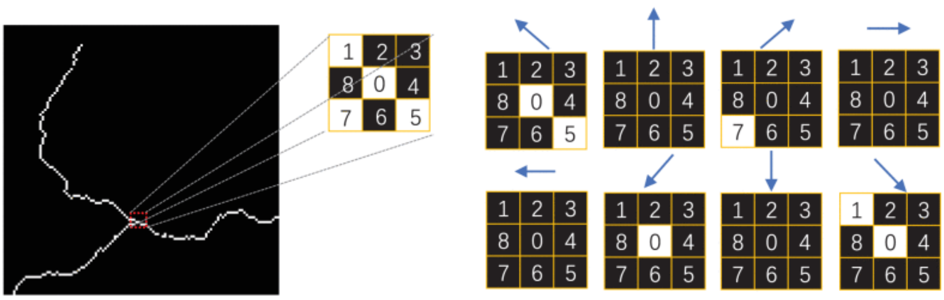

(a) (b) (c)

Figure 3-10 (a) Cracks distribution identification through examination of (b) a 3×3 pixel region and (c) its neighbours [185]

3.3 Expected output of tunnel image processing

3.3.1 Tunnel point clouds and 3D modelling

A 3D model provides an enhanced degree of exact detail for tunnel inspection. Typically, the representation employs point-cloud information gathered by laser scanners to seize the precise placements of millions of points on the tunnel's outer layer with meticulous precision (Figure 3-11). This knowledge is then applied to generate a highly accurate 3D model of the passageway (Figure 3-12).

Within the 3D model, specific parameters like the form, magnitude, and condition of the tunnel surfaces as well as any flaws and irregularities are captured with automatic processing methods. There are numerous tactics for discovering such blemishes within renderings. As an example, colour coding could be employed to indicate how severe each defect is perceived to be, and annotations may also be supplemented to furnish extra facts such as the kind of imperfections, its measurements, and its placement on a schematic.

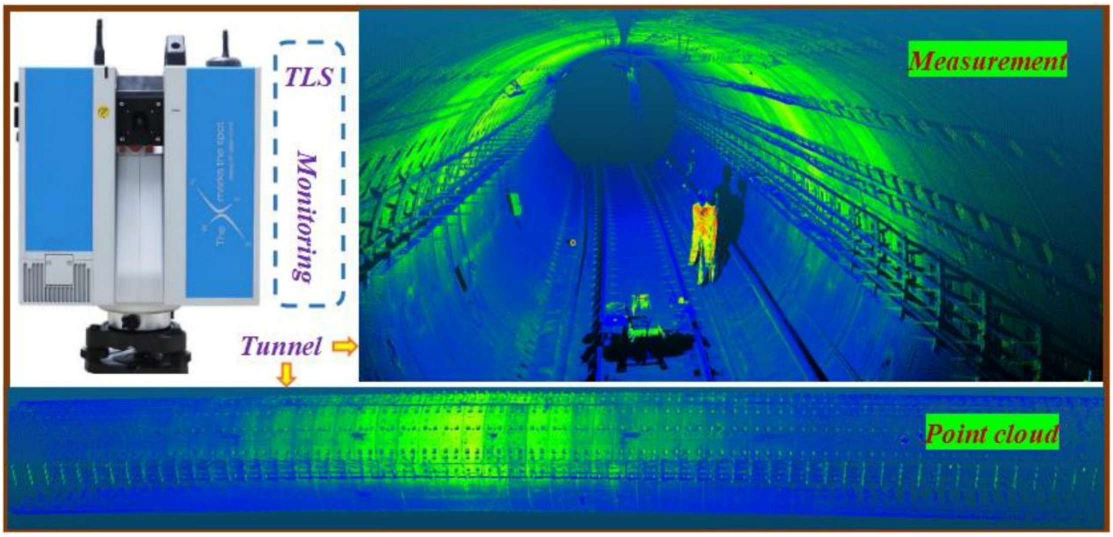

Figure 3-11 Point cloud of a tunnel structure with a terrestrial laser scanner [155]

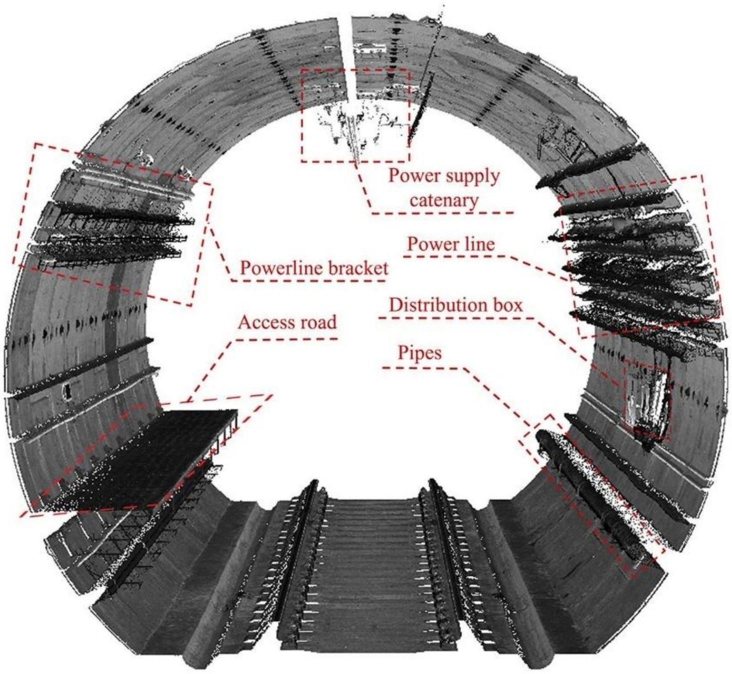

Figure 3-12 3D tunnel model with structural and components' dimensions and position [186]

When conducting tunnel inspections using 3D modelling techniques, specialists typically generate two main types of output: a 3D point cloud or a 3D mesh model. A 3D point cloud depicts the tunnel surfaces as an assortment of individual points in space, whereas a 3D mesh model portrays the surfaces as continuous through the smoothing of corners and edges. These models can be examined and analysed using specialized visualization software like CloudCompare or Autodesk ReCap.

The 3D representation facilitates the identification and quantification of defects such as cracks, spalling, and water leaks while also permitting evaluation of the overall structural integrity of the passageway. Moreover, the digital rendition proves useful for scheduling and carrying out preventative maintenance and restoration efforts as well as for monitoring the effectiveness of such work over the long term (Figure 3-13).

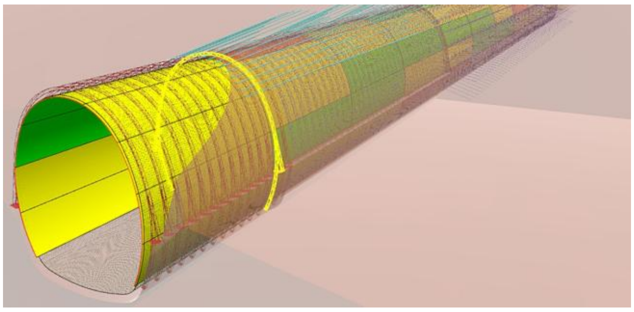

(1) inspection grid and structural elements (lattice girders, reinforcing mesh and rock bolts)

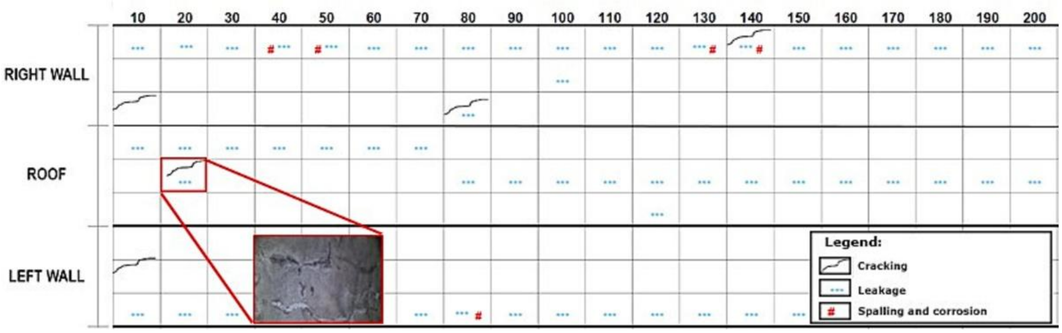

(2) Inspection data of tunnel defect grid

(3) Inspection data in grid deterioration classification

Figure 3-13 An Inspection Digital Twin (IDT) [152]

In summary, 3D modelling for infrastructure inspection within tunnels generates an extremely detailed and accurate digital replication of both the interior and exterior surfaces, comprehensively capturing any irregularities or anomalies present. Applications of the model include defect detection, condition assessment, maintenance planning, repair implementation, and repair outcome tracking across time.

3.3.2 Data extraction for geotechnical inspection

3.3.2.1 Dimension extraction

In the realm of UAV infrastructure inspection, dimension extraction remains the output of interest. This output could be the basis of an infrastructure's condition assessment, identifying potential issues and establishing the necessary corrective actions. The dimensions procured include an infrastructure's most vital parameters, such as the cross-sectional area, diameter, length, slope and curvature of the tunnel.

In the context of UAV inspection in tunnel environments in a more specific light, dimension extraction related to cross-sections is typically measured at regular intervals along the tunnel's length. And tunnel's curvature is quantified in either degrees or radians. In the case of tunnel excavation front monitoring, the front surface is also inspection interest [187] (Figure 3-14).

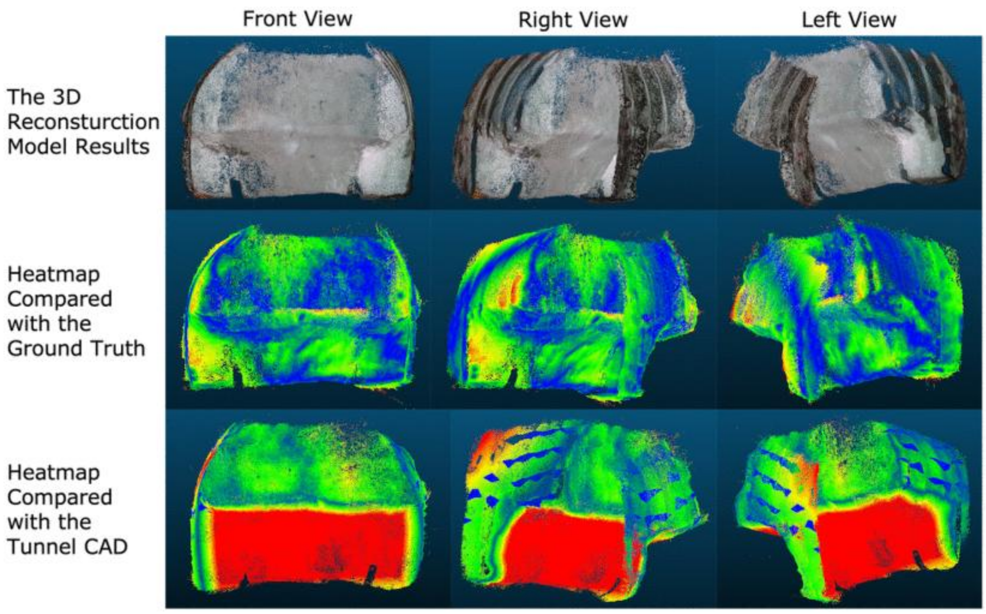

Figure 3-14 Tunnel excavation front dimension extraction during construction in Japan. From left to right: UAV models, deviation compared to laser-scanner data, and to CAD model [187]

These measurements are typically achieved through various advanced 3D modelling strategies, enabled by the extraction of measurements from point cloud data or 3D mesh models, illustrating detailed digital representations of tunnel infrastructure, or conversely by implementing methods for instance 3D model feature extraction, computer vision algorithms or machine learning techniques, followed by the application of specialized software for measurement extraction.

Different from other infrastructures, tunnels are subjected to soil compression loads and will have deformation from millimetres to more since the completion of construction. This deformation is called convergence deformation (Figure 3-15) and is not negligible in tunnel health assessment.

In summary, in the field of UAV inspection in tunnel environments, dimension extraction, among other crucial parameters, is indispensable for a thorough infrastructure condition assessment and the formulation of a course of corrective action.

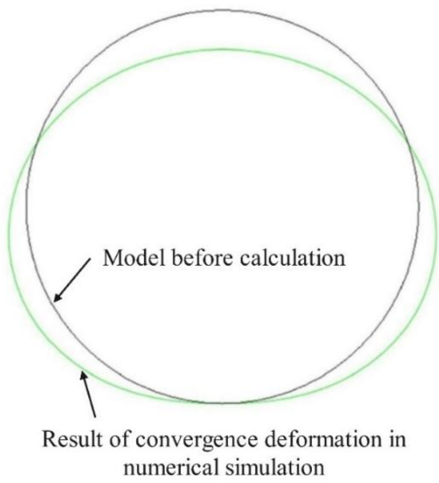

Figure 3-15 Simulation result of convergence deformation in a tunnel [161]

3.3.2.2 Surface defect identification

The organized image dataset could be used for surface defect identification (Figure 3-16). UAV images can be processed with various methods (manual operation, traditional methods, and computer vision techniques). After processing, image pixels are divided into multiple classified types. Each connected cluster of pixels corresponds to a distinct object or region of interest in the image.

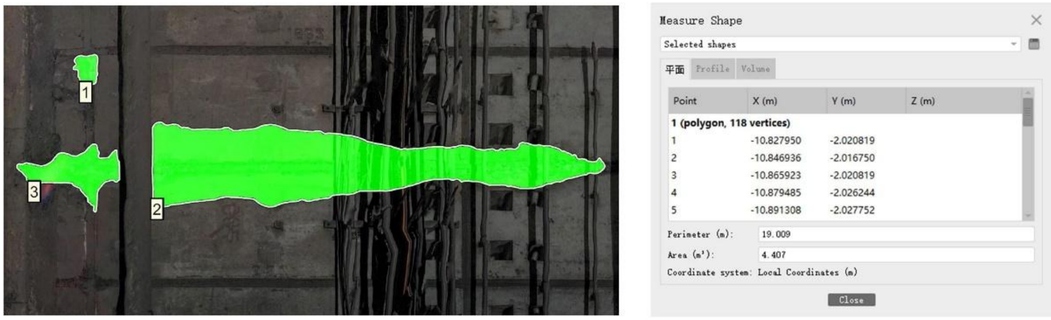

(a) Regions of leakage defects

(b) Result of area measurement

(1) water leakage (with shape measurement) [4]

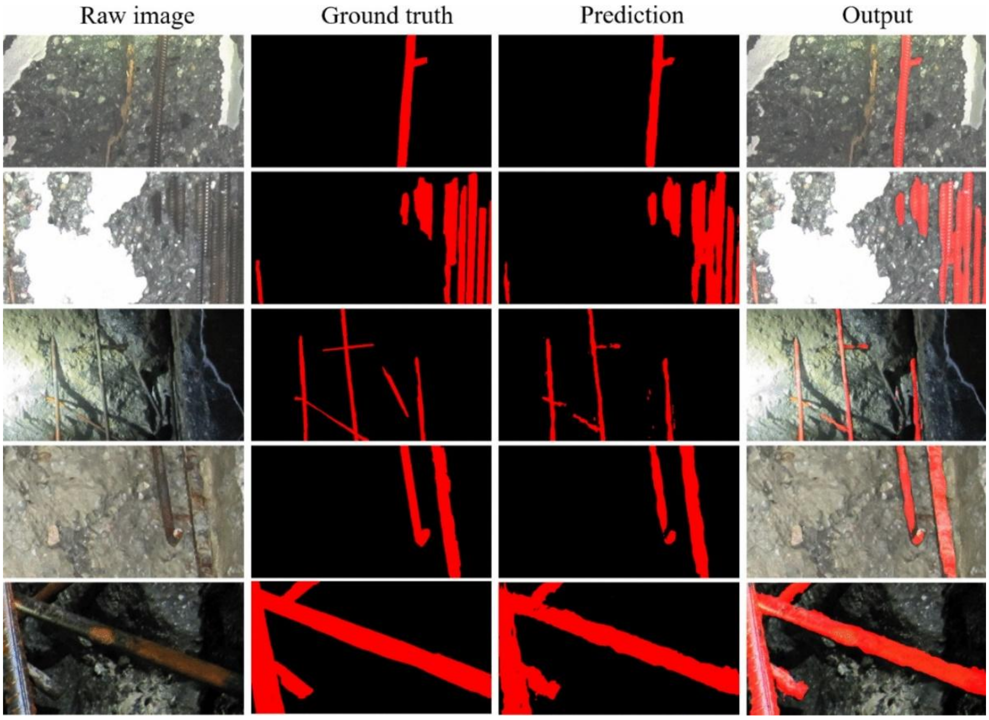

(2) rebar exposure [182]

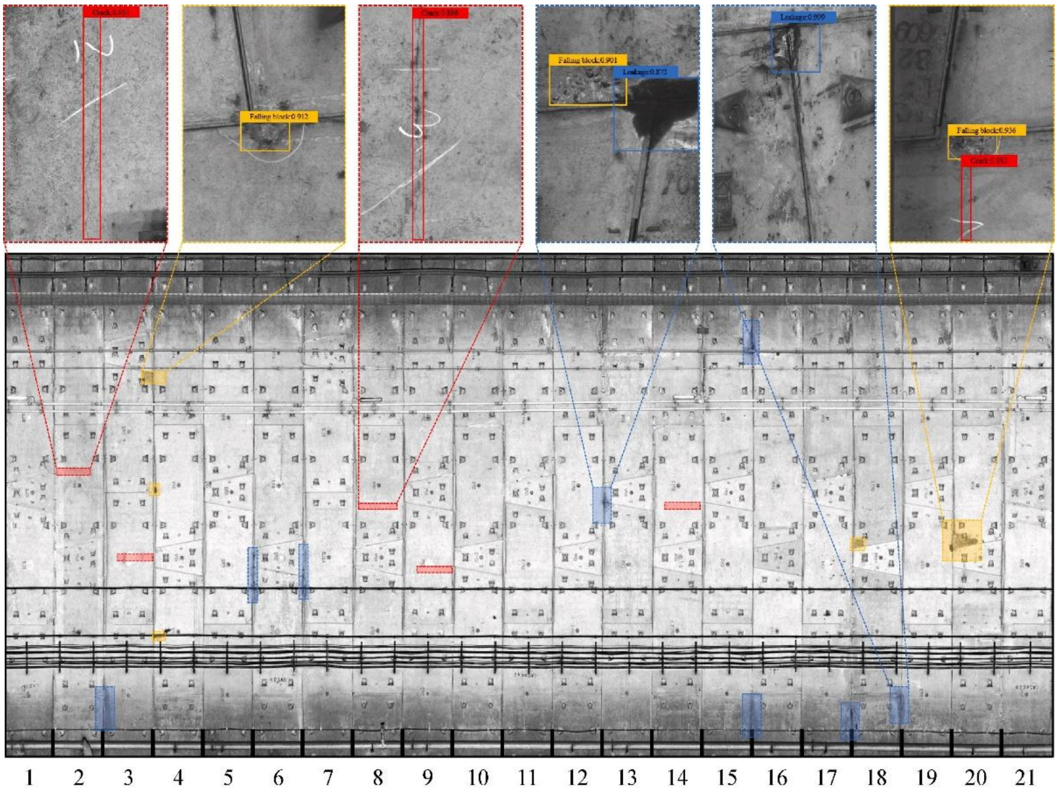

(3) cracks, water leakage and falling blocks on panoramic image [181]

Figure 3-16 Tunnel surface defects

3.3.2.3 Standardized image processing procedure

To cater for different UAV inspection environments, a standardized image processing workflow for tunnel inspection and maintenance is needed in various inspection scenarios. Such workflow should address the UAV inspection applications as the image data are in high volume, inspection may have different scenarios and focus, and sometimes there may be real-time fast processing need.

The high volume of data generated by UAVs requires efficient processing methods, and there is a need for automated image processing techniques to reduce manual intervention [188], [189], [190]. There're also tunnel inspections with real-time UAV image processing needs [182]. However, processing UAV images can be computationally intensive, and real-time processing can be challenging.

In the context of tunnel inspection and maintenance, various tunnel scenarios require specialized image processing algorithms. For example, algorithms for the detection of water leakage, cracks, spalling and other hazards in tunnel structures work for specific scenarios, but no unified algorithms work for satisfactory accuracy for all tunnel scenarios as environmental conditions are not the same.

As algorithms are limited in various specific tunnel inspections [191], [192], standardized data processing methods and protocols should be proposed to ensure consistent data quality across different projects and UAV systems. This includes the workflow for image quality examination, processing, and analysis, as well as the establishment of quality control to ensure the reliability of the results. An example is illustrated in Figure 3-17.

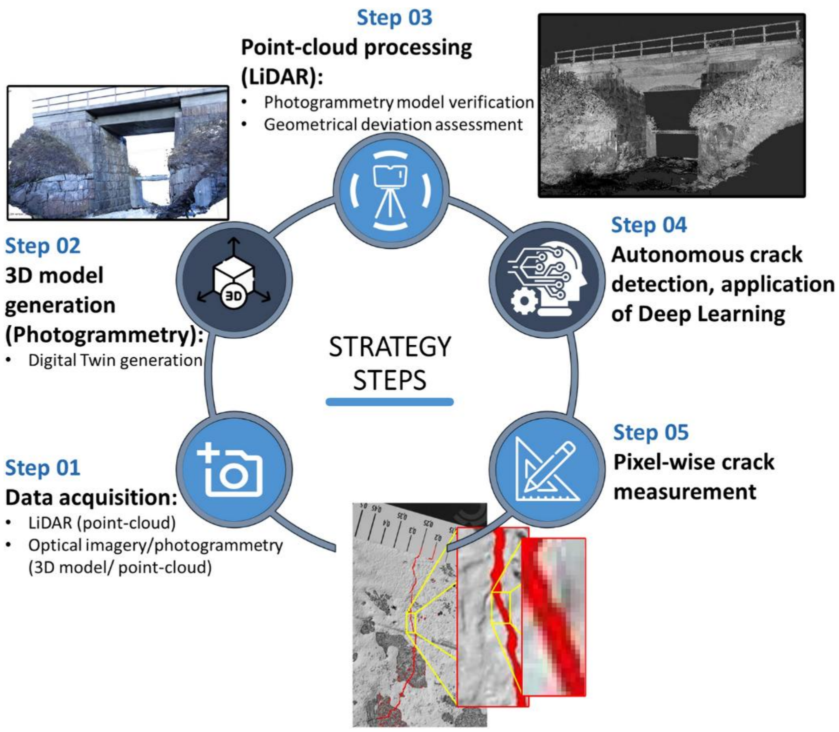

Figure 3-17 An example of autonomous damage detection and quantification workflow

3.4 UAV images-based Tunnel health assessment applications

In recent years, UAVs have been increasingly used for tunnel health assessment applications such as the structural health assessment of underground tunnel linings. Field tests have demonstrated their efficacy in this regard. Equipped with high-resolution cameras, these UAVs capture detailed visual data essential for scrutinizing tunnel lining performance. They are operated to conduct various types of deformation analyses, crack detection, and assessment of the condition of a tunnel lining [193], [194].

UAV-based imaging serves deformation monitoring purposes, facilitating precise measurements of alterations in tunnel geometry over time and the identification of potential deformations or structural concerns. For instance, Bibish utilized UAVs for monitoring sewer tunnel deformations in Japan, showcasing the feasibility and accuracy of this methodology [47].

Another significant application of UAV inspection lies in crack detection. Analysis of images captured by UAVs enables the identification and quantification of cracks in tunnel linings, offering crucial insights for maintenance and repair planning. Notably, Ren achieved high accuracy in crack detection while inspecting a tunnel in China using UAVs [195].

Tunnel lining assessment represents another promising realm for UAV application, circumventing the need for costly and time-consuming manual procedures. Information gleaned from images captured by UAVs, such as colour, texture, and other pertinent details, facilitates assessment. For instance, Ngeljaratan in 2024 conducted a pipeline inspection under the seismic effect, elucidating how UAVs can capture data for subsequent inspection and analysis [196].

Overall, previous field tests have collectively demonstrated the promising potential of Unmanned Aerial Vehicle (UAV)-based imaging technologies for assessing the health of tunnels. However, despite ongoing technological advancements, several challenges persist. These include the development and refinement of automated image analysis techniques that can adapt to the varied conditions of real-world infrastructure, as well as the establishment of industry-wide best practices for conducting UAV-based tunnel inspections. Addressing these challenges is crucial for fully leveraging the advantages that UAV technology offers in the field of tunnel health assessment.

3.5 Summary

The literature review in this chapter highlights the research gap in UAV image processing methods for tunnel inspection. UAV data processing has the capability to present infrastructure's dimension and structural health condition, with the help of geometrical and image processing techniques. The key issues in UAV data processing include the improvement of UAV image data quality, the image processing within 3D structures, noise reduction for dim images, and the performance improvement for tunnel inspection. These aspects make this topic a multidisciplinary problem.

Tunnel model reconstruction is able to create point cloud models using image registration. Key challenges in this field are attributed to the inspection condition variance in terms of illumination intensity, colour, as well as sensor incapability when collecting data from moving equipment. Researchers have proposed intelligent methods to improve the quality of tunnel model reconstruction, the most widely accepted in tunnel point cloud optimisation are model-based surface fitting and ML-based denoising. In addition, UAV image registration is based on computation in 3D space close to the tunnel lining, which makes it more error-sensitive than 2D inspection in open space. To accommodate various tunnel inspection applications, the establishment of standardized data processing protocols is highly desired.

Recent work enables automatic verification and accurate interpretation of the 3D reconstruction model data. Researchers verify the accuracy of the model by comparing the shape of the linings between the tunnel model and the design, aiming to achieve millimetre accuracy. The unique convergence deformation of tunnels can also be used for cross-verification with numerical simulation results. For surface defect identification, image segmentation can be used to provide fast and accurate output. Researchers also train with synthetic data or use crack pattern-aware ML algorithms to enable reliable automatic defect identification and quantification. Future applications of intelligent tunnel health assessment will assist decision-makers in long-term operations.

Despite the recent progress, UAV tunnel image processing still deserves significant development to improve its accuracy, which lags behind that of LiDAR. Therefore, this PhD research will develop and apply practical computational methods, aiming to enhance the accuracy of UAV image-based reconstruction models similar to that of LiDAR data.

4. UAV navigation and 3D reconstruction

4.1 Introduction

This chapter of the methodology focuses on the approach used to gather tunnel surface data in GPS-denied environments using UAVs as well as image processing for infrastructure assessment. The UAVs are equipped with various sensors, such as cameras and infrared sensors, to capture high-quality images and distance measurements from multiple views and angles. A reactive flight control strategy, named Proximity Move-Pause-Photo for Surface Defect Inspection (PMPP-SDI), is proposed, which combines reactive flight control with a grid scanning pattern to ensure stable navigation and high-resolution reconstruction. The acquired image data is then used to generate a 3D point cloud model of the tunnel surface for structural condition assessment, enabling the dimensional measurement and identification of defects like cracks. The advantages and limitations of the method are discussed. Future research directions include the improvement of control/navigation intelligence, data quality, and defect analysis.

4.2 UAV tunnel inspection system overview

4.2.1 Tunnel inspection platform

4.2.1.1 DJI UAV

The DJI Mavic 2 Enterprise Dual (M2ED) is the optimal choice among DJI commercial UAVs for an automatic tunnel inspection platform (Figure 4-1) due to its multi-rotor configuration, compact size, and superior manoeuvrability, enabling it to navigate through narrow passages and confined spaces within tunnels with minimized airflow disturbance. Its compatibility with a variety of sensor payloads, including cameras, thermal imaging, and spotlight, ensures comprehensive data collection for assessing structural integrity and identifying potential hazards. Despite its relatively smaller payload capacity, the M2ED's extended flight time of up to 31 minutes per battery charge minimizes downtime during inspection missions.

Furthermore, it could achieve advanced autonomous flight modes and omnidirectional obstacle avoidance features [197] by enabling programmed autonomous navigation along pre-defined routes while avoiding obstacles. Coupled with its cost-effectiveness compared to larger or specialized platforms, the Mavic 2 Enterprise provides a versatile and efficient solution for those seeking automated tunnel inspection capabilities within budget constraints.

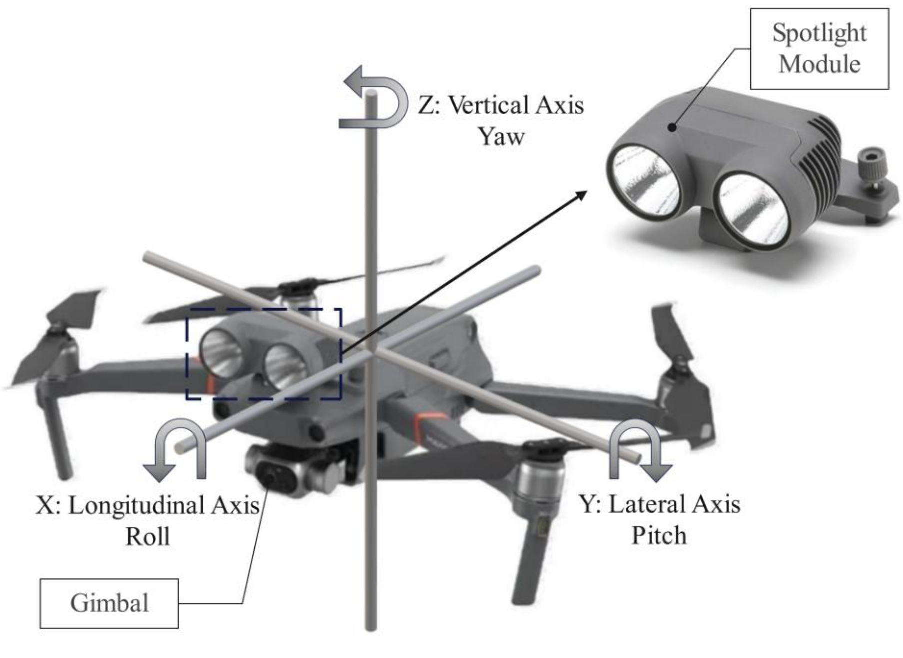

Figure 4-1 UAV scanning system equipped with spotlight module

4.2.1.2 Sensor suite selection

The M2ED UAV platform incorporates a sensor suite that enables its utilization for tunnel inspection tasks (Figure 4-2). The primary sensor is an FC2403 DJI camera with an 85° field of view and a 35mm equivalent focal length, enabling the capture of high-resolution visual data of the tunnel's interior surfaces. This visual data facilitates the detection of defects or anomalies along the tunnel's length. To compensate for low-light conditions within enclosed tunnel environments, the M2ED includes a spotlight module that provides illumination with a maximum luminance of 11 lx at 30 meters and a 17° field of view.

Table 4-1 Mavic 2 Enterprise Dual properties

Take-off Weight	899 g (M2ED Without Accessories), 1100 g (Max Take-off Weight)
Dimensions(L×W×H)	Unfolded + Spotlight：322×242×114 mm
Max hovering time	22 min (spotlight fully on, without wind), 29 min (spotlight-off, no wind).
Camera lens	FOV: approx. 85°; 35 mm format equivalent:24 mm. Aperture: f/2.8; Focus: 0.5 m to ∞; Sensor dimensions: 6.554 [mm] x 4.913 [mm].
Camera still photography modes	Single shot; Interval (2/3/5/7/10/15/20/30/60 s)
Gimbal theoretical controllable range	Tilt: -90 – +30°; Pan: -75 – +75°
Spotlight illuminance	Max luminance: 11lx @ 30m Straight, FOV: 17°
Omnidirectional sensing system	Forward -- Range:0.5 - 20 m (Precision Measurement); 20 - 40 m (Detectable) FOV: Horizontal: 40°, Vertical: 70° Backwards -- Range: 0.5 - 16 m (Precision Measurement); 16 - 32 m (Detectable) FOV: Horizontal: 60°, Vertical: 77° Sides -- Range: 0.5 - 10 m (Precision Measurement) FOV: Horizontal: 80°, Vertical: 65°

Complementing the visual sensors, the M2ED integrates an omnidirectional sensing system comprising multiple range sensors for autonomous navigation and collision avoidance. This system includes forward and backward sensors with respective ranges of 0.5-40m and 0.5-32m for precision measurement and obstacle detection up to 40m and 32m. Additionally, side sensors with a 0.5-10m range enhance situational awareness in the tunnel's lateral dimensions within 10 meters. The data from these range sensors enables path planning, obstacle avoidance, and autonomous flight within the confined tunnel spaces during inspection operations. The combined capabilities of the visual and ranging sensors allow the M2ED to perceive and map the tunnel environment, ensuring operational safety and facilitating autonomous inspection missions.

4.2.2 Inspection task description

4.2.2.1 Inspection objectives

Based on relevant previous investigations, Figure 4-2 briefly illustrates the UAV inspection on tunnel surface for image data acquisition in this study. As previously discussed, the main challenges of UAV tunnel inspection lie in the GPS-denied environment, the cylindrical geometry, the dim environment, and the motion blur in the 3D space. Therefore, this research proposed methods to address these issues.

For navigation, in particular trajectory planning, since the tunnel is a cylindrical infrastructure, movement along the centreline in the inspection area is an optimal method to reduce post-processing errors [20]. In addition, uneven luminance is accounted for by real-time distance data credibility assessment and appropriate control strategy selection. The motion blur is avoided by employing a data acquisition pattern of move-pause-photo to ensure image quality.

Tunnel inspection data collection often requires coverage of long lengths and maximum heights from inside the tunnels. As commercial UAVs are usually designed for a look-down photo mode, gimbal rotation control is used to increase the field of view (FoV) in an inspection task. The method is human-in-loop but saves effort and avoids human operator error, with the traditional operator acting as a supervisor instead.

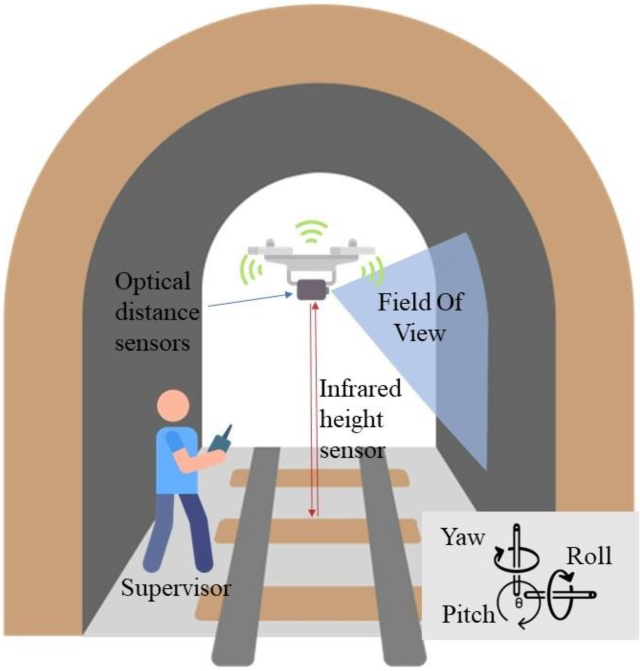

Figure 4-2 Illustration of UAV inspection on tunnel surface.

4.2.2.2 Environmental description

4.2.2.2.1 Structural navigable spaces

Structural navigable spaces pertain to the accessible zones in which UAVs can navigate and conduct inspection tasks, considering the tunnel geometry exclusively. To move along the longitudinal direction in tunnels, UAVs utilize tunnel boundary sensing and move in a parallel direction [198], [199]. The navigable space inside the tunnel refers to an area that maintains a minimum distance of 3 meters from any tunnel linings.

The proposed method aims to facilitate UAV inspections in diverse environmental conditions, with an emphasis on assessing the complexity of these conditions to enhance adaptability. Assessing the complexity of the tunnel geometry plays a crucial role in determining the control strategies in reactive control. For example, railway tunnels generally exhibit simpler geometries and lower lighting conditions compared to road tunnels and shafts.

In particular, railway tunnels with large radii of curvature exceeding 100 meters can be considered as straight along the tunnel axis [200]. Such tunnel geometry can be represented as the simple one as described in scenario A in Figure 4-3 (1). For the complex tunnel geometries, such as those in scenario B (around a layby tunnel section) and scenario C (with a cross passage section), site photographs are provided in Figure 4-3 (2) and (3) to illustrate their complexity. Irrespective of the different scenarios, the tunnel environments have the following characteristics:

1. Tunnel structures do not generate significant airflow that affects the operation of micro-UAVs and the UAV experiences limited control error and drift. This assumption is made because the PMPP-SDI method ensures that the UAV maintains a sufficient distance from the wall to minimize the near-wall effect [201] and vortex. This assumption allows for fast lateral position and yaw adjustments.

2. The tunnels have variations in geometry and lighting conditions. The evaluation of the UAV inspection environment considers both aspects and simplifies the control by considering the more challenging conditions.

3. In tunnel sections with complex geometric conditions, such as layby tunnels and cross passages, additional simplifications are implemented. The tunnel lining is assumed to have negligible curvature near the diameter change. This allows for the lateral position control of UAV to rely solely on the readings of the forward obstacle distance indicator. This assumption is consistent with the geometry of the DPT road tunnel section VCP 16, as shown in Figure 4-3 (2) and (3), which demonstrate an application in a complex tunnel environment.

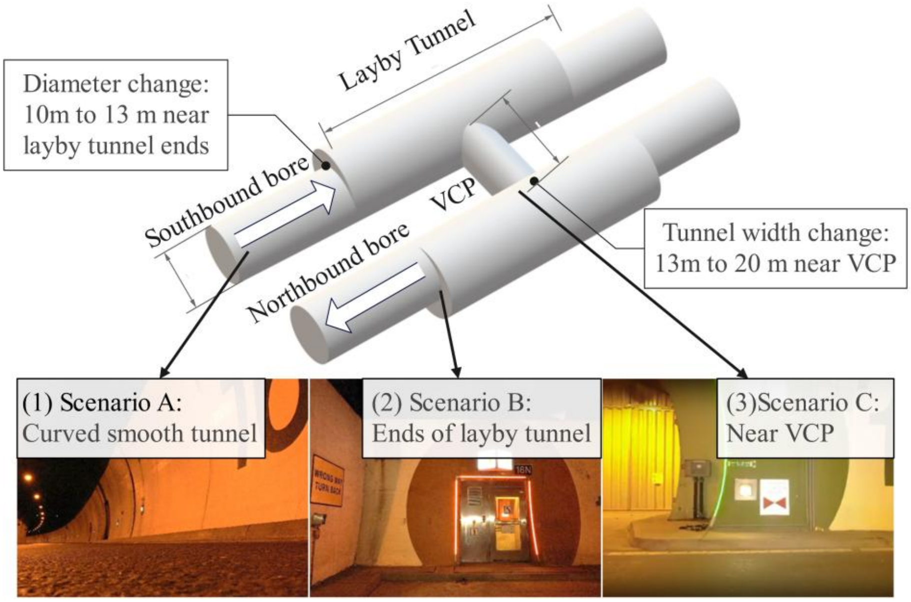

Figure 4-3 Three types of tunnel sections in a tunnel: (1) Scenario A: simple geometry with slightly curved surface (2) Scenario B: small diameter changes and (3) Scenario C: large diameter change.

4.2.2.2.2 Illumination condition

Inspecting tunnel infrastructures with UAVs presents challenges for navigation in low-light and GNSS-deprived conditions [202]. Reliable navigation data acquisition requires a minimum illumination of 15 lx [203] and data evaluation methods to ensure flight safety. In this case, spotlights are used to significantly improve inspection visibility in low-light environments. Headlights are also used for operator safety.

To meet the need for adequate and evenly distributed light intensity, the DJI M2ED UAV is equipped with dual spotlights (Figure 4-4). The auxiliary light setting process includes luminance measurement, spotlight power calculation and field verification tests. As shown in Figure 4-4, the spotlights have an adjustable intensity of up to 11 lx at a range of 30 meters. In a completely dark tunnel with a diameter of 6 m, the luminance of the spotlights is calculated to be 1100 lx at full power. When used for tunnel inspections, the UAV spotlights are fitted with a translucent cover to ensure uniform wall illumination and to avoid shadows on the tunnel lining. After calculation and field testing, a 20% maximum spotlight power setting is used to illuminate the inspection environment and realize power savings. As a final step, the UAV evaluates the data credibility of the visual sensors to implement reactive control of tunnel inspections, as described in the following section 4.2.3.


(1)

(2)

(3)

Figure 4-4 Auxiliary lighting equipment: (1) spotlight module installed on UAV (2) spotlight module with translucent cover (2) headlight for operators.

4.2.3 Qualification for UAV operation

The use of UAVs in tunnel inspection missions requires specialized training and strict adherence to strict safety protocols to ensure that personnel involved in these operations are not at risk and that the infrastructure under assessment is in good working order. The operators piloting the aircraft must have the certifications and qualifications required by the national authority and asset owner. A remote pilot certificate attests to their knowledge of UAV flight operations, airspace regulations, and emergency procedures. In addition, specific training for UAV operators in confined space operations and tunnel environments is required by the tunnel maintenance organisation.

As described in Appendix 8.2, operators need to have a comprehensive understanding of the risk assessment and mitigation strategies that are appropriate to their tunnel inspection task. They also need to be able to fly the UAS with potential hazards tunnel obstructions, limited visibility, confined air flow, hazardous material, and gases. Comprehensive pre-flight checks, rigorous monitoring of flight parameters, and strict adherence to safety protocols should be followed to ensure inspection safety.

Operators should also be trained in emergency response procedures, including collision in the tunnel, loss of communications, and battery failure. Contingency plans and fail-safe mechanisms must be in place to reduce the likelihood or consequences of damage to the UAV, tunnel infrastructure or personnel in the event of any system malfunctions or unexpected events.

4.3 UAV navigation and image acquisition

4.3.1 UAV inspection process

Visual navigation of the UAV is based on its relative position to the tunnel rather than on map information. The UAV’s lateral position adjustment is determined by visual positioning with sufficient UAV light sources. The UAV's altitude is monitored by an infrared sensor operating within 5 meters of the ground. Once the relative position adjustment has been calculated, the remote controller sends motion control commands to the UAV.

4.3.1.1 Move-Hover-Photo pattern

The DJI Mobile Software Development Kit (MSDK) control application embeds the UAV's behavioural logic of this method [204]. Such a reproducible inspection flight is illustrated by a process flow in Figure 4-5. The method is called Proximity Move-Pause-Photo for Surface Defect Inspection (PMPP-SDI) because it moves along the tunnel, scanning the tunnel wall strip by strip as it hovers. It captures high-resolution images of the surrounding environment near the take-off point and of the inspected surfaces along the inspection path. After the inspection, the captured data is aligned and stitched together to create a 3D model of the entire area inspected. Multiple flights can be analysed together, making the inspection task reproducible over time.

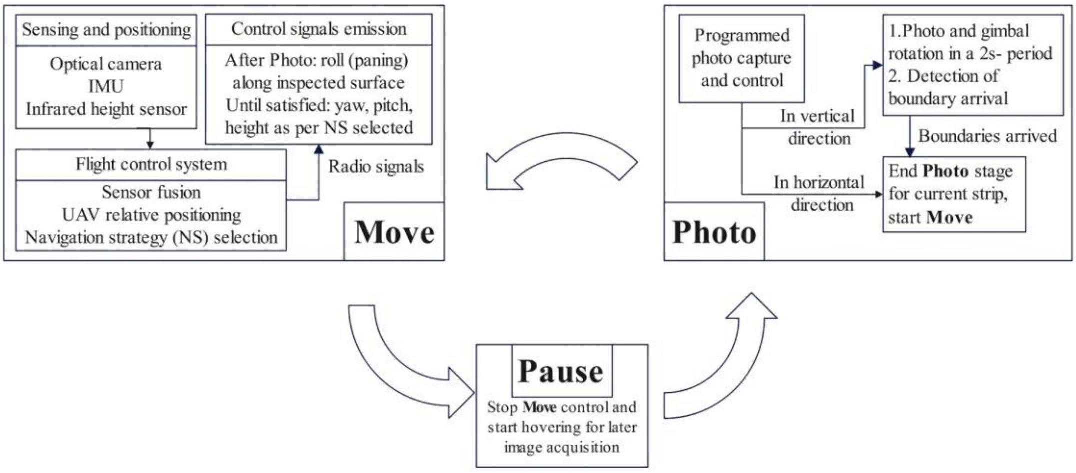

Figure 4-5 Schematic block diagram of the UAV automatic inspection process for navigation and data acquisition.

Data analysis then produces an integrated model that includes the condition of the tunnel sidewalls and part of the tunnel invert. To link images from various flights and to achieve accurate feature alignment, an action of a 240° survey near the take-off point is programmed to the start of each flight, i.e. images of both sidewalls are collected near the take-off points. In small-diameter tunnels, the tunnel inverted sections are scanned together with the tunnel sidewalls. In large-scale tunnels, multiple flights are performed at various altitudes, producing several separate datasets. In each case, the battery replacement includes additional images of the area around the next take-off point. This enables seamless image stitching, ensuring a harmonious and consistent visual representation. Each dataset contains images of the tunnel linings and the ground near the take-off points and along the path. All the data is later stitched together to create a complete 3D reconstruction model.

This PMPP-SDI method controls the UAV tunnel inspection in the following steps:

a) Image acquisition around the take-off point. The image acquisition sequence is a stripe-by-stripe scan of the vertically rotating gimbal, with an overlap rate of more than 70%. In the vicinity of the take-off point, the UAV collects data of both tunnel linings and the ground in between for the convenience of later image registration with datasets from other flights.

b) Assessment of the relative indoor position of the UAV and the environmental conditions. This step is based on sensor readings and determines the preferred UAV navigation strategy.

c) Lateral adjustment and data acquisition. Lateral adjustment is performed in steps according to the UAV navigation strategy. Data acquisition starts after each step of movement. The maximum step length for each movement is limited to less than 1 m to avoid over-adjustment.

d) The UAV moves in an axial direction, fine-tuning its yaw. Each axial movement is around 1.5 m in length to ensure a sufficient side overlap rate (>65%). The yaw adjustment is made according to the data in the four sectors of the front view sensor, after the lateral adjustment has been completed.

e) Repeat the above procedure to inspect all tunnel linings in terms of different sides and heights.

From the operator's perspective, the inspection process includes task initiation, supervision, and completion. Operators begin by specifying navigation parameters to initiate the UAV’s inspection routine. The UAV then operates autonomously, with operators maintaining visual contact to ensure it remains within 10 meters in a curved tunnel. When the inspection is completed or if the UAV exhibits any unusual behaviours, the operators manually stop or suspend the inspection task.

4.3.1.2 Essential technologies for inspection

As mentioned previously, automatic UAV inspection in underground space faces a series of main challenges including GNSS loss, low luminance, and complex inspection space. To address these challenges, some key technologies are employed in previous studies as summarised in Table 4-2, including binocular visual positioning and grid scanning pattern for data acquisition, while point cloud generation and defect classification/ segmentation for post-processing of the collected image data.

Each technology is described in terms of four aspects: target function, object of action, prior knowledge, and principle. For example, binocular visual positioning aims to obtain in real time the distance from the UAV to the nearest obstacles (target function and applications). This technology works in navigation environments with a luminance higher than 15 lx (object of action). It requires obstacles made of materials with good light reflectivity (prior knowledge) to facilitate binocular image depth estimation (principle). In summary, all these technologies are designed for tunnel inspection environments, which are different from typical outdoor UAV flight environments. The key technologies focus on ensuring robustness in terms of precise control, scene scanning, data processing, and information extraction, as detailed in Table 4-2:

Table 4-2 Methods used in the data acquisition and post-processing procedures and applications in similar inspection environments

Aspects / Technologies	Target function	Object of action	Prior knowledge	Principle
Binocular visual positioning	Obtain real-time distance from UAV to nearest obstacles [205]	Navigation environment with luminance greater than 15 lx	Obstacles made of materials with good light reflection	Estimate image depth using binocular vision
Grid scan pattern	Capture 3D structures for tunnel lining textures [20]	Continuous inspection on curved surfaces or inside convex polyhedron space	Time-based UAV gimbal and motion control in DJI MSDK	Extending the FoV by controlling gimbal rotation
Point cloud generation	Generate coloured point cloud models [206]	Image processing given sufficient (>85% frontal and >65% side)	Uniformity, continuity, consistency, and correspondence	Image registration and structure-from-motion (SFM)

		overlap	in the expected output	techniques
Defect classification / segmentation	Identify areas of tunnel linings with various defects [184], [207]	Orthomosaic output of tunnel linings from the point cloud models	Distinct colours or shapes of defects from normal structures.	Use computer vision or manual image segmentation

4.3.2 UAV navigation strategies

In tunnel environments, complex navigable space and low luminance are two major challenges for UAV visual navigation. In order to ensure stable flights and optimal data acquisition, this section proposes three UAV navigation strategies to cope with complex flight conditions. The tunnel navigation method employs reactive control, which allows flexible switching of the motion control logic based on sensor feedback.

In general, the PMPP-SDI method categorizes three reactive navigation strategies for different tunnel scenarios based on geometric complexity and luminance conditions, as shown in Figure 4-6. Surface complexity and variation in tunnel diameter are used to assess the geometry. And luminance conditions greater than 15 lx are sufficient for UAV visual navigation. In Figure 4-6, the surface that the UAV initially faces is surface A, and the opposite is surface B. Scanning of surface B starts from data collection around the take-off point, followed by a one-way flight along surface B.

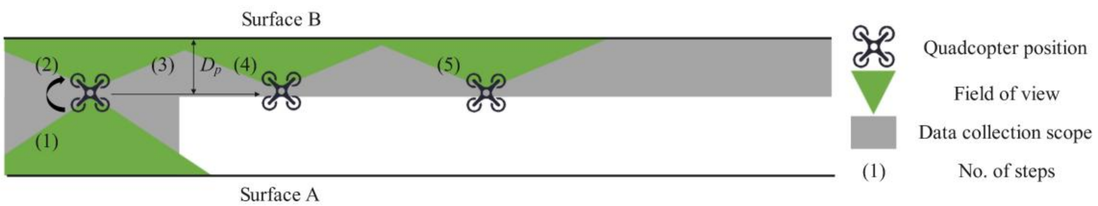

(1) Strategy 1 in Scenario A: Schematic top view of a smooth surface within a simple tunnel exhibiting a small diameter change.

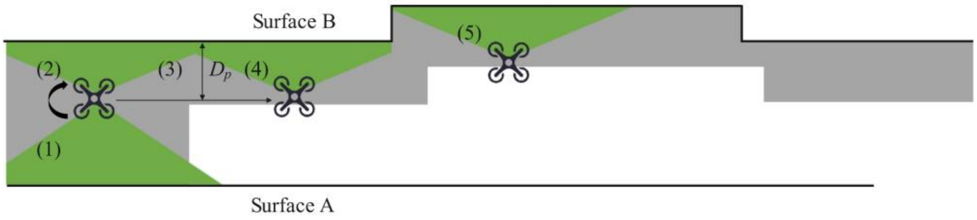

(2) Strategy 2 in Scenario B: Schematic top view of tunnel sections with varying complexity, such as a simple large-diameter tunnel, a complex section with small diameter changes, and a tunnel under weak light conditions.

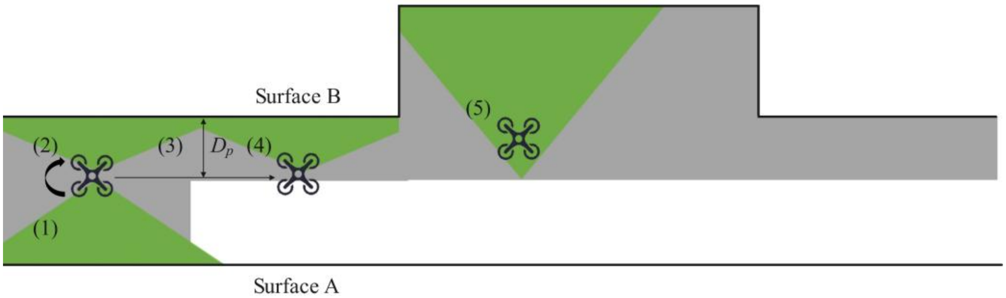

(3) Strategy 3 in Scenario C: Schematic top view of a complex tunnel section with significant changes in diameter and/or low light conditions

Figure 4-6 Three flying strategies for UAV inspection under varying structural and luminance complexity, with the corresponding inspection range.

Table 4-3 presents the control logic, specifying the scenario judgment criteria, flying strategy, and strategy assignment basis for each scenario. Among the three scenarios, the first scenario involves smooth surfaces in small-diameter simple tunnels (e.g., a common railway tunnel) (see Figure 4-6 (1)). These tunnels have a curvature of less than 5°/m and sufficient lighting conditions, allowing the UAV to rely on visual navigation to move along the axis.

The second scenario encompasses complex tunnel sections with slight diameter changes (<15% tunnel diameter), uniform tunnel sections with large diameters, or weak lighting conditions (Figure 4-6 (2)). Here, dual spotlights enhance the performance of the front obstacle distance indicator, but still only provide limited credibility of frontal and back distance readings. The UAV flies at a fixed distance parallel to the wall, making small adjustments to its yaw.

The third scenario represents the most challenging conditions, including large diameter changes (> 15% tunnel diameter) and total darkness (Figure 4-6 (3)). Typically, photographs are taken 4m from the surface to capture sufficient details (1 mm/pixel) of the tunnel surface, including distant structures within the FoV of position (5). However, the UAV does not move forward to capture additional surface detail, as distant structures are of less inspection interest. The UAV maintains a stable flight path along a fixed direction, without adjusting its lateral position or yaw. Data is collected from the surrounding of take-off point and from one side of the tunnel wall.

Table 4-3 UAV navigation strategy corresponding to real-time UAV measurement of tunnel diameter

Tunnel Scenarios	Scenario A	Scenario B	Scenario C
Description	Well-lit small tunnel	Consistent diameter/ large/ dim tunnel	Huge size variation/ dark tunnel
UAV's flying strategy	Strategy 1: Navigate along the tunnel's axis. $D_p = \frac{D_f + D_b}{2}$	Strategy 2: Maintain a constant distance D_p, from the front surface. $D_p = user - defined\ value$	Strategy 3: Makes no lateral adjustment. $D_p = D_f$
Criteria	$D_f + D_b <$ 10m, $\Delta D_f + \Delta D_b < 10\% \times (D_f + D_b)$	Either $10m < D_f + D_b < 20m$ or $\Delta D_b > 0$, $\Delta D_f < 15\% \times (D_f + D_b)$	Either $D_f = 0m$ or $\Delta D_f > 15\% \times (D_f + D_b)$
Sensors' data credibility	High credibility	Limited credibility	Low credibility in complex or dark tunnels
Lateral position/yaw adjustment logic	With reliable visual reading, the adjustments of lateral position and yaw are confident.	With frontal unstable readings and back no readings in a low-luminance setting, only lateral position adjustment is effective.	With a lack of reliable position information, no commands could be made.

* D_f represents the reading of the front obstacle distance sensor in UAV movement and D_b is that of the back.

ΔD_f represents the change of front obstacle distance in two consecutive UAV movements along the tunnel axis and ΔD_b is that of back.

D_p represents the distance D_p between the UAV and its frontal surface of interest.

To better accommodate the tunnel environment, the UAV's control and feedback system continuously adjusts its height, as well as its lateral position and yaw periodically, using the six-way obstacle avoidance visual sensing system and the downward infrared sensing system.

4.3.3 Data acquisition algorithm

UAV tilted aerial photography involves capturing the surface textures of the area being surveyed at tilted angles. Key considerations during the scanning process include selecting appropriate tilt angles, ensuring image overlap, planning comprehensive flight paths, and adjusting camera settings for low-light conditions. To facilitate data acquisition as the UAV pans at each hover point, gimbal control is synchronized with navigation time, enabling sequential surface scanning. The extensive data is then used for tasks such as image registration, point cloud processing, and 3D modelling. The flight control algorithm must comply with safety regulations while maintaining good controllability.

As shown in Figure 4-7, the data acquisition process involves continuous image acquisition following a grid pattern. The grid pattern allows for a better overlap rate compared to other patterns such as sinusoidal waveform after field testing in tunnel environments. Images are preferred over video for close-up shots to avoid rotational blur. After each UAV movement, the motors stop, and the gimbal moves within the *gimbalpitch* value range of (-90°, 20°). It starts at a boundary value and rotates, stabilizes, and captures images at 10° intervals. Each image takes 2 seconds, and this process is repeated until the other boundary is reached (yellow boundary of gimbal movement in Figure 4-8 (1)).

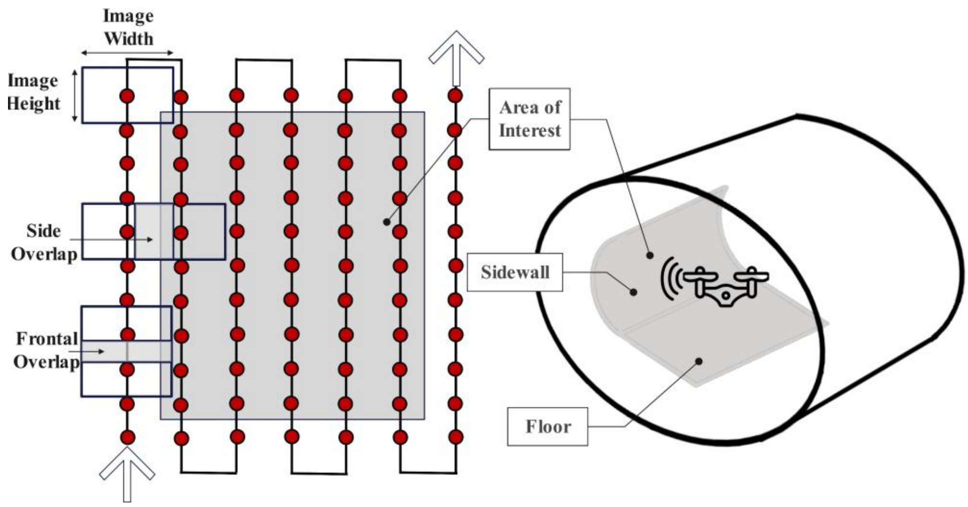

Figure 4-7 Application of 2D grid data acquisition pattern in 3D close-range inspection infrastructure.

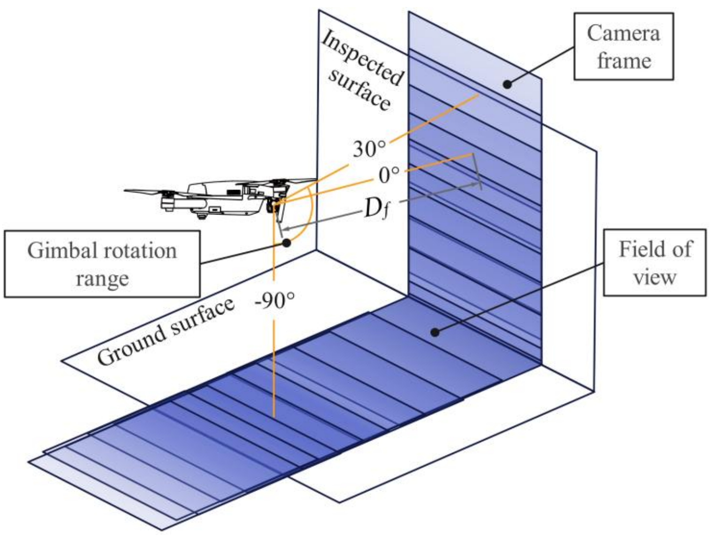

(1) Frontal overlap with varied *gimbalpitch* values at 10° intervals.

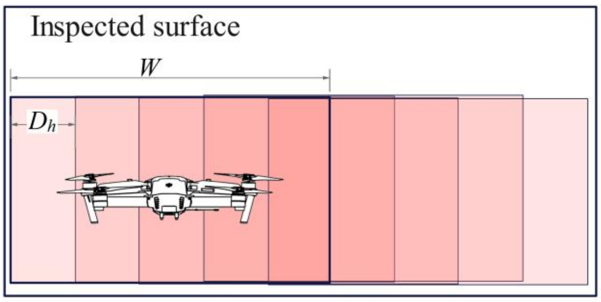

(2) Side overlap achieved through UAV camera panning of D_h.

Figure 4-8 Schematic views of data acquisition range over vertical and horizontal movement (the blue and red boxes represent the camera frames, and the blue and red areas indicate the field of view).

4.3.4 UAV control systems

4.3.4.1 Advancing in the tunnel

In UAV inspection, taking photos while moving may lead to motion blur in the captured images. Instead, the proposed UAV PMPP-SDI method adopts a move-pause-photo motion pattern following a stop-and-go process [208]: This motion involves a sequence of actions where the UAV moves along a designated path, periodically pauses its movement at a certain distance, and captures photos at each pause point. The movement commands are executed step by step in the visual-inertial system until the deviations fall in a tolerant range between UAV real-time and expected positions. Consequently, the limitation of this VINS control system is that it cannot achieve high-precision absolute positioning using only visual localization and turn-based control when the GNSS signals are absent.

Figure 4-8 (2) shows the UAV horizontal panning distance along the tunnel axis D_h. D_h can be verified by camera position data in two adjacent images before and after panning. The value of D_h is calculated to suit the inspection environment and is realized by means of passive control. A positive value for D_h indicates rightward panning, whereas negative for leftward. It is calculated by Equation (1):

$$D_h < (1-\alpha)W \tag{1}$$

Where α is the side overlap rate of the UAV images, and W is the width of the scene in a single frame. W can be calculated using Equation (2):

$$W = 2D_f \, tan\frac{Fov}{2} \tag{2}$$

Where Fov is a constant set to 85° for the M2ED camera. D_f is the frontal distance between the lens and the wall. For example, in the Goggins Hill tunnel with a diameter of 5.8 m, the UAV flies along the tunnel axis, and D_f is set as 2.6 m, accounting for the size of the UAV. Consequently, W is calculated as 4.76 m and D_h as 1.9 m. The default value of D_h is set as 1.5 meters to accommodate the dim inspection environment.

4.3.4.2 Feedback position adjustment

The proposed UAV inspection method uses reactive feedback control to ensure the robustness of UAV control in a new inspection environment. The user-defined preferences for UAV control and gimbal movements include the UAV's heading *yaw* (/°), the *Height* (/m) of the UAV fly path in the tunnel, and a target distance D_p of UAV from the front wall. In practice, D_p is typically set at 4m for most tunnels by default, ensuring safe and stable UAV flights with high image quality.

The above parameters are adjusted based on the control logic presented in Figure 4-9. During the inspection, the *Height* is continuously adjusted, and the *yaw* and D_p are limitedly adjusted before each photo cycle according to the selected flight strategy. This adjustment enables the UAV to move along the slightly curved tunnel axis and resist drifting within the tunnel structures. Meanwhile, operators can monitor flight safety through real-time distance readings from the front and back sensors displayed on the application interface.

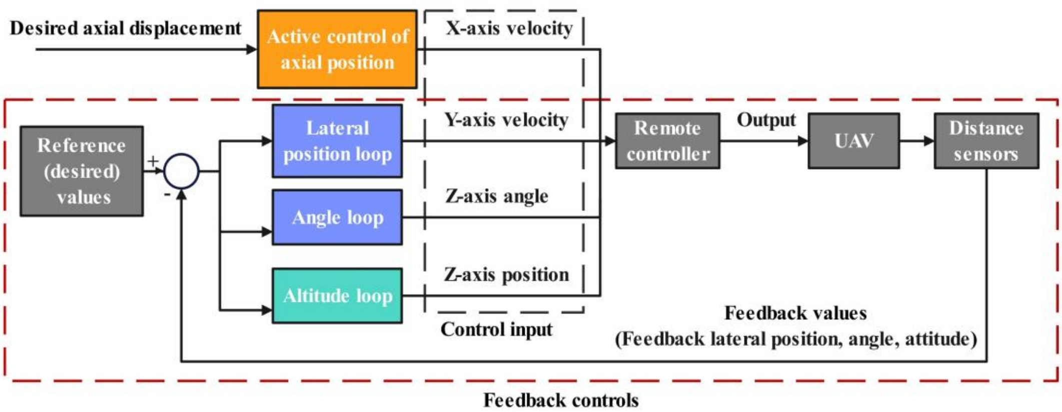

Figure 4-9 Control signal transmission in the UAV position control system.

4.3.4.2.1 Height control

To ensure safety, the UAV's flight path height ranges from 0.5m above the ground to the tunnel crown. The following UAV's real-time height feedback control algorithm aims to keep a constant ground clearance height, regardless of the slope of the tunnel road surface.

Figure 4-10 illustrates its principle. The algorithm utilizes the expected height (*Height*) and the feedback height reading (*Currentheight*) from the infrared sensor to calculate the height control variable (*throttle*):

$$throttle = 2\,Height - Currentheight \tag{3}$$

Where throttle is a position-based control parameter. At zero throttle, UAV flight at approximately 0.5m height. An increase in ground elevation decreases $Currentheight$ and gives UAV an uplift signal from the increased $throttle$. The control range is within 5 meters as infrared sensor accuracy restricts.

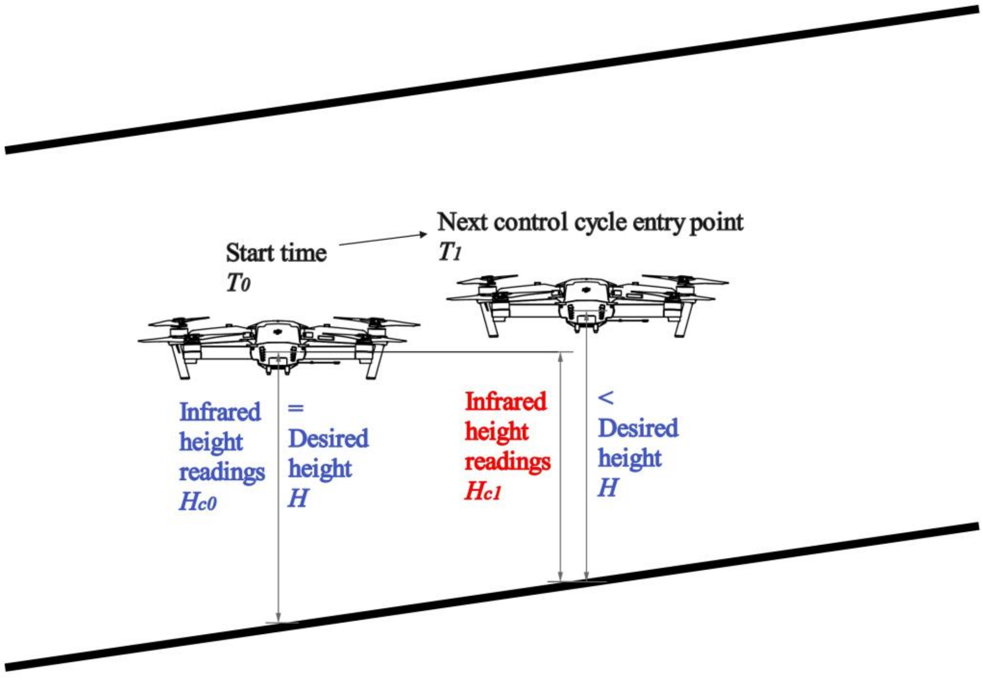

Figure 4-10 Height adjustment control in tunnels with an elevation change.

In general, a higher flight height allows for a larger inspection area due to the UAV's limited vertical FoV. However, for uniform brightness in the surface images, the UAV can't just fly at maximum height. In dark and small tunnels, the spotlights must point upwards to avoid light reflections from the lampshade. As a result, inspections have to be performed from several heights to ensure full coverage of the inspected surface. An initial UAV flight height could be set at 3 meters in the centre of the tunnel, with subsequent inspections performed at other heights.

4.3.4.2.2 Yaw control

The UAV employs visual positioning to correct its heading in the yaw module, with the parameter *yaw* limited to a range of [-180, 180] degrees. To ensure stable hovering during filming, the UAV periodically fine-tunes its orientation using the *yaw* parameter. The *yaw* adjustment amount is calculated from the obstacle distance indicator readings. These readings should be stable and non-zero values for a reliable calculation. The adjustment follows equation (4):

$$yaw' = yaw + \begin{cases} \frac{(D_{l0} - D_{r3})}{|D_{l0} - D_{r3}|} \times 15, & s.t. (D_{l0} - D_{l1}) \times (D_{r2} - D_{r3}) > 0 \wedge D_{l0}, D_{r3} < 20 \\ \frac{(D_{l0} - D_{r3})}{|D_{l0} - D_{r3}|} \times 5, & s.t. D_{l0} \neq D_{r3} \wedge D_{l0}, D_{r3} < 20 \\ 0, & s.t. D_{l1} \,/\, D_{r2} > 20 \end{cases} \tag{4}$$

Where *yaw* is the orientation of UAV in the ground system. D_{l0}, D_{l1}, D_{r2}, D_{r3} are the frontal distance readings in four sectors from the left to the right of the UAV. Assuming that the tunnel curvature has no effect on the difference of the distance readings in four sectors, these readings should have a relationship of $D_{l0} = D_{r3} > D_{l1} = D_{r2}$ as an ideal attitude.

As shown in Figure 4-11, the right UAV attitude corresponds to the first formula in equation (4). To compensate for *yaw* deviation during flight, the UAV makes an anticlockwise yaw adjustment by decreasing the *yaw*. The values of yaw adjustment are constrained to three options: 15°, 5°, or 0° of *yaw* adjustment. In the right situation in Figure 4-11 with red readings, a larger front obstacle distance reading in the right three sectors compared to the left one. As a result, the UAV makes a 15° adjustment anticlockwise.

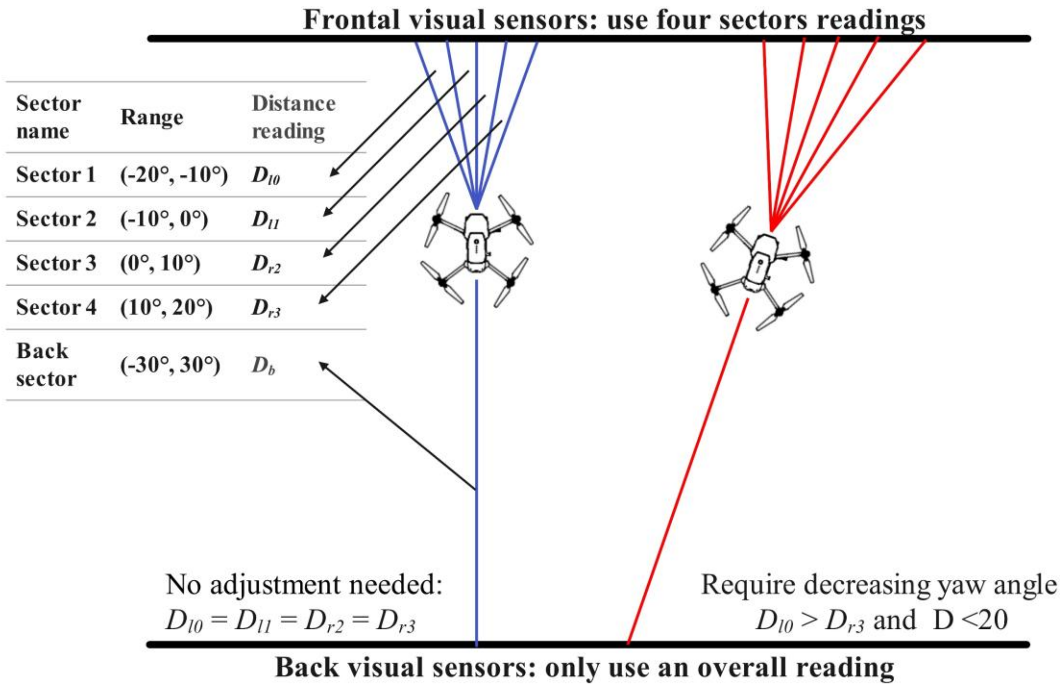

Figure 4-11 Yaw adjustment control using sensor data in a curved tunnel.

The calculation of the *yaw* adjustment should also consider the credibility of distance indicator readings. Otherwise, the UAV attitude in the MSDK may be incorrect. In dim inspection environments, low credibility data may produce readings that are too large or zero. In this case, a conservative adjustment of 0° is made if no data is available, and 7.5° if only sectors 2 and 3 provide readings available for adjustment.

4.3.4.2.3 Lateral position control

The UAV lateral position control in the tunnel is corrected after every rightward panning of approximately 1 m (Figure 4-12). The adjustment in the lateral direction of a UAV is expressed by Equation (5):

$$roll2 = \begin{cases} 2.0, & s.t. \left|D_f - D_p\right| \geq 1.50 \\ 1.6 \times (D_f - D_p), & otherwise \end{cases} \tag{5}$$

Where *roll2* is the frontal distance adjustment over 0.5 seconds. D_f is the frontal distance reading, and D_p is the expected frontal distance reading. After each lateral adjustment, the UAV has 0.2s cushioning time to stabilise to 0 velocity. Using equation (5), the UAV will make 1 - m lateral position adjustments in steps until it is 1.5 m or closer from the expected hover point. Within this range, a final adjustment of 80% of the distance is made to avoid over-adjustment.

In dim conditions, a conservative adjustment is made as distance readings are less reliable. If the distance readings are stable, the movement adjustment is made directly. Otherwise, no feedback adjustment is made. The criterion for stability is that the sum of the front and rear sensor readings changes within 15%. To achieve flight stability, the UAV should take off and land in suitable luminance conditions.

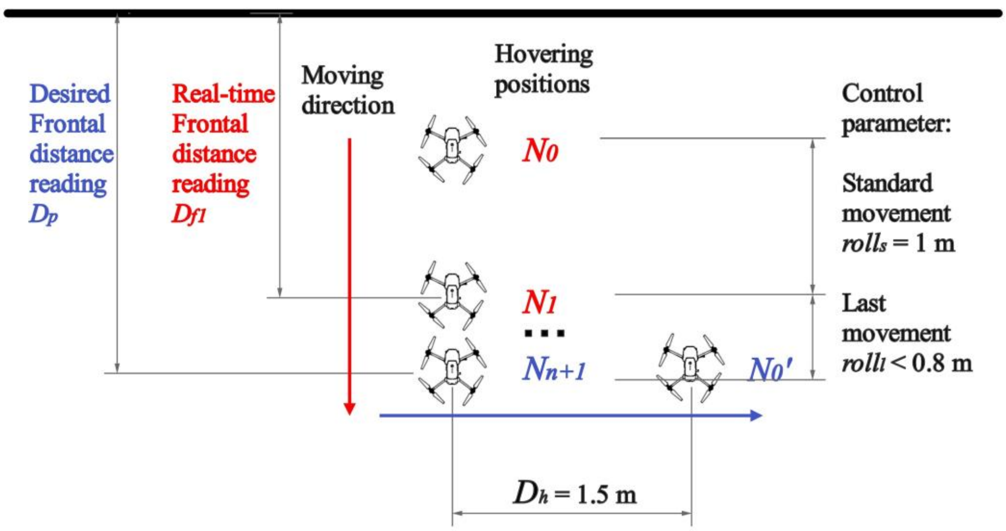

Figure 4-12 Sensor data-driven lateral position control in a well-lit slightly curved tunnel.

4.3.4.3 Human-robot interface

Figure 4-13 illustrates the human-robot interface, with the parameters and their values explained in previous sections. The interface facilitates task initiation and activation through a sequence of operations. Initially, three parameters are set at the top, followed by the activation steps: clicking 'Enable Virtual Stick', 'Take off', and 'Start Flight Control'. Task completion is at the operator's discretion and is performed by selecting 'End flight control', 'Disable Virtual Stick', and manually landing the UAV using the remote controller. Once a two-meter control error happens due to structural or vehicle-caused wind turbulence, the operator lands the UAV and restarts the inspection from the landing point until data acquisition is completed.

The interface displays real-time sensor data for UAV positioning. The '*Height*' parameter indicates the UAV's altitude, while '*getpitch*' represents the gimbal angle, ranging from -90° to 20° throughout each move-pause-photo cycle. The front and back obstacle distances determine the lateral position of the UAV, whereas the 'left and right obstacle distance' values correspond to the readings from the four frontal sensor sectors.

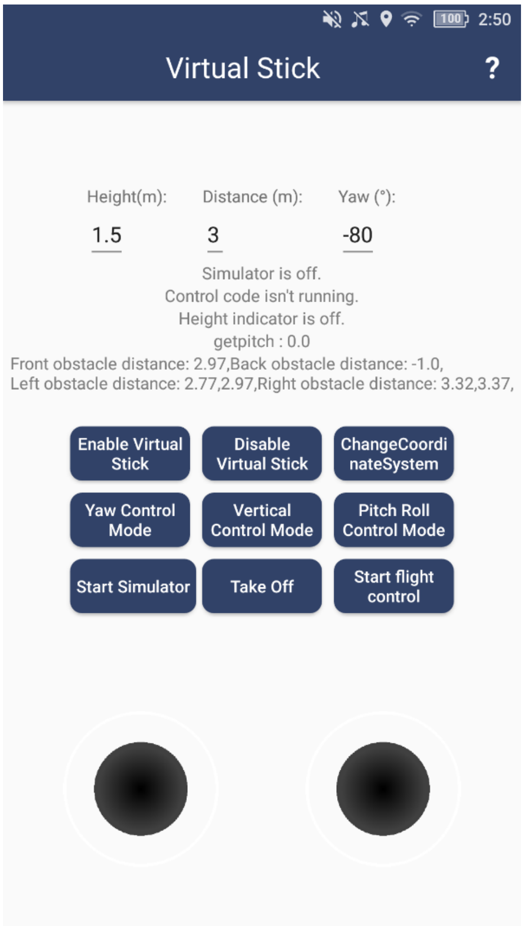

Figure 4-13 Operation interface in DJI MSDK rewritten for tunnel inspection

4.4 UAV tunnel image processing

4.4.1 3D reconstruction workflow

Figure 4-14 depicts the data processing workflow for 3D model generation and defect analysis from a set of images using photogrammetry techniques. The method includes several key steps:

1. Filtration of blurred images: This step removes images that are out of focus or have motion blur, which can affect the accuracy of the final 3D model.

2. Image stitching: Also known as image alignment or mosaicking, this process involves overlapping and aligning images based on common features to create a larger,

seamless image. As an illustration, the Automatic Tie Point (ATP) numbered 2393482 is visible in a total of 83 images for spatial position calculation in Pix4Dmapper.

3. 3D reconstruction: A 3D model was the n constructed using Structure from Motion (SfM) and the scale was restored using a proportional vector of several global dimension measurements of the inspected tunnel areas. Orthomosaics on vertical projection planes were generated after the 3D model construction for subsequent data extraction procedures. The projection creates a Digital Surface Model (DSM) for more manageable data, enabling spatial and defect information extraction.

4. Spatial information extraction using the DSMs: Since the DSM is an image with depth, it is used here to extract spatial information. The spatial information facilitates structural geometry inspection. Combined with camera positions and attitudes, the accuracy of UAV flight trajectory inspection is also investigated. The higher the quality of the reconstruction data, the more subtle dislocations can be detected with this method.

5. Defect identification and quantification: This step involves identifying and quantifying different types of defects in the dataset. Common defect types in concrete structures include cracks, leakages, and spalling of concrete linings. These defects can be identified using various methods, such as manual statistical analysis, feature-based detection, or machine learning techniques.

It should be noted that 3D models constructed solely from imagery and inertial measurements in tunnels may exhibit drift, leading to slight misalignments, with errors growing linearly over the tunnel's length. Key dimensions and vectors are used for scaling but geofencing is supposed to better support model reconstruction.

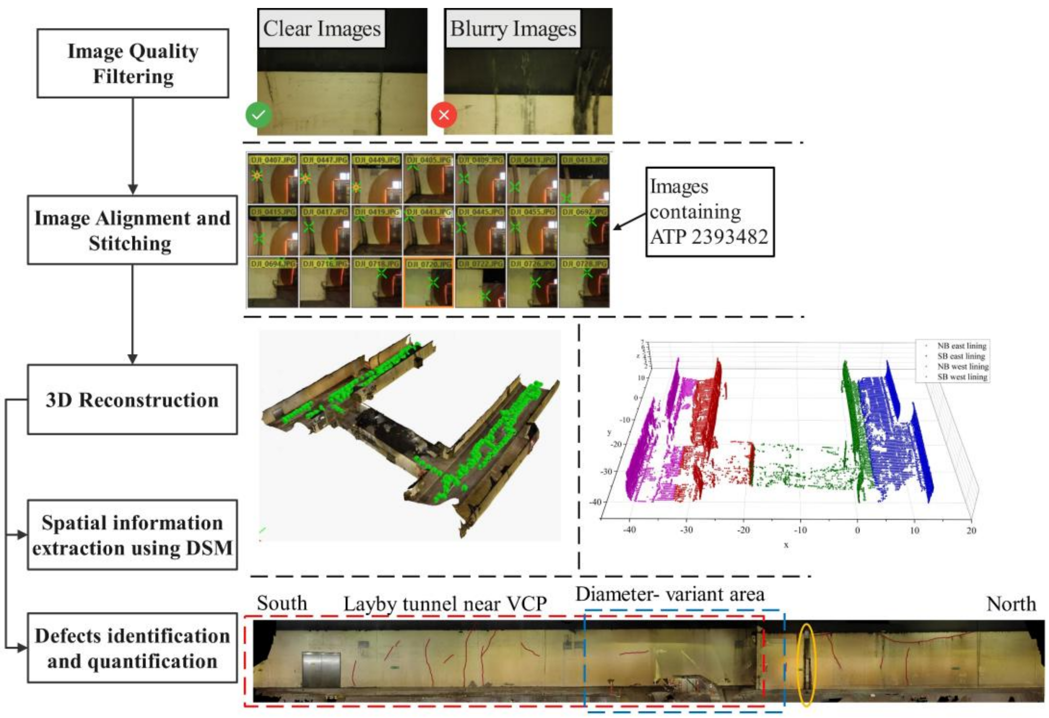

Figure 4-14 Image processing workflow in a tunnel field test

4.4.2 Spatial information extraction

The extraction of spatial information holds utility in two main areas: analysing UAV flight trajectories in automatic control and assessing tunnel lining geometry.

4.4.2.1 Spatial information processing workflow

The extraction of the spatial information of the tunnel in this research must be structured within a user-defined coordinate system, as the geodetic coordinate system is not applicable in GPS-denied tunnels. The spatial information processing workflow is illustrated in Figure 4-15. In this figure, the original tunnel lining coordinates are derived by projection in Pix4Dmapper, using a projection coordinate system where the projection plane is approximately parallel to the tunnel lining. QGIS is then used to generate the location of the cross sections and the tunnel outline. As the camera positions are in a blind coordinate system in Pix4D, coordinate conversion is required for UAV path control. Geometric analysis of the tunnel linings can be performed for tunnel shape analysis.

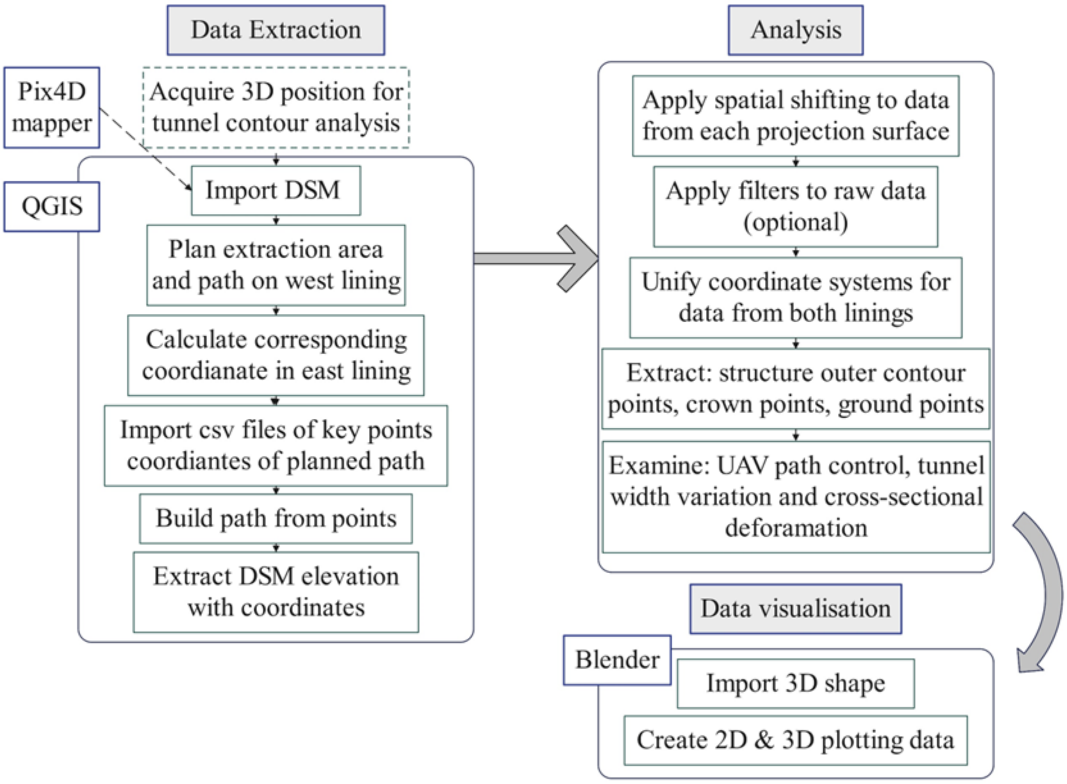

Figure 4-15 Workflow of data extraction and analysis from 3D tunnel model and software in each step

4.4.2.2 Example of coordinate extraction

The data extraction process is depicted in Figure 4-16. For the examination of tunnel geometry, cross-sectional contours are extracted at 0.5-metre intervals. The principle is the same for the extraction of spatial data in each inspection. However, for the study of tunnel deterioration mechanisms, the selection of the locations of the pairs of cross-sections must avoid structural anomalies such as firehoses and sump control panels.

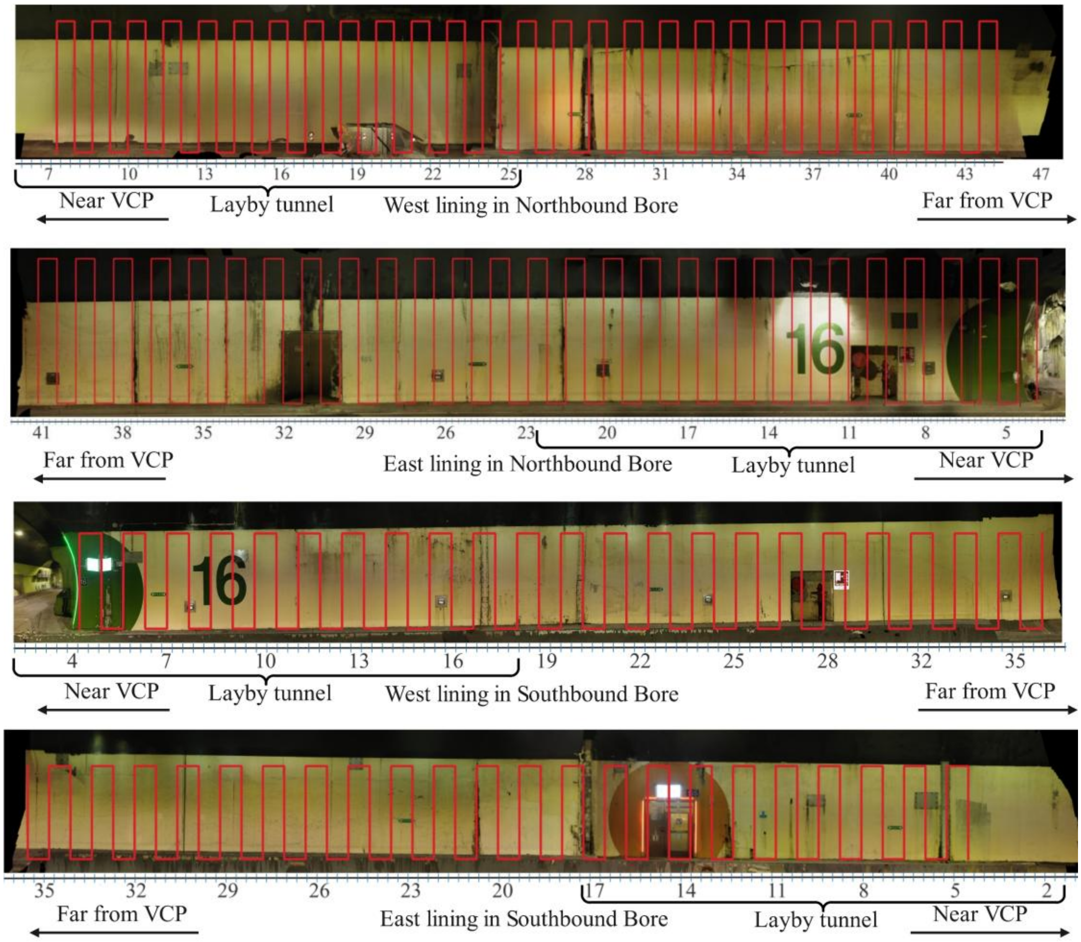

Figure 4-16 Data extraction in four linings (tunnel mileage starts from VCP and is in the unit m)

4.4.2.3 Coordinate conversion

The global coordinate system in Pix4Dmapper is $\boldsymbol{S}$ $(\boldsymbol{x_0}, \boldsymbol{y_0}, \boldsymbol{z_0})$ in Figure 4-17. The coordinate systems of DSMs in DPT are ($\boldsymbol{S_1}$ and $\boldsymbol{S_2}$), which are the data resources. The unified spatial coordinate system $\boldsymbol{S'}$ $(\boldsymbol{x'}, \boldsymbol{y'}, \boldsymbol{z'})$ is created for organizing data. $\boldsymbol{S'}$ share the same positive direction of $\boldsymbol{S_1}$ and the origin of $\boldsymbol{S}$.

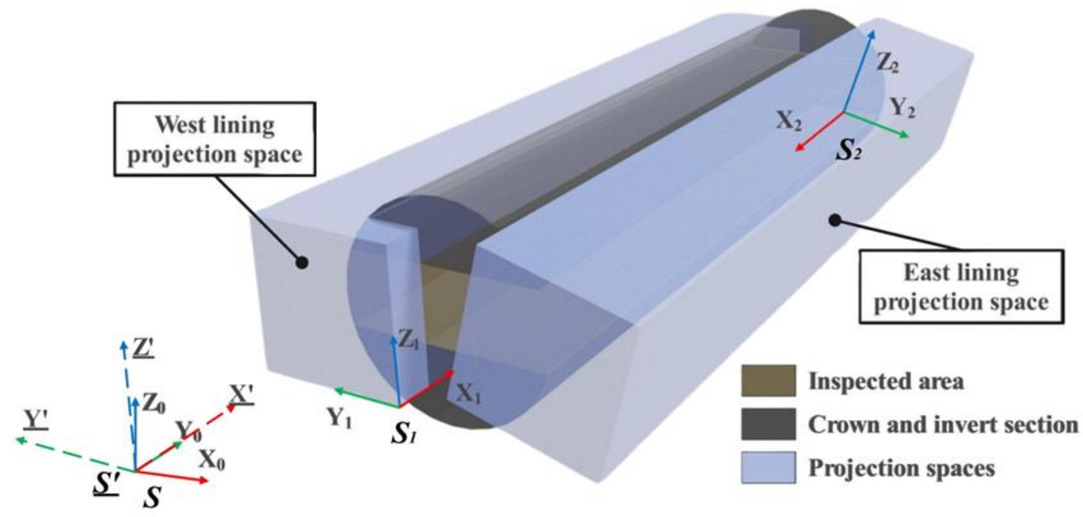

Figure 4-17 Coordinate system conversion schematic (with projection space for DSM and orthomosaic extraction)

The spatial extraction of tunnel linings and cameras enables quantification of UAV control accuracy. The UAV's spatial position is converted from $\boldsymbol{S}$ to $\boldsymbol{S}'$. UAV's position $\boldsymbol{tc}'$ in $\boldsymbol{S_1}$ is calculated using the following Equation (6):

$$\boldsymbol{tc}' = (\boldsymbol{tc} - \boldsymbol{a_1})\ \boldsymbol{R_1} \tag{6}$$

Where UAV's position is $\boldsymbol{tc}$ $(\boldsymbol{x_0}, \boldsymbol{y_0}, \boldsymbol{z_0})$ in $\boldsymbol{S}$, and the orientation is camera rotation $\boldsymbol{Rc}$ [3×3]. $\boldsymbol{a_1}$ is the origins' coordinate difference between $\boldsymbol{S_1}$ and $\boldsymbol{S}'$ and $\boldsymbol{R_1}$ is the rotation matrix from $\boldsymbol{S}$ to $\boldsymbol{S}'$. The rotation matrix $\boldsymbol{R_i}$ could be expressed using yaw ($\boldsymbol{\theta z}$), pitch ($\boldsymbol{\theta x}$), and roll ($\boldsymbol{\theta y}$) in Equation (7):

$$\boldsymbol{R_i} = \boldsymbol{R_z(\theta_z)}\ \boldsymbol{R_x(\theta_x)}\ \boldsymbol{R_y(\theta_y)} =$$

$$\begin{bmatrix} \cos(\theta_z) & -\sin(\theta_z) & 0 \\ \sin(\theta_z) & \cos(\theta_z) & 0 \\ 0 & 0 & 1 \end{bmatrix} \begin{bmatrix} 1 & 0 & 0 \\ 0 & \cos(\theta_x) & -\sin(\theta_x) \\ 0 & \sin(\theta_x) & \cos(\theta_x) \end{bmatrix} \begin{bmatrix} \cos(\theta_y) & 0 & -\sin(\theta_y) \\ 0 & 1 & 0 \\ \sin(\theta_y) & 0 & \cos(\theta_y) \end{bmatrix} \tag{7}$$

In each bore, the west lining coordinates are $\boldsymbol{tp_w}$, and the east lining coordinates are $\boldsymbol{tp_e}$. They are in the form of $(\boldsymbol{x}, -\boldsymbol{elevation}, \boldsymbol{y})$. Their spatial position $\boldsymbol{tp}'$ in $\boldsymbol{S}'$ is calculated using Equation (3):

$$\begin{cases} \boldsymbol{b}_i' = \boldsymbol{a}_i' - \boldsymbol{a}_i' \cdot \boldsymbol{n}_x' \\ \boldsymbol{tp}_w' = \boldsymbol{tp}_w + \boldsymbol{R}_1 \cdot \boldsymbol{b}_1' \\ \boldsymbol{tp}_e' = \boldsymbol{R}_{21}\, \boldsymbol{tp}_e + \boldsymbol{R}_1 \cdot \boldsymbol{b}_2' \end{cases} \tag{3}$$

Where $\boldsymbol{a}_i' = (x_i, y_i, z_i)$ is the deviation between the origins of $\boldsymbol{S}_i$ and $\boldsymbol{S}'$, and $\boldsymbol{n}_x'$ is the x vector of this coordinate system, and $\boldsymbol{b}_i'$ is the projection of $\boldsymbol{a}_i'$ on tunnel cross-sections.

4.4.2.4 Model reconstruction

The three-dimensional reconstruction process aims to generate dense point cloud data in a 3D model of the tunnel interior geometry. Essential preprocessing steps, including noise filtering, outlier removal, and point cloud resampling, are imperative to improve data quality and minimize computational complexity, thereby ensuring precise spatial information extraction. This merged point cloud can be used for geometric modelling, dimensional extraction, and deformation detection. The output includes tunnel mapping, tunnel dimensions measurements (cross-sectional areas/ tunnel outlines in Figure 4-18) and deviations of the point cloud from its expected geometry.

Throughout the reconstruction process, it is essential to consider factors such as the accuracy and resolution requirements, computational efficiency, and the integration of additional data sources (e.g., existing blueprints, and GIS data) to improve the overall quality and reliability of the 3D tunnel model.

A series of processing techniques were employed to eliminate noise and smooth the data set obtained from the tunnel. It was found that in Pix4D, the use of down-sampled images, specifically a small 1/4 image scale and a large (9×9) sliding window, was highly effective in mitigating the impact of low-quality UAV tunnel images that were under-lit or blurry.

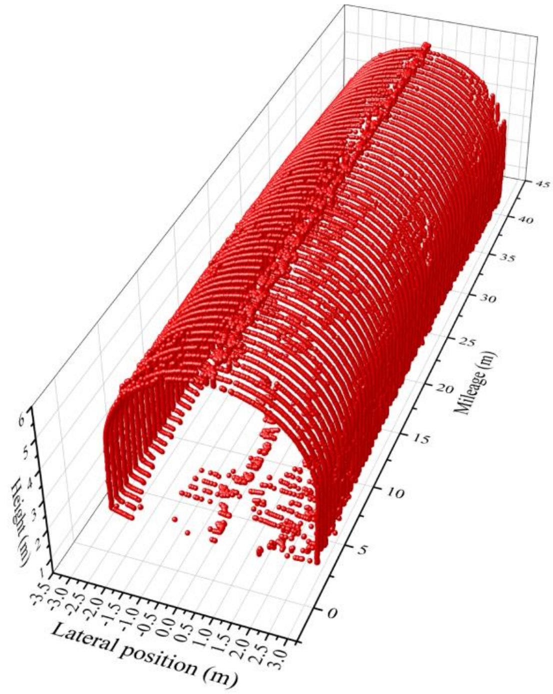

Figure 4-18 Extracted spatial information from a tunnel DSM model.

In addition, a point cloud segmentation algorithm called Seg2Tunnel by Wei [165] also helped to reduce noise. The whole process is illustrated and verified by a segment of tunnel point cloud data in Figure 4-19. The segmentation training dataset is generated from synthetic point cloud data. The synthetic dataset consists of the as-built tunnel shape and user-generated noise within small rectangular areas. This application of Seg2Tunnel to synthetic point cloud data enables fast computation without the pain of labelling noise, which is unevenly distributed in tunnel point clouds in the real world. It's proven to be effective for future fast processing of large point cloud files, but that is not the main research finding of this thesis.

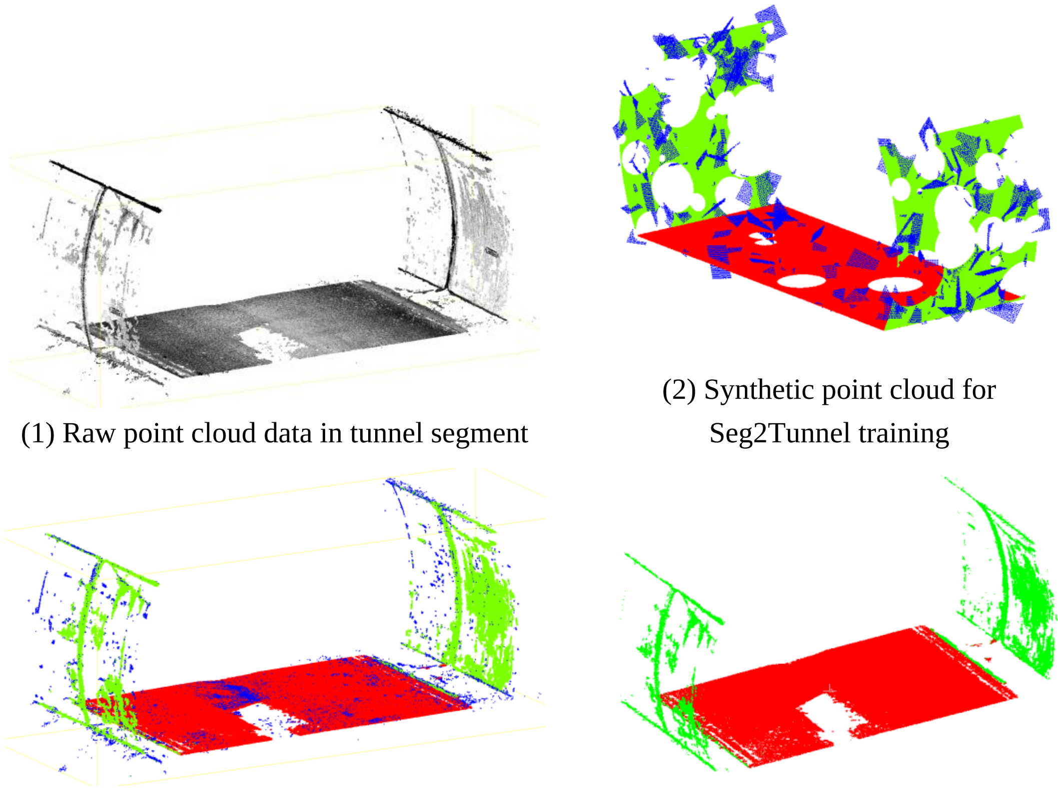

(1) Raw point cloud data in tunnel segment

(2) Synthetic point cloud for Seg2Tunnel training

(3) Segmented point cloud with Seg2Tunnel

(4) Denoised segmented point cloud

Figure 4-19 Denoise process using Seg2Tunnel and synthetic point cloud of 5m length (red for road surface, green for tunnel lining, and blue for noises)

4.4.2.5 UAV navigation verification

The assessment of UAV navigation control accuracy is widely studied. Much research on UAV control is summarized in UAV road and bridge inspection as they navigate along the inspected surface [209]. This section conducts such work in the tunnel by comparison between the actual route and attitude of the flight and the planned route attitude.

The flight trajectory extraction allows for the validation of UAV in lateral and height control accuracy in expected flight area control (Figure 4-20). The UAV heights and lateral distance of the UAV to the nearest tunnel profile can be used as two indices for the verification of the UAV vertical and lateral control accuracy.

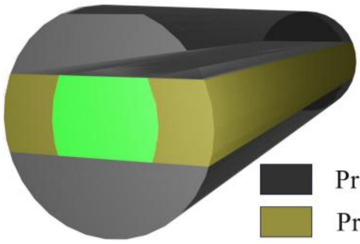

Figure 4-20 Illustration of expected UAV flight area in tunnels

Analysis should be made after removing some outliers due to structural indentation, take-off action and manual supplementary photography. The average computed errors for the automated tie points in a tunnel model construction are listed in Table 4-4. Computational errors are negligible compared to UAV flight deviation.

Table 4-4 Computational errors in relative camera position and orientation

	X [m]	Y [m]	Z [m]	ω [°]	φ [°]	κ [°]
Mean	0.023	0.005	0.036	Nan	1.422	5.160
Sigma	0.011	0.009	0.037	Nan	0.392	6.093

4.4.3 Image processing output

The orthomosaics with coloured textures are used for defect identification and quantification. UAV orthomosaics (Figure 4-21) and DSMs (Figure 4-17) are generated in pairs (see section 4.4.2.2). This allows UAVs to be used for quantifiable defect detection, whereas researchers using LiDAR and cameras need to fuse the data to achieve the same [175]. The efficiency of image processing is also improving as algorithms are developed [157]. Due to the promising future of UAV tunnel inspection, this research aims to figure out the process and challenges of UAV tunnel image defect identification.

In tunnel models, the quality of the models for defect identification could be verified by visual comparison. The quantity of defect identification is verified by the resolution of orthomosaics. In the two following projects, the resolution of 1.1 or 1.4

mm/pixel are acceptable values to measure major defects. Therefore, the following work includes length measurement for cracks and area measurement for water leakage.

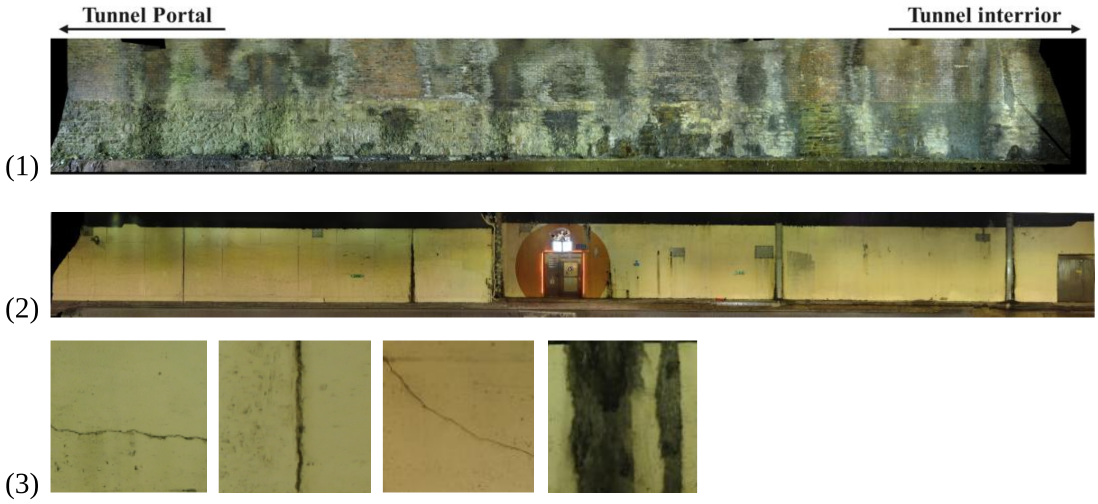

Figure 4-21 Examples of (1) and (2) long stitched images for (3) defect identification

4.5 Summary

This chapter proposed a methodology to address the challenges of automatic UAV tunnel surface defect inspection. The research aims to propose a robust and efficient inspection method for image data acquisition and processing in complex and dark tunnel environments. A method, called Proximity Move-Pause-Photo for Surface Defect Inspection (PMPP-SDI), is proposed by combining reactive flying control strategies with a grid scanning pattern to capture high-quality image data from multiple views and angles. The image data is then used to generate a 3D point cloud model of the tunnel surface for structural condition assessment. Compared to previous studies, this research makes the following contributions:

(1) A UAV navigation and data collection system is proposed for inspections in tunnels, shafts, and other underground sites. It adopts a reactive navigation method that enables the UAV to switch to different strategies according to inspection conditions. This method is designed to handle low light conditions and complex structures by following

the profile of the structure during inspection. However, a limitation of this VINS control system is its inability to achieve high-precision absolute positioning.

(2) Alongside the UAV data acquisition method, we proposed a workflow for processing UAV tunnel image data. This involves the stitching together of images to create orthomosaics and digital surface models (DSMs). The two types of data are generated in pairs. They enable cross-section geometry extraction and the identification of tunnel surface defects. The model optimisation involves applying a small image scale in image registration or applying an ML-based denoise algorithm for point cloud cleaning. The results facilitate the health condition assessment of the tunnel with dimensional and photogrammetric methods.

5. Field Test in a Railway Tunnel

5.1 Introduction

This chapter of the thesis describes a field test in a disused railway tunnel called the Goggins Hill Tunnel with the proposed UAV inspection method. It introduces the data acquisition and assesses the performance of the proposed method in quantifying tunnel surface defects that have been visually identified. The analysis of tunnel surface defects is based on the colour of projected images called orthomosaics. The tunnel surface was divided into specific categories based on their colour characteristics. In addition, the test includes the extraction of deformations and an analysis of the deterioration mechanisms.

5.2 Engineering background

This section introduces the engineering condition of the Goggins Hill Tunnel and the relevant challenges and solutions for UAV inspection.

5.2.1 Goggins Hill Tunnel

The Goggins Hill Tunnel in County Cork, Ireland, is a railway tunnel that was constructed in 1866 as part of the Cork, Bandon, and South Coast Railway. It spans a length of 1,200 meters and has dimensions of 5.6 meters in width and 4.8 meters in height. Designed to accommodate single-track railway traffic, the tunnel features a gradient of 1 in 90. Its construction utilized the "cut and cover" method, which involved excavating a trench and then covering it with a brick and stone arched roof.

Figure 5-1 illustrates the pre-existing and known defects on the tunnel surface from visual inspection, which are mainly influenced by water leakage. This railway tunnel inspection followed the guidelines of the Rail Transit Tunnel Inspection Manual [210], which classifies water leakage into three degrees. Wet masonry corresponds to minor leakage, while active flows with a volume of fewer than and greater than 30 drips per minute represent moderate and major leakage, respectively. In Figure 5-1, (1) shows salt deposits on the tunnel linings, (2) shows minor water leakage, and (3) shows moderate water leakage. As there was no rain on the day of the inspection, no apparent leakage was observed. Moderate water leakage defects are observed in the crown section, while no cracks or misalignment of obvious concern were detected.

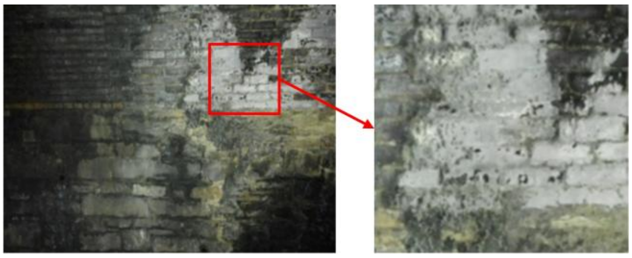

(1) Salt deposit

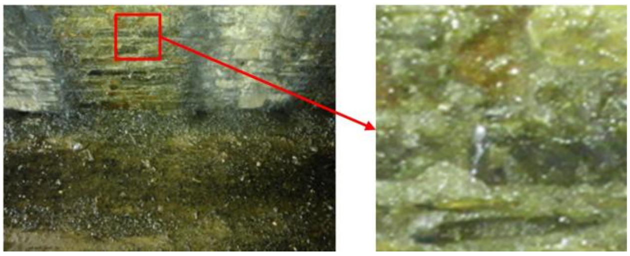

(2) Minor water leakage

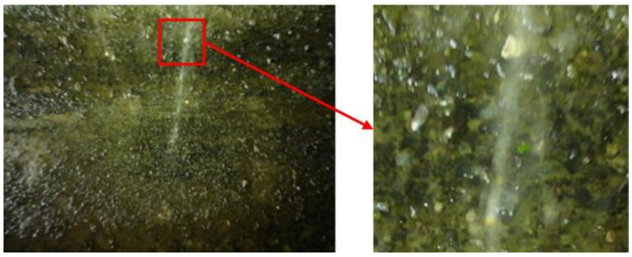

(3) Moderate water leakage.

Figure 5-1 Examples of image data showing identified defects

5.2.2 Challenges and solutions for UAV inspection

The application of the PMPP-SDI method to railway tunnels is a representative case study, as railway tunnels possess distinct structural and luminance characteristics that set them apart from road tunnels. These characteristics are outlined in Table 5-1. Notably, the Goggins Hill railway tunnel exhibits a uniform structure with consistent profile and size, lacking elements such as firehoses and emergency exits, which could introduce inconsistencies to the lining design. Such a consistent structure facilitates visual navigation, with minimal lateral adjustment.

In terms of luminance, railway tunnels generally exhibit dim lighting internally, but brightness increases near the tunnel portal (Figure 5-2). While UAV navigation within the tunnel remains functional under dim natural light conditions, the reduced luminance may affect the quality of acquired tunnel images intended for data analysis. Consequently, insufficient lighting in the tunnel may result in image noise and pose challenges for inspecting cracks and leakages. Besides, slight misalignments may occur in 3D models constructed solely from imagery and inertial measurements. Such errors are supposed to be mitigated by adding more geofencing points to register the geo-information (apart from limited numbers of manual tie points) in later research.

Table 5-1 Challenges and solutions in a weakly lit railway tunnel

Challenges		Solutions
Data acquisition	Dim conditions are not favourable for high-quality data collection	1. Use a spotlight and a headlight. 2. Fly at multiple heights to contain details at each position.
	Slanted light is not favourable for UAV navigation	Fly at least 3 m high to avoid light interference (UAV adopts flying strategy 3 in scenario C).
Data processing	Not clear textures for model reconstruction; Dark environment may produce image noises	1. Add manual tie points (MTPs). 2. Image quality filtering 3. Image pre-processing for extremely low-quality images (denoise, texture enhancement)
	Various exposures in images taken at different positions	Build different models separately for each flight and merge models

(1)

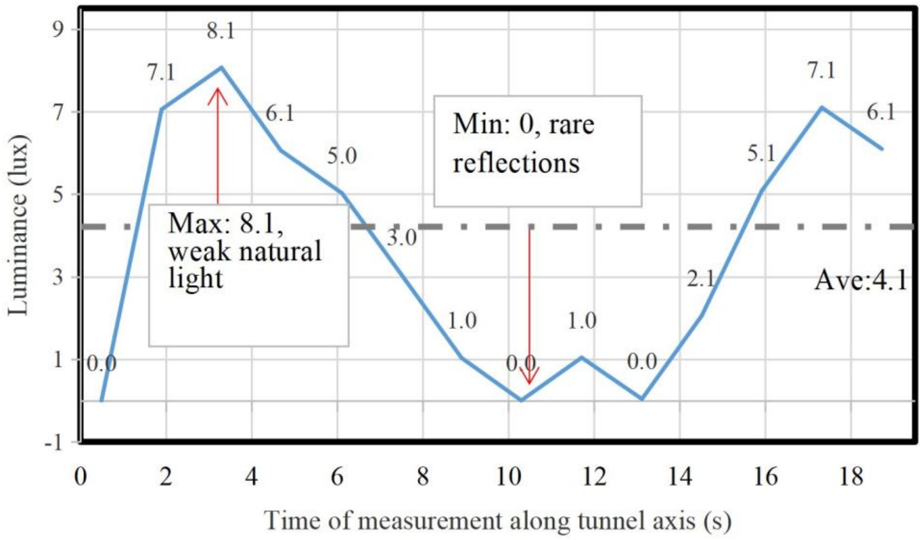

(2)

Figure 5-2 (1) the working scenario and (2) light intensity variation along the tunnel length.

The inspections produced an evenly illuminated image dataset for structural defect inspection. By using images instead of video frames, the dataset avoids motion blur in the camera and reduces storage and computational requirements, compared to similar research that relies on video frames for structural health monitoring. For data acquisition in dark environments, the camera uses spotlights to reduce noise. For optimal image quality in varying luminance conditions, an automatic exposure setting was employed.

5.2.3 3D reconstruction of inspection area

A total of three image datasets were obtained during straight flights, comprising 257, 198, and 184 images, respectively. Image acquisition for each side of the 40-meter tunnel took 30 minutes, totalling 2 hours for multi-view scanning. This duration is comparable to a human inspection but significantly longer than the time required for a LiDAR truck, which can complete the scanning in just a few minutes.

These images had a resolution of 4056×3040 pixels, and the total size of all datasets was 5GB. The PMPP-SDI method captures photos only when the UAV hovers, reducing motion blur compared to video data acquisition or images taken while the UAV is in motion. However, inconsistent lighting conditions lead to some missing and blurred images due to variations in the camera's shutter. After removing the blurred photos, clear images from the three datasets were used for model reconstruction.

The obtained images were of satisfactory quality for post-processing. Out of the 628 images in the dataset, 615 were calibrated (97%) and used for the reconstruction. The Pix4DMapper software, a widely used tool for photogrammetry, generated a median of 14,249 key points per image, with a median of 7,475 matches per calibrated image, as shown in Table 5-2.

Figure 5-3 provides a feature-matching example, where the green cross represents the selected key feature. The flights during the experiments were taken from varying heights, resulting in different views across flights. From the figure, it’s indicated that key features could be identified across adjacent cameras, even with variations in luminance and image-taking angles. To optimize efficiency, flights were computed separately. Since the captured data lacked geographical information, four manual tie points (MTPs) (see Figure 5-4) were used to stitch the three models into a virtual coordinate system.

Table 5-2 Number of 2D Key Points as an Indicator of Feature Matching Accuracy

	Median	Min	Max	Mean

Number of 2D Key points per Image	14249	10642	25803	15016
Number of Matched 2D Key points per Image	7475	295	18026	7773

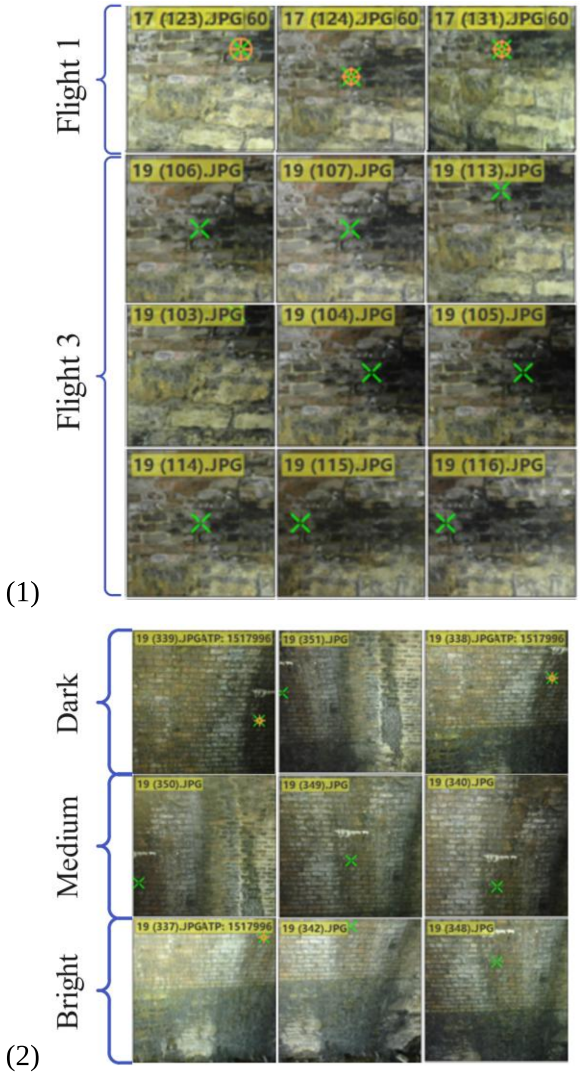

Figure 5-3 Examples of feature matching (1) from various spatial views and (2) in various lighting conditions.

Figure 5-4 is a UAV oblique photogrammetry 3D model of the tunnel lining reconstructed using Pix4Dmapper. The model has a density of 2.8×10^6 points/m3, which is 400 times denser than the LiDAR point cloud density of 7.1×10^3 points/m^3 in a similar tunnel environment [177]. Given the experimental practice that larger A3 UAVs with heavy LiDAR payloads can't fly stably in small diameter tunnels, the consequent research will focus on image data processing from the A2 category drone.

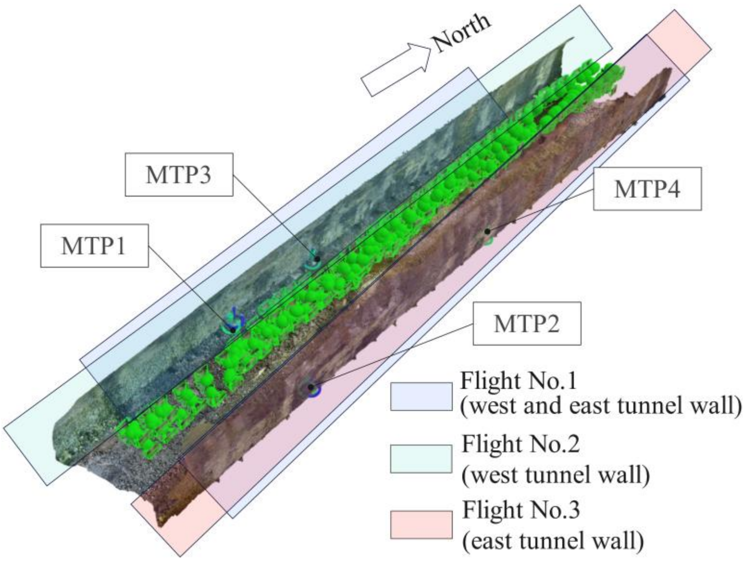

Figure 5-4 3D view of the tunnel lining model and flight paths in three flights, indicated by green dots.

5.3 Surface defect categorisation

Figure 5-5 presents the orthomosaics derived from above the 3D point cloud model, which contains textures on Goggins Hill tunnel linings. The resolution of orthomosaic is 1.1 mm/pixel. Based on the orthophotos, a geotechnical analysis and surface health inspection are conducted for the railway tunnel, using the 256 MB projection of each lining.

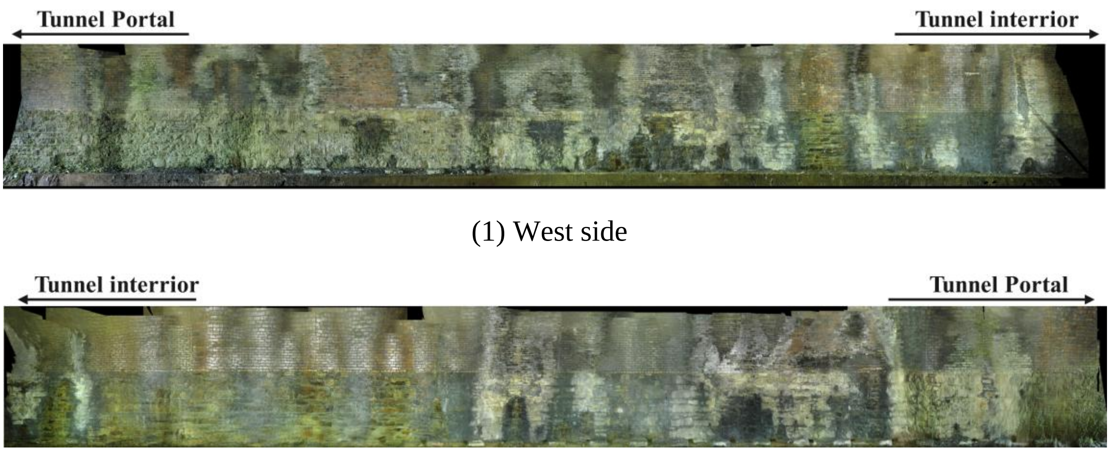

(1) West side

(2) East side

Figure 5-5 Orthomosaic of tunnel lining surfaces on the selected vertical plane

The use of coloured surface textures in orthomosaics facilitates the segmentation process, as evidenced by Figure 5-6 (1) and (2). The original colour of the masonry walls is brick red. On the ageing masonry walls, green patches indicate the presence of microorganisms, while black and white colours indicate salt deposits, likely composed of calcium or sodium salts. Some black salt is observed at the edges of the white salt deposit area, and this darkening of white salt deposits is attributed to exposure to further contaminations, such as diesel soot, atmospheric pollutants, rainwater and humidity, and biological growth. These observations contribute to investigating the distribution and potential tunnel diseases.

To segment the orthomosaics of the salt-contaminated tunnel lining, a combination of manual segmentation and AI method called Segment Anything (SAM) [211] is used. Manual segmentation, along with SAM, is applied due to the excessive textures on the brick and stone surfaces of the tunnel lining. Salt-covered surfaces present challenges in defect identification and segmentation as they have unclear boundaries. SAM aided in providing preliminary results for refined manual segmentation. The final manual segmentation indicated the distribution of different colours, and their engineering interpretations are tabulated in Table 5-3.

(1) West side

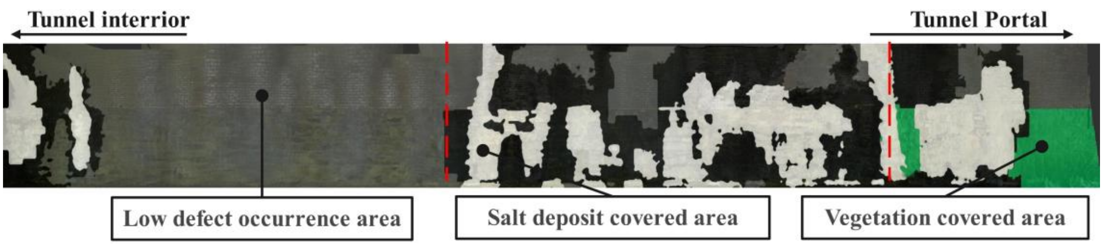

(2) East side

Figure 5-6 Salt deposit segmentation of surface type based on colours of the tunnel lining (green: moss, grey: original wall texture, black: soot or contaminated minerals, white:

calcium/magnesium mineral, and unmasked black background).

Table 5-3 Possible tunnel ageing types from the segmentation results in tunnel linings

Surface colour	Surface defect area		Possible material	Possible ageing types
	West side	East side		
Green	4%	2%	Moss and algae	High moisture, lack of surface cleaning
White	46%	23%	Calcium/iron mineral deposit	Water leakage, salt infiltrated through cracks
Black	28%	28%	Soot from steam engine/coal transportation	Polluted salt infiltration
Original colour	22%	47%	-	-

The colour distribution on the tunnel surfaces reflects the condition of its linings. These west-side tunnel linings have been affected by leakage, resulting in salt infiltration through the masonry gaps. Abnormal colours observed include predominantly white mineral deposits (46% of the total area) and some black deposits (28%). Close to the tunnel portal, green-coloured surfaces are present, while interior parts retain the original colour of the bricks. Some sections show white and black salt deposits. Similarly, the findings can be extrapolated to the east side of the tunnel lining, which can be classified into three distinct zones.

5.4 Spatial information extraction

The following section analyses dimension information extracted from DSMs. The orthogonal projection of the model onto the vertical surface provides a profile of the tunnel side elevation. The DSMs are built from UAV images and 172 camera supplementary images, with the latter completing the model of the tunnel crown for visualisation.

5.4.1 Navigation examination

The three UAV flight paths can be visually examined from Figure 5-4, represented by green dots. The control accuracy is assessed through extracted camera positions in Figure 5-7, indicating that there are limited controlling errors of less than 0.7 meters in the horizontal plane and 0.3 meters in height along the tunnel axis. The standard error in a 38-m flight is approximately 0.3 m for both horizontal position and flight height. The PMPP-SDI method has proven to be effective in navigating through dark and straight tunnel environments, as evidenced by the Goggins Hill railway tunnel.

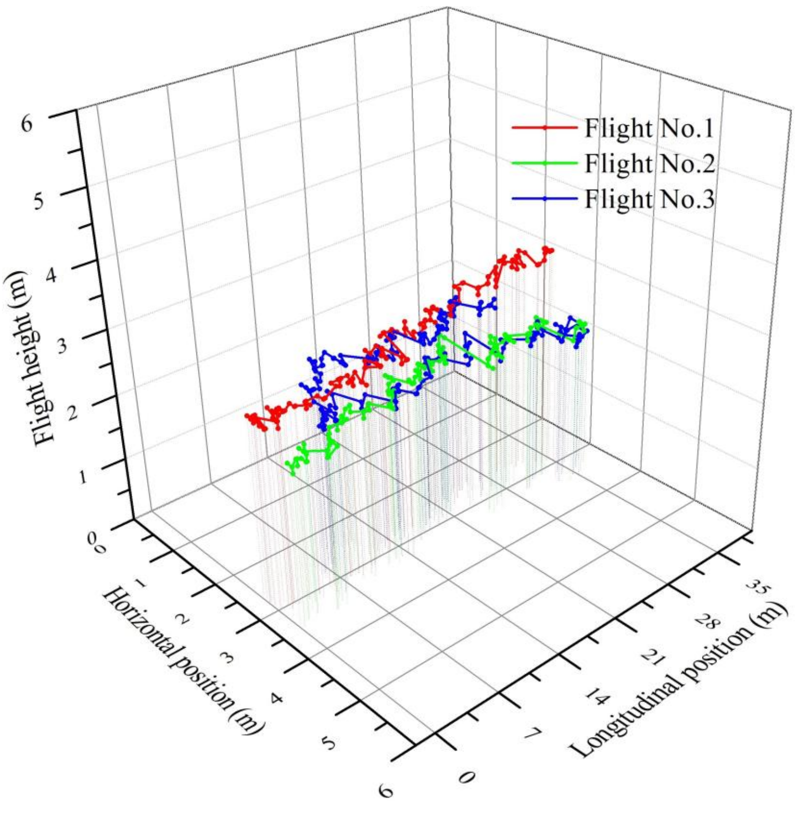

(1) A 3D view of camera positions

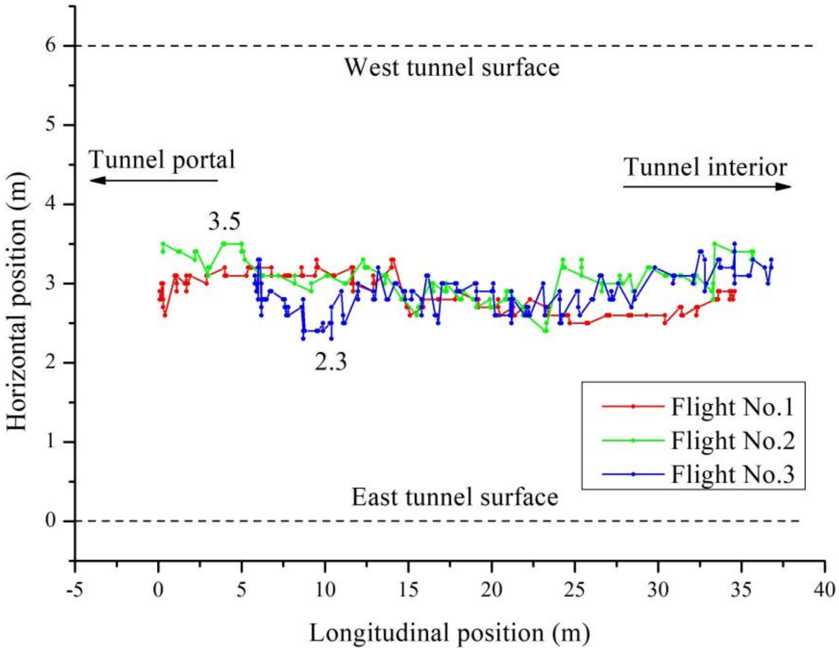

(2) Lateral position

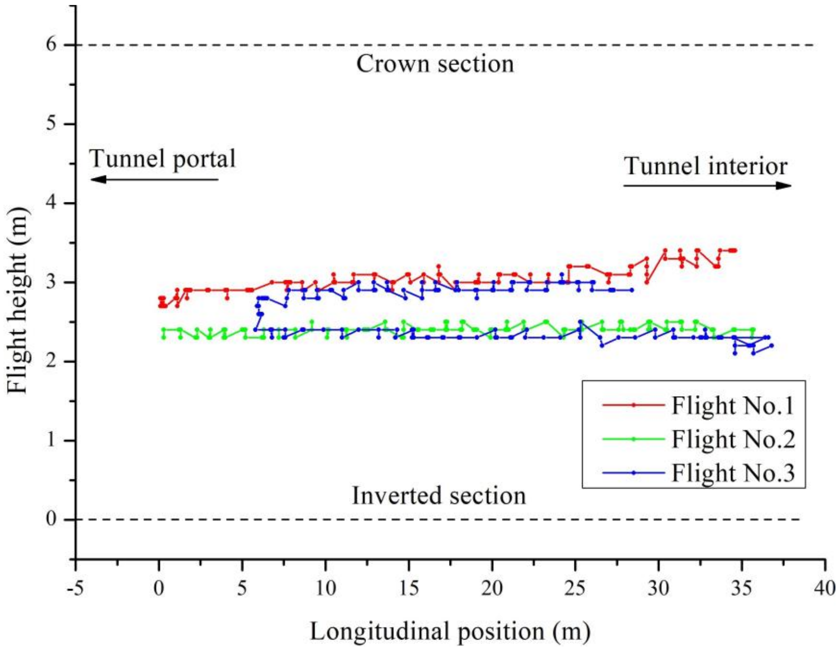

(3) Height

Figure 5-7 Extracted camera positions from the tunnel model.

The satisfactory control accuracy of this method demonstrates the possibility of image acquisition over longer or larger inspection areas through multiple independent inspections. This data acquisition method overcomes battery power limitations and allows for simultaneous inspection by multiple UAVs. An efficient model reconstruction is facilitated by this data acquisition and post-processing method.

5.4.2 Tunnel deformation extraction

From the depth extraction of the DSMs, the full tunnel 3D geometry was reconstructed, see Figure 5-8, and the tunnel linings are shown in red. The dimensions of the reconstructed model were calculated using scale-invariant information. A scale constraint of 5.8 m is used for the tunnel diameter to estimate the global dimension. The inspected length of the tunnel section is estimated to be 38 m.

The accuracy of the model is verified by comparing the laser measurement dataset with that extracted from the DSMs. Table 5-4 shows the comparison of the tunnel widths at the masonry boundary line (see Figure 5-8 (2)) from both data sources. The 3D reconstruction model shows tunnel dimensions in good agreement with the laser measurement.

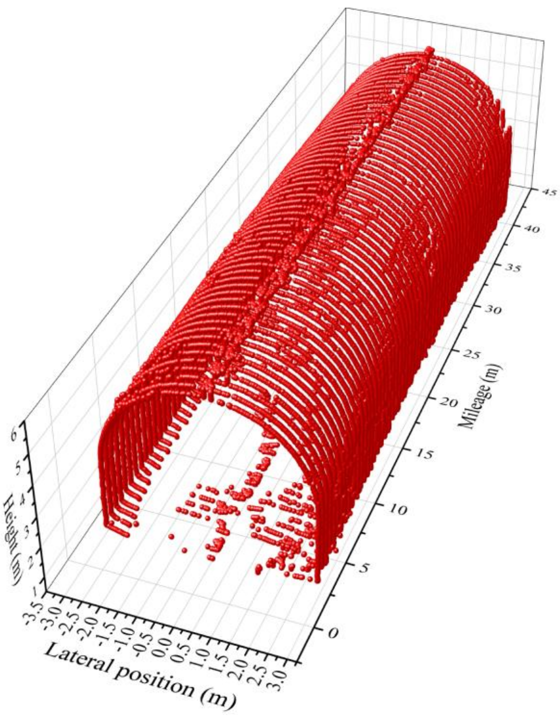

(1) 3D spatial information on tunnel surface

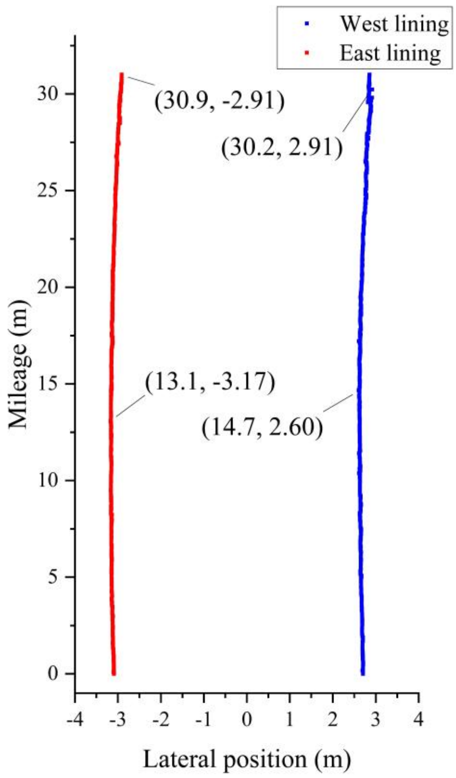

(2) 2D projection of tunnel lining at 2 m height (the interface of bricks and stones).

Figure 5-8 Spatial information extracted from the DSM model.

Table 5-4 Tunnel interior width comparison between laser rangefinder (LR) measurements and values from DSMs

Mileage	0	1.10	2.02	3.02	3.95	5.10	6.04	7.00	7.92
LR width	5.82	5.84	5.83	5.83	5.81	5.81	5.81	5.82	5.81
DSM width	5.80	5.80	5.84	5.81	5.81	5.80	5.79	5.80	5.78
Mileage	9.08	10.01	10.99	11.90	12.97	14.07	15.04	16.06	17.04
LR width	5.81	5.81	5.82	5.82	5.82	5.82	5.82	5.82	5.82
DSM width	5.80	5.80	5.78	5.78	5.79	5.79	5.78	5.77	5.77
Mileage	18.12	19.08	20.01	21.05	22.12	23.05	24.09	24.94	26.12
LR width	5.82	5.82	5.81	5.81	5.82	5.81	5.81	5.81	5.80
DSM width	5.78	5.78	5.78	5.79	5.79	5.80	5.81	5.81	5.82
Mileage	27.17	28.09	29.16	30.15	30.84				
LR width	5.81	5.80	5.82	5.80	5.81				
DSM width	5.81	5.83	5.84	5.78	5.76				

Table 5-4 shows that the deviations between the measured and calculated tunnel internal widths are within five centimetres or less than 1%. These errors in LR measurements can be attributed to the measurement itself on the uneven tunnel surface of bricks and stones, while the errors in DSM measurement are from image reconstruction. These comparisons suggest that the model reconstruction roughly captures the tunnel's geometry. However, for structural deformation detection, the accuracy of both LR and digital model measurements is insufficient. They cannot provide precise measurements to the millimetre for absolute deformation. Although the continuous variation measurements in DSMs enable a rough analysis of deformation trends, they are not yet capable of producing a standalone measurement report, as there is no UAV inspection regulation that is applicable to this scenario.

A possible improvement to the UAV inspection accuracy could be the calibration using total station measurement. A total station measurement of the length of the tunnel will reduce the scale assignment error of selected ATPs and the systematic errors caused by the accuracy of the equipment.

Figure 5-8 (2) shows that while the tunnel width of the Goggins Hill Tunnel does not change much with mileage, the direction of the tunnel axis changes first to the east and then to the west from the tunnel portal into the tunnel interior. This variation results in a 20cm change in lateral position over 19 m of mileage. The observations above demonstrate the reliable and detailed spatial data of the proposed UAV inspection method.

5.5 Deterioration mechanism analysis

The survey area is shown in Figure 5-9 of the geological map of Ireland. This area is characterised by a heterogeneous assemblage of lithologies, including shales, sandstones, calcareous materials and brown podzolic soils, with some acid brown earth. Sandstones are the predominant component. The sandstones in the area let water through easily, which can cause damage. The soil in the area contains iron and aluminium compounds that move downwards. A major fault also crosses the tunnel, which can create stress concentrations and water/mineral passages. The above components provide the geological context and characteristics of the area.

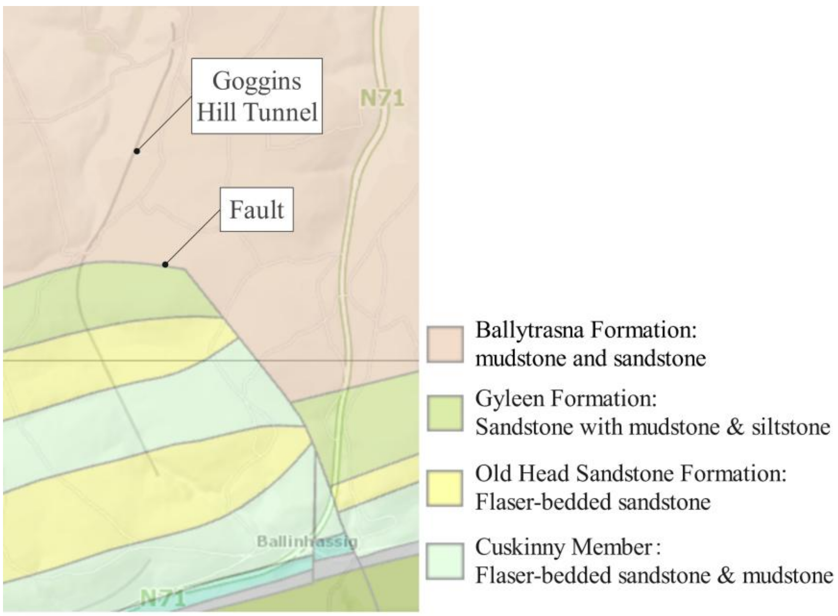

Figure 5-9 Geological context near Goggins Hill Tunnel [212].

The tunnel is at risk from weathering, erosion, and chemical reactions due to the above geology. Scaling of mineral deposits on the tunnel lining reduces the water flow capacity behind the lining and can lead to blockages. The fault perpendicular to the tunnel axis creates shear zones, which further weakens the rock and soil and reduces their ability to withstand external forces. Water ingress along fault planes can saturate the surrounding rock and soil, making the tunnel more susceptible to damage from soil stress and groundwater flow.

Observation on this railway tunnel deterioration mechanism is made mainly from the surface defect distribution on orthomosaics. From Figure 5-6, defects observed in the tunnel interior are likely caused by water leakage, leading to prevalent salt seepage and additional contamination, resulting in white and black deposits on the tunnel lining. As sunlight diminishes and vegetation's impact on the tunnel interior decreases, the growth of salt deposits more becomes prominent and unaffected by vegetation coverage.

(1) West side

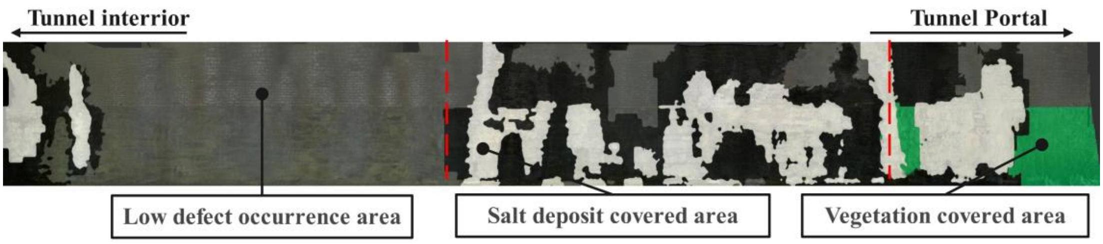

(2) East side

Figure 5-10 Salt deposit segmentation of surface type based on colours of the tunnel lining (green: moss, grey: original wall texture, black: soot or contaminated minerals, white: calcium/magnesium mineral, and unmasked black background).

With regard to construction management, the PMPP-SDI method provides a basis for classifying the condition of the structure. It can be reasonably assumed that the tunnel interior, situated more than 20 meters away from the tunnel entrance, exhibits superior water resistance. Conversely, tunnel linings located closer to the tunnel port, tunnel linings are more vulnerable to sunlight and precipitation. The application of UAV automatic inspection could be expanded to cover a greater length of the tunnel surface, thereby facilitating the observation of the tunnel surface in a fast, continuous and comprehensive manner, as well as long-term monitoring.

5.6 Summary

In summary, the proposed PMPP-SDI method for UAV tunnel inspections exhibits its potential through experiments conducted in dark and straight tunnel environments. It outperforms previous research [213] in UAV structural inspections by achieving the following:

(1) This chapter verified the effectiveness of the automatic PMPP-SDI in areas with GNSS and luminance limitations. A field test was conducted in the Goggins Hill railway tunnel, and it demonstrated the effectiveness and robustness of the proposed method. With a 0.3 m standard controlling error over the range of 38 m in specific scenarios, the automated control significantly reduces subjectivity and operational instability, resulting in considerable time and labour savings compared to traditional manual inspection methods.

(2) The drone tunnel inspection model, despite a geometric error of up to 1%, has been successfully reconstructed from field data. Given field measurements from LR to validate the data quality, the model is found to be more suited for defect analysis rather than tunnel deformation. It delivers accuracy within millimetres for surface defects and within centimetres for tunnel dimensions. While UAV inspection provides data continuity compared to point-based sensors, its accuracy and the brick-and-stone nature

of this tunnel make deformation inspection less interesting. Besides, due to the absence of UAV inspection regulations, the measurements on deformation are not yet sufficient to provide a definitive basis for maintenance.

(3) The tunnel linings are then divided into distinct zones for deterioration mechanism study. These distinct zones are segmented by different surface colours, including white for various salt deposits, green for vegetation etc. along the tunnel axis. The tunnel portal is found to be more affected by various deposits, while closer to the entrance, vegetation coverage is more dominant.

(4) The railway tunnel deterioration in this field test is mainly water and salt ingress from observations of surface defects. This deterioration is mainly attributed to the geological condition from three aspects, soil type, water condition and fault formation. Concretely, the reduced water flow capacity orients from drainage being blocked by the scaling of mineral deposits, the stress concentration zone orients from the fault, and the weakening of soil and rock supporting ability orients from saturation in soil from water ingress.

These findings highlight the potential of UAV technology in industrial applications and emphasize the importance of implementing efficient image-processing techniques. Based upon this study, our next field test will demonstrate the replicability of the PMPP-SDI method in the more structurally complex underground space of the Dublin Port Tunnel. It will address challenges related to unfavourable structural conditions and luminance issues, thus overcoming navigation difficulties effectively. The overall field tests will demonstrate the potential of UAV inspection in various types of tunnels.

6. Field Test in a Road Tunnel

6.1 Introduction

This chapter of the thesis outlines a field test conducted in a complex geometry road tunnel that utilizes the UAV automatic inspection technology to verify the pre-existing and known tunnel deterioration. The test includes an analysis of defects, deformations and deterioration mechanisms. The results of the field test first demonstrate the feasibility and effectiveness of the UAV automatic inspection technology in complex road tunnels. Furthermore, the results provide valuable insights into deterioration identification, as well as supporting previous research on the Twin Tunnel Effect, the VCP effect and the Headwall Effect.

6.2 Engineering background

6.2.1 Dublin Port Tunnel

Dublin Port Tunnel, opened in 2006, serves as a key transportation infrastructure that expands a length of about 4.5km between Dublin Port and Dublin City. It has a variable tunnel periphery, ranging from 10m to 20m, and the tunnel includes two cut-and-cover sections, two bored sections, and one specialized pipe-jacked section under the Dublin-Belfast railway [214]. DPT is structurally comprised of segmental primary lining and in-situ secondary lining and it is a dual-direction twin tunnel consisting of the Northbound Bore (NB) and the Southbound Bore (SB) [215].

6.2.1.1 Tunnel geometry

The inspected section of DPT is a cross-passage twin tunnel section where lining cracking, water leakage and concrete spalling are relatively extensive, compared to other parts of the tunnel [216], as shown in Figure 6-1 (1). These known defects are inherent to the structures including twin bored tunnels, layby tunnels, headwall and VCP, as illustrated in Figure 6-1 (2). The inspection environment of the section features complex geometrical variations along tunnel alignment, posing challenges for UAV inspection route planning and so on.

(1) Tunnel surface defects at UAV inspection area [216]

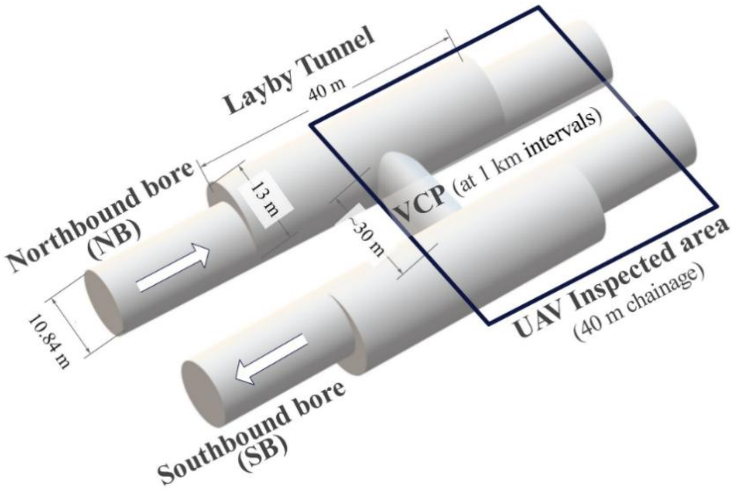

(2) Illustration of the cross-passage twin tunnel section

Figure 6-1 DPT cross-passage twin tunnel section for UAV inspection

The complexity of tunnel geometrical variations poses a challenge to UAV image acquisition, as shown in Figure 6-2. Along the bored tunnel, the circular tunnel is c.a.10

m in internal diameter. Near the start and end of the layby tunnel, there’s an interior periphery change from 10 m to 13 m. Near the VCP where the twin tunnels are connected, the tunnel interior periphery achieves its maximum of 20-40 m. In this condition, the use of UAV enables image collection of 3D components with fewer cameras and more views in DPT than ground vehicles.

(1) Bored tunnel section

(2) Diameter change at layby

(3) Diameter change at VCP

Figure 6-2 Illustration of complex engineering geometry of the DPT section

6.2.1.2 Illumination conditions in DPT

Apart from complex geometry, DPT possesses low-light conditions, unfavourable for UAV inspection. The inconsistent and weak luminance provided by the LEDs is another feature in DPT UAV inspection, as shown in Figure 6-3. DJI manuals require a light intensity of at least 15 lux for reliable UAV navigation. In a tunnel of a close-range inspection environment, an auxiliary light module is employed as an additional source of illumination. The enhanced luminance from the auxiliary light module creates 620 lux at most in the DPT inspection environment for the UAV visual sensors, allowing the production of satisfactory image quality. Due to the structural symmetry of DPT, the area boxed in Figure 6-1 (2) is chosen as the area of interest for UAV inspection where more cracks are observed compared to the opposite symmetrical section.

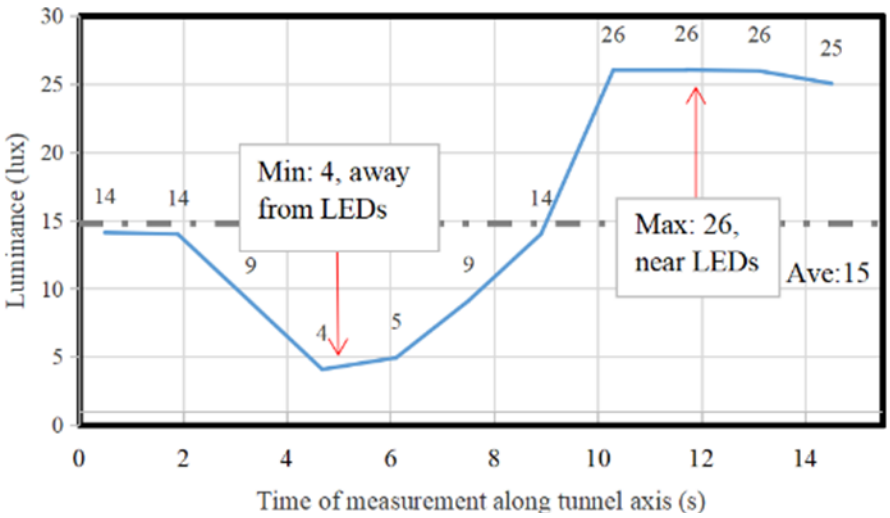

Figure 6-3 Intensity variation of reflective light on tunnel side wall along DPT alignment

6.2.1.3 Research aim

The main objectives of the DPT inspection field test are to evaluate the effectiveness of the UAV inspection method and to assess the health condition of the DPT twin tunnel structure. This paper first investigates the robustness of this navigation method in geometrically complex DPT road tunnels consisting of cross passages, layby sections, headwall, and bored sections, with varying tunnel geometry.

Based on surface defects and deformation analysis, the paper then aims to understand the long-term performance of the cross-passage twin tunnel section, as studies on such behaviour and the effect of VCP and twin tunnel interaction have been limited. An in-depth analysis and quantification of the tunnel defect distribution within the inspection area was carried out to provide information on defect dimensions, locations, density, and severity across the detected region.

Even though previous studies have estimated the tunnel deterioration mechanism from wireless sensor network monitoring [216], an investigation is needed on continuously acquired data to give a more comprehensive picture of the tunnel's long-term performance. Figure 6-4 shows the onsite inspection of the tunnel section using the M2ED UAV. Two example raw images are shown in Figure 6-5.

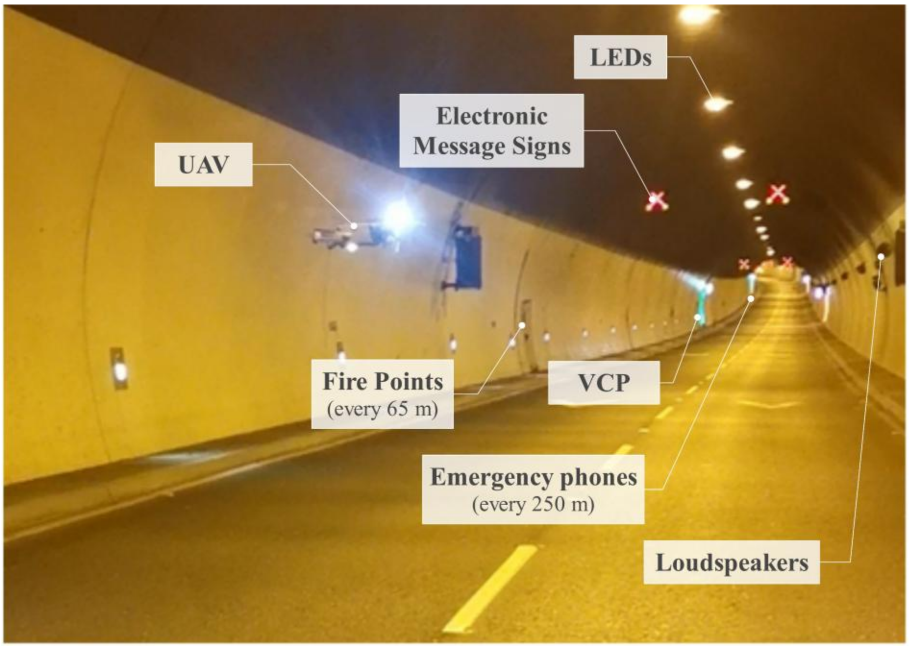

Figure 6-4 Automatic UAV inspection of DPT


Figure 6-5 Example images from raw DPT image dataset

6.2.2 Challenges and solutions for UAV inspection

To enable a cost-effective, efficient, and enhanced monitoring and assessment of the structural health condition of DPT, a reactive UAV-based automatic monitoring and inspection method is employed. The main limitations of the inspection condition for UAVs include a lack of GNSS signal, low light, and complex geometry, rendering precise UAV positioning and data acquisition challenging [217].

One challenge is the VCP existing between twin tunnels, which are designed to meet emergency requirements and facilitate the evacuation of tunnel users and the movement of vehicles. The VCPs complicate the route planning for UAV-based automatic tunnel inspection. In addition, DPT has many facilities on its liner such as signals, signage, fire hydrants, wall-mounted loudspeakers, etc. These factors restrict data collection by methods like rail cars, while UAVs can adapt to such complex environments and collect data on these facilities from multiple views.

Another factor affecting UAV structural health inspection is image processing accuracy. Nevertheless, the advancement of UAV hardware and image-processing algorithms can help enhance tunnel structural health monitoring outcomes with higher definition.

To overcome the limitations and address the challenges in monitoring and inspecting DPT using UAV, this thesis adopts the PMPP-SDI for real-time reactive control in DPT inspection tasks [218]. It enables automated tunnel surface data acquisition, and it strikes a balance between cost and performance. On average, it took 34 minutes to scan one side of the 40-meter tunnel, resulting in over 3 hours for the entire process, including additional time for manual camera operation near the VCP area. While manual inspections could also take several hours, a LiDAR truck can perform LiDAR scanning in just a few minutes.

6.2.3 3D reconstruction of inspection area

This section introduces the model reconstruction results. The visualization of the obtained tunnel model in space is shown in Figure 6-6. The 3D models are created and used for extracting spatial data to study tunnel longitudinal and cross-sectional configuration, and image data are used to study tunnel surface defect distribution. To achieve an accurate visual and inertial model reconstruction, incorporating geofencing points within the tunnel is essential to align the project with real-world conditions, a practice that is particularly relevant in industrial applications.

Figure 6-6 3D model of inspected DPT section (with VCP and layby tunnels)

The extraction of spatial information is crucial in two primary areas: UAV flight trajectory validation for automatic control and assessment of tunnel structural health. Figure 6-7 (1) qualitatively shows the UAV's flight path, which is marked by green dots, aligning with the targeted area. This efficacy of UAV automatic control is further demonstrated by the quantitative analysis of lateral and height control accuracy in tunnels. In addition, spatial information on tunnel linings is extracted to conduct detailed analyses of diameter-variant tunnel geometry.

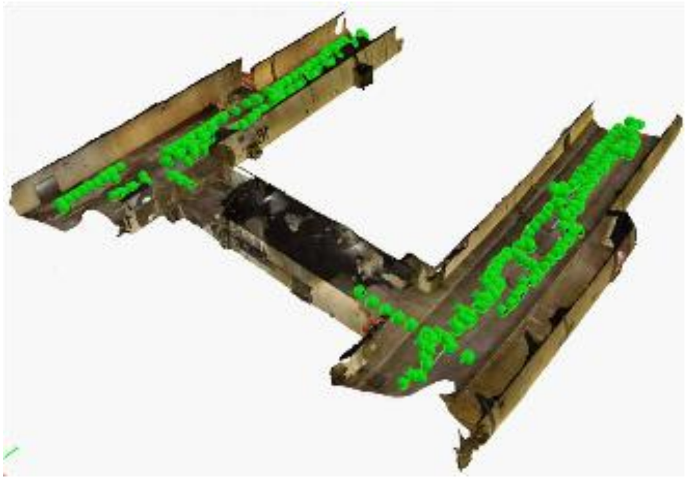

(1) Actual flight trajectory

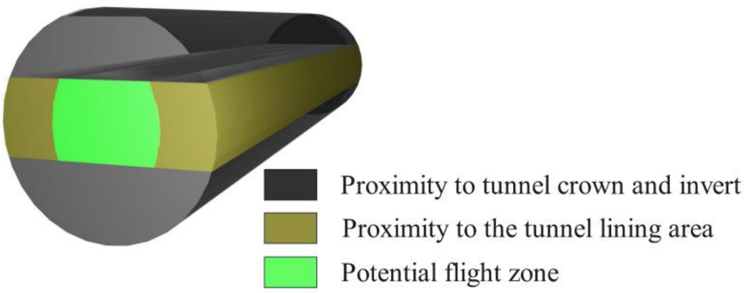

(2) Target flight trajectory

Figure 6-7 Actual and target automated UAV flight trajectory in twin tunnels

The data extraction process is depicted in Figure 6-8. To obtain a comprehensive representation of the geometry across the entire inspection length, cross-sectional contours are extracted at 0.75-metre intervals, as illustrated by the red line in Figure 6-8 (1). The tunnel extraction path is a bundle of cross sections in the vertical direction connected by 0.75m horizontal connections end to end. To study the potential deformation patterns under the influence of VCP, twin tunnel and headwall, 8 cross sections per bore are compared, as demonstrated in Figure 6-8 (2). The selection of cross sections avoids structural abnormalities such as firehose and sump control panel.

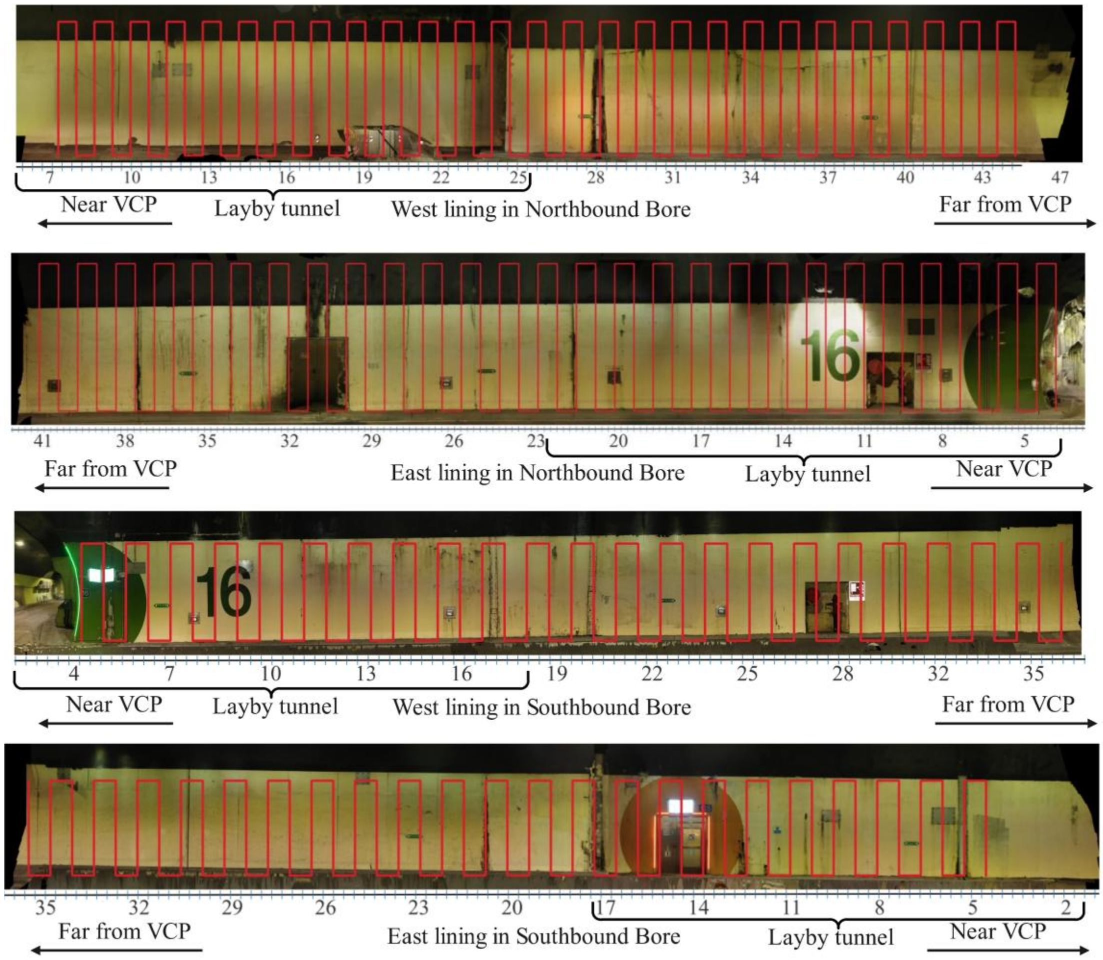

(1) Data extraction in four linings (tunnel mileage starts from VCP and is in the unit m)

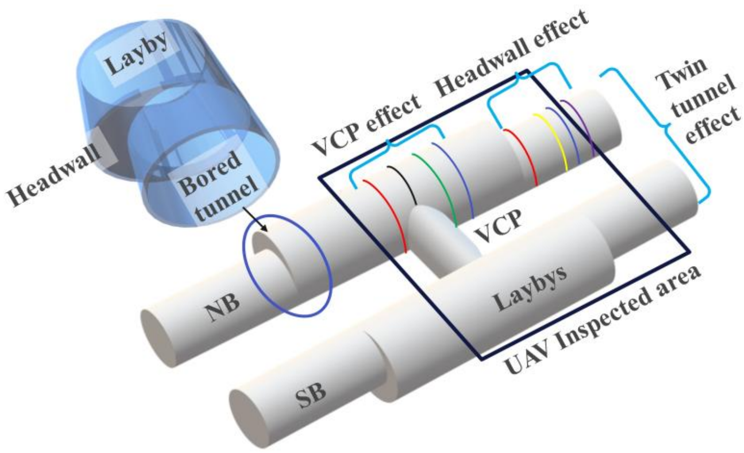

(2) Overview of data extraction at the cross-passage twin tunnel section

Figure 6-8 Cross-section shape extraction in DPT with extraction path in red lines

6.3 Tunnel spatial information

6.3.1 Observations from top view

DSMs from UAV images offer a cheap and spatially continuous way for location monitoring. Figure 6-9(1) gives the extracted spatial locations of all linings presented in the same coordinate system. The top view of the internal periphery of the twin tunnel is shown in Figure 6-9(2). Figure 6-9(2) shows the twin tunnel curvatures generated from the DSMs in both bores. It can be seen the generated tunnel's internal periphery agrees well with the as-built drawings of DPT alignment in the background.

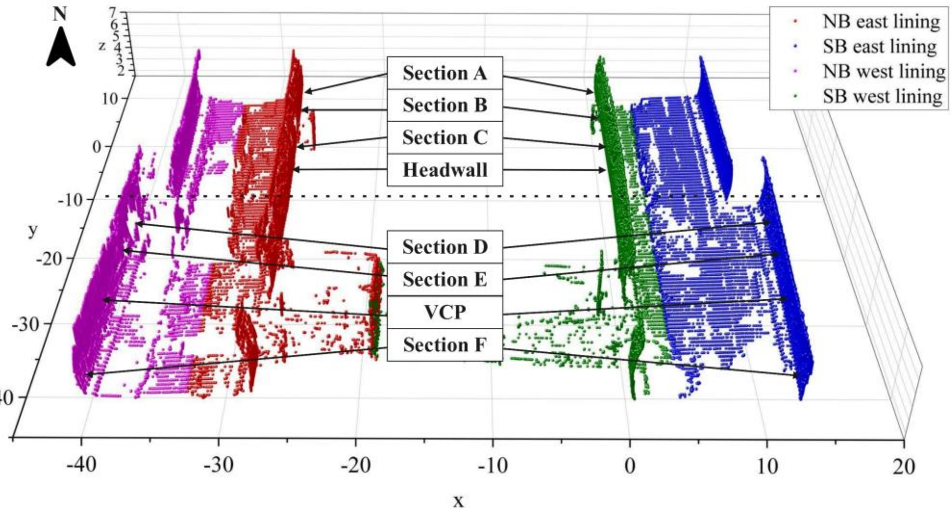

(1) 3D overview of extracted coordinates (m) with key cross-section extraction locations

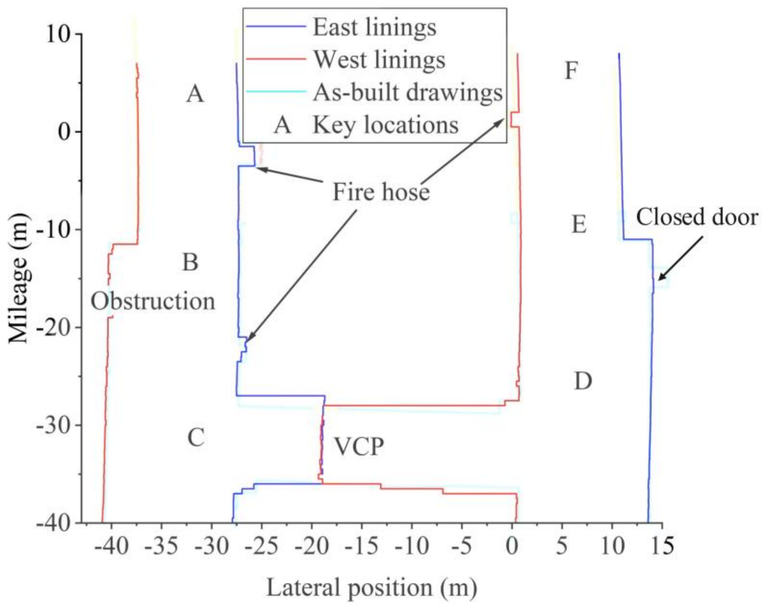

(2) Comparison of tunnel top view from DSM and as-built drawing

Figure 6-9 Spatial information extraction results of DPT inspection

To verify the 3D model reconstruction accuracy, the internal periphery of the tunnel section was measured by a laser rangefinder and then compared with the measurements from the reconstructed model at several key locations, as illustrated in Figure 6-9(2). Table 6-1 presents the comparison between these two sets of data. It can be seen from the data comparison that the reconstruction accuracy allows for very rough deformation trend analysis, similar to the condition in the Goggins Hill Tunnel field test. Some obvious errors appear near the west lining of the layby tunnel of the northbound bore due to obstruction standing near the tunnel linings. The blocking of drone cameras by this obstruction affects the modelling of tunnel linings with flights at different heights. In different flights, obstacles from similar viewpoints also led to some environmental uncertainties resulting in unpredictable noises.

Table 6-1 Interior periphery comparison at key locations of twin tunnels (/m) at around 1.6m height

Tunnel bores	Location	Laser rangefinder	Digital model	Error
Northbound	A (near start)	10.25	10.07	-1.76%
	B (start of layby)	13.30	13.43	0.98%
	C (near VCP)	21.87	21.99	0.55%
Southbound	D (near VCP)	13.24	13.17	-0.53%
	E (end of layby)	10.31	10.25	-0.58%
	F (near end)	10.13	10.16	0.29%

6.3.2 Cross-sectional deformation

6.3.2.1 Observation

Figure 6-9 presents the spatial information extractions of the cross-sections marked in Figure 6-8(2) for tunnel transverse deformation investigation. The noise elimination and smoothing are optimized from computation in Pix4Dmapper. Using blurry and under-lit tunnel images, image processing achieves superior results with a small 1/4 image scale and a large (9×9) sliding window.

According to the technical as-built drawings of DPT in Figure 6-10, the bored tunnel is circular with a radius of 5.145m. The layby tunnel is multi-centre circular, whose inner lining circle has a 5.145m radius, and the outer circle has a 4.491 m radius. Thus, the cross-sectional contours of bored tunnels and outer lining contour of layby tunnels, generated by DSMs, were fitted in circles in Figure 6-10, along with the fitting details.

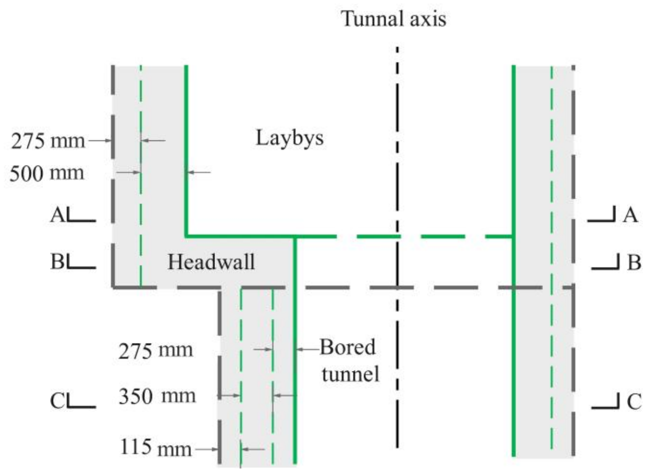

(1) Dimensions of tunnel linings near headwall (top view)

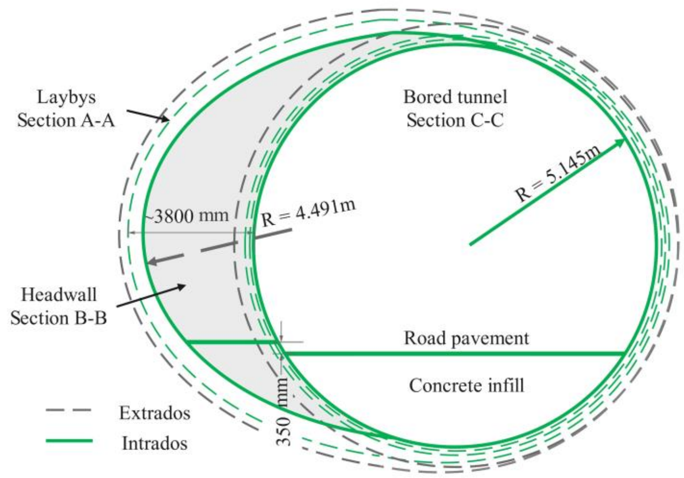

(2) Dimension of cross sections and tunnel diameters (side view)
Figure 6-10 Schematic of layby and bored tunnel geometry

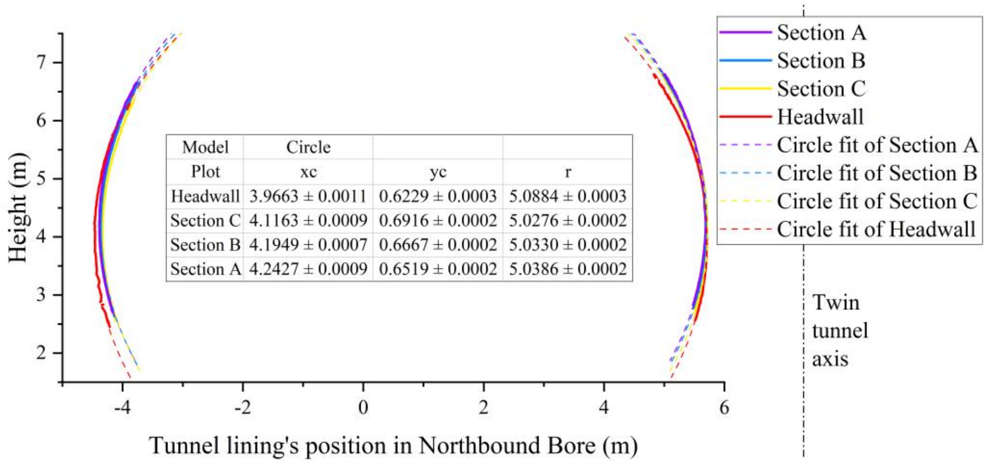

(1) Circular tunnel cross section comparison in NB

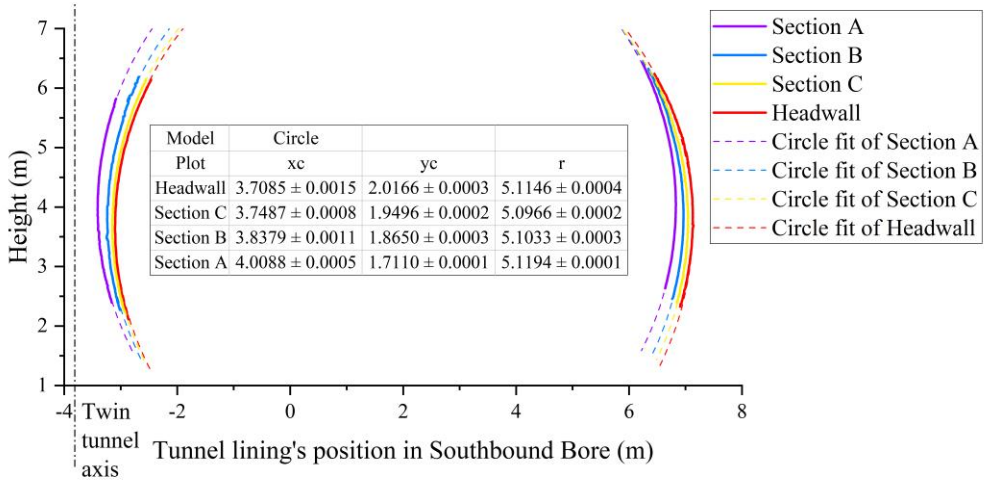

(2) Circular tunnel cross section comparison in SB

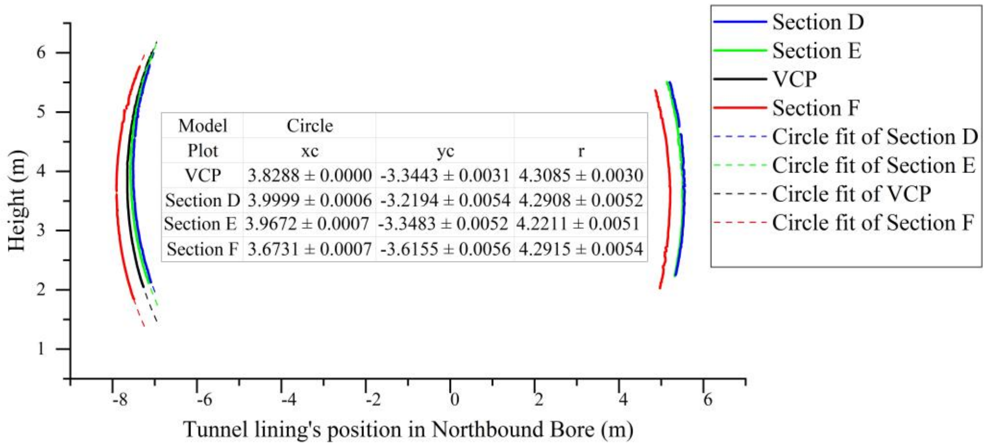

(3) Layby tunnel cross section comparison in NB

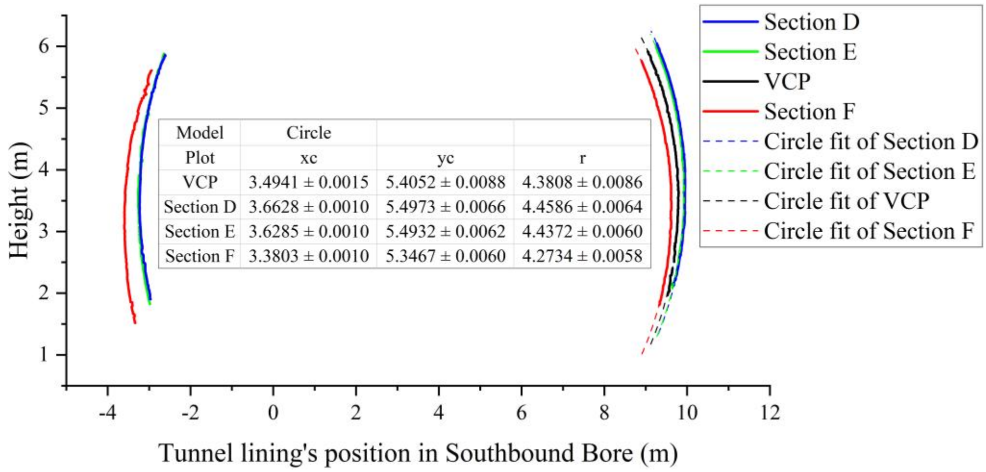

(4) Layby tunnel cross section comparison in SB

Figure 6-11 Cross-sectional spatial information extraction and comparison

Table 6-2 Comparison of radius of the fitted tunnel linings

Group	Fitted radius at marked cross-sections (m)			
Bored tunnel (Internal radius R=5.145m)	Headwall	Section C	Section B	Section A
	5.09 (NB)	5.03	5.03	5.04
	5.11 (SB)	5.10	5.10	5.12
Layby tunnel (Outer radius R=4.491m)	VCP	Section F	Section E	Section D
	4.31 (NB)	4.29	4.22	4.29
	4.38 (SB)	4.27	4.25	4.26

The radii of the fitted circles of the selected cross sections are given in Figure 6-11, and the comparison between the generated radius and the as-built radius of the tunnel sections is given in Table 6-2. The circle fitting of the cross sections has millimetres-level accuracy, but the deviation between the inner width of measured and fitted cross sections is at centimetres-level. This level of error can be attributed to the quality of camera sensors and lack of calibration. While tunnel deformation in crack-densified areas is normally no larger than the centimetres level, the radius in Table 6-2 can't reflect accurate inner width but rather its variation trend over mileage. Observation on tunnel lining deformation trend should be studied qualitatively from the tunnel lining shape.

6.3.2.2 Deformation pattern analysis

When comparing the as-built and generated bored tunnel contours at the marked sections, the fitted headwall section had a radius several millimetres to centimetres larger than the average radius of the three northern bored tunnel sections (Section A, Section B, Section C). This can be attributed to the higher stiffness at the headwall cross section that limits the development of its cross-sectional deformation.

Regarding the contour comparison between as-built and fitted layby sections, the layby sections are all compressed towards the twin tunnel centreline, in consistency with the twin tunnel effect concluded in [216] and illustrated in Figure 6-12 (1). In addition, the fitted VCP section experienced smaller compression compared to other sections (Section D, Section E and Section F). The observation corresponds to the VCP effect summarised in [216], [219] that the small compression at the layby section close to the VCP can be ascribed to the horizontal pushback from VCP, as demonstrated in Figure 6-12 (2).

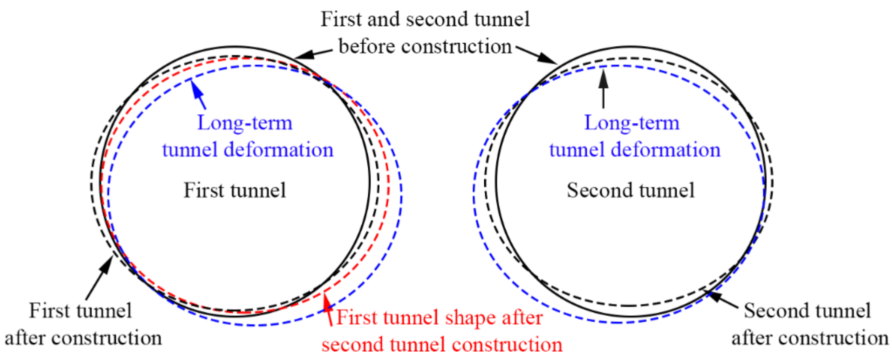

(1) Tunnel deformation under twin tunnel effect ([216])

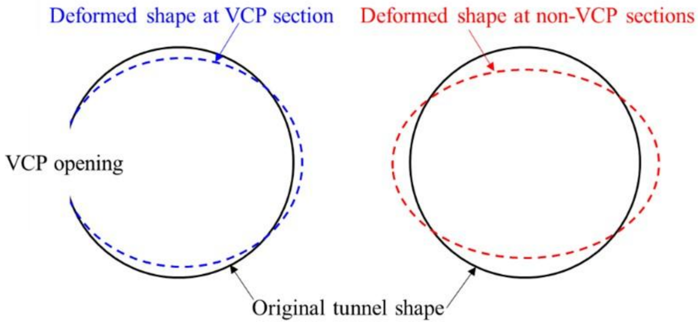

(2) Tunnel deformation under VCP effect (modified from [219])

Figure 6-12 Twin tunnel effect and VCP effect

6.4 Surface defect identification

The UAV orthomosaics and DSMs are generated in pairs. Orthomosaics enable quantifiable defect detection, while researchers using LiDAR and cameras need to fuse the data to achieve the same. The efficiency of image processing also continues to improve with the development of algorithms [157]. Due to the advantages, the following part focuses on knowledge of tunnel deterioration patterns. Some images from handheld camera are used for the reconstruction of the background area for visualization, where the UAV is not supposed to inspect.

6.4.1 Orthomosaic accuracy

The orthomosaics of DPT have a resolution of 1.4mm/pixel for identification and length measurement of cracks with water leakage. Previous studies have analysed the accuracy of 3D UAV model reconstruction. In some studies, a resolution of 0.2mm/pixel for static images was adopted for tunnel lining inspections [157]; and another has a resolution of 20-30 mm/pixel for UAV stitched images for road pavement crack identification [197]. The resolution of this research is satisfactory for major crack and leakage identification in DPT.

Another UAV reconstruction quality assessment metric is the defect reflection level index, such as the metric ‘pavement condition index’ (PCI) for highway surface assessment [179], [220]. This index gives defect identification results along with confidence levels, allowing for a more detailed inspection if a larger unified dataset is generated in further inspections [180].

6.4.2 Defect types

In general, tunnel structural health condition assessment includes inspection of lining cracks, spalling, and water leakage. The acquired UAV data is used to detect and verify the potential defect types and distribution, and this information is used for structural health assessment. Based on the approach described in section 4.4, the orthomosaics of the four tunnel sidewalls at the selected twin tunnel section are generated and displayed in Figure 6-13.

In the post-processing phase, the locations of all cracks and leakage were marked out in red and yellow respectively. Blue rectangles are marked as diameter-variant areas where the headwall connects the layby and bored tunnel, while red rectangles correspond to all layby areas. Figure 6-1 shows the defect types and distributions in the selected section of DPT.

From Figure 6-13 (a), many cracks occur in the middle of the layby enlargement side of the NB (west lining) while the diameter variant area where the headwall is housed sees almost no cracks. Leakage was observed at positive drains located in the bored tunnel. For the east lining of the NB tunnel, there were barely any cracks observed but slight leakage in the layby tunnel area that is far from the VCP, as in Figure 6-13 (b). In Figure 6-13 (c), cracks were observed at the layby tunnel section further away from the VCP. Similarly, Figure 6-13 (d) shows water leakage concentrating at positive drains and some vertical cracks at the north side of the SB east lining.

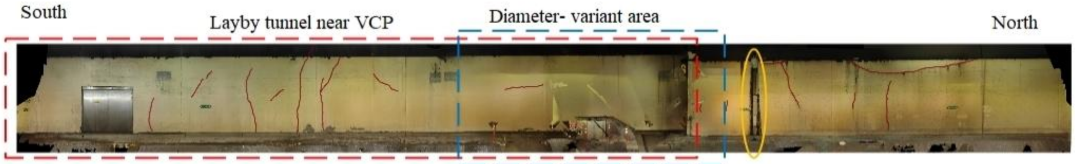

(a) Northbound bore west lining

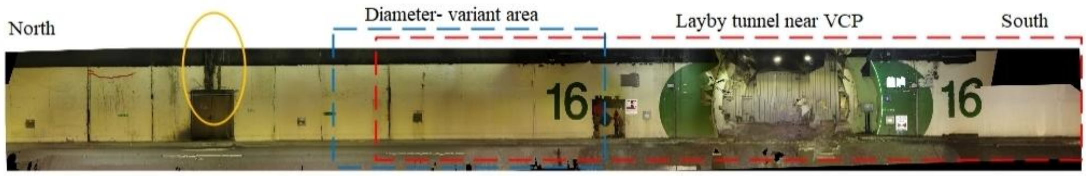

(b) Northbound bore east lining

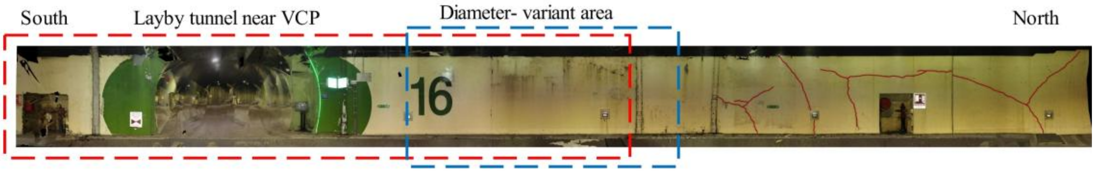

(c) Southbound bore west lining

(d) Southbound bore east lining

Figure 6-13 Defect identification in the DSM from UAV images

Table 6-3 Defect patterns in the selected section of DPT

Defect	Images	Locations	Defect	Images	Locations
Horizontal cracks	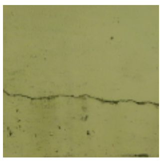	- Middle of the tunnel side wall - Away from VCP	Vertical cracks		- From the tunnel shoulder to the foot
Diagonal cracks		- At various heights - Away from VCP	Water ingress		Tunnel shoulder main/along construction joint.

6.4.3 Defect quantification

6.4.3.1 Crack distribution

Table 6-4 presents the quantification of two major defects (cracks and water leakage), with their number and size. The identification and quantification of defects were conducted by counting the pixels of the area of the defects of interest in the orthomosaics. Major cracks range in length from around 0.85 to 7.2 meters.

Figure 6-13 presents observations that verify the previous finding on the local deterioration patterns of tunnels. The number of cracks observed in diameter-variant areas is notably lower than in other areas, indicating that these areas exhibit greater resistance to deformation. This is attributed to the structural stiffness provided by the headwall, which connects the bored tunnel to the layby tunnel (see grey area in Figure 6-10, with a thickness of 2m).

Table 6-4 Quantification of tunnel defects

Defect type		Location	Length/area
Major cracks	Horizontal crack	SB east lining	2.40m
	Vertical cracks	SB west lining	3.78m, 2.26m, 2.09m (within layby) 0.84m, 3.33m 3.21m (outside layby)
	Diagonal cracks		2.16m, 1.26m (within layby) 2.71m (outside layby)
	Horizontal cracks		2.14m (within layby) 1.92m 7.13m (outside layby)
	Vertical cracks	NB east lining	2.24m, 2.46 m (outside layby)
	Horizontal cracks	NB west lining	1.44m, 5.43m
	Diagonal cracks		2.13m, 1.81m, 2.73m, 4.14m, 2.84m
	Vertical crack		1.82m
Water leakage		SB east lining	1.07m×2.33m (width/m × height/m)
		SB west lining	0.82m×1.97m
		NB east lining	0.26m×2.69m, 0.41m×0.67m, 0.35m×0.84m

Figure 6-13 (a) shows that most cracks are concentrated in the central area of the west layby enlargement, with a higher density in contrast to the diameter-variant area in non-VCP sections. This suggests that the strength and stiffness of the lining (due to the tunnel configuration) increased less around the central area of the layby tunnel, resulting in a greater subsequent increase in tunnel internal forces and deformation.

Figure 6-13 (b) and (c) demonstrate that the area surrounding the VCP in the layby tunnel exhibits minimal cracking, in contrast to the other side of the same bore, as shown in Figure 6-13 (a) and (d), respectively. This phenomenon may be attributed to the pushback from the VCP at the layby-VCP conjunction area, which results in strengthening and stiffening in the lateral compression responses at the layby-VCP connection, as illustrated by Figure 6-12 (2).

Meanwhile, the defect distribution patterns give evidence to infer the tunnel's deterioration mode. It's noted that NB tunnel linings generally have more cracks than SB ones. The underlying mechanism may be attributed to the presence of a maintenance tunnel, which weakened the ground arching for NB lining as illustrated in Figure 6-14 [221]. In Figure 6-13 (a), most of the lining cracks are vertical cracks while some as diagonal cracks [222], in line with previous findings that vertical cracks are the dominant type of tunnel cracks [223], [224]. Furthermore, the west linings of both NB and SB tunnels (Figure 6-13 (a) and (c)) exhibit a higher crack density than the east linings (Figure 6-13 (b) and (d)). These vertical crack distributions in the west & east linings are most likely associated with the longitudinal tunnel bending deformation mode [216]. Figure 18 illustrates that the curved tunnel geometry results in tension on the east side of the linings of both the NB and SB tunnels. The red, yellow and green arrows indicate the inferred relative density of crack defects on the concrete surface, which is high, middle and low occurrence respectively.

In summary, crack distribution can be employed to infer and validate the tunnel deformation mode. Firstly, the headwall effect, layby effect and VCP effect have been validated. The distribution of cracks appears to be more prevalent in the NB than in the SB, and more in the west linings than the east linings. These observations may be attributed to the weakened ground arching for NB and weaker resistance to tension on west linings due to the tunnel longitudinal bending mode. Additionally, it's possible that the observed asymmetric crack distribution may also be attributed to the combined effect of the tunnel structure configuration, local geological variability, a slightly earlier construction time of NB than SB and VCP, and other factors. Further research would necessitate a more comprehensive understanding of these factors to confirm their role in this phenomenon.

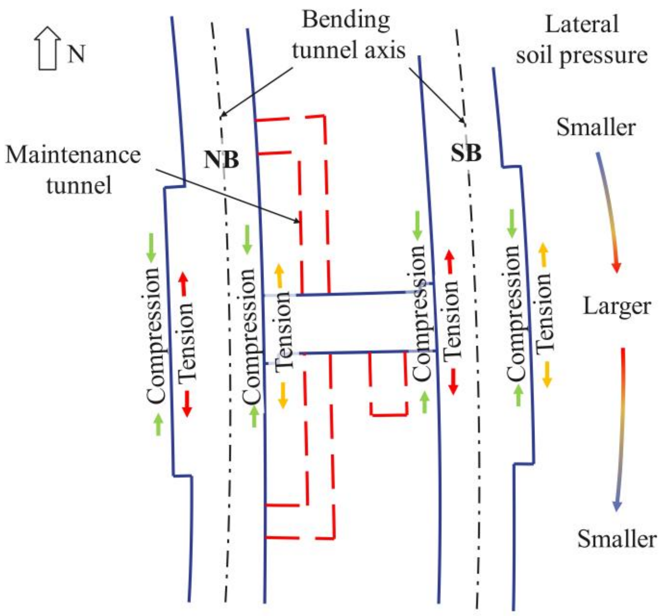

Figure 6-14 Schematic of the tunnel construction plan

6.4.3.2 Water leakage

The quantification of water leakage with their number and size is presented in Table 6-4. Regarding water leakage in DPT, maintenance records indicate greater hydraulic deterioration in the northern part of the tunnel, as exemplified by the orthomosaics in Figure 6-13. Water leakage penetrates the tunnel lining through various channels, such as positive drains, construction joints, and lining cracks. The leakage of groundwater into the tunnel comes with intruding dark ground particles, indicating ground erosion and/or weathering behind the tunnel lining [216].

Despite that there is no clear pattern of water leakage distribution within the inspected area in Figure 6-8, the presence of progressive water leakage, together with the indicative ground erosion/weathering, leads to a decrease in the strength and mechanical properties of rock masses, and an increase in ground pressure acting on tunnel lining. This means that an increasing tunnel internal forces and deformation is imminent. In the long term, the propagation of concrete cracks aggravates water leakage (i.e., a growing amount of water leakage into the tunnels), and in turn, the development of water infiltration also exacerbates lining cracking, contributing to an increasing tunnel deformation [216].

(1) From lining cracks (2) From positive drains (3) Through construction joints

Figure 6-15 Water leakage example in orthomosaics

In summary, the quantification of lining cracks shows that the diameter-variant area sees a scarce number of cracks due to its higher stiffness than the surrounding areas, the concentration of cracks in the middle of NB west lining is associated with the VCP effect, and the non-presence of cracks around the layby-VCP conjunction area could be attributed to the strengthening/stiffening in lateral compression responses at the conjunction. In comparison, the quantification of water leakage shows no clear pattern of distribution within the inspected area, but such leakage mainly comes from construction joints, cracks, and drains.

6.5 Summary

This research has undertaken an automated inspection of a cross-passage twin tunnel section with layby enlargement. The proposed UAV inspection method uses UAV-captured images for the assessment of structural health conditions, particularly structural deformation and surface defects. The novelty of this word is in its successful application of a workflow for data interpretation, which uses DSMs to analyse tunnel deformation and orthomosaics for tunnel lining defect quantification. In summary, the primary discoveries and contributions of this paper can be listed as follows:

(1) The proposed automated image acquisition methodology PMPP-SDI in UAV control was validated during the inspection task in the diameter-variant cross-passage twin tunnel section, demonstrating the method's efficacy across a comprehensive spectrum of inspection conditions. The accuracy of lateral and height control is 0.6m and 0.1m, respectively.

(2) The comprehensive image processing workflow enables the extraction of tunnel configuration data from digital surface models (DSMs) and the identification of tunnel lining defects from orthomosaics. A comparison between the profiles in DSMs and the as-built lining profiles showed that (i) the deformation observed at the headwall was less significant than in other sections due to its higher stiffness, which limits the development of cross-sectional deformation; (ii) the layby sections were all compressed towards the twin tunnel centreline due to the effect of twin tunnel interaction; (iii) the fitted VCP section experienced a smaller degree of compression compared to other sections (i.e., Section D, Section E and Section F), which corresponds to the VCP effect

(horizontal pushback from VCP). More detailed analysis with better accuracy may be achieved through a geofenced model with location information from infrastructures.

(3) The orthomosaics revealed two main types of tunnel defects: lining cracks and water leakage. The quantification of lining cracks demonstrates the headwall effect, that is, fewer cracks develop in diameter-variant areas due to the higher structural stiffness because of the thickened headwall. The layby effect exhibits a higher density of cracks in the central area of the layby enlargement than in the other layby areas due to less strengthening in the area. The VCP effect shows an absence of cracks in the NB east lining and SB west lining around the layby-VCP conjunction area, in comparison to the opposite side of the same tunnel (NB west lining and SB east lining) due to strengthening/stiffening in lateral compression responses at layby-VCP connection. The vertical cracks are dominant in the west lining of NB, and they are likely to be associated with the differential deformation of the tunnel section induced by longitudinal bending. The greater number of cracks in NB linings than those in SB linings might be related to the additional maintenance tunnel that weakens the ground arching.

(4) In contrast, the quantification of water leakage shows no discernible pattern of distribution within the inspected area. However, it was observed that such water leakage is primarily attributable to construction joints, lining cracks and tunnel drains.

(5) The limitations of this research include the cm-level accuracy in tunnel configuration extraction and the lack of a comprehensive understanding of multiple tunnel deterioration factors. The former limits the certainty of quantification of tunnel deformation based on UAV images. Further improvement in inspection accuracy could be achieved by using a total station to provide a calibration basis. Otherwise, UAV is just a secondary method to provide supplementary deformation information for more accurate inspection. Further improvement in the understanding of tunnel deterioration

mode will require more multi-method measurements.

7. Conclusion and future work

7.1 Introduction

Regular inspection of tunnel structures is essential for asset maintenance and relevant repairs to ensure structural safety and serviceability. In general, the structural health inspection of tunnels includes defects such as surface cracks, concrete spalling, water leakage and drainage system blockage. Traditionally, tunnels were mainly inspected by manual methods that are time-consuming, labour-intensive, subjective, and costly. The emergence of more advanced technologies, like automated robots, complements the manual inspection of large-scale geotechnical assets. One of the promising robotic tools for automatic tunnel inspection and assessment is UAV, featuring low equipment cost, no installation and de-installation, non-destructive inspection, continuous measurements at structural scale, automated control, and versatility of image-based data processing. This robotic approach makes long-term subsurface structural health monitoring a possibility, enabling automatic identification of structural damage and aiding in gaining insight into the deterioration mechanism of tunnel assets. Image data acquisition is possible at a low cost, together with the adaptability to different types of geotechnical assets, such as shafts, tunnels, and pipelines.

However, GNSS-independent UAV sensing and autonomous navigation research are limited in small UAVs, static data acquisition, and inside well-lit environments and require human supervision in the loop. Now automatic flight methods are improved in all aspects, including visual localization, pose estimation, obstacle avoidance, path planning, and scene recognition. Challenges and opportunities in this research field include the development of sensors and unmanned systems for large-range operational requirements, and the adaptation to dynamic scenarios, such as luminance variations, and structural change in environments. To address the above issues, this research developed an automatic UAV tunnel inspection method and verified its effectiveness through field tests.

7.2 Summary of research

At the outset of this study, several key research questions were posed regarding the potential application of UAV inspection to tunnel inspection tasks. This section will present a summary of the responses to these questions.

***Research question 1*: what, how and to what extent do the tunnel environments impact the application of UAV in tunnel infrastructure inspection?**

Tunnel environments can significantly impact the high-quality UAV data acquisition in tunnel infrastructure inspection. This research pointed out the three aspects that negatively impact the UAV tunnel inspection, that is lighting conditions, GPS availability, and flight path obstruction. Lighting conditions in tunnels often have low light conditions, which can make it challenging for drones to collect image data. This can affect the quality of the inspection as clear and well-lit images are crucial for identifying structural issues. GPS availability in tunnels, unlike open-air environments, is typically a GPS-denied environment. This lack of GPS signal can decrease drone manipulation precision and cause automatic flight interference, making it difficult for the UAV to navigate accurately within the tunnel. Flight path restrictions are often a result of the tunnel geometry, which can interfere with the UAV's flight path. The air turbulence in confined tunnels can affect the UAV's ability to maintain a steady and controlled flight, placing additional demands on the UAV's weight for a thorough and accurate inspection. The close proximity of the flight path to the inspected surface also means that data processing takes place in 3D space, with more distortion than on the road surface and terrain reconstruction, which takes place almost entirely in 2D space.

Despite these challenges, technological advancements are enabling more effective use of UAVs in automatic tunnel inspections. The UAV spotlight module provides sufficient light for navigation and data acquisition. A review of the literature in chapters 2 and 3 also indicates that multi-sensor fusion can enhance localisation accuracy in low-luminance and GNSS-denied underground conditions. This is achieved using complementary sensors such as optical and LiDAR sensors, and multi-cameras. To address the effect of weak textures on localisation, learning-based algorithms further enhance the depth perception of monocular sensors. CV-based navigation algorithms are capable of effective navigation in complex 3D spaces. In theory, DRL can offer a depth map; however, its wide application is limited by its adaptability and training cost in complex unknown environments.

In conclusion, while tunnel environments do present unique challenges for the application of UAVs in tunnel infrastructure inspection, ongoing technological advancements are helping to mitigate these issues and enhance the effectiveness of UAV-based inspections. However, their application might be constrained by the limitations of arithmetic power and the necessity of pre-training in light-weight UAVs in some small-diameter tunnels.

<u>Research question 2</u>: How can UAV tunnel inspection improve its navigational performance in a cost-effective manner? How can they address the various inspection conditions in tunnel environments?

This research proposed in Chapter 4 a methodology called Proximity Move-Pause-Photo for Surface Defect Inspection (PMPP-SDI) for automatic and adaptive UAV tunnel surface defect inspection. It combines reactive navigation strategies with a grid scan pattern to acquire high-quality image data from multiple views and angles. The aim is to achieve a robust and efficient inspection method for image data acquisition and processing in complex and dark tunnel environments, while human pilots are only responsible for the supervision of UAV inspection tasks. The choosing of methodology is highly related to the limitation of computational power on the MSDK.

This proposed method adopts the visual positioning and predefined reactive controlling code on MSDK to improve UAV navigation. As the majority of the navigation methodologies outlined in Chapters 2 and 3 necessitate the carriage of substantial payloads such as additional sensors and onboard computers, it may render them unsuitable for small-dimension or geometrically complex tunnels, where heavier UAVs experience greater air turbulence and flight instability. The preprogrammed codes with visual positioning in tunnels, in contrast, are more convenient as the tunnel has a semi-known cylinder geometry. To maintain consistent image quality, the UAV could be guided along a route by maintaining a constant horizontal distance from the tunnel lining. Consequently, this research employs MSDK to achieve a balance between drone behaviour and the computational cost on board.

The proposed method also gives the UAV adaptability in various tunnels by including a vision-based autonomous inspection framework for drones to switch to the UAV navigation route. This allows the drone to automatically fly along a predefined route in unknown and dynamic tunnel environments while continuously capturing images of the tunnel surface. The MSDK can adjust drone parameters (e.g. overlap rate, inspection area, heading, and flight direction between video frames) for different underground infrastructure conditions.

Research question 3**: What potential outcomes could have been achieved through the automatic UAV data processing process?**

The automatic UAV data processing process in tunnel inspections could potentially achieve several outcomes:

1. 3D model creation: The data processing workflow initially produces 3D models utilising Pix4Dmapper. The accuracy of these models is verified by comparing the shape of the linings between the tunnel model and the design. The quality of 3D models is improved with AI-trained denoise modules. These models include complete tunnel scenes and surface details, which produce DSM and orthomosaics for further analysis of structural condition assessment.

2. Flight routine examination: The process examines the results of the field test flight routine by retrieving spatial information from DSMs. The data extraction uses geographical information reading software Q-GIS. This allows for the comparison of the designated routine with the actual routine over the inspection length.

3. Surface defect detection and verification: The orthomosaics generated from the organised image dataset can be used for surface defect identification. The stitched tunnel lining images are processed using various methods, including manual operation, traditional methods, and computer vision techniques. Image segmentation on orthomosaics produces the basis of surface defect (cracks, water leakage or spalling) distribution and quantification at pixel-level or millimetre-level. Distinct defect zones are also categorized. This categorization allows for the verification of pre-existing observations and provides complementary information for tunnel deterioration analysis. Machine learning algorithms trained with defect or crack pattern-aware data enable reliable automatic defect identification and quantification.

4. Dimension extraction: UAV infrastructure inspection compares the as-built infrastructure information with the extracted information from the DSM. The extraction of dimensions such as the cross-sectional area, diameter, length, slope, and curvature of the tunnel is of interest. These dimensions form the basis of an infrastructure’s condition assessment, helping to identify potential issues and establish necessary corrective actions.

At the current stage, UAV tunnel inspection is still a developing application, lacking the industry experience and regulatory standards to back up standalone UAV inspections. It complements, rather than replaces, existing manual inspection methods in tunnel deterioration analysis. There is significant room for development in UAV tunnel image processing to improve accuracy. Future research could focus on improving the quality of UAV image data, processing images within 3D structures, reducing noise in dim images and improving performance for tunnel inspection. With more advanced hardware and further system developments, the technology could lead to more efficient and accurate tunnel inspections.

7.3 Contributions

To address the significant need for tunnel inspection in long-term health assessment, this research proposed a robust and efficient inspection method for image data acquisition and processing, specially designed for complex and dark tunnel environments. Two field tests in railway and road tunnels are performed to validate its effectiveness.

Results answer the question of how stable UAV inspections are and what tunnel deterioration patterns are revealed from the inspections. The navigation is kept along the tunnel surface in an acceptable controlling precision. Corresponding tunnel deterioration observations are obtained with the aid of the digital information from UAV inspection:

(1) The PMPP-SDI applies inspection routes that follow the structure's contours. With a 0.3 m standard controlling error over the range of 38 m in a railway tunnel, and lateral and height control is 0.6m and 0.1m in a road tunnel, the automated control validates its adaptability in dark and geometrically complex structures. The UAV inspection method outperforms human inspection by significantly reducing subjectivity and

operational instability.

(2) The Goggins Hill Railway Tunnel linings are under the impact of moisture. Its orthomosaics are divided into distinct zones based on surface colours. The materials on surface linings include vegetation, coal/soot, and mineral deposits. It can be assumed that the tunnel interior, situated more than 20 meters away from the tunnel entrance, exhibits superior water resistance. Conversely, tunnel linings located closer to the tunnel port, tunnel linings are more vulnerable to leakage, sunlight, and precipitation.

(3) The DPT road tunnel linings have deformation and defects due to the geometrical complex structure. The headwall and VCP areas avoid defects (major diagonal crack density) and deformation (variant in centimetre’s level) in their vicinity, while the twin tunnel induces ellipsification in the tunnel cross sections. Consequently, the quantification of lining cracks demonstrates fewer cracks develop in diameter-variant areas due to the higher structural stiffness in the vicinity of diameter-variant areas, which is a consequence of the thickened headwall. The higher density of cracks in the middle of the layby enlargement (VCP section) than in the other layby areas (non-VCP sections) could be attributed to the VCP effect.

(4) Tunnel deterioration mechanisms in DPT are assumed to be due to the combined effect of the tunnel structure configuration, local geological variability, a slightly earlier construction time of NB than SB and VCP, and other factors. The vertical cracks observed in the west lining of NB are likely to be associated with the differential deformation of the tunnel section induced by longitudinal bending. Such tunnel axis bending might trigger stress concentrations and related deterioration in the inner side of tunnel bending. Besides, the greater number of cracks in NB linings than those in SB linings might be related to the additional maintenance tunnel that weakens the ground arching. More detailed analysis with better accuracy may be achieved through a geofenced model with location information from infrastructures.

7.4 Limitations and Recommendations

The proposed method has several limitations despite its strengths. The basic limitation is related to the dependence on adequate luminance conditions for visual navigation and data collection. The largest limitation of UAV inspection is due to the incapability of the camera sensors to catch images in motion and low-light environment, it might lead to lower accuracy compared to LiDAR or total station results. Further research could use a total station for calibration, instead of creating a virtual coordinate system.

Another limitation is the incapability of UAV attitude adjustment over large air turbulence. Given current UAV computational power, this method has some difficulty in performing real-time onboard defect detection and classification. Future work aims to address limitations and enhance performance and applicability using artificial intelligence, focusing on improving control/navigation intelligence, data quality, and defect analysis.

7.5 Final thoughts and implications

The most significant distinction between UAV inspection and other sensor-based inspections is the capability of integrating sensors in a highly versatile platform. UAVs possess the advantage of being programmed for automatic inspection tasks and adaptive routines in various underground structures, including tunnels, shafts, and caverns. However, as a disadvantage, the quality of the resulting dataset is largely dependent on the hardware and data acquisition methodology. This research has managed to conduct the best practices in UAV tunnel lining inspection and integrated the knowledge gained from numerous trials and experiments to create an automatic and adaptable task for UAVs to perform. On the other hand, the development of hardware has consistently proven to be an effective means of updating the research body. At the time when this research commenced, the initial option was the DJI M2ED, and the UAV with better performance has since been released in a new version.

As computer vision continues to evolve, the post-processing phase will become increasingly efficient with the advent of more sophisticated techniques for understanding tunnel-catered model construction and defect identification. This research represents a further step forward from photogrammetry, which primarily focuses on overviews of open areas on 2D planes, to close-range 3D structure reconstruction. One point to note is that, in comparison to the mainstream UAV inspection environment and previous research on similar outdoor buildings and infrastructures, UAVs in tunnels will produce datasets with unfavourable issues, such as obvious blurriness and under-exposure. One possible solution is to use a global window, a small image processing scale, and segmental algorithms to improve the computer's vision. In this way, UAVs can understand defect features in a meaningful way. In the end, through repeated field tests and data interpretation in numerous scenarios, I found that inspecting tunnels with a UAV designed for outdoor tasks is like sending children to a new playground. Once they know the way to correctly understand the environment, they will be happy to tell us where the treasures (structural health information) are.

8. Appendices

8.1 Detailed procedure for UAV data acquisition in coastal geoheritage protection

8.1.1 Introduction

UAV-captured imagery plays a pivotal role in documenting various cultural and geological heritage sites [225], [226], [227], [228]. In particular, geoheritage sites, such as rock formations[229] and landscapes, are extensively documented through UAV-based surveys, providing meticulously detailed 3D scenarios [230] crucial for conservation planning. Additionally, UAV surveys contribute significantly to the documentation and analysis of delicate locales like rock art [231] and historic buildings [232], [233], supporting researchers, conservators, and governmental organizations such as the British Geological Survey (BGS) [234] in their preservation efforts.

During the COVID-19 pandemic, virtual tours have emerged as practical substitutes for experiencing geological heritage sites [235], [236], [237], providing immersive encounters and heightening public consciousness of their importance[238]. Virtual reality models, facilitated by drone-captured imagery, play a pivotal role in promoting tourism, advancing geological research, and supporting conservation initiatives [239]. Drones facilitate rapid image capture, real-time monitoring, online presentations [240], [241], and hazard assessment, with their manoeuvrability [242] and endurance making them invaluable tools for site inspection and heritage mapping [243].

This appendix serves as a detailed guide to UAV data acquisition procedures for coastal geoheritage protection, utilizing UAV automatic inspection technology in open-air environments. Unlike traditional geotechnical studies, which often necessitate invasive land excavation or drilling, drones serve as non-invasive tools. Covering flight planning, UAV setup, data collection, and post-processing, it showcases UAVs' capacity to access previously inaccessible elevated or remote locations [244] and create virtual reality scenarios for enhanced geological feature visualization and analysis. The appendix emphasizes the significance of UAVs in safeguarding coastal geoheritage, showcasing their cost-effectiveness and effectiveness in gathering top-tier data to bolster conservation and management endeavours.

The following part presents a field inspection within a coastal geopark, showcasing the innovative use of UAV technology to acquire images for heritage conservation and tourism promotion. It highlights the role of UAVs in documenting geological features, historical mining sites, and inaccessible coastal areas, contributing to the preservation and promotion of geological heritage.

8.1.2 UAV coastal inspection procedures

The Copper Coast UNESCO Global Geopark, formed through Ordovician era (460mya) underwater volcanic eruptions and intrusions and shaped by more recent glacial activity during the last Irish glacial maximum (circa 15ka bp), presents a unique geological landscape characterized by coastal sandy beaches running alongside imposing cliffs[245], [246], [247]. Within this expanse, three distinct beaches featuring geological heritage sites stand out: Tankardstown Engine House, Trá na mBó, and Ballydowane. Notably, Ballydowane beach exhibits a heightened susceptibility to visible rockfalls, while also featuring a sea stack beyond the shoreline which displays clear signs of human excavation. This particular sea stack is situated in a remote and challenging location, rendering both access and photographic documentation difficult. As part of the Geopark’s requirement to conduct coastal inspection and geohazard monitoring, capturing video footage of these features was essential. The distance between the cliffs and the sea surface varies, spanning from 5 to 30 meters, owing to the alternating high and low tide cycles, each lasting four hours and recurring twice daily. Adhering to safety protocols, the UAV maintained a horizontal clearance greater than its flight height.

To capture the scene details of the immersive virtual tour drone images for 360° Panoramic images [248]were collected, and to investigate a geological site on the sea a Waypoint mission was used to collect information about a 3D object from a moving drone [249].

8.1.2.1 Methods of 360° Panoramic Image Acquisition

The acquisition of panoramic images was carried out under favourable weather conditions, including low tides, abundant sunlight, and minimal wind, ensuring strong satellite signals. The UAV was operated using the Litchi software, positioned approximately 30 meters away from the cliffs, hovering at an altitude of approximately 20 meters to capture environmental images. The configuration of the image acquisition grid was adjusted to meet specific requirements, typically ranging between 5 to 7 rows and 7 to 8 columns, resulting in a total of 35 to 49 photographs. The entire task was completed in approximately two minutes. Fixed exposure parameters were based on the brightest direction during image capture, ensuring consistent exposure levels, suitability for seamless merging, and the preservation of image details.

8.1.2.2 Methods of Waypoint Flight Image Acquisition

The UAV operation was managed through Litchi software, with the UAV following a predetermined sequence of waypoints defined by GPS coordinates and initial take-off altitude for navigation to points of interest (Figure 8-1). The UAV executed predefined filming manoeuvres at the commencement and conclusion of each waypoint. The GPS localization accuracy was approximately within a 3-meter radius. The UAV captured a one-minute video by circumnavigating a 4-meter-high sea stack feature, maintaining a horizontal distance of 15 meters, while alternating between altitudes ranging from 10 to 20 meters during flight.

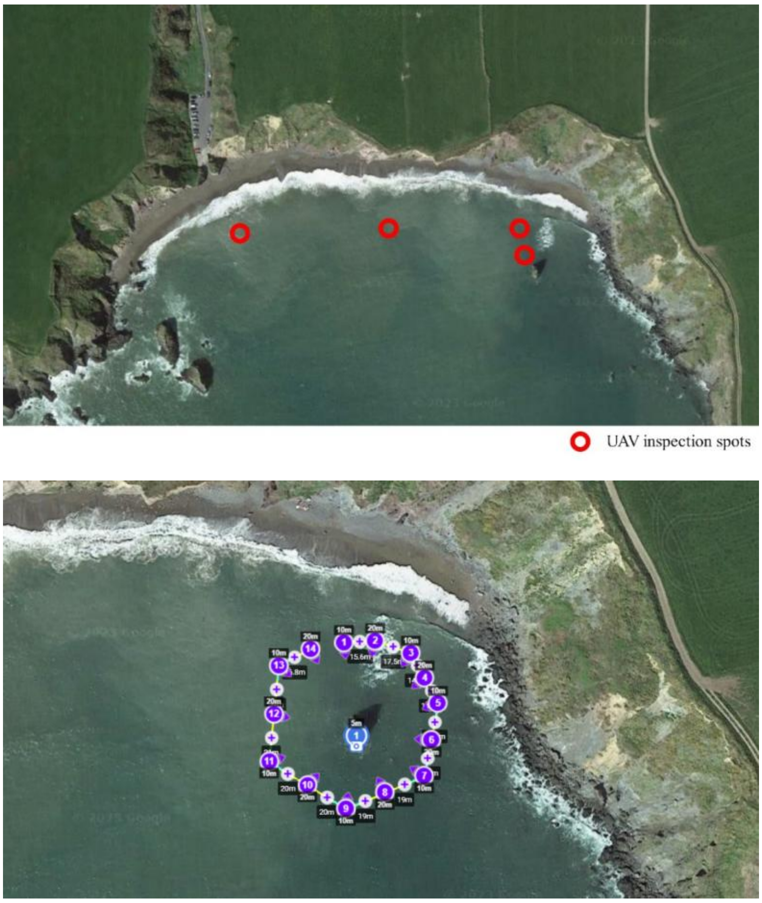

(1)

(2)

Figure 8-1 (1) Locations for collecting panoramic image data (2) Stereoscopic image collection points for waypoint missions

8.1.2.3 Image Stitching Methods

8.1.2.3.1 Image Assessment

The process of panoramic image stitching enables the organization of UAV-captured images for online presentations. To ensure seamless stitching, it is imperative that these images maintain consistent exposure levels and encompass enough static features for alignment. Capturing the images as close to the shoreline as possible during low tide minimizes the presence of wave textures in the image set, facilitating the subsequent image stitching process. The drone collected a total of 1,098 photos, occupying 7.38 gigabytes of storage, along with a video utilizing 0.78 gigabytes of storage. These files were examined and stored on Google Drive (accessible at Google Drive). It is worth noting that images taken in GPS-identical open spaces may undergo texture changes over a short period of time. Consequently, the same locations can be revisited during subsequent flights for the purpose of long-term monitoring.

8.1.2.3.2 Image Alignment and Stitching

The PTGUI software is employed for image stitching. Image alignment is based on the principle of comparing scenic images and matching the corresponding textures. Using the collected data, 23 panoramas were created from these photos utilizing PTGui. From the resulting panoramas, the top 2, 4, and 4 were selected for Tankarzetown Engine House, Trá na mBó, and Ballydowane, respectively.

8.1.2.3.3 Image Enhancement (Sky Patching)

The creation of a complete 360-degree panoramic image involves a technique known as "sky patching." This method entails replacing any black portions within the image with content recognition, typically accomplished using software such as Adobe Photoshop. The replacement is positioned in correspondence with the central region of the image captured by the UAV.

8.1.2.3.4 Image Export

Stitched 360-degree panoramic images of the coastal area are exported (Figure 8-2). These images encompass all the necessary information for creating a comprehensive panorama.


(1)
(2)

Figure 8-2 Stitched 360 panoramas for virtual tour

8.1.3 Virtual tour and geological assessment

8.1.3.1 Virtual tour displays

Images captured by drones are used to create virtual tours, providing an immersive virtual travel experience for remote visitors. From UAV images, an online draft of a VR tourism presentation (Figure 8-3) was designated for tourism promotion, which can be accessed at https://coppercoastgeopark.com/copper-coast-virtual-field-trip/. To create the tour the images were analysed by an expert in the local geological heritage and annotated with informational text and images to communicate the geological heritage to viewers.

The use of displays can enhance the visibility of geological [250]and mining heritage sites [245], [251], which in turn can attract more tourists. Some other potential benefits include convenience in environmental monitoring and attraction management. For example, imagery data can help to monitor environmental changes in coastal geological heritage areas, or better understand, protect, and maintain this geological heritage.

(1)

(2)

Figure 8-3 An online example of interactive VR tours containing (1) geological information and (2) site information

8.1.3.2 Description of geological heritage features

By analysing high-resolution images of geological heritage areas, their current state can be assessed, including cliff surface texture and rock weathering. These assessments are essential for the conservation and management of the geological heritage. Table 8-1 is used to summarize geological features, including rock categories and geological changes:

Table 8-1 Observed geological features and locations

Rock categories	Igneous rock (Rhyolite, columnar Rhyolite, Andesite, Basalt other intermediate and mafic lithologies)	Cliff West (Tankardstown), Cliff East (Tankardstown), Cliff west (Trá na mBó)
	Sedimentary rock (red sandstone, conglomerate, and Holocene era	Cliff east (Trá na mBó), Ballydowane, Helvic Head, Comeragh Mountains

	glacial sediments)	(Engine house), Stage cove, Cliff East (Trá na mBó)
Geological features	Fluvial sedimentary sequence stratigraphy	Cliff East (Tankardstown), Ballydowane, Tra Na Mbo (east side)
	Mineralisation (Chalcopyrite veins)	Cliff west (Trá na mBó)
	Quartz Deformation – shear zones and brecciated wall rock	Tra Na Mbo (west side)
	Ice-scoured bedrock (silt, sand, gravel)	Stage cove/ Trá na mBó
	Structural features indication plate tectonics - faulting	Cliff east (Trá na mBó), Ballydowane
	Secondary mineralisation (secondary copper minerals: Atacamite, Langite, Connellite)	Stage cove, Trá na mBó
	Artificial (Adits, mine shaft)	Cliff East (Trá na mBó), Ballydowane

In addition, the exploration capabilities of the UAS were demonstrated. Figure 8-4 shows part of the virtual tour obtained by the UAV exploring the possibility of the presence of traces of human mining activities in previously unknown areas. There is a dark coloured sea cave which shows evidence of human extraction in line with the likely appearance of mineralised quartz vein features on the west side in Figure 8-4 (1), whose close-up image is shown in Figure 8-4 (2).

(1) 

(2) 

Figure 8-4 Demonstration of drone photography's capability in exploring remote and inaccessible locations. (1) overview (2) close-up image

8.1.4 Summary

In this part, the utility of drones for collecting aerial images of coastal tourist sites and enabling long-term online tourism presentations was explored, based on insights from the Copper UNESCO Global Geopark. Ideal weather conditions for effective data acquisition include favourable lighting, low tide, minimal wind interference, and robust satellite signal reception. Moreover, proximity to the inner coastline is vital to ensure sufficient static texture for seamless image stitching. The drone-based image collection, including 360° panoramic images, resulted in approximately 8 GB of image and video data.

The geological characteristics of monitoring sites, including Rhyolite, Andesite, Sandstone, and glacial sediments, have been meticulously documented, yielding valuable insights into rock classifications and geological transformations in otherwise inaccessible areas. Notably, the acquisition of this data would not have been feasible without the use of UAVs. This collected information forms the essential bedrock for the development of a VR virtual tour platform, which in turn advances the promotion of geological heritage education. Furthermore, drones have demonstrated their efficacy in exploring remote and challenging terrains, exemplified by their pivotal role in uncovering cave entrances along the rugged outer coastline of Ballydowane.

8.2 Qualifications for tunnel inspection

Below the Table 8-2 is some key information in UAV tunnel inspection application concerning UAV operations.

Table 8-2 Details of Works

Task type:	Tunnel lining crack image collection within the VCP 16 section of DPT
Description of the task/activity:	Open category drone flight within the VCP 16 section of the tunnel. Work includes flight trial and video acquisition of the tunnel wall at VCP16 section of Dublin Tunnel. The basic aim is to test the drone performance under weak GPS, low- luminance and spatial restricted area. The advanced aim is to obtain clear videos that are suitable for post processing, which contain details of crack shape and dimension.
Location	Dublin Tunnel – VCP 16 section (drone flying along the centreline of the cross section in VCP 16)
Key tools:	Key equipment: DJI Mavic 2 Pro (a C2 drone in open category A2) C2 drone is weighted more than 900g but less than 4kg; and A2 category certificate allow for the operation close to people. Certification of theoretical knowledge exam for open category A2 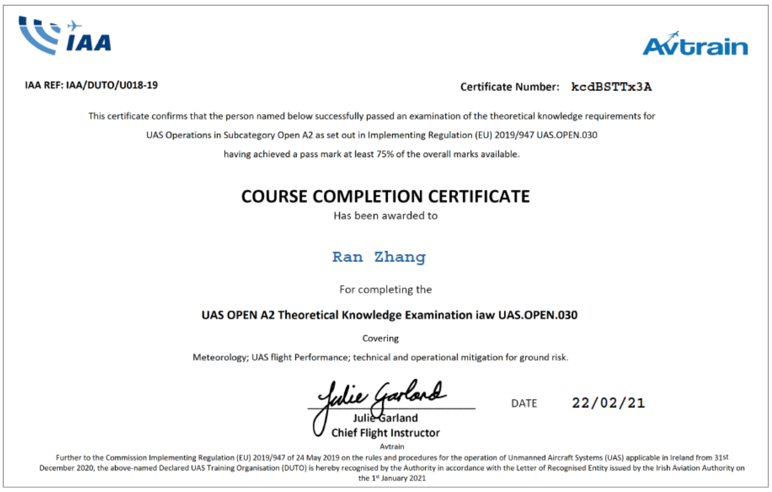 IAA REF: IAA/DUTO/U018-19 Certificate Number: kcdBSTTx3A This certificate confirms that the person named below successfully passed an examination of the theoretical knowledge requirements for UAS Operations in Subcategory Open A2 as set out in Implementing Regulation (EU) 2019/947 UAS.OPEN.030 having achieved a pass mark at least 75% of the overall marks available. **COURSE COMPLETION CERTIFICATE** Has been awarded to Ran Zhang For completing the **UAS OPEN A2 Theoretical Knowledge Examination iaw UAS.OPEN.030** Covering Meteorology; UAS flight Performance; technical and operational mitigation for ground risk. Julie Garland Chief Flight Instructor Avtrain DATE 22/02/21 Further to the Commission Implementing Regulation (EU) 2019/947 of 24 May 2019 on the rules and procedures for the operation of Unmanned Aircraft Systems (UAS) applicable in Ireland from 31st December 2020, the above-named Declared UAS Training Organisation (DUTO) is hereby recognised by the Authority in accordance with the Letter of Recognised Entity issued by the Irish Aviation Authority on the 1st January 2021 Certification of IAA drone license

	 Drone controller Marker pen
Key materials:	Accessories of drones: Batteries Battery Charging Hub. Battery to Power Bank Adapter. Low-Noise Propeller (pair). Mavic 2 Should
Specific identified residual hazards:	For drone testing, drone operation residual hazards with low GPS: Partial failure or loss of navigation systems. Take-off and landing incidents as under-shooting or overrunning. Turbulence caused by moving vehicles. Ground risk of drone: Uninvolved persons break into the flying zone. Drone collisions with tunnel linings, lighting, and ventilation system. Privacy, security, data protection risk, noise: Information of uninvolved person recorded by drone. Exposure to loud operation noise of around 70 dB
Required specific staff training and competence:	Site Safety Induction and Safe Pass Safe remove and change batteries and broken accessories Location of underground services DJI go 4 training Drone flight competence certified (already obtained) Safe termination of operation in case of emergency
Sequence of operations:	The whole task can be generally divided into two main operations: preparation and flight: Preparation of drone flight -- Before entering Dublin Tunnel on full closure nights (…) Preparation of drone flight -- During the tunnel full closure from 22:00pm to 5:00am

	Then check the following issue about the flight safety, which includes: 1. Ensure the remote-control device, mobile device, and Intelligent Flight Battery are fully charged. 2. Ensure the Intelligent Flight Battery and the propellers are mounted securely. 3. Ensure the aircraft arms and propellers are unfolded. 4. Ensure the gimbal and camera are functioning normally. 5. Ensure that there is nothing obstructing the motors and that they are functioning normally. 6. Ensure that DJI GO 4 is successfully connected to the aircraft. 7. Ensure that the camera lens and Vision System sensors are clean. 8. Use only genuine DJI parts or parts certified by DJI. Preparing the Aircraft (…) Preparing the Remote Controller (…) Take-off/Landing Procedures (…) During the filming To keep fly safe, the process for filming must be in an appropriate environment (…) Also, for the good quality of the film, the pilot should always keep to the following rules during the flight: Choose the camera settings that best suit filming needs. Settings include photo format and exposure compensation. Perform flight tests to establish flight routes and to preview scenes. Push the control sticks gently to keep the aircraft movement smooth and stable. Video check Zoom and check if the cracks on the sidewall are clear.
Temporary supports and props needed to facilitate the works:	(e.g., isolation, traffic management) Traffic management to guarantee no external vehicle passing during flight Traffic management to avoid assembly of uninvolved persons Attentive operation of drones under low-speed mode Avoid interference with other onsite works
Fall protection measures:	Low power could be harmless regarding the drone operation environment. The drone will automatically find an appropriate place to land. Propeller protector is installed to reduce the harm of accidental falling.

And the risk assessment table is given in Table 8-3Table 8-2. In the table, each potential hazard / risk associated with the operation is listed and their assessment. And the abbreviations in the table are: Pre-control and Post-control Risk Rating (RR): How likely (L) is it that a person would be injured while the task is being performed, if there were no controls at all (no training, no PPE, no isolation, no traffic management…)? What would the likely severity (S) of the injury be?

Table 8-3 Risk Assessment Worksheet

Work	Drone flight in tunnel		
Hazard	Danger to the Public / Staff / Others (Drone collisions with tunnel interior or individuals), Moving Object, Traffic Management (controlled and co-ordinated), Exposure to loud operational noise		
Injury type	Bruises and abrasions		
Pre control	L	S	RR
	2	3	6
Control measures	System calibration beforehand. All defective equipment to be removed from site immediately. Ensure relevant certification is in place for equipment. Only trained and competent operatives use drone according to verified methodology, and flight work is supervisor-accompanied. Implement procedures for halting or altering drone operations if moving objects approach the drone's flight path. Keep distance to the drone to avoid collision with operatives or operation noises. Report defects to supervisor without delay.		
Post- Control	L	S	RR
	1	2	2
Residual Hazard	Residual hazards during drone operations within tunnel environments may include the possibility of collisions within restricted flying zones that do not house critical equipment. These collisions can be attributed to factors such as partial failure or loss of navigation systems, as well as unforeseen force majeure events.		

References

[1] J. Shahmoradi, A. Mirzaeinia, P. Roghanchi, and M. Hassanalian, 'Monitoring of Inaccessible Areas in GPS-Denied Underground Mines using a Fully Autonomous Encased Safety Inspection Drone', in *AIAA Scitech 2020 Forum*, Orlando, FL: American Institute of Aeronautics and Astronautics, Jan. 2020. doi: 10.2514/6.2020-1961. Available: https://arc.aiaa.org/doi/10.2514/6.2020-1961. [Accessed: Apr. 06, 2021]

[2] *GB/T 18316-2008. Specifications for inspection and acceptance of quality of digital surveying and mapping achievements[S]*. 2008.

[3] F. Y. Toriumi, T. N. Bittencourt, and M. M. Futai, 'UAV-based inspection of bridge and tunnel structures: an application review', *Rev. IBRACON Estrut. Mater.*, vol. 16, p. e16103, May 2022, doi: 10.1590/S1983-41952023000100003

[4] Y. Xue, P. Shi, F. Jia, and H. Huang, '3D reconstruction and automatic leakage defect quantification of metro tunnel based on SfM-Deep learning method', *Underground Space*, vol. 7, no. 3, pp. 311–323, Jun. 2022, doi: 10.1016/j.undsp.2021.08.004

[5] 'Reliable VTOL Drones from JOUAV', *JOUAV*. Available: https://www.jouav.com/. [Accessed: Dec. 22, 2022]

[6] 'Shenzhen Feima Robotics Co. Ltd.' Available: https://www.feimarobotics.com/en/productDetailD200. [Accessed: Dec. 22, 2022]

[7] 'Yuneec – Quadcopters & Aerial Drones'. Available: https://us.yuneec.com/. [Accessed: Dec. 22, 2022]

[8] 'Elios 3 - Digitizing the inaccessible'. Available: https://www.flyability.com/elios-3. [Accessed: Dec. 22, 2022]

[9] 'Geospatial Data Analytics for the Enterprise'. Available: https://www.precisionhawk.com. [Accessed: Dec. 22, 2022]

[10] A. Otto, N. Agatz, J. Campbell, B. Golden, and E. Pesch, 'Optimization approaches for civil applications of unmanned aerial vehicles (UAVs) or aerial

drones: A survey', *Networks*, vol. 72, no. 4, pp. 411–458, 2018, doi: 10.1002/net.21818

[11] L. Attard, C. J. Debono, G. Valentino, and M. Di Castro, 'Tunnel inspection using photogrammetric techniques and image processing: A review', *ISPRS Journal of Photogrammetry and Remote Sensing*, vol. 144, pp. 180–188, Oct. 2018, doi: 10.1016/j.isprsjprs.2018.07.010

[12] J. Wang and T. Ueda, 'A review study on unmanned aerial vehicle and mobile robot technologies on damage inspection of reinforced concrete structures', *Structural Concrete*, vol. 24, no. 1, pp. 536–562, 2023, doi: 10.1002/suco.202200846

[13] S. Sreenath, 'A Systematic Literature Survey of Unmanned Aerial Vehicle Based Structural Health Monitoring', Theses, Dissertations and Capstones, Marshall University, United States, 2020. Available: https://mds.marshall.edu/etd/1341. [Accessed: May 02, 2023]

[14] R. V. Ermakov, I. K. Kuz'menko, E. N. Skripal', A. A. Seranova, D. E. Gutsevich, A. V. Abakumov, D. Yu. Livshits, K. D. Chekhovskaya, and A. A. L'vov, 'Aspects of Designing a Fail-Safe Flight and Navigation System for Unmanned Aerial Vehicles', in *2019 26th Saint Petersburg International Conference on Integrated Navigation Systems (ICINS)*, Saint Petersburg, Russia: IEEE, May 2019, pp. 1–5. doi: 10.23919/ICINS.2019.8769411. Available: https://ieeexplore.ieee.org/document/8769411

[15] S. A. I. Stent, C. Girerd, P. J. G. Long, and R. Cipolla, 'A Low-Cost Robotic System for the Efficient Visual Inspection of Tunnels', in *Proceedings of the International Symposium on Automation and Robotics in Construction*, IAARC Publications, p. 8.

[16] H. Kazunori and Y. Hirofumi, 'Free-Flow Tunnel Inspection Support Devices Aiming at Labor Saving of Visual Checking', *Journal of Robotics and Mechatronics*, vol. 32, no. 4, pp. 832–839, Aug. 2020, doi: 10.20965/jrm.2020.p0832

[17] D. Lattanzi and G. Miller, 'Review of Robotic Infrastructure Inspection Systems', *Journal of Infrastructure Systems*, vol. 23, no. 3, p. 04017004, Sep. 2017, doi: 10.1061/(ASCE)IS.1943-555X.0000353

[18] F. Panella, N. Roecklinger, L. Vojnovic, Y. Loo, and J. Boehm, 'Cost-benefit analysis of rail tunnel inspection for photogrammetry and laser scanning', *The*

International Archives of the Photogrammetry, Remote Sensing and Spatial Information Sciences, vol. 43, pp. 1137–1144, Aug. 2020, doi: 10.5194/isprs-archives-XLIII-B2-2020-1137-2020

[19] A. Ouyang, V. Di Murro, M. Cull, R. Cunningham, J. A. Osborne, and Z. Li, 'Automated pixel-level crack monitoring system for large-scale underground infrastructure – A case study at CERN', *Tunnelling and Underground Space Technology*, vol. 140, p. 105310, Oct. 2023, doi: 10.1016/j.tust.2023.105310

[20] C. H. Tan, M. Ng, D. S. B. Shaiful, S. K. H. Win, W. J. Ang, S. K. Yeung, H. B. Lim, M. N. Do, and S. Foong, 'A smart unmanned aerial vehicle (UAV) based imaging system for inspection of deep hazardous tunnels', *Water Practice and Technology*, vol. 13, no. 4, pp. 991–1000, Dec. 2018, doi: 10.2166/wpt.2018.105

[21] Y. Xue, S. Zhang, M. Zhou, and H. Zhu, 'Novel SfM-DLT method for metro tunnel 3D reconstruction and Visualization', *Underground Space*, vol. 6, no. 2, pp. 134–141, Apr. 2021, doi: 10.1016/j.undsp.2020.01.002

[22] N.-B. Jing, X.-M. Ma, and W. Guo, '3D Reconstruction of Underground Tunnel Using Kinect Camera', in *2018 International Symposium on Computer, Consumer and Control (IS3C)*, 2018, pp. 278–281. doi: 10.1109/IS3C.2018.00077

[23] F. Kendoul, 'Survey of advances in guidance, navigation, and control of unmanned rotorcraft systems', *Journal of Field Robotics*, vol. 29, 2012, doi: 10.1002/rob.20414. Available: https://www.semanticscholar.org/paper/36703336d75aca03ca6aaf5720053a982fa5fea0

[24] M. Mattei and L. Blasi, 'Smooth Flight Trajectory Planning in the Presence of No-Fly Zones and Obstacles', *Journal of Guidance, Control, and Dynamics*, vol. 33, no. 2, pp. 454–462, 2010, doi: 10.2514/1.45161

[25] H.-A. Langåker, H. Kjerkreit, C. L. Syversen, R. J. Moore, Ø. H. Holhjem, I. Jensen, A. Morrison, A. A. Transeth, O. Kvien, G. Berg, T. A. Olsen, A. Hatlestad, T. Negård, R. Broch, and J. E. Johnsen, 'An autonomous drone-based system for inspection of electrical substations', *International Journal of Advanced Robotic Systems*, vol. 18, no. 2, p. 17298814211002973, Mar. 2021, doi: 10.1177/17298814211002973

[26] S. Ross, N. Melik-Barkhudarov, K. S. Shankar, A. Wendel, D. Dey, J. A. Bagnell, and M. Hebert, 'Learning Monocular Reactive UAV Control in Cluttered Natural

Environments'. arXiv, Nov. 07, 2012. doi: 10.48550/arXiv.1211.1690. Available: http://arxiv.org/abs/1211.1690. [Accessed: Jun. 26, 2022]

[27] T. Wright, T. Hanari, K. Kawabata, and B. Lennox, 'Fast In-situ Mesh Generation using Orb-SLAM2 and OpenMVS', in *2020 17th International Conference on Ubiquitous Robots (UR)*, Jun. 2020, pp. 315–321. doi: 10.1109/UR49135.2020.9144879

[28] M. Morita, H. Kinjo, S. Sato, T. Sulyyon, and T. Anezaki, 'Autonomous flight drone for infrastructure (transmission line) inspection (3)', in *2017 International Conference on Intelligent Informatics and Biomedical Sciences (ICIIBMS)*, Nov. 2017, pp. 198–201. doi: 10.1109/ICIIBMS.2017.8279692

[29] H. Kinjo, M. Morita, S. Sato, T. Suriyon, and T. Anezaki, 'Infrastructure (transmission line) check autonomous flight drone (1)', in *2017 International Conference on Intelligent Informatics and Biomedical Sciences (ICIIBMS)*, Nov. 2017, pp. 206–209. doi: 10.1109/ICIIBMS.2017.8279694

[30] X. Kong, X. Li, X. Song, Y. Tian, and D. Kong, 'An accurate and reliable positioning methodology for land vehicles in tunnels based on UWB/INS integration', *Meas. Sci. Technol.*, vol. 33, no. 9, p. 095107, Jun. 2022, doi: 10.1088/1361-6501/ac7122

[31] A. Halder and D. Chakravarty, 'Investigation of wireless tracking performance in the tunnel-like environment with particle filter', *MMEP*, vol. 5, no. 2, pp. 93–101, Jun. 2018, doi: 10.18280/mmep.050206

[32] Y. Lin, F. Gao, T. Qin, W. Gao, T. Liu, W. Wu, Z. Yang, and S. Shen, 'Autonomous aerial navigation using monocular visual-inertial fusion', *J. Field Robotics*, vol. 35, no. 1, pp. 23–51, Jan. 2018, doi: 10.1002/rob.21732

[33] Y. Li, Y. Wang, and D. Wang, 'Multiple RGB-D sensor-based 3-D reconstruction and localization of indoor environment for mini MAV', *Computers & Electrical Engineering*, vol. 70, pp. 509–524, Aug. 2018, doi: 10.1016/j.compeleceng.2017.08.011

[34] K. Schmid, P. Lutz, T. Tomić, E. Mair, and H. Hirschmüller, 'Autonomous Vision-based Micro Air Vehicle for Indoor and Outdoor Navigation: Autonomous Vision Based MAV for Indoor and Outdoor Navigation', *J. Field Robotics*, vol. 31, no. 4, pp. 537–570, Jul. 2014, doi: 10.1002/rob.21506

[35] K. Mohta, M. Watterson, Y. Mulgaonkar, S. Liu, C. Qu, A. Makineni, K. Saulnier,

K. Sun, A. Z. Zhu, J. Delmerico, K. Karydis, N. A. Atanasov, G. Loianno, D. Scaramuzza, K. Daniilidis, C. J. Taylor, and V. R. Kumar, 'Fast, autonomous flight in GPS-denied and cluttered environments', *Journal of Field Robotics*, vol. 35, pp. 101–120, 2017, doi: 10.1002/rob.21774

[36] F. Outay, H. A. Mengash, and M. Adnan, 'Applications of unmanned aerial vehicle (UAV) in road safety, traffic and highway infrastructure management: Recent advances and challenges', *Transportation Research Part A: Policy and Practice*, vol. 141, pp. 116–129, Nov. 2020, doi: 10.1016/j.tra.2020.09.018

[37] Y. Tan, S. Li, H. Liu, P. Chen, and Z. Zhou, 'Automatic inspection data collection of building surface based on BIM and UAV', *Automation in Construction*, vol. 131, p. 103881, Nov. 2021, doi: 10.1016/j.autcon.2021.103881

[38] A. Macario Barros, M. Michel, Y. Moline, G. Corre, and F. Carrel, 'A Comprehensive Survey of Visual SLAM Algorithms', *Robotics*, vol. 11, no. 1, p. 24, Feb. 2022, doi: 10.3390/robotics11010024

[39] Y. Z. Ayele, M. Aliyari, D. Griffiths, and E. L. Droguett, 'Automatic Crack Segmentation for UAV-Assisted Bridge Inspection', *Energies*, vol. 13, no. 23, p. 6250, Jan. 2020, doi: 10.3390/en13236250

[40] S. Khattak, H. Nguyen, F. Mascarich, T. Dang, and K. Alexis, 'Complementary Multi–Modal Sensor Fusion for Resilient Robot Pose Estimation in Subterranean Environments', in *2020 International Conference on Unmanned Aircraft Systems (ICUAS)*, Sep. 2020, pp. 1024–1029. doi: 10.1109/ICUAS48674.2020.9213865

[41] S. Jordan, J. Moore, S. Hovet, J. Box, J. Perry, K. Kirsche, D. Lewis, and Z. T. H. Tse, 'State-of-the-art technologies for UAV inspections', *IET Radar, Sonar & Navigation*, vol. 12, no. 2, pp. 151–164, 2018, doi: 10.1049/iet-rsn.2017.0251

[42] K. Kabbabe Poleo, W. J. Crowther, and M. Barnes, 'Estimating the impact of drone-based inspection on the Levelised Cost of electricity for offshore wind farms', *Results in Engineering*, vol. 9, p. 100201, Mar. 2021, doi: 10.1016/j.rineng.2021.100201

[43] S. Ge, F. Pan, D. Wang, and P. Ning, 'Research on An Autonomous Tunnel Inspection UAV based on Visual Feature Extraction and Multi-sensor Fusion Indoor Navigation System', in *2021 33rd Chinese Control and Decision Conference (CCDC)*, May 2021, pp. 6082–6089. doi: 10.1109/CCDC52312.2021.9602626

[44] L. Zhang, H. Zhao, S. Hou, Z. Zhao, H. Xu, X. Wu, Q. Wu, and R. Zhang, 'A Survey on 5G Millimeter Wave Communications for UAV-Assisted Wireless Networks', *IEEE Access*, vol. 7, pp. 117460–117504, 2019, doi: 10.1109/ACCESS.2019.2929241

[45] G. He, X. Huang, Y. Xu, J. Qin, and K. Sun, 'Cable tunnel unmanned aerial vehicle location and navigation method based on ultra wideband and depth camera fusion', *IET Electrical Systems in Transportation*, vol. 13, no. 1, p. e12068, 2023, doi: 10.1049/els2.12068

[46] C. J. O. Salaan, Y. Okada, S. Mizutani, T. Ishii, K. Koura, K. Ohno, and S. Tadokoro, 'Close visual bridge inspection using a UAV with a passive rotating spherical shell', *Journal of Field Robotics*, vol. 35, no. 6, pp. 850–867, 2018, doi: 10.1002/rob.21781

[47] B. Bibish, H. Toriya, Y. Fissha, H. Ikeda, N. Owada, B. B. Sinaice, T. Adachi, and Y. Kawamura, 'UAV Based 3D Photogrammetric Modelling in Underground Inaccessible Tunnel'. Preprints, May 19, 2023. doi: 10.20944/preprints202305.1429.v1. Available: https://www.preprints.org/manuscript/202305.1429/v1. [Accessed: Feb. 05, 2024]

[48] 'Design and Optimization of an Encased Drone for Underground Mining Applications', *AIAA SciTech Forum*. doi: 10.2514/6.2021-0696. Available: https://arc.aiaa.org/doi/10.2514/6.2021-0696. [Accessed: Jul. 15, 2022]

[49] G. R. Freire, R. F. Cota, M. Hudyma, and Y. Potvin, 'Capture of images in inaccessible areas in an underground mine using an unmanned aerial vehicle', Australian Centre for Geomechanics, Oct. 2017. doi: 10.36487/ACG_rep/1710_54_Freire. Available: https://papers.acg.uwa.edu.au/p/1710_54_Freire/. [Accessed: Jul. 15, 2022]

[50] K. Boudergui, F. Carrel, T. Domenech, N. Guénard, J.- Poli, A. Ravet, V. Schoepff, and R. Woo, 'Development of a drone equipped with optimized sensors for nuclear and radiological risk characterization', in *2011 2nd International Conference on Advancements in Nuclear Instrumentation, Measurement Methods and their Applications*, Jun. 2011, pp. 1–9. doi: 10.1109/ANIMMA.2011.6172936

[51] L. Galtarossa, L. F. Navilli, and M. Chiaberge, 'Visual-Inertial Indoor Navigation Systems and Algorithms for UAV Inspection Vehicles', *Industrial Robotics - New Paradigms*, Feb. 2020, doi: 10.5772/intechopen.90315. Available:

https://www.intechopen.com/books/industrial-robotics-new-paradigms/visual-inertial-indoor-navigation-systems-and-algorithms-for-uav-inspection-vehicles. [Accessed: Apr. 06, 2021]

[52] J. Quenzel, M. Nieuwenhuisen, D. Droeschel, M. Beul, S. Houben, and S. Behnke, 'Autonomous MAV-based Indoor Chimney Inspection with 3D Laser Localization and Textured Surface Reconstruction', *J Intell Robot Syst*, vol. 93, no. 1–2, pp. 317–335, Feb. 2019, doi: 10.1007/s10846-018-0791-y

[53] D. Kominiak, S. S. Mansouri, C. Kanellakis, and G. Nikolakopoulos, 'MAV Development Towards Navigation in Unknown and Dark Mining Tunnels', in *2020 28th Mediterranean Conference on Control and Automation (MED)*, Sep. 2020, pp. 1015–1020. doi: 10.1109/MED48518.2020.9183142

[54] J. F. Chow, B. B. Kocer, J. Henawy, G. Seet, Z. Li, W. Y. Yau, and M. Pratama, 'Toward Underground Localization: Lidar Inertial Odometry Enabled Aerial Robot Navigation', *arXiv:1910.13085 [cs, eess]*, Oct. 2019, Available: http://arxiv.org/abs/1910.13085. [Accessed: Apr. 06, 2021]

[55] A. Brunel, A. Bourki, C. Demonceaux, and O. Strauss, 'SplatPlanner: Efficient Autonomous Exploration via Permutohedral Frontier Filtering', in *2021 IEEE International Conference on Robotics and Automation (ICRA)*, 2021, pp. 608–615. doi: 10.1109/ICRA48506.2021.9560896

[56] H. D. Tuan, A. A. Nasir, A. V. Savkin, H. V. Poor, and E. Dutkiewicz, 'MPC-Based UAV Navigation for Simultaneous Solar-Energy Harvesting and Two-Way Communications', *IEEE Journal on Selected Areas in Communications*, vol. 39, no. 11, pp. 3459–3474, 2021, doi: 10.1109/JSAC.2021.3088633

[57] G. Li, R. Ge, and G. Loianno, 'Cooperative Transportation of Cable Suspended Payloads With MAVs Using Monocular Vision and Inertial Sensing', *IEEE Robotics and Automation Letters*, vol. 6, no. 3, pp. 5316–5323, Jul. 2021, doi: 10.1109/LRA.2021.3065286

[58] J. Liu, W. Gao, and Z. Hu, 'Bidirectional Trajectory Computation for Odometer-Aided Visual-Inertial SLAM', *IEEE Robot. Autom. Lett.*, vol. 6, no. 2, pp. 1670–1677, Apr. 2021, doi: 10.1109/LRA.2021.3059564

[59] G. Evangelidis and B. Micusik, 'Revisiting Visual-Inertial Structure-From-Motion for Odometry and SLAM Initialization', *IEEE Robot. Autom. Lett.*, vol. 6, no. 2, pp. 1415–1422, Apr. 2021, doi: 10.1109/LRA.2021.3057564

[60] Z. Ding, T. Yang, K. Zhang, C. Xu, and F. Gao, 'VID-Fusion: Robust Visual-Inertial-Dynamics Odometry for Accurate External Force Estimation', p. 7.

[61] D. Cheng, H. Shi, M. Schwerin, M. Crivella, L. Li, and H. Choset, 'A Compact and Infrastructure-free Confined Space Sensor for 3D Scanning and SLAM', in *2020 IEEE SENSORS*, Oct. 2020, pp. 1–4. doi: 10.1109/SENSORS47125.2020.9278586

[62] F. Nobre and C. Heckman, 'Learning to calibrate: Reinforcement learning for guided calibration of visual–inertial rigs', *The International Journal of Robotics Research*, vol. 38, no. 12–13, pp. 1388–1402, Oct. 2019, doi: 10.1177/0278364919844824

[63] M. Zhang, M. Zhang, Y. Chen, and M. Li, 'IMU Data Processing For Inertial Aided Navigation: A Recurrent Neural Network Based Approach', p. 7.

[64] C. Pfeiffer, S. Wengeler, A. Loquercio, and D. Scaramuzza, 'Visual attention prediction improves performance of autonomous drone racing agents', *PLOS ONE*, vol. 17, no. 3, p. e0264471, Mar. 2022, doi: 10.1371/journal.pone.0264471

[65] P. Foehn, E. Kaufmann, A. Romero, R. Penicka, S. Sun, L. Bauersfeld, T. Laengle, G. Cioffi, Y. Song, A. Loquercio, and D. Scaramuzza, 'Agilicious: Open-source and open-hardware agile quadrotor for vision-based flight', *Science Robotics*, vol. 7, no. 67, p. eabl6259, Jun. 2022, doi: 10.1126/scirobotics.abl6259

[66] W. Feng, B. Zhang, J. Röning, X. Zong, and T. Yi, 'Panoramic stereo sphere vision', in *Intelligent Robots and Computer Vision XXX: Algorithms and Techniques*, SPIE, Feb. 2013, pp. 38–44. doi: 10.1117/12.2004580. Available: https://www.spiedigitallibrary.org/conference-proceedings-of-spie/8662/866206/Panoramic-stereo-sphere-vision/10.1117/12.2004580.full. [Accessed: Dec. 22, 2022]

[67] T. Yamashita, Y. Kajiwara, C. T. Raabe, T. Tsuchiya, and S. Suzuki, 'AUTONOMOUS FLIGHT OF UNMANNED MULTICOPTER USING SUPER WIDE-ANGLE STEREO VISION SYSTEM', p. 9.

[68] 'Inertial Navigation Systems - IVAO - International Virtual Aviation Organisation'. Available: https://mediawiki.ivao.aero/index.php?title=Inertial_Navigation_Systems#Introduction. [Accessed: Jun. 27, 2022]

[69] T. H. Nguyen, T.-M. Nguyen, and L. Xie, 'Range-Focused Fusion of Camera-

IMU-UWB for Accurate and Drift-Reduced Localization', *IEEE Robotics and Automation Letters*, vol. 6, no. 2, pp. 1678–1685, Apr. 2021, doi: 10.1109/LRA.2021.3057838

[70] T. Qin, P. Li, and S. Shen, 'VINS-Mono: A Robust and Versatile Monocular Visual-Inertial State Estimator', *IEEE Transactions on Robotics*, vol. 34, no. 4, pp. 1004–1020, Aug. 2018, doi: 10.1109/TRO.2018.2853729

[71] Z. Hou, J. Qi, and M. Wang, 'Fusing Optical Flow and Inertial Data for UAV Motion Estimation in GPS-denied Environment', in *2019 Chinese Control Conference (CCC)*, Jul. 2019, pp. 7791–7796. doi: 10.23919/ChiCC.2019.8866551

[72] R. Opromolla, G. Fasano, G. Rufino, M. Grassi, and A. Savvaris, 'LIDAR-inertial integration for UAV localization and mapping in complex environments', in *2016 International Conference on Unmanned Aircraft Systems (ICUAS)*, Jun. 2016, pp. 649–656. doi: 10.1109/ICUAS.2016.7502580

[73] S. Suzuki and Faculty of Textile Science and Technology, Shinshu University 3-15-1 Tokida, Ueda-shi, Nagano 386-8567, Japan, 'Integrated Navigation for Autonomous Drone in GPS and GPS-Denied Environments', *JRM*, vol. 30, no. 3, pp. 373–379, Jun. 2018, doi: 10.20965/jrm.2018.p0373

[74] H. Li, A. V. Savkin, and B. Vucetic, 'Collision Free Navigation of a Flying Robot for Underground Mine Search and Mapping', in *2018 IEEE International Conference on Robotics and Biomimetics (ROBIO)*, Kuala Lumpur, Malaysia: IEEE, Dec. 2018, pp. 1102–1106. doi: 10.1109/ROBIO.2018.8665108

[75] P. Tripicchio, M. Satler, M. Unetti, and C. A. Avizzano, 'Confined spaces industrial inspection with micro aerial vehicles and laser range finder localization', *International Journal of Micro Air Vehicles*, vol. 10, no. 2, pp. 207–224, Jun. 2018, doi: 10.1177/1756829318757471

[76] Y. Bi, M. Lan, J. Li, K. Zhang, H. Qin, S. Lai, and B. M. Chen, 'Robust autonomous flight and mission management for MAVs in GPS-denied environments', in *2017 11th Asian Control Conference (ASCC)*, 2017, pp. 67–72. doi: 10.1109/ASCC.2017.8287144

[77] S. S. Mansouri, C. Kanellakis, D. Kominiak, and G. Nikolakopoulos, 'Deploying MAVs for autonomous navigation in dark underground mine environments', *Robotics and Autonomous Systems*, vol. 126, p. 103472, Apr. 2020, doi: 10.1016/j.robot.2020.103472

[78] C. H. Vong, R. Ravitharan, P. Reichl, J. Chevin, and H. Chung, 'Small Scale Unmanned Aerial System (UAS) for Railway Culvert and Tunnel Inspection', in *ICRT 2017: Railway Development, Operations, and Maintenance*, Chengdu, China: American Society of Civil Engineers, Mar. 2018, pp. 1024–1032. doi: 10.1061/9780784481257.102

[79] E. Jones, J. Sofonia, C. Canales, S. Hrabar, F. Kendoul, and J. W, 'Advances and applications for automated drones in underground mining operations', The Southern African Institute of Mining and Metallurgy, Jun. 2019. doi: 10.36487/ACG_rep/1952_24_Jones. Available: https://papers.acg.uwa.edu.au/p/1952_24_Jones/. [Accessed: Jul. 18, 2022]

[80] C. N. C. Baylis, D. R. Kewe, E. W. Jones, and J. Wesseloo, 'Mobile drone LiDAR structural data collection and analysis', Australian Centre for Geomechanics, Nov. 2020. doi: 10.36487/ACG_repo/2035_16. Available: https://papers.acg.uwa.edu.au/p/2035_16_Baylis/. [Accessed: Jul. 15, 2022]

[81] S. Jung, D. Choi, S. Song, and H. Myung, 'Bridge Inspection Using Unmanned Aerial Vehicle Based on HG-SLAM: Hierarchical Graph-Based SLAM', *Remote Sensing*, vol. 12, no. 18, Art. no. 18, Jan. 2020, doi: 10.3390/rs12183022

[82] F. Cunha and K. Youcef-Toumi, 'Ultra-Wideband Radar for Robust Inspection Drone in Underground Coal Mines', in *2018 IEEE International Conference on Robotics and Automation (ICRA)*, 2018, pp. 86–92. doi: 10.1109/ICRA.2018.8461191

[83] W. Shule, C. M. Almansa, J. P. Queralta, Z. Zou, and T. Westerlund, 'UWB-Based Localization for Multi-UAV Systems and Collaborative Heterogeneous Multi-Robot Systems', *Procedia Computer Science*, vol. 175, pp. 357–364, Jan. 2020, doi: 10.1016/j.procs.2020.07.051

[84] L. R. Pinto, A. Vale, Y. Brouwer, J. Borbinha, J. Corisco, R. Ventura, A. M. Silva, A. Mourato, G. Marques, Y. Romanets, S. Sargento, and B. Gonçalves, 'Radiological Scouting, Monitoring and Inspection Using Drones', *Sensors*, vol. 21, no. 9, Art. no. 9, Jan. 2021, doi: 10.3390/s21093143

[85] A. Çakir and S. Akpancar, '3D Simultaneous Positioning and Mapping in Dark, Closed Spaces with an Autonomous Flying Robot', *ACTA POLYTECH HUNG*, vol. 17, no. 7, pp. 7–23, 2020, doi: 10.12700/APH.17.7.2020.7.1

[86] K. Fujiuchi and H. Toda, 'Autonomous 4-rotor Helicopter 10 m-range Movement Control System by Using Two Search Lights and the Evaluation', in *DEStech*

Transactions on Computer Science and Engineering, Guilin, China: DEStech Publications, Apr. 2017, pp. 559–564. doi: 10.12783/dtcse/aics2016/8255

[87] M. Petrlík, T. Báča, D. Heřt, M. Vrba, T. Krajník, and M. Saska, 'A Robust UAV System for Operations in a Constrained Environment', *IEEE Robotics and Automation Letters*, vol. 5, no. 2, pp. 2169–2176, Apr. 2020, doi: 10.1109/LRA.2020.2970980

[88] C. Kanellakis, S. S. Mansouri, M. Castaño, P. Karvelis, D. Kominiak, and G. Nikolakopoulos, 'Where to look: a collection of methods forMAV heading correction in underground tunnels', *IET Image Processing*, vol. 14, no. 10, pp. 2020–2027, 2020, doi: 10.1049/iet-ipr.2019.1423

[89] D. Li, W. Yang, X. Shi, D. Guo, Q. Long, F. Qiao, and Q. Wei, 'A Visual-Inertial Localization Method for Unmanned Aerial Vehicle in Underground Tunnel Dynamic Environments', *IEEE Access*, vol. 8, pp. 76809–76822, 2020, doi: 10.1109/ACCESS.2020.2989480

[90] S. S. Mansouri, P. Karvelis, C. Kanellakis, D. Kominiak, and G. Nikolakopoulos, 'Vision-based MAV Navigation in Underground Mine Using Convolutional Neural Network', in *IECON 2019 - 45th Annual Conference of the IEEE Industrial Electronics Society*, Oct. 2019, pp. 750–755. doi: 10.1109/IECON.2019.8927168

[91] K. Kou, G. Yang, W. Zhang, C. Wang, Y. Yao, and X. Zhou, 'Autonomous Navigation of UAV in Dynamic Unstructured Environments via Hierarchical Reinforcement Learning', in *2022 International Conference on Automation, Robotics and Computer Engineering (ICARCE)*, Dec. 2022, pp. 1–5. doi: 10.1109/ICARCE55724.2022.10046655

[92] Elmokadem T. and Savkin A. V., 'A method for autonomous collision-free navigation of a quadrotor UAV in unknown tunnel-like environments', *Robotica*, vol. 40, no. 4, pp. 835–861, Apr. 2022, doi: 10.1017/S0263574721000849

[93] J. Sandino, F. Vanegas, F. Gonzalez, and F. Maire, 'Autonomous UAV Navigation for Active Perception of Targets in Uncertain and Cluttered Environments', in *2020 IEEE Aerospace Conference*, Mar. 2020, pp. 1–12. doi: 10.1109/AERO47225.2020.9172808

[94] E. Zheng and J. Chen, 'A Method for Corrosion Image Acquisition of Chimney Inner', in *2019 Chinese Control And Decision Conference (CCDC)*, Jun. 2019, pp. 6411–6415. doi: 10.1109/CCDC.2019.8833044

[95] R. S. Pahwa, K. Y. Chan, J. Bai, V. B. Saputra, M. N. Do, and S. Foong, ‘Dense 3D Reconstruction for Visual Tunnel Inspection using Unmanned Aerial Vehicle’, in *2019 IEEE/RSJ International Conference on Intelligent Robots and Systems (IROS)*, Nov. 2019, pp. 7025–7032. doi: 10.1109/IROS40897.2019.8967577

[96] S. Weiss, D. Scaramuzza, and R. Siegwart, ‘Monocular-SLAM–based navigation for autonomous micro helicopters in GPS-denied environments’, *Journal of Field Robotics*, vol. 28, 2011, doi: 10.1002/rob.20412. Available: https://www.semanticscholar.org/paper/6eb662ef35ec514429c5ba533b212a3a512c3517

[97] J. J. Engel, T. Schöps, and D. Cremers, ‘LSD-SLAM: Large-Scale Direct Monocular SLAM’, 2014, doi: 10.1007/978-3-319-10605-2_54. Available: https://www.semanticscholar.org/paper/c13cb6dfd26a1b545d50d05b52c99eb87b1c82b2

[98] I. Konovalenko, E. Kuznetsova, A. Miller, B. Miller, A. Popov, D. Shepelev, and K. Stepanyan, ‘New Approaches to the Integration of Navigation Systems for Autonomous Unmanned Vehicles (UAV)’, *Sensors*, vol. 18, no. 9, Art. no. 9, Sep. 2018, doi: 10.3390/s18093010

[99] H.-M. Chuang, D. He, and A. Namiki, ‘Autonomous Target Tracking of UAV Using High-Speed Visual Feedback’, *Applied Sciences*, 2019, doi: 10.3390/app9214552. Available: https://www.semanticscholar.org/paper/ec364b6f0b2938ff8b2f16fa8c4783b8ddc2e87e

[100] Z. Lin, B. Lu, X. Mou, and X. Zhang, ‘Application of Improved Optical Flow Algorithm in Quadrotor UAV’, in *2021 6th International Symposium on Computer and Information Processing Technology (ISCIPT)*, Jun. 2021, pp. 269–274. doi: 10.1109/ISCIPT53667.2021.00061

[101] A. P. Tanchenko, A. M. Fedulin, R. R. Bikmaev, and R. N. Sadekov, ‘UAV Navigation System Autonomous Correction Algorithm Based on Road and River Network Recognition’, *Gyroscopy Navig.*, vol. 11, no. 4, pp. 293–299, Oct. 2020, doi: 10.1134/S2075108720040100

[102] J. Delaune, D. S. Bayard, and R. Brockers, ‘Range-Visual-Inertial Odometry: Scale Observability Without Excitation’, *IEEE Robotics and Automation Letters*, vol. 6, no. 2, pp. 2421–2428, Apr. 2021, doi: 10.1109/LRA.2021.3058918

[103] C. Zhao, B. Fan, J. Hu, Q. Pan, and Z. Xu, ‘Homography-based camera pose

estimation with known gravity direction for UAV navigation', *Sci. China Inf. Sci.*, vol. 64, no. 1, p. 112204, Dec. 2020, doi: 10.1007/s11432-019-2690-0

[104] L. Zhou, G. Huang, Y. Mao, S. Wang, and M. Kaess, 'EDPLVO: Efficient Direct Point-Line Visual Odometry', p. 7.

[105] M. Scheiber, J. Delaune, S. Weiss, and R. Brockers, 'Mid-Air Range-Visual-Inertial Estimator Initialization for Micro Air Vehicles', p. 7.

[106] V. Knyaz and V. Kniaz, 'Object recognition for UAV navigation in complex environment', in *Image and Signal Processing for Remote Sensing XXVI*, SPIE, Sep. 2020, pp. 154–166. doi: 10.1117/12.2574078. Available: https://www.spiedigitallibrary.org/conference-proceedings-of-spie/11533/115330P/Object-recognition-for-UAV-navigation-in-complex-environment/10.1117/12.2574078.full. [Accessed: Jun. 08, 2022]

[107] A. A. Deraz, O. Badawy, M. A. Elhosseini, M. Mostafa, H. A. Ali, and A. I. El-Desouky, 'Deep learning based on LSTM model for enhanced visual odometry navigation system', *Ain Shams Engineering Journal*, p. 102050, Nov. 2022, doi: 10.1016/j.asej.2022.102050

[108] L. Madhuanand, F. Nex, and M. Y. Yang, 'Self-supervised monocular depth estimation from oblique UAV videos', *ISPRS Journal of Photogrammetry and Remote Sensing*, vol. 176, pp. 1–14, Jun. 2021, doi: 10.1016/j.isprsjprs.2021.03.024

[109] 'Towards monocular vision-based autonomous flight through deep reinforcement learning | Elsevier Enhanced Reader'. doi: 10.1016/j.eswa.2022.116742. Available: https://reader.elsevier.com/reader/sd/pii/S0957417422002111?token=B4E8361FAED76ABF1A5C28925E9821E07AEC13286FEF0863F89823A7A91355A8429F26B4C90A5686274248A1524C6D07&originRegion=eu-west-1&originCreation=20230316151602. [Accessed: Mar. 16, 2023]

[110] N. U. Akmandor and T. Padir, 'Reactive Navigation Framework for Mobile Robots by Heuristically Evaluated Pre-sampled Trajectories', *ArXiv*, vol. abs/2105.08145, 2021, doi: 10.35708/RC1870-126265. Available: https://www.semanticscholar.org/paper/0d8882a2941d67be18a651e68d0c4c0f74f8cadd

[111] A. Basiri, V. Mariani, G. Silano, M. Aatif, L. Iannelli, and L. Glielmo, 'A survey on the application of path-planning algorithms for multi-rotor UAVs in precision

agriculture', *The Journal of Navigation*, vol. 75, no. 2, pp. 364–383, Mar. 2022, doi: 10.1017/S0373463321000825

[112] H. Niu, Y. Lu, A. Savvaris, and A. Tsourdos, 'An energy-efficient path planning algorithm for unmanned surface vehicles', *Ocean Engineering*, vol. 161, pp. 308–321, Aug. 2018, doi: 10.1016/j.oceaneng.2018.01.025

[113] R. Omar, C. K. N. Hailma, and S. elia nadira, 'Performance comparison of path planning methods', vol. 10, pp. 8866–8872, Jan. 2015.

[114] L. Campos-Macías, R. Aldana-López, R. de la Guardia, J. I. Parra-Vilchis, and D. Gómez-Gutiérrez, 'Autonomous navigation of MAVs in unknown cluttered environments', *Journal of Field Robotics*, vol. 38, no. 2, pp. 307–326, 2021, doi: 10.1002/rob.21959

[115] J.-W. Lee, W. Lee, and K.-D. Kim, 'An Algorithm for Local Dynamic Map Generation for Safe UAV Navigation', *Drones*, vol. 5, no. 3, p. 88, Aug. 2021, doi: 10.3390/drones5030088

[116] F. Raheem and M. M.Badr, 'Development of Modified Path Planning Algorithm Using Artificial Potential Field (APF) Based on PSO for Factors Optimization', *American Scientific Research Journal for Engineering, Technology, and Sciences*, vol. 37, pp. 316–328, Nov. 2017.

[117] M. Garber, S. Rathinam, and R. Sharma, 'A grid-based path planning approach for a team of two vehicles with localization constraints', *2017 International Conference on Unmanned Aircraft Systems (ICUAS)*, pp. 516–523, 2017, doi: 10.1109/ICUAS.2017.7991489

[118] R. S. Pahwa, K. Y. Chan, J. Bai, V. B. Saputra, M. N. Do, and S. Foong, 'Dense 3D Reconstruction for Visual Tunnel Inspection using Unmanned Aerial Vehicle', *arXiv:1911.03603 [cs]*, Nov. 2019, Available: http://arxiv.org/abs/1911.03603. [Accessed: Jun. 28, 2021]

[119] T. Elmokadem, 'A 3D Reactive Navigation Method for UAVs in Unknown Tunnel-like Environments', in *2020 Australian and New Zealand Control Conference (ANZCC)*, Nov. 2020, pp. 119–124. doi: 10.1109/ANZCC50923.2020.9318346. Available: https://ieeexplore.ieee.org/document/9318346. [Accessed: Jan. 22, 2024]

[120] C. Shang, L. Cheng, Q. Yu, X. Wang, R. Peng, Y. Chen, H. Wu, and Q. Zhu, 'Micro aerial vehicle autonomous flight control in tunnel environment', in *2017*

9th International Conference on Modelling, Identification and Control (ICMIC), Kunming: IEEE, Jul. 2017, pp. 93–98. doi: 10.1109/ICMIC.2017.8321597. Available: http://ieeexplore.ieee.org/document/8321597/. [Accessed: Jan. 22, 2024]

[121] B. Lindqvist, S. S. Mansouri, J. Haluška, and G. Nikolakopoulos, 'Reactive Navigation of an Unmanned Aerial Vehicle With Perception-Based Obstacle Avoidance Constraints', *IEEE Transactions on Control Systems Technology*, vol. 30, no. 5, pp. 1847–1862, Sep. 2022, doi: 10.1109/TCST.2021.3124820

[122] C. Kanellakis, P. S. Karvelis, S. S. Mansouri, A.-A. Agha-Mohammadi, and G. Nikolakopoulos, 'Towards Autonomous Aerial Scouting Using Multi-Rotors in Subterranean Tunnel Navigation', *IEEE Access*, vol. 9, pp. 66477–66485, 2021, doi: 10.1109/ACCESS.2021.3076578

[123] R. P. Padhy, F. Xia, S. K. Choudhury, P. K. Sa, and S. Bakshi, 'Monocular Vision Aided Autonomous UAV Navigation in Indoor Corridor Environments', *IEEE Trans. Sustain. Comput.*, vol. 4, no. 1, pp. 96–108, Jan. 2019, doi: 10.1109/TSUSC.2018.2810952

[124] E. Yel and N. Bezzo, 'A Meta-Learning-based Trajectory Tracking Framework for UAVs under Degraded Conditions', in *2021 IEEE/RSJ International Conference on Intelligent Robots and Systems (IROS)*, Sep. 2021, pp. 6884–6890. doi: 10.1109/IROS51168.2021.9635918

[125] T. Hebecker, R. Buchholz, and F. Ortmeier, 'Model-Based Local Path Planning for UAVs', *J Intell Robot Syst*, vol. 78, no. 1, pp. 127–142, Apr. 2015, doi: 10.1007/s10846-014-0097-7

[126] M. Khalaf-Allah, 'Particle Filtering for Three-Dimensional TDoA-Based Positioning Using Four Anchor Nodes', *Sensors*, vol. 20, no. 16, Art. no. 16, Jan. 2020, doi: 10.3390/s20164516

[127] H. Li, A. V. Savkin, and B. Vucetic, 'Autonomous Area Exploration and Mapping in Underground Mine Environments by Unmanned Aerial Vehicles', *Robotica*, vol. 38, no. 3, pp. 442–456, Mar. 2020, doi: 10.1017/S0263574719000754

[128] B. Bendris and J. Cayero Becerra, 'Design and Experimental Evaluation of an Aerial Solution for Visual Inspection of Tunnel-like Infrastructures', *Remote Sensing*, vol. 14, no. 1, Art. no. 1, Jan. 2022, doi: 10.3390/rs14010195

[129] F. Vanegas and F. Gonzalez, 'Enabling UAV Navigation with Sensor and

Environmental Uncertainty in Cluttered and GPS-Denied Environments', *Sensors*, vol. 16, no. 5, Art. no. 5, May 2016, doi: 10.3390/s16050666

[130] S. S. Mansouri, M. Castaño, C. Kanellakis, and G. Nikolakopoulos, 'Autonomous MAV Navigation in Underground Mines Using Darkness Contours Detection', in *Computer Vision Systems*, D. Tzovaras, D. Giakoumis, M. Vincze, and A. Argyros, Eds., in Lecture Notes in Computer Science, vol. 11754. Cham: Springer International Publishing, 2019, pp. 164–174. doi: 10.1007/978-3-030-34995-0_16. Available: http://link.springer.com/10.1007/978-3-030-34995-0_16. [Accessed: Jan. 24, 2024]

[131] O. Bouhamed, H. Ghazzai, H. Besbes, and Y. Massoud, 'Autonomous UAV Navigation: A DDPG-Based Deep Reinforcement Learning Approach', in *2020 IEEE International Symposium on Circuits and Systems (ISCAS)*, Seville, Spain: IEEE, Oct. 2020, pp. 1–5. doi: 10.1109/ISCAS45731.2020.9181245. Available: https://ieeexplore.ieee.org/document/9181245/. [Accessed: Jun. 01, 2022]

[132] T. Guo, N. Jiang, B. Li, X. Zhu, Y. Wang, and W. Du, 'UAV navigation in high dynamic environments: A deep reinforcement learning approach', *Chinese Journal of Aeronautics*, vol. 34, no. 2, pp. 479–489, Feb. 2021, doi: 10.1016/j.cja.2020.05.011

[133] M. H. Lee and J. Moon, 'Deep Reinforcement Learning-based UAV Navigation and Control: A Soft Actor-Critic with Hindsight Experience Replay Approach', arXiv, arXiv:2106.01016, Jun. 2021. doi: 10.48550/arXiv.2106.01016. Available: http://arxiv.org/abs/2106.01016. [Accessed: Jun. 04, 2022]

[134] Y. Yang, K. Zhang, D. Liu, and H. Song, 'Autonomous UAV Navigation in Dynamic Environments with Double Deep Q-Networks', in *2020 AIAA/IEEE 39th Digital Avionics Systems Conference (DASC)*, 2020, pp. 1–7. doi: 10.1109/DASC50938.2020.9256455

[135] N. Mandel, F. V. Alvarez, M. Milford, and F. Gonzalez, 'Towards Simulating Semantic Onboard UAV Navigation', in *2020 IEEE Aerospace Conference*, Mar. 2020, pp. 1–15. doi: 10.1109/AERO47225.2020.9172771

[136] K. Edgerton, G. Throneberry, A. Takeshita, C. M. Hocut, F. Shu, and A. Abdelkefi, 'Numerical and experimental comparative performance analysis of emerging spherical-caged drones', *Aerospace Science and Technology*, vol. 95, p. 105512, Dec. 2019, doi: 10.1016/j.ast.2019.105512

[137] T. Özaslan, S. Shen, Y. Mulgaonkar, N. Michael, and V. Kumar, 'Inspection of

Penstocks and Featureless Tunnel-like Environments Using Micro UAVs', in *Field and Service Robotics: Results of the 9th International Conference*, L. Mejias, P. Corke, and J. Roberts, Eds., in Springer Tracts in Advanced Robotics. Cham: Springer International Publishing, 2015, pp. 123–136. doi: 10.1007/978-3-319-07488-7_9. Available: https://doi.org/10.1007/978-3-319-07488-7_9. [Accessed: Dec. 07, 2021]

[138] M. Dave, R. Patel, I. Joshi, and B. Goradiya, 'Versatile Multipurpose Crashproof UAV: Machine Learning and IoT approach', in *2020 International Conference for Emerging Technology (INCET)*, Belgaum, India: IEEE, Jun. 2020, pp. 1–7. doi: 10.1109/INCET49848.2020.9154141. Available: https://ieeexplore.ieee.org/document/9154141/. [Accessed: Apr. 06, 2021]

[139] F. SA, 'What Does a Drone Cage Do? Use Cases, Types & Indoor Inspections'. Available: https://www.flyability.com/drone-cage. [Accessed: Apr. 08, 2024]

[140] B. B. Kocer, T. Tjahjowidodo, M. Pratama, and G. G. L. Seet, 'Inspection-while-flying: An autonomous contact-based nondestructive test using UAV-tools', *Automation in Construction*, vol. 106, p. 102895, Oct. 2019, doi: 10.1016/j.autcon.2019.102895

[141] Y. Song, T. Kim, M. Lee, S. Rho, J. Kim, J. Kang, and S.-C. Yu, 'Development of Safety-Inspection-Purpose Wall-Climbing Robot Utilizing Aerial Drone with Lifting Function', in *2021 18th International Conference on Ubiquitous Robots (UR)*, Jul. 2021, pp. 411–416. doi: 10.1109/UR52253.2021.9494637

[142] W. T. Moss, 'Miniature Autonomous Robots for Pipeline Inspection', Thesis, 2016. Available: https://oaktrust.library.tamu.edu/handle/1969.1/158949. [Accessed: Dec. 17, 2021]

[143] Y. Higashi and S. AKAHORI, 'Verification of an EPM system for an Aerial Inspection Robot and Close-up Image Shooting'. Available: https://www.jstage.jst.go.jp/article/aem/1/0/1_179/_article/-char/ja/. [Accessed: Dec. 17, 2021]

[144] P. Sanchez-Cuevas, P. Ramon-Soria, B. Arrue, A. Ollero, and G. Heredia, 'Robotic System for Inspection by Contact of Bridge Beams Using UAVs', *Sensors*, vol. 19, no. 2, p. 305, Jan. 2019, doi: 10.3390/s19020305

[145] H. Oleynikova, M. Burri, Z. Taylor, J. Nieto, R. Siegwart, and E. Galceran, 'Continuous-time trajectory optimization for online UAV replanning', *2016 IEEE/RSJ International Conference on Intelligent Robots and Systems (IROS)*,

pp. 5332–5339, 2016, doi: 10.1109/IROS.2016.7759784

[146] V. Usenko, L. Stumberg, A. Pangercic, and D. Cremers, 'Real-time trajectory replanning for MAVs using uniform B-splines and a 3D circular buffer', *2017 IEEE/RSJ International Conference on Intelligent Robots and Systems (IROS)*, pp. 215–222, 2017, doi: 10.1109/IROS.2017.8202160

[147] F. Chen, Y. Lu, Y. Li, and X. Xie, 'Real-time active detection of targets and path planning using UAVs', in *2021 IEEE International Conference on Robotics and Automation (ICRA)*, 2021, pp. 391–397. doi: 10.1109/ICRA48506.2021.9561365

[148] J. Ji, Z. Wang, Y. Wang, C. Xu, and F. Gao, 'Mapless-Planner: A Robust and Fast Planning Framework for Aggressive Autonomous Flight without Map Fusion', in *2021 IEEE International Conference on Robotics and Automation (ICRA)*, 2021, pp. 6315–6321. doi: 10.1109/ICRA48506.2021.9561460

[149] D. Schleich and S. Behnke, 'Search-based Planning of Dynamic MAV Trajectories Using Local Multiresolution State Lattices', in *2021 IEEE International Conference on Robotics and Automation (ICRA)*, 2021, pp. 7865–7871. doi: 10.1109/ICRA48506.2021.9560969

[150] M. Alnuaimi and M. G. Perhinschi, 'Alternative approaches for UAV dead reckoning based on the immunity paradigm', *Aerospace Science and Technology*, vol. 98, p. 105742, Mar. 2020, doi: 10.1016/j.ast.2020.105742

[151] Y. Chen, N. González-Prelcic, and R. W. Heath, 'Collision-Free UAV Navigation with a Monocular Camera Using Deep Reinforcement Learning', in *2020 IEEE 30th International Workshop on Machine Learning for Signal Processing (MLSP)*, Sep. 2020, pp. 1–6. doi: 10.1109/MLSP49062.2020.9231577

[152] L. Bellini Machado and M. Massao Futai, 'Tunnel performance prediction through degradation inspection and digital twin construction', *Tunnelling and Underground Space Technology*, vol. 144, p. 105544, Feb. 2024, doi: 10.1016/j.tust.2023.105544

[153] H. Huang, X. Wang, Y. Hu, and P. Tan, 'Accuracy Analysis of Visual Odometer for Unmanned Rollers in Tunnels', *Electronics*, vol. 12, no. 20, Art. no. 20, Jan. 2023, doi: 10.3390/electronics12204202

[154] W. Qiu, L. Jian, Y. Cheng, and H. Bai, 'Three-Dimensional Reconstruction of Tunnel Face Based on Multiple Images', *Advances in Civil Engineering*, vol.

2021, p. e8837309, Apr. 2021, doi: 10.1155/2021/8837309

[155] X. Xu, Z. Wang, P. Shi, W. Liu, Q. Tang, X. Bao, X. Chen, and H. Yang, ‘Intelligent monitoring and residual analysis of tunnel point cloud data based on free-form approximation’, *Mechanics of Advanced Materials and Structures*, vol. 30, no. 8, pp. 1703–1712, Mar. 2023, doi: 10.1080/15376494.2022.2041775

[156] D. Ma, H. Fang, N. Wang, G. Pang, B. Li, J. Dong, and X. Jiang, ‘A low-cost 3D reconstruction and measurement system based on structure-from-motion (SFM) and multi-view stereo (MVS) for sewer pipelines’, *Tunnelling and Underground Space Technology*, vol. 141, p. 105345, Nov. 2023, doi: 10.1016/j.tust.2023.105345

[157] M. Lei, L. Liu, C. Shi, Y. Tan, Y. Lin, and W. Wang, ‘A novel tunnel-lining crack recognition system based on digital image technology’, *Tunnelling and Underground Space Technology*, vol. 108, p. 103724, Feb. 2021, doi: 10.1016/j.tust.2020.103724

[158] X. Liu, L. Zhu, Y. Wang, and Z. Yu, ‘A crack detection system of subway tunnel based on image processing’, *Measurement and Control*, vol. 55, no. 3–4, pp. 164–177, Mar. 2022, doi: 10.1177/00202940211062015

[159] Y. Zhou, A. Ji, L. Zhang, and X. Xue, ‘Attention-enhanced sampling point cloud network (ASPCNet) for efficient 3D tunnel semantic segmentation’, *Automation in Construction*, vol. 146, p. 104667, Feb. 2023, doi: 10.1016/j.autcon.2022.104667

[160] R. B. Rusu and S. Cousins, ‘3D is here: Point Cloud Library (PCL)’, in *2011 IEEE International Conference on Robotics and Automation*, May 2011, pp. 1–4. doi: 10.1109/ICRA.2011.5980567. Available: https://ieeexplore.ieee.org/abstract/document/5980567?casa_token=21hq-WXCS7MAAAAA:Xm4bgOXg2X8bf7XMiZCzphGRYDoqxZAXJK4cnrNH6O-J-u4NP-QgZls_2soiEoPhuwD16LNB0Q. [Accessed: Apr. 18, 2024]

[161] X. Xie and X. Lu, ‘Development of a 3D modeling algorithm for tunnel deformation monitoring based on terrestrial laser scanning’, *Underground Space*, vol. 2, no. 1, pp. 16–29, Mar. 2017, doi: 10.1016/j.undsp.2017.02.001

[162] D.-Y. Duan, W.-G. Qiu, Y.-J. Cheng, Y.-C. Zheng, and F. Lu, ‘Reconstruction of shield tunnel lining using point cloud’, *Automation in Construction*, vol. 130, p. 103860, Oct. 2021, doi: 10.1016/j.autcon.2021.103860

[163] W. Qiu and Y.-J. Cheng, ‘High-Resolution DEM Generation of Railway Tunnel Surface Using Terrestrial Laser Scanning Data for Clearance Inspection’, *J. Comput. Civ. Eng.*, vol. 31, no. 1, p. 04016045, Jan. 2017, doi: 10.1061/(ASCE)CP.1943-5487.0000611

[164] Z. Kang, L. Zhang, L. Tuo, B. Wang, and J. Chen, ‘Continuous Extraction of Subway Tunnel Cross Sections Based on Terrestrial Point Clouds’, *Remote Sensing*, vol. 6, no. 1, Art. no. 1, Jan. 2014, doi: 10.3390/rs6010857

[165] W. Lin, B. Sheil, P. Zhang, B. Zhou, C. Wang, and X. Xie, ‘Seg2Tunnel: A hierarchical point cloud dataset and benchmarks for segmentation of segmental tunnel linings’, *Tunnelling and Underground Space Technology*, vol. 147, p. 105735, May 2024, doi: 10.1016/j.tust.2024.105735

[166] F. Wang, J. Shi, H. Huang, D. Zhang, and D. Liu, ‘A horizontal convergence monitoring method based on wireless tilt sensors for shield tunnels with straight joints’, *Structure and Infrastructure Engineering*, vol. 17, no. 9, pp. 1194–1209, Sep. 2021, doi: 10.1080/15732479.2020.1801767

[167] H. Cui, X. Ren, Q. Mao, Q. Hu, and W. Wang, ‘Shield subway tunnel deformation detection based on mobile laser scanning’, *Automation in Construction*, vol. 106, p. 102889, Oct. 2019, doi: 10.1016/j.autcon.2019.102889

[168] Y. Zhang, X. Ren, J. Zhang, and Z. Ma, ‘A Method for Deformation Detection and Reconstruction of Shield Tunnel Based on Point Cloud’, *Journal of Construction Engineering and Management*, vol. 150, no. 3, p. 04024006, Mar. 2024, doi: 10.1061/JCEMD4.COENG-14225

[169] K. Ishikawa and T. Odaka, ‘High precision localization for periodic tunnel inspections’, *SICE Journal of Control, Measurement, and System Integration*, vol. 17, no. 1, pp. 42–55, Dec. 2024, doi: 10.1080/18824889.2024.2313819

[170] M.-H. Le, C.-H. Cheng, and D.-G. Liu, ‘An Efficient Adaptive Noise Removal Filter on Range Images for LiDAR Point Clouds’, *Electronics*, vol. 12, no. 9, Art. no. 9, Jan. 2023, doi: 10.3390/electronics12092150

[171] Y. Zhou, S. Wang, X. Mei, W. Yin, C. Lin, Q. Hu, and Q. Mao, ‘Railway Tunnel Clearance Inspection Method Based on 3D Point Cloud from Mobile Laser Scanning’, *Sensors*, vol. 17, no. 9, Art. no. 9, Sep. 2017, doi: 10.3390/s17092055

[172] Y.-J. Cheng, W. Qiu, and J. Lei, ‘Automatic Extraction of Tunnel Lining Cross-Sections from Terrestrial Laser Scanning Point Clouds’, *Sensors*, vol. 16, no. 10,

Art. no. 10, Oct. 2016, doi: 10.3390/s16101648

[173] A. Sánchez-Rodríguez, M. Soilán, M. Cabaleiro, and P. Arias, 'Automated Inspection of Railway Tunnels' Power Line Using LiDAR Point Clouds', *Remote Sensing*, vol. 11, no. 21, Art. no. 21, Jan. 2019, doi: 10.3390/rs11212567

[174] N. Zhu, Y. Jiaa, and L. Luo, 'TUNNEL POINT CLOUD FILTERING METHOD BASED ON ELLIPTIC CYLINDRICAL MODEL', *Int. Arch. Photogramm. Remote Sens. Spatial Inf. Sci.*, vol. XLI-B1, pp. 735–740, Jun. 2016, doi: 10.5194/isprsarchives-XLI-B1-735-2016

[175] K. Loupos, A. D. Doulamis, C. Stentoumis, E. Protopapadakis, K. Makantasis, N. D. Doulamis, A. Amditis, P. Chrobocinski, J. Victores, R. Montero, E. Menendez, C. Balaguer, R. Lopez, M. Cantero, R. Navarro, A. Roncaglia, L. Belsito, S. Camarinopoulos, N. Komodakis, and P. Singh, 'Autonomous robotic system for tunnel structural inspection and assessment', *International Journal of Intelligent Robotics and Applications*, vol. 2, no. 1, pp. 43–66, Mar. 2018, doi: 10.1007/s41315-017-0031-9

[176] Z. Cao, D. Chen, Y. Shi, Z. Zhang, F. Jin, T. Yun, S. Xu, Z. Kang, and L. Zhang, 'A Flexible Architecture for Extracting Metro Tunnel Cross Sections from Terrestrial Laser Scanning Point Clouds', *Remote Sensing*, vol. 11, no. 3, Art. no. 3, Jan. 2019, doi: 10.3390/rs11030297

[177] C. Yi, D. Lu, Q. Xie, S. Liu, H. Li, M. Wei, and J. Wang, 'Hierarchical tunnel modeling from 3D raw LiDAR point cloud', *Computer-Aided Design*, vol. 114, pp. 143–154, Sep. 2019, doi: 10.1016/j.cad.2019.05.033

[178] Z. Gao, F. Li, Y. Liu, T. Cheng, Y. Su, Z. Fang, M. Yang, Y. Li, J. Yu, and Q. Zhang, 'Tunnel contour detection during construction based on digital image correlation', *Optics and Lasers in Engineering*, vol. 126, p. 105879, Mar. 2020, doi: 10.1016/j.optlaseng.2019.105879

[179] R. A. Pietersen, 'Automated Method for Airfield Pavement Condition Index Determination', Master Theses, Massachusetts Institute of Technology. Available: http://rightsstatements.org/page/InC-EDU/1.0/

[180] X. Peng, X. Zhong, C. Zhao, A. Chen, and T. Zhang, 'A UAV-based machine vision method for bridge crack recognition and width quantification through hybrid feature learning', *Construction and Building Materials*, vol. 299, p. 123896, Sep. 2021, doi: 10.1016/j.conbuildmat.2021.123896

[181] D. Li, Q. Xie, X. Gong, Z. Yu, J. Xu, Y. Sun, and J. Wang, ‘Automatic defect detection of metro tunnel surfaces using a vision-based inspection system’, *Advanced Engineering Informatics*, vol. 47, p. 101206, Jan. 2021, doi: 10.1016/j.aei.2020.101206

[182] C. Feng, H. Zhang, Y. Li, S. Wang, and H. Wang, ‘Efficient real-time defect detection for spillway tunnel using deep learning’, *J Real-Time Image Proc*, vol. 18, no. 6, pp. 2377–2387, Dec. 2021, doi: 10.1007/s11554-021-01130-x

[183] X. Cheng, X. Hu, K. Tan, L. Wang, and L. Yang, ‘Automatic Detection of Shield Tunnel Leakages Based on Terrestrial Mobile LiDAR Intensity Images Using Deep Learning’, *IEEE Access*, vol. 9, pp. 55300–55310, 2021, doi: 10.1109/ACCESS.2021.3070813

[184] Z. Yang, W. C. Lee, H. N. Chan, and M. Ge, ‘A Real-time Tunnel Surface Inspection System using Edge-AI on Drone’, in *2022 IEEE International Conference on Mechatronics and Automation (ICMA)*, Aug. 2022, pp. 749–754. doi: 10.1109/ICMA54519.2022.9856230

[185] J. Liao, Y. Yue, D. Zhang, W. Tu, R. Cao, Q. Zou, and Q. Li, ‘Automatic Tunnel Crack Inspection Using an Efficient Mobile Imaging Module and a Lightweight CNN’, *IEEE Transactions on Intelligent Transportation Systems*, vol. 23, no. 9, pp. 15190–15203, Sep. 2022, doi: 10.1109/TITS.2021.3138428

[186] B. Shi, M. Yang, J. Liu, B. Han, and K. Zhao, ‘Rail transit shield tunnel deformation detection method based on cloth simulation filtering with point cloud cylindrical projection’, *Tunnelling and Underground Space Technology*, vol. 135, p. 105031, May 2023, doi: 10.1016/j.tust.2023.105031

[187] Z. Xu, B. Chen, X. Zhan, Y. Xiu, C. Suzuki, and K. Shimada, ‘A Vision-Based Autonomous UAV Inspection Framework for Unknown Tunnel Construction Sites With Dynamic Obstacles’, *IEEE Robot. Autom. Lett.*, vol. 8, no. 8, pp. 4983–4990, Aug. 2023, doi: 10.1109/LRA.2023.3290415

[188] H. Huang, Q. Li, and D. Zhang, ‘Deep learning based image recognition for crack and leakage defects of metro shield tunnel’, *Tunnelling and Underground Space Technology*, vol. 77, pp. 166–176, Jul. 2018, doi: 10.1016/j.tust.2018.04.002

[189] Y. Dong, J. Wang, Z. Wang, X. Zhang, Y. Gao, Q. Sui, and P. Jiang, ‘A Deep-Learning-Based Multiple Defect Detection Method for Tunnel Lining Damages’, *IEEE Access*, vol. 7, pp. 182643–182657, 2019, doi: 10.1109/ACCESS.2019.2931074

[190] Y. Xu, D. Li, Q. Xie, Q. Wu, and J. Wang, ‘Automatic defect detection and segmentation of tunnel surface using modified Mask R-CNN’, *Measurement*, vol. 178, p. 109316, Jun. 2021, doi: 10.1016/j.measurement.2021.109316

[191] H. H. Chu, R. Cao, and L. Deng, ‘A collaborative inspection system composed of quadruped and flying robot for crack segmentation in tunnel environment’, in *Expanding Underground - Knowledge and Passion to Make a Positive Impact on the World*, CRC Press, 2023.

[192] A. Mirzazade, C. Popescu, J. Gonzalez-Libreros, T. Blanksvärd, B. Täljsten, and G. Sas, ‘Semi-autonomous inspection for concrete structures using digital models and a hybrid approach based on deep learning and photogrammetry’, *J Civil Struct Health Monit*, vol. 13, no. 8, pp. 1633–1652, Dec. 2023, doi: 10.1007/s13349-023-00680-x

[193] K. Jang, S. Park, H. Jung, H. Yoo, and Y.-K. An, ‘Deep learning-based 3D digital damage map of vertical-type tunnels using unmanned fusion data scanning’, *Automation in Construction*, vol. 162, p. 105397, Jun. 2024, doi: 10.1016/j.autcon.2024.105397

[194] R. Ali, J. Zeng, and Y.-J. Cha, ‘Deep learning-based crack detection in a concrete tunnel structure using multispectral dynamic imaging’, in *Smart Structures and NDE for Industry 4.0, Smart Cities, and Energy Systems*, SPIE, Apr. 2020, pp. 12–19. doi: 10.1117/12.2557900. Available: https://www.spiedigitallibrary.org/conference-proceedings-of-spie/11382/1138203/Deep-learning-based-crack-detection-in-a-concrete-tunnel-structure/10.1117/12.2557900.full. [Accessed: Mar. 25, 2024]

[195] Y. Ren, J. Huang, Z. Hong, W. Lu, J. Yin, L. Zou, and X. Shen, ‘Image-based concrete crack detection in tunnels using deep fully convolutional networks’, *Construction and Building Materials*, vol. 234, p. 117367, Feb. 2020, doi: 10.1016/j.conbuildmat.2019.117367

[196] L. Ngeljaratan, E. E. Bas, and M. A. Moustafa, ‘Unmanned Aerial Vehicle-Based Structural Health Monitoring and Computer Vision-Aided Procedure for Seismic Safety Measures of Linear Infrastructures’, *Sensors*, vol. 24, no. 5, Art. no. 5, Jan. 2024, doi: 10.3390/s24051450

[197] M. A. A. Sourav, M. Mahedi, H. Ceylan, S. Kim, C. Brooks, D. Peshkin, R. Dobson, and M. Brynick, ‘Evaluation of Small Uncrewed Aircraft Systems Data in Airfield Pavement Crack Detection and Rating’, *Transportation Research Record*, vol. 2677, no. 1, pp. 653–668, Jan. 2023, doi:

10.1177/03611981221101030

[198] A. S. Matveev and A. V. Savkin, 'Proofs of Technical Results Justifying an Algorithm of Reactive 3D Navigation of a Mobile Robot through an Unknown Tunnel', *arXiv e-prints*, p. arXiv:1803.00803, Mar. 2018, doi: 10.48550/arXiv.1803.00803

[199] A. S. Matveev, V. V. Magerkin, and A. V. Savkin, 'A method of reactive control for 3D navigation of a nonholonomic robot in tunnel-like environments', *Automatica*, vol. 114, p. 108831, Apr. 2020, doi: 10.1016/j.automatica.2020.108831

[200] A. V. Savkin and C. Wang, 'A method for collision free navigation of non-holonomic 3D robots in unknown tunnel like environments', in *2017 IEEE International Conference on Robotics and Biomimetics (ROBIO)*, Macau: IEEE, Dec. 2017, pp. 936–940. doi: 10.1109/ROBIO.2017.8324537

[201] D. C. Robinson, H. Chung, and K. Ryan, 'Numerical investigation of a hovering micro rotor in close proximity to a ceiling plane', *Journal of Fluids and Structures*, vol. 66, pp. 229–253, Oct. 2016, doi: 10.1016/j.jfluidstructs.2016.08.001

[202] H. Liang, S.-C. Lee, W. Bae, J. Kim, and S. Seo, 'Towards UAVs in Construction: Advancements, Challenges, and Future Directions for Monitoring and Inspection', *Drones*, vol. 7, no. 3, p. 202, Mar. 2023, doi: 10.3390/drones7030202

[203] 'Mavic 2 Enterprise Series - Specifications - DJI', *DJI Official*. Available: https://www.dji.com/ie/mavic-2-enterprise/specs. [Accessed: Jul. 14, 2023]

[204] 'Mobile SDK Introduction - DJI Mobile SDK Documentation'. Available: https://developer.dji.com/mobile-sdk/documentation/introduction/mobile_sdk_introduction.html. [Accessed: Mar. 27, 2023]

[205] Z. Chen, X. Luo, and B. Dai, 'Design of Obstacle Avoidance System for Micro-UAV Based on Binocular Vision', in *2017 International Conference on Industrial Informatics - Computing Technology, Intelligent Technology, Industrial Information Integration (ICIICII)*, Dec. 2017, pp. 67–70. doi: 10.1109/ICIICII.2017.87

[206] Y. Pan, Y. Dong, D. Wang, A. Chen, and Z. Ye, 'Three-Dimensional

Reconstruction of Structural Surface Model of Heritage Bridges Using UAV-Based Photogrammetric Point Clouds', *Remote Sensing*, vol. 11, no. 10, p. 1204, Jan. 2019, doi: 10.3390/rs11101204

[207] Y. Tan, G. Li, R. Cai, J. Ma, and M. Wang, 'Mapping and modelling defect data from UAV captured images to BIM for building external wall inspection', *Automation in Construction*, vol. 139, p. 104284, Jul. 2022, doi: 10.1016/j.autcon.2022.104284

[208] R. Mudura, A. Trif, B. Nedelcu, and C. Bara, 'Calculate the Volume of Landfill Cristeşti, Mureş Using the Classical Method and Digital Terrain Model Using Pictures from Uav', in *14th International Multidisciplinary Scientific Geoconference (SGEM) 2014*, Albena, Bulgaria,: Общество с ограниченной ответственностью СТЕФ92 Технолоджи, 2014, pp. 113–120. doi: 10.5593/SGEM2014/B22/S9.015

[209] S. Agnisarman, S. Lopes, K. Chalil Madathil, K. Piratla, and A. Gramopadhye, 'A survey of automation-enabled human-in-the-loop systems for infrastructure visual inspection', *Automation in Construction*, vol. 97, pp. 52–76, Jan. 2019, doi: 10.1016/j.autcon.2018.10.019

[210] W. Bergeson, S. L. Ernst, and United States. Federal Highway Administration, 'Tunnel Operations, Maintenance, Inspection, and Evaluation (TOMIE) Manual', FHWA-HIF-15-005, Jul. 2015. Available: https://rosap.ntl.bts.gov/view/dot/42887. [Accessed: Nov. 28, 2023]

[211] A. Kirillov, E. Mintun, N. Ravi, H. Mao, C. Rolland, L. Gustafson, T. Xiao, S. Whitehead, A. C. Berg, W.-Y. Lo, P. Dollár, and R. Girshick, 'Segment Anything', *arXiv e-prints*, p. arXiv:2304.02643, Apr. 2023, doi: 10.48550/arXiv.2304.02643

[212] 'Story Map Series'. Available: https://dcenr.maps.arcgis.com/apps/MapSeries/index.html?appid=a30af518e87a4c0ab2fbde2aaac3c228. [Accessed: Jun. 23, 2023]

[213] R. Ali, D. Kang, G. Suh, and Y.-J. Cha, 'Real-time multiple damage mapping using autonomous UAV and deep faster region-based neural networks for GPS-denied structures', *Automation in Construction*, vol. 130, p. 103831, Oct. 2021, doi: 10.1016/j.autcon.2021.103831

[214] N. Mullally, 'Dublin Port Tunnel Project'. Available: https://dublintunnel.ie/wp-content/uploads/pdf/dublin-tunnel-press-pack.pdf. [Accessed: Oct. 04, 2023]

[215] A. Gillarduzzi, ‘Investigating property damage along Dublin Port Tunnel alignment’, *Proceedings of the Institution of Civil Engineers - Forensic Engineering*, vol. 167, no. 3, pp. 119–130, Aug. 2014, doi: 10.1680/feng.13.00024

[216] C. Wang, M. Friedman, and Z. Li, ‘Monitoring and assessment of a cross-passage twin tunnel long-term performance using Wireless Sensor Network’, *Canadian Geotechnical Journal*, Jan. 2023, doi: 10.1139/cgj-2022-0224. Available: https://cdnsciencepub.com/doi/abs/10.1139/cgj-2022-0224. [Accessed: May 29, 2023]

[217] M. Y. Arafat, M. M. Alam, and S. Moh, ‘Vision-Based Navigation Techniques for Unmanned Aerial Vehicles: Review and Challenges’, *Drones*, vol. 7, no. 2, Art. no. 2, Feb. 2023, doi: 10.3390/drones7020089

[218] R. Zhang, G. Hao, K. Zhang, and Z. Li, ‘Reactive UAV-based automatic tunnel surface defect inspection with a field test’, *Automation in Construction*, vol. 163, p. 105424, Jul. 2024, doi: 10.1016/j.autcon.2024.105424

[219] Z. Li, K. Soga, and P. Wright, ‘Long-term performance of cast-iron tunnel cross passage in London clay’, *Tunnelling and Underground Space Technology*, vol. 50, pp. 152–170, Aug. 2015, doi: 10.1016/j.tust.2015.07.005

[220] Md. A. A. Sourav, H. Ceylan, C. Brooks, D. Peshkin, S. Kim, R. Dobson, C. Cook, O. Brouillette, and C. and E. E. Iowa State University. Department of Civil, ‘Small Unmanned Aircraft System for Pavement Inspection: Task 4—Execute the Field Demonstration Plan and Analyze the Collected Data’, DOT/FAA/TC-22/35, Nov. 2022. doi: 10.21949/1524511. Available: https://rosap.ntl.bts.gov/view/dot/64743. [Accessed: Aug. 09, 2023]

[221] K. Soga, R. G. Laver, and Z. Li, ‘Long-term tunnel behaviour and ground movements after tunnelling in clayey soils’, *Underground Space*, vol. 2, no. 3, pp. 149–167, Sep. 2017, doi: 10.1016/j.undsp.2017.08.001

[222] D. O. ’Brien, J. Andrew Osborne, E. Perez-Duenas, R. Cunningham, and Z. Li, ‘Automated crack classification for the CERN underground tunnel infrastructure using deep learning’, *Tunnelling and Underground Space Technology*, vol. 131, p. 104668, Jan. 2023, doi: 10.1016/j.tust.2022.104668

[223] H. Wang, H. Huang, Y. Feng, and D. Zhang, ‘Characterization of Crack and Leakage Defects of Concrete Linings of Road Tunnels in China’, *ASCE-ASME Journal of Risk and Uncertainty in Engineering Systems, Part A: Civil*

Engineering, vol. 4, no. 4, p. 04018041, Dec. 2018, doi: 10.1061/AJRUA6.0000989

[224] G. Xu, C. He, Z. Chen, C. Liu, B. Wang, and Y. Zou, ‘Mechanical behavior of secondary tunnel lining with longitudinal crack’, *Engineering Failure Analysis*, vol. 113, p. 104543, Jul. 2020, doi: 10.1016/j.engfailanal.2020.104543

[225] X. Gu, K. Xiong, J. Zhang, and H. Chen, ‘A Comprehensive Analysis on Integrity Conservation of World Natural Heritage Site and Buffer Zone Tourism Development with an Implication for Karst Heritage Sites’, *Geoheritage*, vol. 15, no. 1, p. 8, Dec. 2022, doi: 10.1007/s12371-022-00779-5

[226] P. Mansilla-Quiñones, H. Manríquez, and A. Moreira-Muñoz, ‘Virtual Heritage: A Model of Participatory Knowledge Construction Toward Biogeocultural Heritage Conservation’, in *Global Geographical Heritage, Geoparks and Geotourism: Geoconservation and Development*, R. B. Singh, D. Wei, and S. Anand, Eds., in Advances in Geographical and Environmental Sciences. Singapore: Springer, 2021, pp. 75–94. doi: 10.1007/978-981-15-4956-4_5. Available: https://doi.org/10.1007/978-981-15-4956-4_5. [Accessed: Oct. 20, 2023]

[227] S. Granados-Bolaños, A. Quesada-Román, and G. E. Alvarado, ‘Low-cost UAV applications in dynamic tropical volcanic landforms’, *Journal of Volcanology and Geothermal Research*, vol. 410, p. 107143, Feb. 2021, doi: 10.1016/j.jvolgeores.2020.107143

[228] G. Tronti, F. Vergari, I. M. Bollati, F. Belisario, M. Del Monte, M. Pelfini, and P. Fredi, ‘From landslide characterization to nature reserve management: The “Scialimata Grande di Torre Alfina” landslide Geosite (Central Apennines, Italy)’, *J. Mt. Sci.*, vol. 20, no. 3, pp. 585–606, Mar. 2023, doi: 10.1007/s11629-022-7596-y

[229] S. Mineo, G. Pappalardo, and S. Onorato, ‘Geomechanical Characterization of a Rock Cliff Hosting a Cultural Heritage through Ground and UAV Rock Mass Surveys for Its Sustainable Fruition’, *Sustainability*, vol. 13, no. 2, p. 924, Jan. 2021, doi: 10.3390/su13020924

[230] K. Themistocleous, ‘The Use of UAVs for Cultural Heritage and Archaeology’, in *Remote Sensing for Archaeology and Cultural Landscapes*, D. G. Hadjimitsis, K. Themistocleous, B. Cuca, A. Agapiou, V. Lysandrou, R. Lasaponara, N. Masini, and G. Schreier, Eds., in Springer Remote Sensing/Photogrammetry. Cham: Springer International Publishing, 2020, pp. 241–269. doi: 10.1007/978-

3-030-10979-0_14. Available: http://link.springer.com/10.1007/978-3-030-10979-0_14. [Accessed: Feb. 20, 2024]

[231] S. Berquist, G. Spence-Morrow, F. Gonzalez-Macqueen, B. Rizzuto, W. Y. Álvarez, S. Bautista, and J. Jennings, 'A new aerial photogrammetric survey method for recording inaccessible rock art', *Digital Applications in Archaeology and Cultural Heritage*, vol. 8, pp. 46–56, Mar. 2018, doi: 10.1016/j.daach.2018.03.001

[232] Abdalrahman Ramzi Qubaa, Rayan Ghazi Thannoun, and Rwaed Muwafaq Mohammed, 'UAVs/drones for photogrammetry and remote sensing: Nineveh archaeological region as a case study', *World J. Adv. Res. Rev.*, vol. 14, no. 3, pp. 358–368, Jun. 2022, doi: 10.30574/wjarr.2022.14.3.0539

[233] D. Ebolese, M. Lo Brutto, and G. Dardanelli, 'UAV SURVEY FOR THE ARCHAEOLOGICAL MAP OF *LILYBAEUM* (MARSALA, ITALY)', *The International Archives of the Photogrammetry, Remote Sensing and Spatial Information Sciences*, vol. XLII-2-W11, pp. 495–502, May 2019, doi: 10.5194/isprs-archives-XLII-2-W11-495-2019

[234] 'How we use drones', *British Geological Survey*. Available: https://www.bgs.ac.uk/about-bgs/our-work/how-we-use-drones/. [Accessed: Oct. 20, 2023]

[235] M. Hincapie, L. M. Cifuentes, A. Valencia-Arias, and J. Quiroz-Fabra, 'Geoheritage and immersive technologies: bibliometric analysis and literature review', *Episodes Journal of International Geoscience*, vol. 46, no. 1, pp. 101–115, Mar. 2023, doi: 10.18814/epiiugs/2022/022016

[236] N. Cayla, 'An Overview of New Technologies Applied to the Management of Geoheritage', *Geoheritage*, vol. 6, no. 2, pp. 91–102, Jun. 2014, doi: 10.1007/s12371-014-0113-0

[237] F. Pasquaré Mariotto and F. L. Bonali, 'Virtual Geosites as Innovative Tools for Geoheritage Popularization: A Case Study from Eastern Iceland', *Geosciences*, vol. 11, no. 4, Art. no. 4, Apr. 2021, doi: 10.3390/geosciences11040149

[238] G. S. Rossi, M. D. G. M. Garcia, and C. L. M. Bourotte, 'Educational Materials on Geosciences: Analysis from UNESCO Global Geoparks and Potential for Application to Protected Areas', *Geoconservation Research*, vol. 5, no. 1, pp. 165–194, Jun. 2022, doi: 10.30486/gcr.2022.1958014.1106

[239] D. Jankauskienė, I. Kuklys, L. Kuklienė, and B. Ruzgienė, 'Surface modelling of a unique heritage object: use of UAV combined with camera and LiDAR for mound inspection', in *26th Annual International Scientific Conference 'Research for Rural Development 2020'*, Jelgava, Latvia: The Latvia University of Life Sciences and Technologies, Oct. 2020, pp. 207–212. doi: 10.22616/rrd.26.2020.030

[240] C. Fassoulas, E. Nikolakakis, and S. Staridas, 'Digital Tools to Serve Geotourism and Sustainable Development at Psiloritis UNESCO Global Geopark in COVID Times and Beyond', *Geosciences*, vol. 12, no. 2, Art. no. 2, Feb. 2022, doi: 10.3390/geosciences12020078

[241] F. Pasquaré Mariotto, V. Antoniou, K. Drymoni, F. L. Bonali, P. Nomikou, L. Fallati, O. Karatzaferis, and O. Vlasopoulos, 'Virtual Geosite Communication through a WebGIS Platform: A Case Study from Santorini Island (Greece)', *Applied Sciences*, vol. 11, no. 12, Art. no. 12, Jan. 2021, doi: 10.3390/app11125466

[242] 'Inspire 2 - DJI', *DJI Official*. Available: https://www.dji.com/ie/inspire-2. [Accessed: Oct. 20, 2023]

[243] N. M. Shaffie and E. H. B. Ariffin, 'BEACH PROFILE USING UNMANNED AERIAL VEHICLE IMAGERY', *Universiti Malaysia Terengganu Journal of Undergraduate Research*, vol. 3, no. 4, Art. no. 4, Oct. 2021, doi: 10.46754/umtjur.v3i4.242

[244] M. Gil-Docampo, S. Peña-Villasenín, A. M. S. Bettencourt, J. Ortiz-Sanz, and S. Peraleda-Vázquez, '3D geometric survey of cultural heritage by UAV in inaccessible coastal or shallow aquatic environments', *Archaeological Prospection*, vol. n/a, no. n/a, May 2023, doi: 10.1002/arp.1901. Available: https://onlinelibrary.wiley.com/doi/abs/10.1002/arp.1901. [Accessed: Oct. 20, 2023]

[245] M. Parkes, R. Meehan, and S. Préteseille, 'The Geological Heritage of Waterford', 2012.

[246] M. Parkes, S. Gatley, and V. Gallagher, 'Old Volcanic Stories—Bringing Ancient Volcanoes to Life in Ireland's Geological Heritage Sites', *Geosciences*, vol. 11, no. 2, Art. no. 2, Feb. 2021, doi: 10.3390/geosciences11020052

[247] R. K. Dowling and D. Newsome, *Global Geotourism Perspectives*. Oxford: Goodfellow Publishers Ltd, 2010.

[248] I. Santos, R. Henriques, G. Mariano, and D. I. Pereira, ‘Methodologies to Represent and Promote the Geoheritage Using Unmanned Aerial Vehicles, Multimedia Technologies, and Augmented Reality’, *Geoheritage*, vol. 10, no. 2, pp. 143–155, Jun. 2018, doi: 10.1007/s12371-018-0305-0

[249] ‘Integration of low altitude aerial & terrestrial photogrammetry data in 3D heritage building modeling | IEEE Conference Publication | IEEE Xplore’. Available: https://ieeexplore.ieee.org/abstract/document/6287166. [Accessed: Oct. 20, 2023]

[250] C. Glanville and S. Gatley, ‘Geoheritage conservation developments in Ireland – an update’, *Irish Journal of Earth Sciences*, vol. 40, no. 1, pp. 115–129, 2022.

[251] F. Hurley, ‘A Preliminary Account of an Archaeological Excavation at Tankardstown (Knockmahon) Copper Mine, Bunmahon, Co. Waterford’, *Journal of the Mining Heritage Trust of Ireland*, vol. 5, pp. 11–14, 2005.